



Swansea University
Prifysgol Abertawe

Understanding and Engineering of Sub-gap States in Photodetection

Submitted to
Swansea University

in fulfilment of the requirements for the Degree of
Doctor of Philosophy

Submitted by

Christina Kaiser

1st supervisor: Paul Meredith
2nd supervisor: Ardalan Armin

2022

Abstract

Emerging applications for light sensing, including wearable electronics, internet of things and autonomous driving, are pushing conventional semiconductors technologies to their limits when it comes to ease of fabrication, power consumption and device design. Organic semiconductors are considered next-generation absorber materials for photodetection in the visible and near infrared part of the electromagnetic spectrum, which hold some promise of addressing the aforementioned problems of conventional materials. So far, only a handful of companies are putting organic semiconductors to the test for commercial photodetectors, however, research on organic photodetectors is thriving – in particular on photodetectors with a diode architecture called photodiodes. The goal is to make flexible, light-weight devices with improved performance metrics and high stability to realize viable alternatives to conventional photodiodes. The performance limits of organic photodiodes are often associated with the presence of electronic states with energies below the bandgap edge – the so-called sub-gap states. A powerful tool to study the properties of sub-gap states is to measure the external quantum efficiency (EQE), however, the subsequent analysis is complicated by the presence of static disorder and optical interference. In the first part of this work, it is shown how the true absorption coefficient can be extracted from a series of interference affected sub-gap EQE spectra of organic photodiodes with different thicknesses. In consequence, the effect of chemical structure modification on the absorption coefficient in the spectral range of charge transfer absorption is demonstrated. By adjusting the molecular energy levels through target chemical substitutions, a redshift and an increase of the oscillator strength are achieved. The increased spectral coverage in the near infrared is then exploited in micro-cavity photodiodes. The second part of this work deals with the sub-gap absorption coefficient of donor and acceptor materials and how it is affected by the molecular energy level offset. For materials with low energetic offset, it is shown that the sub-gap absorption coefficient follows the Urbach rule in the spectral range of excitonic absorption, dictating the broadening of the sub-gap absorption coefficient at energies right below the bandgap. Lastly, the origin of the high dark current in organic photodiodes is identified as non-radiative recombination via mid-gap trap states. An upper limit to the specific detectivity is calculated that is expected viable in organic photodiodes. The findings of this thesis contribute to the understanding of the sub-gap states by studying their absorption features and distinguishing them from the ubiquitous optical interference effects. The spectroscopic observation of mid-gap trap states is linked to the dark current generation dictating the upper performance limits of organic photodiodes.

Declaration

This work has not previously been accepted in substance for any degree and is not being concurrently submitted in candidature for any degree.

Signature:  (Christina Kaiser)

Date: 15 March 2022

This thesis is the result of my own investigations, except where otherwise stated. Where correction services have been used, the extent and nature of the correction is clearly marked in a footnote.

Other sources are acknowledged by footnotes giving explicit references. A bibliography is appended.

Signature:  (Christina Kaiser)


Date: 15 March 2022

I hereby give consent for my thesis, if accepted, to be available for photocopying and for inter-library loan, and for the title and summary to be made available to outside organisations.

Signature:  (Christina Kaiser)

Date: 15 March 2022

The University's ethical procedures have been followed and, where appropriate, that ethical approval has been granted.

Signature:  (Christina Kaiser)

Date: 15 March 2022

Acknowledgments

I would like to express my gratitude to my supervisors **Prof. Paul Meredith** and **Dr. Ardalan Armin**, who gave me the opportunity to work on those interdisciplinary topics at the edge between chemistry, applied physics and electrical engineering. They took the calculated risk of employing someone with a chemistry background and gave me the freedom to finish ongoing projects from my Master thesis and to develop at my own pace. I cannot thank them enough for the discussions we had, the proofreading, their bright ideas and vision for my projects as well as the confidence they always displayed in me and my capabilities. Secondly, I am especially grateful to **Dr. Oskar J. Sandberg**, who provided the theoretical framework and guidance for the publications on Urbach energy and mid-gap mediated dark current. Without his contributions, I would have never come so far! Thirdly, my special thanks go to **Prof. Dr. Ir. Koen Vandewal** from the Hasselt University, who already supported me during my Master thesis and stayed a constant companion during my Ph.D. journey. To this point, I am also grateful to **Dr. Sam Gielen** from Hasselt University: The two weeks with him in the lab may have been the most productive two weeks during my Ph.D., while the writing process on our joint publications may have been just the most efficient writing process during my Ph.D. Moreover, I have had the privilege of working with **Prof. Qianqian Lin** and his group in Wuhan University, who made me feel warmly welcomed and provided constant support during my stay. At this point, I would also like to thank **Dr. Wei Li** and his wife **Huijun Zhang**, without whom my adventures in Wuhan would have been only half as memorable. Strongly appreciated was also Dr. Wei Li's indispensable support in the cleanroom and his readiness to supply me with devices in the shortest amount of time humanly possible. Special thanks go to **Dr. Stefan Zeiske**, my fellow Ph.D. student in crime, for all the laughing and grumbling during laboratory build-up and national lockdown – without him lockdown would have been unbearably lonely. Moreover, I would like to thank the support team of the Sêr Sam group including **Rhian Jones**, **Heather Evans**, **Paul Hughes** and **Ryan Bigham**, who made my life at Swansea University much more carefree leaving me with more time for the essentials. And of course, I will never forget each and every Sêr Sam group member with whom I had the fortune to discuss, to laugh, to travel and to learn new things. My time in Swansea will always be cherished. Abgesehen von meinen Kollegen, möchte ich auch Danke sagen an die einzigartige, bald "Dr.", **Kristina Ditte** für die emotionale Unterstützung und unsere Freundschaft, auf die ich mich immer verlassen konnte und kann. Zum Schluss geht mein herzlichster Dank geht an meine Familie bestehend aus **Valentina**, **Katharina** and **Ralf**. Nach Hause kommen war noch nie so schön gewesen.

Contents

List of Publications	x
List of Acronyms	xiii
List of Figures	xiv
List of Tables	xvii
1 Introduction	1
2 Fundamentals and Concepts	4
2.1 Light Absorption in Organic Thin Films	4
2.1.1 Optics of Thin Films	4
2.1.2 Conjugated Organic Molecules	9
2.1.3 Franck-Condon Principle	12
2.1.4 Marcus Theory	14
2.1.5 Static Disorder	15
2.1.6 Charge Transfer Absorption	18
2.2 Electronic Processes in Organic Photodiodes	21
2.2.1 Bands and Fermi Levels	21
2.2.2 Charge Generation	24
2.2.3 Free Charge Carrier Recombination	26
2.2.4 Charge Transport	28
2.3 Characterization of Organic Photodiodes	31
2.3.1 External Quantum Efficiency and Responsivity	31
2.3.2 Current-Voltage Characteristics	32
2.3.3 Sources of Noise	34
2.3.4 Specific Detectivity and Noise Equivalent Power	36
2.3.5 Linear Dynamic Range	37
2.3.6 Photodetector Speed	39
2.4 Organic Near-infrared Photodiodes	42
2.4.1 Organic Semiconductors for Photodetection	42
2.4.2 Bulk Heterojunction Organic Photodiodes	43
2.4.3 Organic Photodetectors with Charge Collection Narrowing . . .	45
2.4.4 Micro-cavity Enhanced Organic Photodetectors	46
2.4.5 Organic Photodetectors with Photomultiplication	47

3	Experimental Methods	49
3.1	Materials	50
3.2	Device Fabrication	51
3.2.1	Solution Processed Devices	51
3.2.2	Thermally Evaporated Devices	55
3.3	Spectroscopic Ellipsometry	55
3.4	Light Current-Voltage Characterization	56
3.5	Dark Current-Voltage Characterization	56
3.6	External Quantum Efficiency Measurements	57
3.7	Electrical Noise Measurements	58
3.8	Linear Dynamic Range	60
3.9	Frequency Response	62
4	Determining Subgap Absorption Coefficients	64
4.1	Experimental Sub-gap Absorption Coefficient	65
4.2	Optical Constants from Spectroscopic Ellipsometry	66
4.3	Numerical Sub-gap Absorption Coefficient	67
4.4	External Quantum Efficiency Simulations	72
4.5	Absorption of Trap States	74
4.6	Noise Equivalent External Quantum Efficiency	75
4.7	Conclusions	76
5	Manipulating the Charge Transfer Absorption for Narrowband Light Detection in the Near-Infrared	77
5.1	Bispyranylidene for Near-Infrared Detection	78
5.2	Spectral Line-shape of the External Quantum Efficiency	79
5.3	Influence of Substitution on Charge Transfer Absorption	83
5.4	Cavity Enhanced Near-Infrared Detectors	84
5.5	Conclusions	86
6	Universal Urbach Rule for Organic Semiconductors	87
6.1	Disorder Induced Broadening of the Sub-gap Absorption Coefficient	88
6.2	Definition of the Apparent Urbach Energy	89
6.3	Apparent Urbach Energy Spectra	89
6.4	Influence of Optical Interference on the Apparent Urbach Energy	92
6.5	Temperature-dependent External Quantum Efficiency	95
6.6	Modelling the Sub-gap Absorption Coefficient	95
6.7	Radiative Open-Circuit Voltage Losses	101
6.8	Conclusions	102
7	Intrinsic Detectivity Limits of Organic Near-Infrared Detectors	104
7.1	Current-Voltage Characteristics of Narrow-gap Photodiodes	105
7.2	Specific Detectivity of Narrow-gap Photodiodes	108
7.3	Intrinsic Non-radiative Voltage Losses	113
7.4	Conclusion	115

8	Mid-gap Trap State Mediated Dark Current in Organic Photodiodes	116
8.1	External Quantum Efficiency of Narrow-gap Photodiodes	117
8.2	Temperature Dependent Dark Current Measurements	119
8.3	New Diode Equation based on Shockley-Read-Hall	121
8.4	New Specific Detectivity Limit based on Shockley-Read-Hall Recombination	124
8.5	Open-circuit Voltage in the Limit of Shockley-Read-Hall Recombination	126
8.6	Conclusions	127
9	Conclusions and Outlook	128
9.1	Conclusions	128
9.2	Outlook	130
A	Manipulating the Charge Transfer Absorption for Narrowband Light Detection in the Near-Infrared	132
A.1	Device Architecture	132
A.2	Cyclic Voltammetry	133
A.3	Density Functional Theory Calculations	134
B	Universal Urbach Rule for Organic Semiconductors	137
B.1	Temperature-dependent EQE	137
B.2	Marcus Theory for Unequal Potentials	138
C	Mid-gap Trap State Mediated Dark Current in Organic Photodiodes	140
C.1	Absorbance Spectra of Low-Gap Donor Polymers	140
C.2	Current-Voltage Characteristics of Low-gap Blends	141
C.3	EQE _{EL} Spectra	142
C.4	Shockley-Read-Hall Recombination Mediated Dark Current	143
	Bibliography	146

List of Publications

Peer Reviewed Articles

1. C. Kaiser, S. Zeiske, P. Meredith, A. Armin, *Determining Ultralow Absorption Coefficients of Organic Semiconductors from the Sub-Bandgap Photovoltaic External Quantum Efficiency*, Adv. Opt. Mater. **8**, 1901542 (2019).
2. C. Kaiser, K. S. Schellhammer, J. Benduhn, B. Siegmund, M. Tropiano, O. Zeika, F. Ortmann, P. Meredith, A. Armin, K. Vandewal, *Manipulating the Charge Transfer Absorption for Narrowband Light Detection in the Near-Infrared*, Chem. Mater. **31**, 9325 (2019).
3. S. Gielen, C. Kaiser, F. Verstraeten, J. Kublitski, J. Benduhn, D. Spoltore, P. Verstappen, W. Maes, P. Meredith, A. Armin, K. Vandewal, *Intrinsic Detectivity Limits of Organic Near-Infrared Photodetectors*, Adv. Mater. **32**, 2003818 (2020).
4. C. Kaiser, O. J. Sandberg, N. Zarrabi, W. Li, P. Meredith, A. Armin, *A Universal Urbach Rule for Disordered Organic Semiconductors*, Nat. Commun. **12**, 3988 (2021).
5. C. Kaiser, O. J. Sandberg, S. Zeiske, S. Gielen, W. Maes, K. Vandewal, P. Meredith, A. Armin, *Mid-gap Trap State Mediated Dark Current in Organic Photodiodes*, in press (2021).
6. S. Zeiske, C. Kaiser, P. Meredith, A. Armin, *Sensitivity of Sub-Bandgap External Quantum Efficiency Measurements of Solar Cells under Electrical and Light Bias*, ACS Photonics **7**, 256 (2019).
7. R. Kerremans, C. Kaiser, W. Li, N. Zarrabi, P. Meredith, A. Armin, *The Optical Constants of Solution-Processed Semiconductors – New Challenges with Perovskites and Non-Fullerene Acceptors*, Adv. Opt. Mater. **8**, (2020).
8. A. Armin, N. Zarrabi, O. J. Sandberg, C. Kaiser, S. Zeiske, W. Li, P. Meredith, *Limitations of Charge Transfer State Parameterization Using Photovoltaic External Quantum Efficiency*, Adv. Energy Mater. **10**, 2001828 (2020).
9. J. Kublitski, A. Hofacker, B. K. Boroujeni, J. Benduhn, V. C. Nikolis, C. Kaiser, D. Spoltore, H. Kleemann, A. Fischer, F. Ellinger, K. Vandewal, K. Leo, *Reverse*

Dark Current in Organic Photodetectors and the Major Role of Traps as Source of Noise, Nat. Commun. **12**, 551 (2021).

10. N. Zarrabi, O. J. Sandberg, C. Kaiser, J. Subbiah, D. J. Jones, P. Meredith, A. Armin, *Experimental Evidence Relating Charge-Transfer-State Kinetics and Strongly Reduced Bimolecular Recombination in Organic Solar Cells*, J. Phys. Chem. Lett. **11**, 10519 (2020).

Patents

1. O. Zeika, C. Kaiser, K. Vandewal, B. Siegmund, J. Benduhn, M. Tropicano *Bispyranilidene, Dithiobispyranilidene Und Diselenobispyranilidene Und Deren Verwendung*, DE102019114456A1 (2019).

List of Acronyms

A	acceptor
BHJ	bulk heterojunction
CMOS	complementary metal-oxide semiconductor
CT	charge transfer
CV	cyclic voltammetry
D	donor
D-A	donor-acceptor
D:A	donor:acceptor
DFT	density functional theory
DOS	density of states
DUT	device under test
EA	electron affinity
eq	equivalent
et al.	et alii (latin: and others)
EL	electroluminescence
ETL	electron transport layer
FFT	fast fourier transform
FWHM	full width at half maximum
HOMO	highest occupied molecular orbital
HTL	hole transport layer
IAPP	Institut for Applied Physics and Photonic Materials
IP	ionization potential
IQE	internal quantum efficiency
LDR	linear dynamic range
LUMO	lowest unoccupied molecular orbital
Me	methyl
M _w	molecular weight
NEP	noise equivalent power
NIR	near-infrared
OLED	organic light emitting diode
OMe	methoxy
OPD	organic photodetector
OSC	organic solar cell
PCE	power conversion efficiency
PDS	photothermal deflection spectroscopy
Ph	phenyl
RBW	resolution bandwidth
RT	room temperature

SNR	signal-to-noise ratio
(s)EQE	(sensitive) external quantum efficiency
UV	ultraviolet
UV-Vis	ultraviolet-visible
VIS	visible

List of Figures

2.1	Light propagation in a multi-layer stack	5
2.2	Transfer matrix simulations	7
2.3	Electric field distribution in a cavity-enhanced photodiode	8
2.4	Molecular structures of some important organic semiconductors	10
2.5	Basics of molecular orbital theory	11
2.6	Franck-Condon principle	13
2.7	Stokes shift and reciprocity between absorption and emission spectra	14
2.8	Marcus theory applied to optical transitions	15
2.9	Density of states in disordered organic and crystalline inorganic semiconductors	16
2.10	Charge transfer absorption at molecular interfaces	18
2.11	Fermi-Dirac distributions in function of temperature, doping and illumination	22
2.12	Bandgaps and energy levels in organic and inorganic semiconductors	24
2.13	Different types of excitons	25
2.14	Jablonski-diagram for charge generation and recombination in organic semiconductors	26
2.15	Recombination pathways in organic semiconductors	27
2.16	Current-voltage characteristics under illumination and in the dark	33
2.17	Noise spectral density	35
2.18	Linear dynamic range	38
2.19	Device architecture of a bulk heterjunction organic photodiode	45
2.20	Device architecture of an organic photodiode with charge collection narrowing	46
2.21	Device architecture of a bulk heterjunction organic photodiode	47
2.22	Device architecture of an organic photodiode with photomultiplication	48
3.1	Layout of solution-processed organic photodiodes	52
3.2	Layout of vacuum-deposited organic photodiodes	55
3.3	Experimental setup of the EQE apparatus	58
3.4	Experimental setup for noise measurements	59
3.5	Exemplary noise current spectra	60
3.6	Experimental setup of the LDR apparatus	61
3.7	Photocurrent in function of light attenuation	62
3.8	Experimental setup for measuring the frequency response	63

4.1	Spectroscopic ellipsometry obtained refractive indices of PBTTT:PC ₇₁ BM and PBDB-T:ITIC	67
4.2	Process flow to numerically obtain the sub-gap absorption coefficient	69
4.3	Absorptance and IQE of PBDB-T:ITIC photodiodes	70
4.4	Absorptance and IQE of PBTTT:PC ₇₁ BM photodiodes	71
4.5	Experimental and simulated EQE spectra of PBDB-T:ITIC and PBTTT:PC ₇₁ BM	72
4.6	Gaussian fit to the sub-gap absorption coefficient of PBTTT:PC ₇₁ BM	74
4.7	Simulated sub-gap absorptance for different active layer thicknesses	74
4.8	Noise equivalent EQE of the PBDB-T:ITIC photodiode	76
5.1	Chemical structure of the molecules with a bi(thio)pyranylidene core	79
5.2	EQE spectra of D8:C ₆₀ and D1:C ₆₀ organic photodiodes	80
5.3	EQE of the D:C ₆₀ photodiodes under reverse bias	81
5.4	Calculated “IQE” of D:C ₆₀ photodiodes under reverse bias	81
5.5	IQE of D:C ₆₀ photodiodes at 0 V	82
5.6	Gaussian fit parameters in function of molecular substitution	83
5.7	EQE of photodiodes with and without cavity enhancement	84
5.8	FWHM of cavity enhanced photodiodes	86
5.9	Voltage dependent noise spectra of cavity enhanced photodiodes	86
6.1	D:A blends with different energetic offsets between E_{CT} and E_{opt}	90
6.2	m-MTDATA sensitized PC ₇₁ BM solar cells	91
6.3	Thickness dependence of sub-gap EQE spectra	94
6.4	Transfer matrix simulation of the sub-gap absorption coefficient	94
6.5	Temperature dependent sub-gap EQE spectra of organic photodiodes	96
6.6	Temperature dependent sub-gap EQE spectra of a silicon photodiode	97
6.7	Model for the sub-gap absorption coefficient	98
6.8	Sub-gap EQE as a function of T and E_{CT}	99
6.9	Static disorder and exciton bandgap energy	100
6.10	Fitting the sub-gap EQE	100
6.11	Simulating the absorption coefficient derived for MA-type rate and Gaussian DOS	100
6.12	Radiative open-circuit voltage limit for low-offset systems	102
7.1	Chemical structures of narrow-gap donor polymers.	105
7.2	Experimental V_{OC} as a function of the ratio I_{SC} to I_D	107
7.3	Spectral responsivity of the PTTQ(HD):PC ₇₁ BM photodiode	109
7.4	LDR of the PTTBAI and PBTQ(OD) based photodiodes	110
7.5	Experimental and calculated noise for narrow-gap photodiodes in function of voltage	112
7.6	Experimental and calculated D^* for narrow-gap photodiodes at -2 V	112
7.7	$\Delta V_{OC,NR}$ as a function of E_{CT}	114
8.1	Molecules structures of the narrow-gap donor polymers	118

8.2	Radiative dark saturation current for wide-gap and narrow-gap blends .	119
8.3	Temperature dependent $J - V$ measurements	120
8.4	Arrhenius plots of J_D at different voltages	121
8.5	Arrhenius plots of J_D for commercial IR photodetectors	122
8.6	Experimental dark $J - V$ characteristics and upper D^* limit	123
8.7	General trend in performance metrics of narrow-gap photodiodes dominated by SRH recombination.	127
A.1	Cyclic voltammetry of bi(thio)pyranylidenes	133
A.2	HOMO energy levels of bi(thio)pyranylidenes	134
A.3	HOMO orbital extension of bi(thio)pyranylidenes	136
A.4	“Dihedral angles” of bi(thio)pyranylidenes	136
B.1	Temperature-dependent EQE and apparent Urbach energy spectra . .	137
B.2	Marcus theory for unequal potentials	138
B.3	Generalized Marcus rate assuming different reorganization energies . .	139
C.1	Absorptance spectra of low-gap polymers	140
C.2	Current-Voltage Characteristics (I) of narrow-gap blends	141
C.3	Current-Voltage Characteristics (II) of narrow-gap blends	142
C.4	EQE _{EL} spectra	142

List of Tables

3.1	Electron-donating organic semiconductors	50
3.2	Electron-accepting organic semiconductors	51
3.3	Organic semiconductors used as transport layers	51
3.4	Device fabrication I	53
3.5	Device fabrication II	54
4.1	Measured and simulated thicknesses of PBTTT:PC ₇₁ BM and PBDB-T:ITIC active layers	68
4.2	Fit parameters describing the CT absorption of PBTTT:PC ₇₁ BM	69
7.1	Device performance parameters for organic narrow-gap photodiodes	106
7.2	Device performance parameters of narrow-gap photodiodes.	114
8.1	Fit parameters describing the SRH mediated dark current	124
A.1	Device architecture for cavity-enhanced photodetectors	132
A.2	CV results under consideration of relaxation and polarization effects	135

Chapter 1

Introduction

Technologies enabling light detection became indispensable for the majority of the world population in the 21st century. This includes the fibre optical photodetectors for telecommunication, solar cells for power generation, x-ray detection for medical diagnostics and image sensors for the ubiquitous smartphones. Moreover, new applications for photodetectors are constantly emerging, such as light sensors for the internet of things¹ and wearable electronics^{2,3}. This is reflected in different market forecasts: For example, according to the Photodiode Sensor Market Research Report, the photodiode market revenue was 492 Million USD in 2020, and is expected to reach 766 Million USD by 2026.⁴ Photodetectors convert an optical signal into an electrical signal based on different working principles including photoemission, photoconduction and thermal detection. In light of the fast progress made on silicon chip manufacturing in the last decades, the silicon photodiode has become the most frequently used type of photodetector in the wavelength range between 200 nm and 1100 nm, with the latter wavelength marking the optical bandgap of silicon. As a semiconductor, silicon utilizes the photoconductive effect, where additional mobile charge carriers are generated through photoexcitation, thereby changing the conductivity of the material. Conventional inorganic semiconductors are characterized by high charge-carrier mobility, small exciton binding energy and high stability. For example, the electron and hole mobilities in silicon are $1450 \text{ cm}^2/(\text{V s})$ and $450 \text{ cm}^2/(\text{V s})$, respectively.⁵ Despite that, there are drawbacks to conventional semiconductors including a complicated and expensive manufacturing processes, mechanical inflexibility and high driving voltage, which limit its practical applications in large-area, flexible, low-cost and portable devices.^{6,7}

Organic semiconductors are organic molecules that are able to absorb light and emit photons like all organic materials, but are also conductive like conventional inorganic semiconductors despite lower charge carrier mobilities. The high absorption coefficient $>10^5 \text{ cm}^{-1}$ of organic semiconductors makes them interesting for photodetection, where the best performances are achieved for much thinner layers than with conventional devices on the order of microns. Among the most efficient organic photodetectors are organic photodiodes, where the photoactive layer is a bulk heterojunction comprising a highly intermixed blend of electron-donating semiconductor (donor; D) and an electron-accepting semiconductor (acceptor; A)

sandwiched between a top and bottom contacts in a vertically stacked device architecture. While ultra-high speed operations are not foreseeable with those devices due to comparably low charge carrier mobilities⁸ (in disordered organic semiconductors $\mu = 10^{-3} \dots 10^1 \text{ cm}^2/(\text{Vs})$), their strengths are complementary to the conventional semiconductors. This pertains to flexible form factor geometries as well as extremely low cost and low embodied energy manufacturing from earth abundant materials. For those reasons, organic semiconductor are highly researched for applications such as solar cells, spectroscopy and imaging with currently a few pioneer companies starting the commercial exploitation of those technologies.^{9,10} The reverse principle of light emission is already commercially successful in the form of organic light emitting diodes used for display applications in smartphones and for large area lighting.¹¹ Of particular interest for next generation photodetectors is the near-infrared (NIR) in the wavelength range between 750 nm to 1700 nm. The ubiquitous silicon photodiodes only cover wavelengths below 1100 nm, while conventional lower bandgap semiconductors such as indium gallium arsenide, mercury cadmium telluride or lead sulfide contain rare or toxic materials, are costly in manufacturing and do not allow for flexible and light-weight applications.

Efforts to extend the photoresponse of organic photodiodes further into the NIR, include the synthesis of low gap materials and the development of novel device architectures exploiting electro-optical effects, such as charge collection narrowing (CCN) and optical cavity enhancement to boost the external quantum efficiency in the sub-gap range. Doing so, the operational spectral window of organic photodiodes was extended up to 1700 nm, however, with the best specific detectivities (D^*) above 1500 nm only reaching modest levels of 10^{10} Jones.¹² The longer wavelength range remained unattainable despite the implementation of optical and electrical amplification that can boost the external quantum efficiency (EQE) to as high as 50000 %.¹³ The main obstacle for achieving higher D^* has proven to be the large dark current I_D , or more precisely the electrical shot noise produced by it at typical operational bias (-0.5 V to -2 V). For photodiodes operating at zero bias voltage, a similar problem still exists due to the thermal noise which is related to parasitic and dynamic resistance of the diode. The origin of the high dark current is typically explained by either non-optimized device layouts or properties of the active layer. Non-optimized device layouts including pinholes in the active layer and misaligned energy levels at the semiconductors/metal interface result in shunt current I_{shunt} and injection currents, respectively. Regarding intrinsic material properties, the origin of the high dark current is often associated with sub-gap states such as charge transfer (CT) states or mid-gap trap states, which are assumed to be recombination centres mediating the dark current generation. Their absorption features are sometimes observed in the sub-gap EQE, but in some cases are also heavily convoluted with resonance modes of the photodiode acting as a low quality optical micro-cavity.

The aim of the work presented in this thesis is to study sub-gap states in organic semiconductors and how they influence the dark current and D^* of organic photodiodes. Understanding the EQE dependence on the active layer thickness and energetics of donor and acceptor is crucial to mitigate D^* losses arising from higher

dark current and noise levels. For a broad overview on the topic of organic photodiodes, Chapter 2 describes the fundamental processes in organic semiconductors such as absorption and current generation. Moreover, the main performance metrics of photodetectors are introduced and some sophisticated device architectures developed for the NIR light detection with organic photodiodes are presented. Chapter 3 explains the experimental methods used for fabrication and characterization of the photodiodes described in this thesis. The most important experimental tool used in the framework of this thesis has proven to be the sub-gap EQE measurement. The experimental results are shown and analysed in the Chapters 4 to 8. In Chapter 4, the impacts of optical interference on spectral lineshape of organic semiconductor photodiodes are demonstrated. For the work described in Chapter 5, a series of narrow-gap NIR photodiodes was fabricated based on optical micro-cavities. To do so, the molecular structure of the donor material was manipulated successfully to shift the response window up to wavelengths of 1665 nm. In Chapter 6, it was shown that in D:A blends, the exponential decay of the sub-gap EQE follows the Urbach rule with the thermal energy describing the sub-gap broadening. This results in a lower limit to the sub-gap broadening for a given temperature, from which the static disorder of the blend can be extracted and the radiative limit can be calculated. In Chapters 7 and 8, the origin of the large dark current observed in organic photodiodes is investigated. The first important conclusion is that optimized photodiodes with narrow-gap D:A blends present a great platform to study the dark saturation current, as the shunt current is not dominating the current-voltage ($I - V$) characteristics in small reverse bias. For a large number of narrow-gap D:A blends, it is concluded that non-radiative recombination lowers D^* with respect to the intrinsic upper limit of D^* given by band-to-band recombination of an background limited infrared photodetector by four orders of magnitude at 2000 nm. This makes it unlikely for organics to compete with inorganic photodiodes above 2000 nm. Using temperature dependent $I - V$ measurements, the origin of the large non-radiative dark saturation current was shown to be charge carrier generation and recombination via mid-gap trap states. Taking into account the trap dynamics via Shockley-Read-Hall statistics, a new diode equation is derived, which, in good approximation, can describe the trend observed between the dark current and the open-circuit voltage. Lastly, in Chapter 9 the key findings emerging from the research described in this thesis are summarized and the scope for future studies on organic photodiodes is presented.

Chapter 2

Fundamentals and Concepts

2.1 Light Absorption in Organic Thin Films

Optoelectronic devices such as organic photodetectors and solar cells depend on the fundamental interaction between light and matter. This includes the absorption and emission of light as a result of exciton generation and recombination in organic semiconducting thin films, which are at the heart of any organic optoelectronic device. To understand experimental absorption and emission spectra, and related photocurrent measurements, optoelectronic processes have to be considered in single molecules and in the bulk while taking into account the optics of the sample, which is architecture dependent. This chapter introduces the fundamentals of thin-film optics followed by a detailed description of absorption phenomena based on the energetic landscape of single molecules and clusters of molecules. Special emphasis is paid to the absorption in the sub-gap spectral range, including charge transfer states and the steepness of the absorption tail.

2.1.1 Optics of Thin Films

The absorption of light is a fundamental physical process, which cannot be quantified directly from the experiment. In spectroscopy, the measurably quantities are called reflectance R and transmittance T and are typically obtained experimentally from a material film on glass as depicted in Figure 2.1. The transmittance T of a sample equals the ratio of incoming to outgoing light intensity.

$$T = \frac{I_{\text{out}}}{I_{\text{in}}}. \quad (2.1)$$

The light attenuation through the sample comprises different processes including reflection at interfaces, absorption and scattering at non-uniformities of the medium. To obtain the absorption coefficient of a material from simple R and T measurements of a thin-film on glass sample, one needs to consider at least the fraction of reflected light at the different interfaces in the thin-film stack as shown in Figure 2.1.

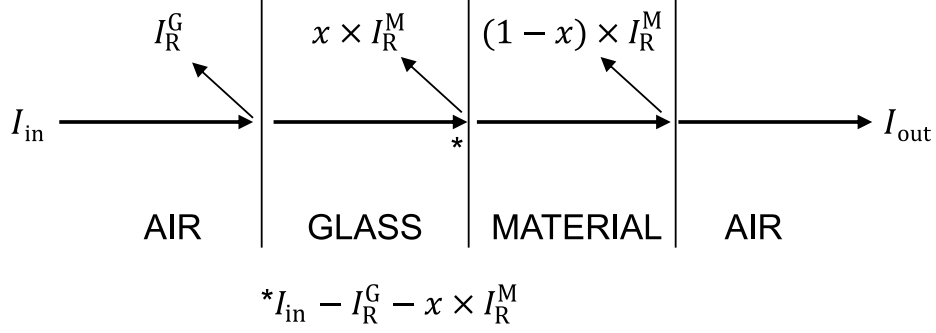


Figure 2.1: Schematic illustration of light propagation through a simple material-on-glass sample for conventional R and T measurements with the glass side facing the incident light beam.

To good approximation in the visible and the NIR, glass is transparent to the incident light but causes reflection at the air/glass interface with the intensity I_{R}^{G} amounting to a typical reflection loss of 4 %. This is called Fresnel reflection and depends upon the mismatch of refractive indices at the glass/film interface. The light intensity incident on the film equals $I_{\text{in}} - I_{\text{R}}^{\text{G}} - x \times I_{\text{R}}^{\text{M}}$, where I_{R}^{G} is light reflected at the glass/film and film/air interface. For strongly absorbing materials, the fraction of light reflected at the film/air interface can be neglected. The measured R can therefore be expressed as

$$R = \frac{I_{\text{R}}^{\text{G}} - x \times I_{\text{R}}^{\text{M}}}{I_{\text{in}}} \quad (2.2)$$

and the transmittance of the material T^{M} follows as

$$T^{\text{M}} = \frac{I_{\text{out}}}{I_{\text{in}} - I_{\text{R}}^{\text{G}} - x \times I_{\text{R}}^{\text{M}}} = \frac{T \times I_{\text{in}}}{I_{\text{in}} - I_{\text{R}}^{\text{G}} - x \times I_{\text{R}}^{\text{M}}} = \frac{T \times I_{\text{in}}}{I_{\text{in}} - R \times I_{\text{in}}} = \frac{T}{1 - R}. \quad (2.3)$$

For a uniform film along the path of the light, T^{M} is defined by the Beer-Lambert law as

$$T^{\text{M}} = e^{-\alpha l}, \quad (2.4)$$

where α is the absorption coefficient of the material film on glass and l is the thickness of the film. α is typically given in dimensions of cm^{-1} and can be used to obtain the absorption cross-section σ via $\alpha = \sigma n$ if the number density of absorbing sites n is known. An exponential decay of light intensity, as given by the Beer-Lambert law, is also obtained from the simplest solution of the Maxwell's equations reading

$$E(z, t) = E_0 e^{i(\bar{k}z - wt)} \quad (2.5)$$

in a dielectric medium. $E(z, t)$ is an electric field oscillating perpendicular to the propagation direction z with the complex wave vector \bar{k} . E_0 is the maximum wave amplitude and w is the angular frequency. The light propagation in the dielectric medium depends on the complex refractive index \bar{n} , whose real part is the refractive

index n and imaginary part is the extinction coefficient κ , i.e. $\bar{n} = n + i\kappa$. Using the dispersion relation $\bar{k} = \frac{w\bar{n}}{c}$, eq. 2.5 can be rewritten as

$$\begin{aligned} E(z, t) &= E_0 e^{i(\frac{w\bar{n}z}{c} - wt)} \\ &\dots \\ E(z, t) &= E_0 e^{\frac{-w\kappa z}{c}} e^{i(kz - wt)}, \end{aligned} \quad (2.6)$$

with c being the speed of light in vacuum. The wavelength λ is related to w via $\lambda = \frac{2\pi c}{w}$ and hence eq. 2.6 can be rewritten as

$$E(z, t) = E_0 e^{\frac{-2\pi\kappa z}{\lambda}} e^{i(kz - wt)}. \quad (2.7)$$

Since light intensity is proportional to $[E(z, t)]^2$, the relative loss of transmitted to incident light intensity is therefore given by the factor $e^{-\frac{4\pi\kappa z}{\lambda}}$. In analogy to the Beer-Lambert law from eq. 2.4, this damping factor equals $e^{-\alpha l}$ where $\alpha = \frac{4\pi\kappa}{\lambda}$ and the thin-film thickness l is the path length of the light in propagation direction z .

As demonstrated, α can be obtain from simple R and T measurements for an absorbing film on glass using reasonable approximations. From α , it is possible to calculate the ratio of absorbed to incident light intensity which is called the absorptance A . For a free-standing film with minimal reflectance at the film/air interface, A can be approximated by $A = \alpha l$. In opto-electronic devices, it is important to know the quantity of absorbed photons in the absorber layer to evaluate the conversion efficiency from photons to electrons. Typical opto-electronic devices, however, comprise a complicated multilayer stack including highly reflective metal contacts, which modify the optical field distribution within the device strongly making it impossible to use the simple $A = \alpha l$ approximation to obtain A of the active layer.

It is therefore common practice, to simulate the optical field in the device using analytical expressions in the so-called transfer matrix formalism. This requires knowledge of the optical constants n and κ for every layer of the stack, which can be obtained from R and T measurements or spectroscopic ellipsometry. The transfer matrix describes the electric field distribution as a superposition of planar waves resulting from reflection and transmission of an incident light beam at all interfaces and interlayers. The idea is illustrated in Figure 2.2 for a typical multilayer stack with m layers, where the light is incident from left to right. In any layer j ($0 \leq j \leq m$) with the thickness h_j , the total electric field E_j at any point comprises a forward travelling electric field E_j^+ and a backward travelling electric field E_j^- , i.e. $E_j = E_j^+ + E_j^-$, incident at an angle θ_j . For example, considering an ambient plane wave travelling the forward direction with the complex amplitude E_0^+ incident onto the 0th interface, it will be partially reflected resulting in a backwards travelling wave with the complex amplitude E_0^- . In glass, the forward travelling wave E_1^+ consists solely of the transmitted wave if glass is considered an incoherent layer, hence neglecting optical interference within the layer. The thickness of organic thin film semiconductors, however, is typically on the order of the wavelength of incident light in the visible and NIR, and hence interference effects must be taken into account. The relation between

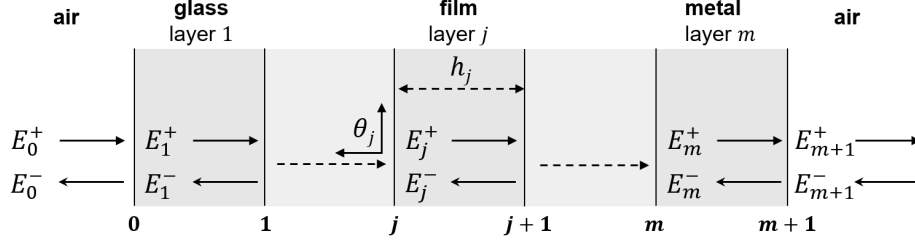


Figure 2.2: Schematic illustration of the electric fields in a multilayer stack where the light is incident on the glass being the first layer and metal being the last layer. The total number of layers is m , whereas j is the running index for all the layers. The electric field in each layer is the sum over a forward and backwards travelling component, E_j^+ and E_j^- , respectively. E_1^+ denotes the transmitted electric field after the first interface and E_{m+1}^+ is the transmitted electric field after m interfaces.

the complex amplitudes of the electric field at any point in the device with respect to the incident electric field can be expressed by the following matrix

$$\begin{pmatrix} E_0^+ \\ E_0^- \end{pmatrix} = \frac{C_1 C_2 \dots C_{m+1}}{t_1 t_2 \dots t_{m+1}} \begin{pmatrix} E_{m+1}^+ \\ E_{m+1}^- \end{pmatrix}, \quad (2.8)$$

where C_j is the propagation matrix with the matrix elements

$$C_j = \begin{pmatrix} e^{-ik_j} & r_j e^{-ik_j} \\ r_j e^{ik_j} & e^{ik_j} \end{pmatrix}. \quad (2.9)$$

Following the dispersion relation as employed in eq. 2.6, the wave vector k_j can be expressed as

$$k_j = \frac{2\pi h_j}{\lambda} \bar{n}_j \cos \theta_j, \quad (2.10)$$

where k_j describes the complex amplitude of the propagating wave in the layer j depending on \bar{n}_j , the layer thickness h_j and the angle of incidence θ . Note that eq. 2.6 considered normal incidence $\theta = 0^\circ$. The reflection and transmission between the $(j-1)$ th and j th layer in eq. 2.8 are given by the Fresnel transmission and reflection coefficient t_j and r_j , respectively. For light with the electric field perpendicular (s polarized) to the plane of incidence, r_j and t_j can be expressed as

$$r_j = \frac{\bar{n}_{j-1} \cos \theta_{j-1} - \bar{n}_j \cos \theta_j}{\bar{n}_{j-1} \cos \theta_{j-1} + \bar{n}_j \cos \theta_j} \quad (2.11)$$

$$t_j = \frac{2\bar{n}_{j-1} \cos \theta_{j-1}}{\bar{n}_{j-1} \cos \theta_{j-1} + \bar{n}_j \cos \theta_j}. \quad (2.12)$$

Using eq. 2.8, the total electric field $E_j(x, \lambda)$ at a position x can then be calculated in relation to E_0^+ . Since E_0^+ is typically known in the experiment for all λ , the absorptance spectrum $A_j(\lambda)$ of the j th layer can be calculated by summing over all positions within the layer ($0 \leq x \leq h_j$) according to

$$A_j(\lambda) = \alpha_j(\lambda) n_j(\lambda) \sum_{x=0}^{h_j} |E_j(\lambda, x)|^2. \quad (2.13)$$

glass / Ag (25 nm) / ZnO (30 nm) / **P3HT:PC₇₁BM (90 nm)** / MoO (7 nm) / Ag (100 nm)

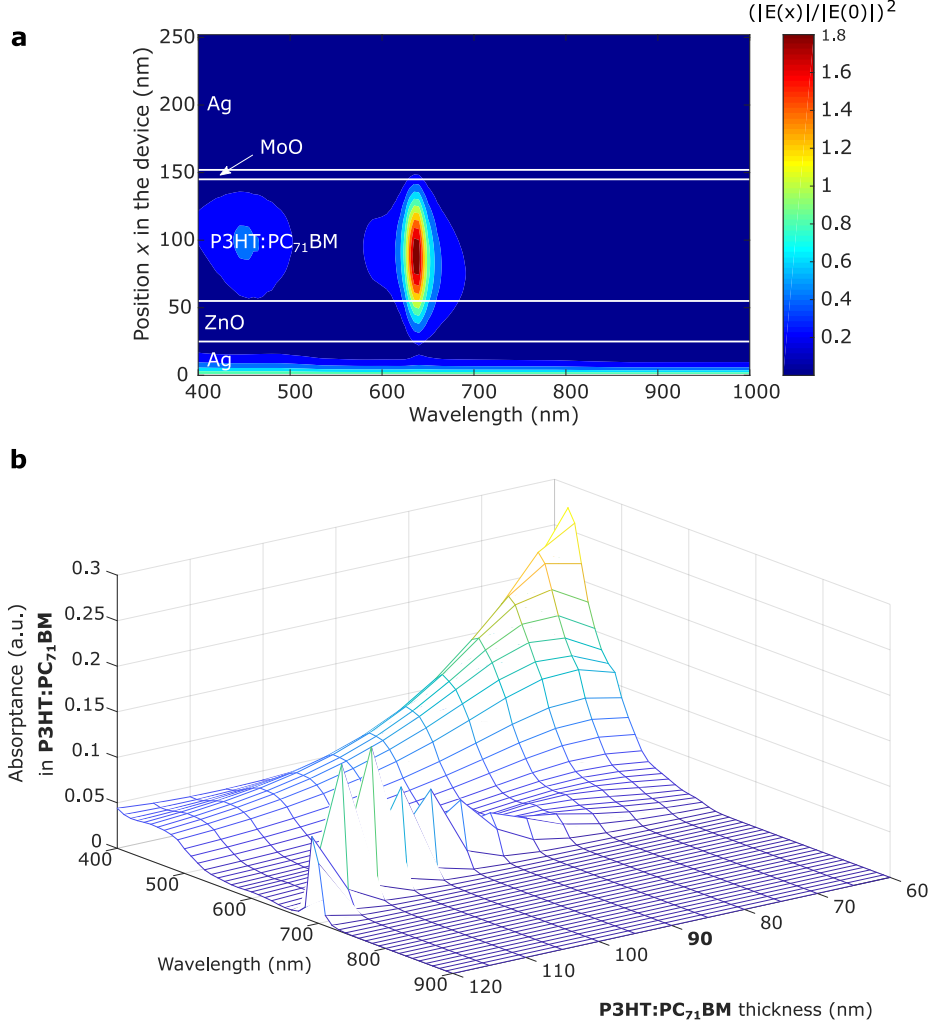


Figure 2.3: **a** Simulated optical field distribution in a micro-cavity device with the first resonance peaking at 630 nm in the P3HT:PC₇₁BM active layer. **b** Absorptance of the active layer as a function of wavelength and layer thickness showing a red-shift of the resonance peak as the P3HT:PC₇₁BM thickness increases.

Consequently, the optical field distribution and the absorptance in every layer of a thin film device can be simulated using the transfer matrix method. The principle is demonstrated in Figure 2.3 for a typical multi-stack architecture used for organic solar cells comprising a semitransparent silver (Ag) top electrode, a electron-conducting zinc oxide (ZnO) interlayer, the active layer with a blend of poly(3-hexylthiophen-2,5-diyl) and [6,6]-phenyl-C₇₁-butyric acid methyl ester (P3HT:PC₇₁BM), the hole-conducting layer molybdenum oxide (MoO_x, $x < 3$) and a fully reflective bottom Ag electrode. Figure 2.3a shows a contour plot of the normalized light intensity of the device with the layer thicknesses as indicated. Given the high reflectance of the Ag top and bottom electrodes, an optical micro-cavity for the incoming light of the wavelength

$$\lambda_m = \frac{2L\bar{n}}{m}, \quad (2.14)$$

is formed, where L is the effective cavity thickness, \bar{n} is the average refractive index of the organic layer between the electrodes and m is a natural number denoting the

resonance order. The resonance is formed as a result of constructive optical interference of the light trapped between the top and bottom electrode. Several conclusions can be drawn from the transfer matrix simulations of the optical field shown in Figure 2.3a. The first order resonance with $m = 1$ peaks at around 630 nm which is covered by the main absorption band of P3HT:PC₇₁BM. Consequently, the optical field maximum is expected to be strongly damped by the absorption of the active layer. Moreover, the spatial position of the optical field maximum is within the active layer, which ensures a maximal photo-response. Figure 2.3b shows a surface plot of A of the active layer as a function of wavelength and active layer thickness. By changing the P3HT:PC₇₁BM thickness from 60 nm to 120 nm, the resonance peak shifts towards longer wavelengths as expected from eq. 2.14. Notably, A is always below 0.3, which is due to the reflectance of incoming light at the top electrode in a semi-transparent cell. In a standard solar cell, A is generally higher, but parasitic absorption of the transport layers has to be taken into account.

The presented example shows how the optical field distribution can be modified using a semi-transparent top electrode. In this example, the resonance is strongly damped by the high absorption coefficient of P3HT:PC₇₁BM resulting in a rather weak cavity effect. The cavity effect can be strongly enhanced by (i) using absorber materials with a lower absorption coefficient at the resonance wavelengths¹⁴, (ii) optical spacers to modify the optical field distribution¹⁵ and (iii) by using distributed Bragg reflectors (DBRs) to decrease parasitic absorption losses at the electrodes¹⁶. The aforementioned methods are commonly employed to fabricate narrow-gap photodetectors with full width at half maximum down to 18 nm.¹⁶ For photovoltaic applications, where broadband absorption of the solar spectrum is desired, the top contact should be highly transparent hereby reducing the cavity effect. However, weak interference patterns superimposed on $A(\lambda)$ can be modelled using the transfer matrix method and therefore used to increase the photocurrent response.¹⁷ Optimizing the absorptance of the solar cell is especially important for indoor photovoltaic applications for an arbitrary light spectrum or for semi-transparent solar cells meant for the integration into the facades of conventional buildings.

2.1.2 Conjugated Organic Molecules

Organic semiconductors are conjugated organic macromolecules that can be grouped into small molecules, polymers and fullerenes. The molecular structures of some well-known candidates from each group are shown in Figure 2.4. Early studies on organic semiconductors focused on their conductive properties as organic materials were believed to be solely insulating. In 1977, Shirakawa reported on highly conductive oxidized and iodine-doped polyacetylene, for which he, together with Alan J. Heeger and Alan G. MacDiarmid, later received the Nobel prize in Chemistry for “The discovery and development of conductive polymers”.¹⁸ On the molecular level, the conductivity of those materials is explained by the concept of conjugation – a key principle in organic chemistry. A common characteristic of conjugated molecules is the carbon (C) backbone, in which a single C atom is always covalently bound to three

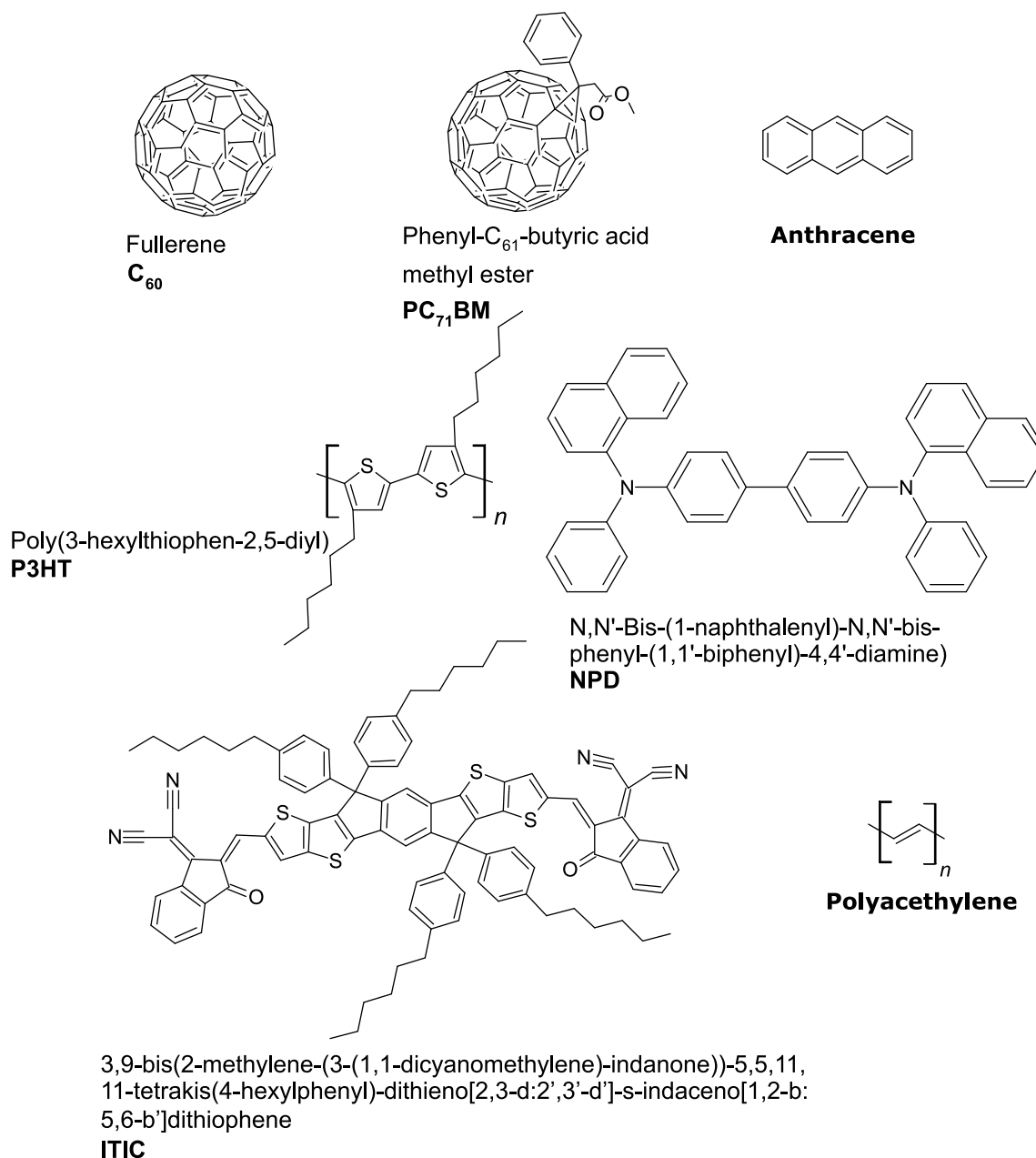


Figure 2.4: Molecular structures of some important organic semiconductors comprising fullerenes (C_{60} and $PC_{71}BM$), small molecules (Anthracene, NPD and ITIC) and polymers (P3HT and polyacetylene). A common characteristic of organic semiconductors is the conjugation along the C–C backbone indicated by alternating double and single bonds.

adjacent atoms comprising two C atoms and one hydrogen (H) atom. This bonding is explained by the hybridization of one 2s and two 2p orbitals of a carbon atom forming 3 degenerate sp^2 hybrid orbitals as illustrated in Figure 2.5a. The remaining 2p orbital is higher in energy than the sp^2 hybrid orbitals and oriented perpendicular to the plane described by those.

The simplest conjugated molecule is ethene whose molecular structure is shown in Figure 2.5b. The C–C bond in ethene is the result of two adjacent sp^2 hybrid orbitals (and p-orbitals) overlapping to form a so-called σ bond (and π -bond). The new bonds represent the bonding state of new molecular orbitals (σ and π orbitals) formed as the

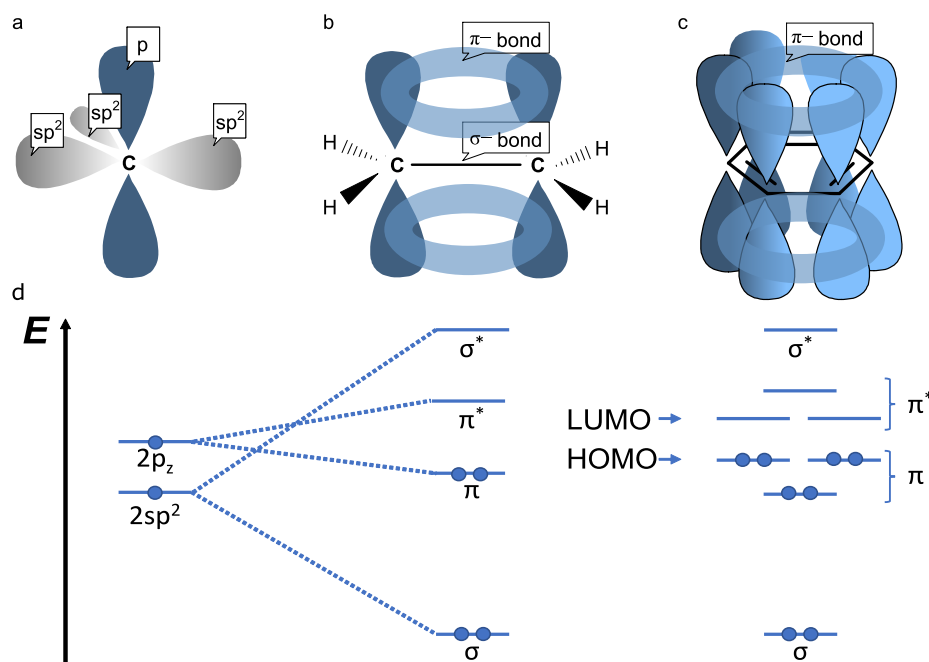


Figure 2.5: **a** Graphic representation of the atomic orbitals of an sp^2 hybridized C-atom. **b** π orbital formation through the overlap of adjacent p_z orbitals in ethene. The σ -bond is the result of two sp^2 hybrid orbital overlapping along the C–C binding axis. **c** Benzene is a fully conjugated systems in which the π -orbitals are delocalized above and below the ring plane. **d** Simplified MO scheme illustrating the spatial distribution of an sp^2 hybridized atomic orbitals and the energy splitting that occurs when mixing atoms orbitals to form molecular orbitals (σ and π orbitals) in ethene and benzene

results of mixing atomic orbitals. In the framework of quantum mechanics, the formation of a molecular orbital (MO) is described by MO theory. It postulates that mixing n atomic orbitals results in n MO orbitals with an equal amount of bonding states of lower energy and antibonding states (typically marked with a star *) of higher energy. At 0 K, the bonding states are fully occupied and the antibonding states are empty because they are energetically less favourable according to the Aufbau principle.

Figure 2.5d illustrates the occupation of energetic states of (i) an isolated sp^2 hybridized C-atom, (ii) ethene and (iii) benzene – a six-membered, fully conjugated C-ring. Benzene is an important building block of organic semiconductors and it can be regarded as the unit cell for most aromatic system. The conjugation in benzene is facilitated by six sp^2 hybridized C atoms. According to MO theory, three π orbitals and three π^* orbitals are formed from the six p_z whose spatial orientation is illustrated in Figure 2.5d. Consequently, the binding π MOs are formed below and above the C ring plane causing benzene to take an almost planar molecular conformation to enhance the orbital overlap.

At the same time, the π MOs are not equal in energy, i.e., among the three bonding states there are two of equal energy and one of lower energy. In contrast, among the antibonding states, there are two of equal energy and one of higher energy. In accordance to the Aufbau principle, the low lying energy states of the bonding π MOs are occupied first by electrons up to the so called highest occupied molecular orbital (HOMO), whereas the antibonding states remain empty. The energetically lowest lying π^* orbital is called the lowest unoccupied molecular orbital (LUMO). The energy difference between the HOMO and the LUMO is the bandgap and therefore a crucial

concept for understanding photoexcitation as well as electronic processes in organic semiconductors. Photoexcitation over the HOMO–LUMO gap typically yields the strongest and most redshifted absorption band of a conjugated molecule. This can be simply regarded as a $\pi - \pi^*$ transition in which one electron is promoted from the HOMO to the LUMO. The resulting excited state is a quasi-particle consisting of one electron and one hole, which are strongly bound in organic molecules. This quasi-particle can have two possible spin configurations: parallel (T_n) and anti-parallel (S_n). The lowest possible energy state is called ground state (S_0) and it is characterized by an anti-parallel spin configuration. The photoexcitation of a triplet state is unlikely as the dipole transition moment becomes zero. For example, the optical transition from the singlet ground state to the first excited triplet state ($S_0 \rightarrow T_0$) is suppressed by many orders of magnitude. In this thesis, absorption refers solely to the photoexcitation of excited singlet states.

To manipulate the absorption bands of organic semiconductors, the HOMO–LUMO gap can be engineered through molecular functionalization by modifying the electron density in the π -system through introduction of electron donating moieties like methoxy ($-\text{OMe}$), methyl ($-\text{CH}_3$) and amino ($-\text{NH}_2$) groups or electron withdrawing groups like fluorid ($-\text{F}$) and cyanid ($-\text{CN}$). Electron donating groups often possess fully occupied orbitals with lone pairs of electrons, which can participate in the π system by increasing its electron-density. As a consequence, HOMO and LUMO energies of the molecule are raised. It is important to note that HOMO and LUMO are theoretical constructs from MO theory applying to single molecules in vacuum. The experimental quantities, that are most often obtained for bulk organic semiconductors are ionisation potential and electron affinity, which are closely related to HOMO and LUMO energy levels as described in Section 2.2.1.

2.1.3 Franck-Condon Principle

Assuming a two-level system with monoenergetic HOMO and LUMO energy levels, one obtains a well-defined optical gap with a sharp absorption onset at low energies. However, the absorption bands typically observed in organic thin-film spectroscopy are spectrally broad. The main broadening mechanisms are: (i) simultaneous excitation of electronic and vibrational modes (electron-phonon coupling) and (ii) static disorder that is the standard deviation of the Gaussian distribution of HOMO and LUMO energies in the bulk. In the following, the broadening due to electron-phonon coupling in the high frequency limit will be discussed with the help of the Franck-Condon principle. Section 2.1.4 will discuss Marcus theory for electron-phonon coupling in the low frequency limit, while Section 2.1.5 will refer to the absorption band broadening due to static disorder.

The photoexcitation of electronic states is always accompanied by the excitation of vibrational sub-levels – a process that is referred to as electron-phonon coupling. Electron-phonon coupling is often described by the Franck-Condon principle, which is used to explain spectral features in electronic-vibrational spectroscopy corresponding to high-frequency normal modes with the vibrational frequency ω . A stretching

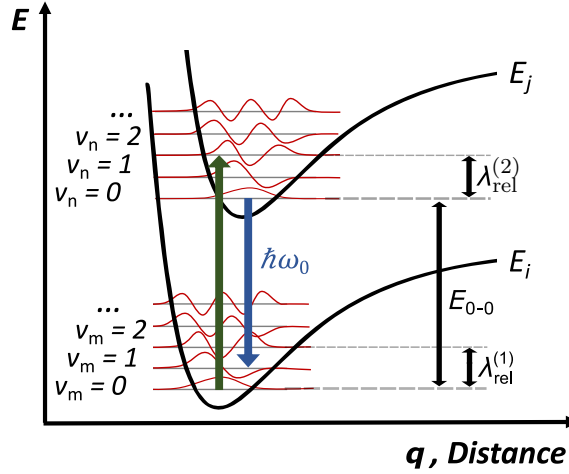


Figure 2.6: Graphical representation of the vibrational sub-levels of the electronic ground state i and excited state j , and the corresponding probability densities. According to the Franck-Condon principle, the interatomic distance remains invariant during the transition. The arrows show possible optical transitions (green arrow represents absorption and blue arrow emission).

vibration of a C-C double bond in a conjugated molecule has an energy in the range of $\omega \approx 150 - 200$ meV and hence $kT \ll \hbar\omega$.¹⁹

The Franck-Condon principle is illustrated in Figure 2.6, where the electronic ground state energy E_i and excited state energy E_j are shown for a simple diatomic molecule as a function of the bond length q . Reducing q leads to an exponential increase in the potential energy as the nuclei experience electrostatic repulsion. Increasing q eventually leads to the dissociation of the bond after which the nuclei no longer “see” each other and the potential energy becomes independent of q . The excited state is generally of weaker bonding because of the population of an antibonding state and hence the shift to higher q . To realize the quantum mechanical treatment, the potential energy surfaces are further quantized into vibrational states ν_m and ν_n of the electronic ground state and the excited state, respectively, hence the molecule is said to be in a vibronic state. A Boltzmann population of the vibronic states is assumed. At $T = 0$ K, only the thermodynamic equilibrium $\nu_m = 0$ is populated.

To arrive to the Franck-Condon principle describing the probability of a vibronic transition, the absorption of a photon with the energy $\hbar\omega$ has to be regarded as an instantaneous process in comparison to the motion of the nuclei. Hence, the absorption process is represented by a vertical arrow. The Franck-Condon principle states that the transition rate k_{ijmn} depends on the Franck-Condon factor FC_{ijmn} , describing the vibronic wavefunction overlap, and the dipole transition moment d_{mn} that depends on the electronic spatial and spin selection rules:

$$k_{ijmn} = FC_{ijmn} \cdot d_{mn}. \quad (2.15)$$

k_{ijmn} can be used to describe the probability that a photon will be absorbed or emitted. In the case of high-frequency modes, where $\hbar\omega \gg kT$, emission and absorption occur at distinct photon energies corresponding to vibronic transitions between the ground state and the excited state with a relative intensity depending on k_{ijmn} . The discrete nature of absorption and emission bands is illustrated in Figure 2.7. Moreover, the

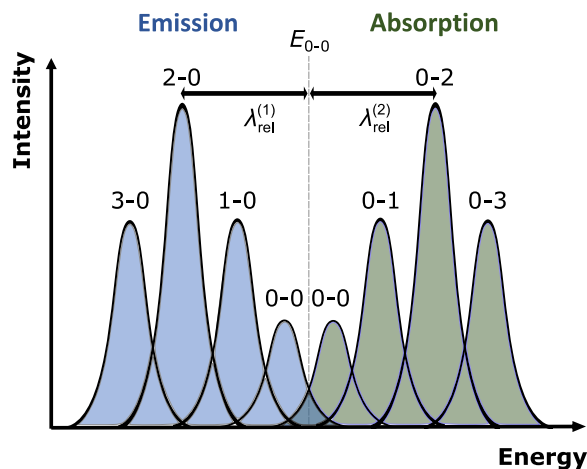


Figure 2.7: Fine structure of absorption and emission bands due to the quantization of the electronic levels into vibrational sub-levels. Strong optical transitions are expected between vibrational levels with high orbital overlap. The energy difference between the peak emission and absorption is called Stokes shift and equals twice the reorganization energy λ .

Franck-Condon-principle says that emission and absorption spectra are reciprocal and therefore symmetrical to the zero-phonon line energy E_{0-0} . For the example shown in Figure 2.6, $k_{ij02} > k_{ij00}$ due a higher wave function overlap between vibronic states $\nu_m = 0$ and $\nu_n = 2$. If the molecule is in a higher vibrational state of the excited state ($\nu_n = 1, 2, \dots$), it will first relax into the vibrational ground state (e.g. $\nu_n = 0$) via vibrational relaxation before radiative emission can occur. Vibrational relaxation describes the energy dissipation to the environment mediated by intramolecular deformation of the molecule and intermolecular motions of the lattice in solid phase or the solvent in solution.²⁰ The intramolecular contributions are the relaxation energy of the ground state $\lambda_{rel}^{(1)}$ and of the excited state $\lambda_{rel}^{(2)}$ as shown in Figure 2.6 and Figure 2.7. $\lambda_{rel}^{(1)}$ and $\lambda_{rel}^{(2)}$ can be obtained from density functional theory calculations. For intramolecular relaxation in the limit of weak intermolecular electronic, the total energy dissipated is the so called reorganization energy λ with $\lambda = \lambda_{rel}^{(1)} + \lambda_{rel}^{(2)}$.²¹⁻²³ After vibrational relaxation to $\nu_n = 0$ of an excited state n , radiative emission occurs to the vibronic levels $\nu_m = 0, 1, 2, \dots$ of the electronic ground state m .

2.1.4 Marcus Theory

In large organic molecules, high frequency vibrational modes (e.g. C-C and C-H bond stretchings) are convoluted with low-frequency modes (e.g. ring-breathing modes) leading to an overall broadening of the absorption band. Low-frequency modes are characterized by $kT \gg \hbar\omega$ and can therefore be treated classically by a continuous harmonic oscillator approximation as demonstrated in Figure 2.8 for the ground state i and the excited state j . Originally developed for electron transfer reactions, a Marcus-type transfer can only occur in the dark if the reactants undergo fluctuations in the nuclear coordinates, which requires an additional energy contribution via the previously introduced reorganization energy λ .²⁴ Marcus theory is both applicable to electron transfer reaction as well as optical transitions. Here, Marcus theory for optical transition will be considered for the nonadiabatic case when the nuclear motion is

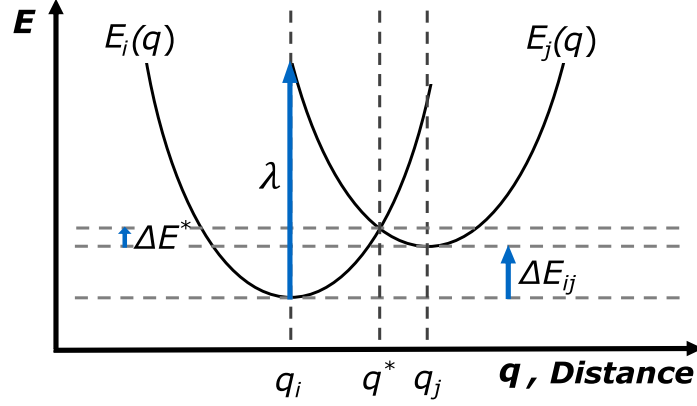


Figure 2.8: Schematic illustration of the potential energy surfaces E_i and E_j for the ground state and the excited state as a function of the nuclear coordinates q .

assumed to be decoupled from the motion of electrons similar to Chapter 2.1.3.

Figure 2.8 sketches the potential energies E_i and E_j of the ground state i and the excited state j as a function of the nuclear coordinates q similar as in Figure 2.6 for the illustration of the Franck-Condon principle. In Marcus theory, E_i and E_j are approximated by harmonic oscillators around the potential minimum with the nuclear coordinates q_i and q_j for the ground state and excited state, respectively. To conserve the energy of the system, an optical transition can only occur when E_i and E_j intersect at the nuclear coordinate q^* . The system therefore has to overcome a potential barrier of the height ΔE^* , which can be written as

$$\Delta E^* = \frac{(\lambda - E + \Delta E_{ij})^2}{4\lambda}, \quad (2.16)$$

where E is the photon energy and λ is the reorganization energy. For charge transfer in the dark, $E = 0$. Starting from Fermi's Golden about the transition between two states and assuming a thermal distribution of states, the transition rate k_{ij} can be formulated as

$$k_{ij} = \frac{2\pi}{\hbar} \frac{|V_{ij}|^2}{\sqrt{4\pi\lambda kT}} \exp\left(-\frac{(\lambda - E + \Delta E_{ij})^2}{4\lambda kT}\right), \quad (2.17)$$

where k is the Boltzmann constant and $|V_{ij}|^2$ is the interstate coupling, which is related to the Franck-Condon factor. Importantly, the presented theory assumes equivalent λ for the ground state and the excited state, i.e. equivalent curvatures of E_i and E_j .

2.1.5 Static Disorder

So far, we have considered only the molecular picture of organic semiconductors. Herein, frontier orbitals were introduced to explain the concept of electron-phonon coupling via the Franck-Condon principle and Marcus theory. On a macroscopic scale, the semiconducting properties arise from the clustering of molecules forming a solid. Since the molecules are hold together by weak Van-der-Waals forces, organic semiconductors in thin film form are mostly disordered at the short range

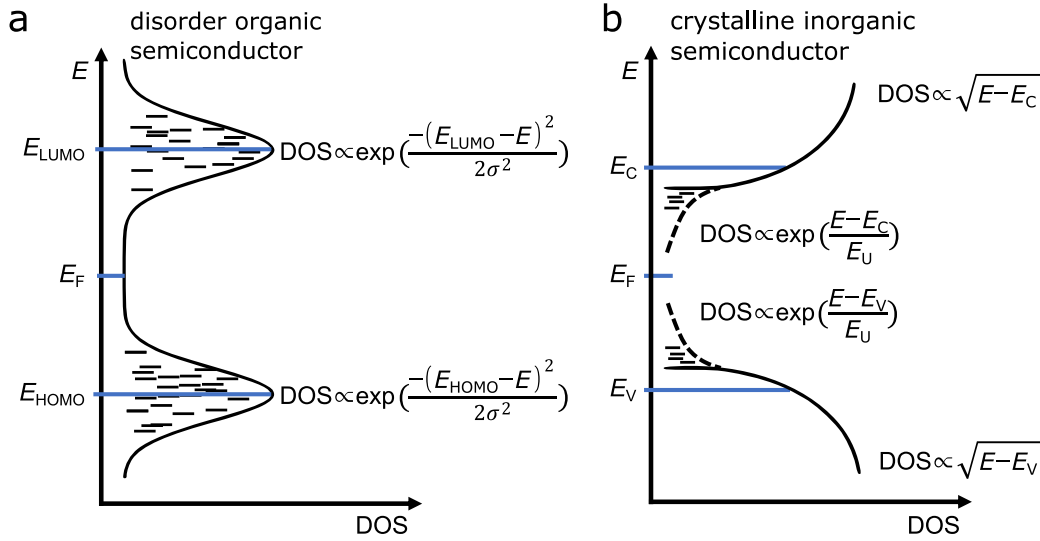


Figure 2.9: **a** Gaussian distribution of discrete HOMO and LUMO energy levels in an organic thin film. **b** Schematic illustration of the electronic structure of an inorganic, banded semiconductors with continuous conduction and valence band, and an exponential sub-gap DOS.

(molecule-molecule interfaces) as well as at the long range (morphology). Varying levels of crystallinity can be achieved depending on the material and processing technique. Small molecules, which are planar and aromatic such as NPD or anthracene, form stacked layers upon vacuum evaporation or sublimation achieving the highest degree of crystallinity possible in organic semiconductors.

Conjugated polymers with long C-C chains like P3HT are solely solution-processable and contain sterically demanding groups such as long alkyl-chains resulting in a semi-crystalline morphology. In polymers, the conjugation along the C-C chain is typically broken into shorter segments due to atomic defects and chain folding. Van-der-Waals forces between conjugated segments of different polymers or within the same folded polymer chain can lead to short-range order resulting in semi-crystalline thin-films, but higher degrees of crystallinity known from vacuum-deposited small molecules or inorganic semiconductors are not achieved due to lack of long-range order.²⁵ Moreover, polymers are less defined than small molecules as their synthesis yields chains of different length, which cannot be fully separated. The molecular weight (M_W) is therefore given within a certain range, e.g. $M_W = 54.000$ g/mol to 75.000 g/mol.

Clearly, the energetic landscape of the thin film will strongly depend on the material as well as spatial variations within the thin film induced by morphological effects. The resulting energetic disorder of the HOMO and LUMO energy levels is often described by the Gaussian disorder model (GDM),²⁶ where the density of states (DOS) for the HOMO energy levels, for example, is written as

$$\text{DOS}_{\text{HOMO}}(E) = \frac{1}{\sqrt{2\pi}\sigma_s^2} \exp \left[\frac{-(E - E_{\text{HOMO}})^2}{2\sigma_s^2} \right]. \quad (2.18)$$

The static disorder σ_s and the HOMO energy level E_{HOMO} represent the standard deviation and the median of the Gaussian distribution, respectively. DOS_{HOMO} is number of HOMO energy levels per unit volume per unit energy that holes are allowed

to occupy. An analogous expression to eq. 2.18 can be written for the LUMO energy levels. σ_s is routinely used in the description of dispersive charge transport.²⁷ Herein, “static” refers to the absence of temperature dependence of the DOS. A graphic representation of the Gaussian DOS of the HOMO and LUMO energy levels in an organic semiconductor is shown in Figure 2.9.

Importantly, the DOS of an organic semiconductor comprises discrete energy levels due to the localized character of molecular orbitals. This is in contrast to banded crystalline semiconductors in which covalently bound atoms, with relatively short nearest neighbour distances, form a lattice. The atomic orbitals, which are a spatial representations of the electronic wavefunction, are delocalized over the entire crystal and can be described by Bloch functions. This leads to the formation of continuous bands in which the electrons can move freely. The density of states in the conduction band for $E > E_C$ near the bottom of one conduction band, can be written as

$$\text{DOS}(E) = \frac{1}{2\pi^2} \left(\frac{2m_e^*}{\hbar^2} \right)^{3/2} \sqrt{E - E_C}, \quad (2.19)$$

where E_C is the conduction band edge and $2m_e^*$ is the effective mass of the electrons.⁵ An analogous expression is valid for the valence band for $E < E_V$ with $2m_h^*$ as the effective mass of the holes.

As shown in Figure 2.9, inorganic semiconductors are characterized by an electronic gap where no energy states are available to be populated by electrons or holes. However, even in single crystals, there is a non-zero probability of localized trap states within the band gap, which arise from imperfections of the crystal due to defects, impurities or grain boundaries. In inorganic solid-state semiconductors, sensitive measurements in the sub-gap spectral range reveal an exponentially decaying sub-gap absorption tail. The slope of the absorption tail as a function of temperature is often characterized by the so-called Urbach energy E_U such that the sub-gap absorption coefficient $\alpha(E, T)$ can be described as

$$\alpha(E, T) = \alpha_0 \exp\left(\frac{E - E_{on}}{E_U(X, T)}\right), \quad (2.20)$$

where E_{on} is the energy onset of the tail correlated to the bandgap energy and α_0 is the above-gap absorption coefficient. E_U depends on the temperature T and the morphology, where X includes the effect of σ_s . The term Urbach energy originates from early studies by Franz Urbach in 1953 for the α of silver halide emulsions. For such emulsions, no effect of X was observed such that $E_U = kT$.²⁸ In banded neat and compound semiconductors, $E_U(X, T)$ at room temperature can take values between 5 eV to 100 eV depending on the material and its morphology.^{29–33} In early literature^{34,35} on amorphous hydrogenated silicon (α :Si-H), $E_U(X, T)$ was shown to saturate to a constant $E_U(X)$ in the low temperature limit. Using the Einstein solid model to account for the thermal occupancy of phonon states, X was extracted from a fit to the experimental $E_U(X, T)$. Notably, a unifying theory (for materials of different chemical bonding and morphology) relating X to the density of trap states (DOS_t) and their absorption is still lacking.^{36,37} Nevertheless, the broadening of the exponential sub-gap α banded inorganic semiconductors is believed to arise from the direct

photoexcitation of exponentially distributed trap states. E_U is therefore sometimes used to characterise the broadening of the DOS_t via

$$\text{DOS}_t(E) = N_C \exp\left[\frac{E - E_C}{E_U}\right]. \quad (2.21)$$

2.1.6 Charge Transfer Absorption

The discussion on the sub-gap spectral range in organic semiconductors is dominated by charge transfer (CT) absorption. CT absorption is often observed in blends of two or more organic semiconductors as a low-energy contribution to the most red-shifted absorption band of the neat phase material. In a binary blend, one material is called donor (D) and the other is called acceptor (A) depending on the affinity of the molecules to donate or accept an electron during the electron-transfer process at the D:A interface. The concept of blending D and A to enhance exciton dissociation will be discussed in Chapter 2.2.2. The CT absorption band results from the photoexcitation of intermolecular CT states that can form at the D:A interface. CT states absorb light at longer wavelengths than the optical gaps of the neat materials. Moreover, the absorption coefficient α in the spectral range of CT absorption is typically 2 to 3 orders lower than that of above-gap absorption. The energy of the CT states, E_{CT} , is often given roughly as the difference between the HOMO of the donor ($E_{\text{HOMO,D}}$) and the LUMO of the acceptor ($E_{\text{LUMO,A}}$) as illustrated in Figure 2.10. This approach can give a first estimate of the CT energy, however, the real value is typically lower due to the exciton binding energy of the CT state (E_{CT}^b). D:A blends with an energy difference between E_{CT} and the lowest singlet state energy of the acceptor $E_{S1,A}$ below 300 meV are often considered low-offset blends, and large offset when this energy difference is greater than 300 meV.^{38–40}

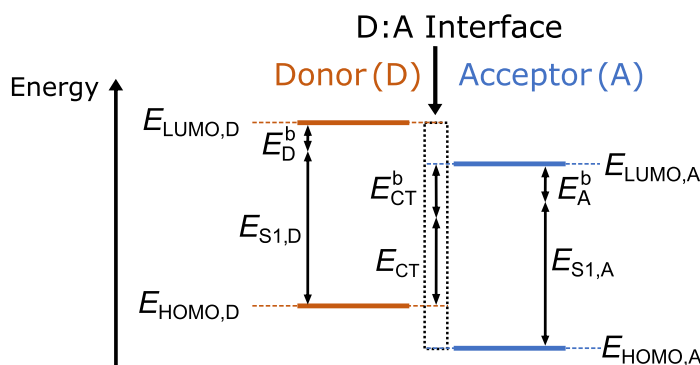


Figure 2.10: Simplified illustration of the HOMO and LUMO energy levels of D and A in the blend. The CT energy equals roughly the difference between the HOMO energy of the donor ($E_{\text{HOMO,D}}$) and the LUMO energy of the acceptor ($E_{\text{LUMO,A}}$) minus the CT exciton binding energy (E_{CT}^b). The intramolecular exciton binding energy in the acceptor phase (E_A^b) is lower than the intermolecular binding energy of an interfacial CT exciton (E_{CT}^b).

To describe the photoexcitation of CT states, the non-adiabatic Marcus-theory in the high temperature limit is often used,⁴¹ which was presented in Chapter 2.1.6. In the GDM, the distribution HOMO and LUMO energy levels is described by a Gaussian-like function (see Chapter 2.1.5) and therefore also the distribution of E_{CT} energies in the bulk. From the integral of the DOS of CT states times the probability that those states are occupied (given by the Marcus rate), the multimode CT absorption coefficient is derived as

$$\alpha_{\text{CT}}(E) = \frac{f_{\text{CT}}}{E\sqrt{4\pi\lambda_{\text{CT}}kT}} \exp\left(-\frac{(\lambda_{\text{CT}} - E + E_{\text{CT}})^2}{4\lambda_{\text{CT}}kT}\right). \quad (2.22)$$

f_{CT} is the oscillator strength which depends on the electronic coupling between CT ground state and the CT excited state. The CT energy E_{CT} and the reorganization energy λ_{CT} include the effect of static disorder (or inhomogeneous broadening) via

$$\begin{aligned} E_{\text{CT}} &= E_{\text{CT},0} - \frac{\sigma_s^2}{2kT}, \\ \lambda_{\text{CT}} &= \lambda_{\text{CT},0} + \frac{\sigma_s^2}{2kT}. \end{aligned} \quad (2.23)$$

$E_{\text{CT},0}$ and $\lambda_{\text{CT},0}$ parametrize α_{CT} in the case of a monoenergetic DOS, when $\sigma_s = 0$. For $\sigma_s > 0$, α_{CT} is redshifted with respect to the monoenergetic α_{CT} . In literature, eq. 2.22 is often used to extract the material-specific parameters E_{CT} and λ_{CT} from the experimental α spectrum in the spectral range of CT absorption. The origin of line width broadening of α_{CT} can be twofold: a high λ_{CT} , which stems from electron-phonon coupling described in Marcus theory, or a high σ_s , which is assumed to be temperature independent. Recent temperature dependent studies of α_{CT} suggested that solely the dynamic vibrational broadening is responsible for the broadening of α_{CT} and not the effect of σ_s .^{42–44}

The detection of CT absorption features requires very sensitive techniques such as photothermal deflection spectroscopy (PDS), Fourier transform photocurrent spectroscopy (FTPS) or sensitive external quantum efficiency measurements (sEQE). PDS measures directly the thermal dissipation of absorbing states in a thin film on glass and therefore does not rely on photocurrent measurements. In contrast, FTPS and sEQE require a full device stack with electrodes to extract the photocurrent, which may impose device properties such as wavelength dependent charge collection efficiency or interference effects (see Section 2.2.2) onto the photocurrent spectrum. The disadvantages of PDS lay in a complicated experimental setup and data analysis, as well as a relatively low sensitivity to α of about 1 cm^{-1} .^{45–47} Recently, sEQE measurements were demonstrated to be sensitive to photocurrents that are equivalent to an α of around 10^{-4} cm^{-1} .⁴⁸

To extract CT state parameters from the spectral line shape of the experimental sEQE spectrum, two assumptions are typically made in literature in order to relate the sub-gap α to the sEQE spectrum. First, it is assumed that charge collection efficiency at sub-gap energies is excitation energy independent, hence $\text{EQE} \propto A$. This has been shown by multiple groups for efficient D:A blends.^{49–51} Moreover, the spectral line-shape of α and the absorbance A in the sub-gap tail are related via $A \approx 2\alpha d$, where

d is the active layer thickness and the factor 2 takes into account the reflection of incoming light at the bottom electrode. For optically thin films of 80 nm to 150 nm, it is often assumed that interferences effects are negligible since the active layer thickness is well below the wavelength of incoming light.⁵²

2.2 Electronic Processes in Organic Photodiodes

The previous section focused on absorption phenomena in organic semiconductors. Absorption of light leads to exciton formation and subsequent exciton dissociation into mobile charge carriers in efficient photodiodes. The mobile charge carriers are then transported to the electrodes under the effect of an electric field inducing a photocurrent in the external circuit. In addition to photocurrent generated under illumination, electronic devices generate dark current, which is the result of leakage current or recombination processes in the bulk or at the contacts. Some recombination processes are fundamentally linked to the materials, while others can be avoided using smart device fabrication. Understanding losses occurring during free charge carrier generation and recombination is a prerequisite for achieving high device efficiencies. This section discusses processes involved in the photon-to-electron conversion as well as the dark current generation emphasizing the differences between organic semiconductors and crystalline inorganic semiconductors typically used for light sensing applications.

2.2.1 Bands and Fermi Levels

It is important to introduce the basic principles of banded inorganic semiconductors, since the underlying principles and terminology are often applied to organic semiconductors within boundaries. As mentioned earlier, banded crystalline semiconductors are covalently bound atoms forming a lattice. The atomic orbitals, which are a spatial representations of the electronic wave function, are delocalized over the entire crystal and can be described by Bloch functions in the framework of the Kronig-Penney model. This leads to the formation of continuous bands, where electrons can move freely. The important physics concern the energetically highest occupied band (valence band, where the upper edge has the energy E_V) and the lowest unoccupied band (conduction band, where the upper edge has the energy E_C). Electrons can be excited to the conduction band leaving behind an empty state in the valence band that is called a hole. The range of energies for which there are no bands to be occupied is called the bandgap E_g , where $E_g = E_C - E_V$. In the dark, the occupation of these bands is governed by Fermi-Dirac statistics. The probability distribution of the number of electrons with the energy E is described by the Fermi-Dirac function

$$f(E) = \frac{1}{\exp\left(\frac{E-E_F}{kT}\right) + 1}, \quad (2.24)$$

where E_F is the Fermi energy that lies very close to the middle of the bandgap in an intrinsic semiconductors as schematically shown in Figure 2.11a. At absolute zero, $f(E) = 1$ for electron energies below the Fermi energy and $f(E) = 0$ for electron energies greater than the Fermi energy. At higher temperatures, a larger fraction of the electrons occupy the conduction band leaving an equivalent amount of holes behind in the valence band. The probability distribution of the number of holes with the energy E

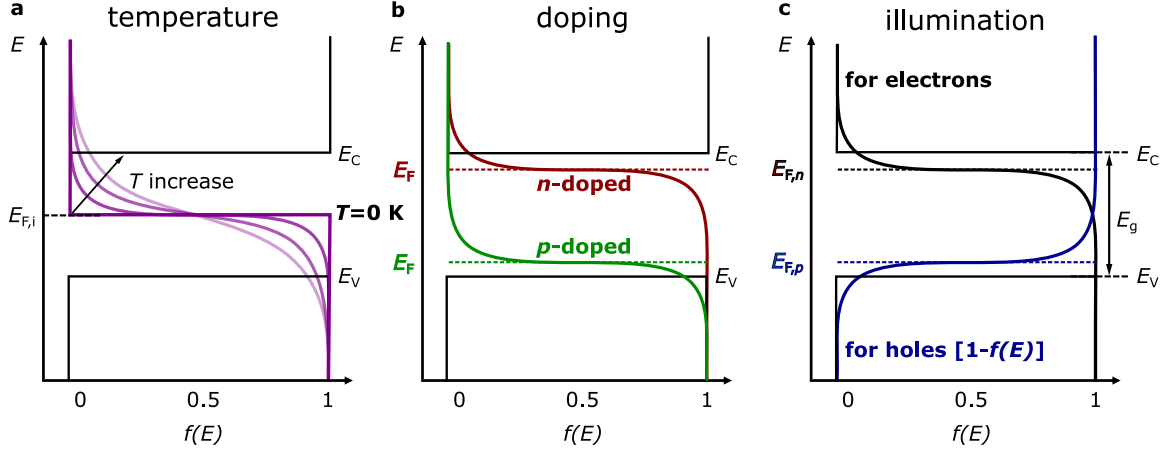


Figure 2.11: Schematic illustration of the Fermi-Dirac distribution for three different cases: an intrinsic semiconductor at absolute zero and higher temperatures (a); an n -doped and p -doped semiconductor with shifted Fermi-levels in thermal equilibrium (b) and a semiconductor in quasi-equilibrium under illumination resulting in Fermi-level splitting (c).

is therefore given by $1 - f(E)$. The occupation of the conduction band, and the valence band, is given by

$$\begin{aligned} n &= \int_{E_C}^{\infty} \text{DOS}(E) f(E) dE = N_C \exp\left(-\frac{E_C - E_F}{kT}\right), \\ p &= \int_{-\infty}^{E_V} \text{DOS}(E) (1 - f(E)) dE = N_V \exp\left(-\frac{E_F - E_V}{kT}\right), \end{aligned} \quad (2.25)$$

where n and p are the electron and hole densities, and N_C and N_V are the ‘effective DOS’ that are accessible at kT to be occupied within the conduction and valence band. For an intrinsic semiconductor,

$$np = n_i^2 = N_C N_V \exp\left(-\frac{E_g}{kT}\right), \quad (2.26)$$

while the np product stays unchanged. E_F can be shifted towards the conduction or valence band upon addition of dopants (controlled amount of impurities) resulting in an increased equilibrium electron (called n -doped) or hole concentration (called p -doped) as shown in Figure 2.11b. When light with energy greater than the bandgap is incident on the semiconductor, it can excite electrons across the bandgap thus generating additional free charge carriers. As a result, the semiconductor is no longer in thermal equilibrium, but in quasi-equilibrium where the occupancy of valence band and conduction band is given by the quasi-Fermi levels $E_{F,n}$ for electrons and $E_{F,p}$ for holes as shown in Figure 2.11c. The occupation of the conduction band, and the valence band, in quasi-equilibrium, is now given by

$$\begin{aligned} n &= N_C \exp\left(-\frac{E_C - E_{F,n}}{kT}\right), \\ p &= N_V \exp\left(-\frac{E_{F,p} - E_V}{kT}\right), \end{aligned} \quad (2.27)$$

with $np > n_i^2$ and

$$np = N_C N_V \exp\left(-\frac{E_g}{kT}\right) \exp\left(\frac{E_{F,n} - E_{F,p}}{kT}\right) = n_i^2 \exp\left(\frac{E_{F,n} - E_{F,p}}{kT}\right). \quad (2.28)$$

Increasing the number of free charge carriers upon illumination is called photoconductivity, which is a core principle of solar cells and photodiodes. While concepts like Fermi-levels, Fermi-level splitting and bandgap are useful for understanding the working principles of organic semiconductors, they fail to account for the molecular nature and localized electronic states of organic semiconductors. As previously shown in Figure 2.9, the HOMO and LUMO energy levels of molecules in a solid follow a Gaussian distribution, where the energy difference between the centre of the distribution can be seen as the electronic gap, or often called bandgap. However, the wave function of the HOMO (or LUMO) is delocalized over a few neighbouring molecules or even a single molecules such that no delocalized bands are formed in disordered organic semiconductors. To account for the molecular nature of the electronic properties, the ionization potential IP and the electron affinity EA are often used instead of valence and conduction band edge. For molecules, the IP describes the energy required to remove an electron from the HOMO of an isolated molecules in gaseous phase, whereas the EA describes the energy required for the addition of an electron to the LUMO. The electronic bandgap in organic semiconductors corresponds to the difference between IP and EA , which is different to the optical gap E_{opt} that is the energy required for the lowest optical transition ($S_0 \rightarrow S_1$).⁵³ The difference between the E_{opt} and E_g is the binding energy E^b which typically amounts to about 500 meV for conjugated polymers,^{54–56} but was also reported to up to 1.5 eV for conjugated molecules like C₆₀.^{57,58} Note, that in crystalline inorganic semiconductors E^b is only in the order of a few meV and therefore much lower than in organic semiconductors. This is of great importance for the free charge carrier generation as discussed in Section 2.2.2.

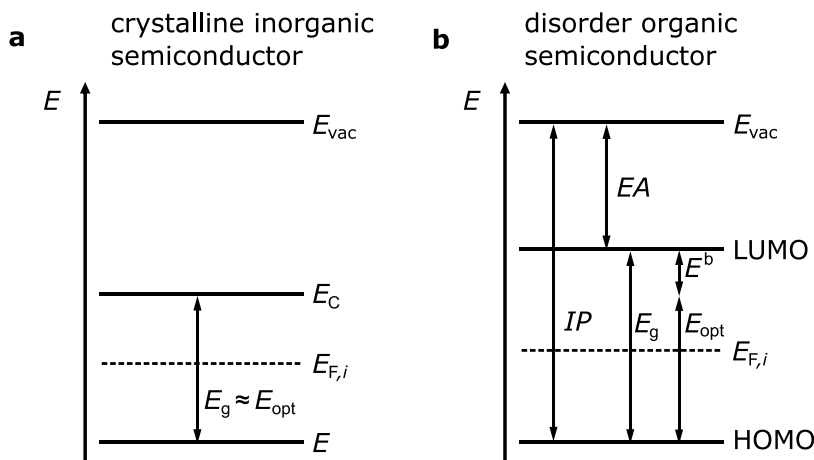


Figure 2.12: Illustration of gap energies in a crystalline inorganic semiconductor (a) and in a disordered organic semiconductor (b). The band diagram in a crystalline semiconductor is characterized by the conduction and valence band edges, E_C and E_V , respectively, in reference to the vacuum energy level E_{vac} . The molecular nature of organic semiconductors prevents the formation of energy bands. Instead, the HOMO and LUMO energy levels are given, which represent the mean of the respective Gaussian distributions of molecular energy level present in the bulk. The electronic gap E_g equals the sum of optical gap E_{opt} and the electron-hole pair binding energy E^b , that is at least one order of magnitude higher in organic semiconductors in comparison to crystalline inorganic semiconductors. Moreover, the ionization potential IP and electron affinity EA are often used to characterize the energy levels.

2.2.2 Charge Generation

The generation of free charge carriers proceeds via three subsequent steps: First, excitons are generated via photoexcitation. In organic semiconductors, those excitons are primarily singlet excitons, but also direct photoexcitation of sub-gap states takes place to a small extent as discussed in Section 2.1.6. Second, the excitons diffuse within the material with a characteristic diffusion length depending on the dielectric constant of the material. Third and last, the excitons dissociate into free charge carriers. In disordered organic semiconductors, the electrostatic screening is weak due to typical dielectric constants of $\epsilon \approx 3 - 4$ resulting in E^b between 0.3 eV to 1 eV in the neat phase material.⁵⁸ Since E^b is much greater than thermal energy at room temperature, the predominant type of excitons are spatially localized singlet excitons of the Frenkel type. In contrast, electric charges in crystalline semiconductors are strongly screened by a large dielectric constant $\epsilon > 10$. Consequently, the Coulomb interaction between an electron and a hole is weak, and hence the excitons tend to be delocalized over multiple atoms. A schematic illustration of the spatial extension of different types of excitons is shown in Figure 2.13. Excitons in inorganic crystals are called Mott-Wannier excitons with $E^b \approx 10$ meV. The splitting of Mott-Wannier excitons can therefore be regarded as instantaneous with respect to photoexcitation.

In a blend of two organic semiconductors, an intermediate state between a Frenkel and Mott-Wannier exciton exists – the so-called CT exciton or simply CT state. The CT state is an intermolecular exciton delocalized over two neighbouring molecules (D and A). The binding energy of CT states (E_{CT}^b) is strongly debated in literature and was previously estimated to be between a few tens to 100 meV depending on the materials and techniques used to measure the parameter.^{51,59–61} Since this is much lower than E^b of singlet excitons, dissociation of CT states is much more likely at room

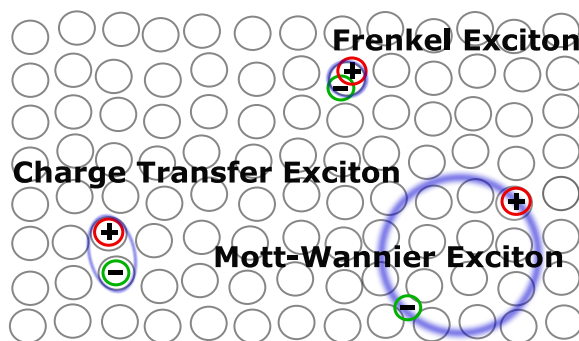


Figure 2.13: Sketch of the different types of excitons observed typically in semiconductors comprising (i) weakly bound Mott-Wannier excitons in banded semiconductors, (ii) intramolecular, strongly bound Frenkel excitons in molecular solids and (iii) intermolecular charge transfer (CT) excitons in molecular solids, which can be regarded as an intermediate case between (i) and (ii).

temperature. The formation of a CT state as an intermediate step between singlet excitons and free charge carriers and is therefore a prerequisite for efficient exciton dissociation.^{49,50,62} The most efficient organic photodiodes and solar cells have a photoactive layer that comprises an interpenetrating network of nano-sized phase domains of D and A, which also provide percolation pathways to electrodes.⁶³ That way, the nearest D:A interface is within the diffusion length of a Frenkel-type singlet exciton generated somewhere in the bulk to ensure efficient charge generation. This type of heterojunction is called bulk heterojunction (BHJ). More detailed information on photodiodes with a bulk heterojunction are provided in Section 2.4.

Figure 2.14 shows the electronic states involved in free charge carrier generation including singlet state, CT state and free electrons and holes in the charge-separated (CS) state. Note, that black and grey lines indicate the electronic levels and the vibrational sublevels, respectively. While the optical generation of excitons into the different vibrational levels occurs in accordance with the Franck-Condon principle, exciton recombination always proceeds from the lowest vibrational level, since vibrational relaxation is on a faster timescale than electronic excitations. According to Figure 2.14, two steps are necessary for free charge carrier generation: The formation of a CT state with the rate constant k_{CT} and the subsequent dissociation with the rate constant k_{CS} . These pathways are in kinetic competition with radiative and non-radiative recombination of CT states, and the encounter of free charge carriers resulting in the formation of CT states (encounter rate β_{enc}). Generally, the energetic offset between the first singlet exciton energy E_{S1} and the E_{CT} is considered as the driving force of exciton dissociation (marked as ΔE_{CT} in Figure 2.14). In the framework of non-adiabatic Marcus theory in the high-temperature limit, an increase in ΔE_{CT} can be linked to higher k_{CT} rates, which was also experimentally shown for binary blends with fullerene acceptors.^{64,65} The more recent types of non-fullerene acceptors (NFAs) have a very low ΔE_{CT} , but still yield efficient charge generation.^{38,66} The charge generation in NFA containing blends with vanishingly small energetic offset is therefore still under debate.^{66–68}

Another topic under debate is the process of charge separation with the rate constant k_{CS} from the relaxed CT state manifold to the CS state with an associated potential barrier of E_{CT}^b being the energy difference between the relaxed CT state and

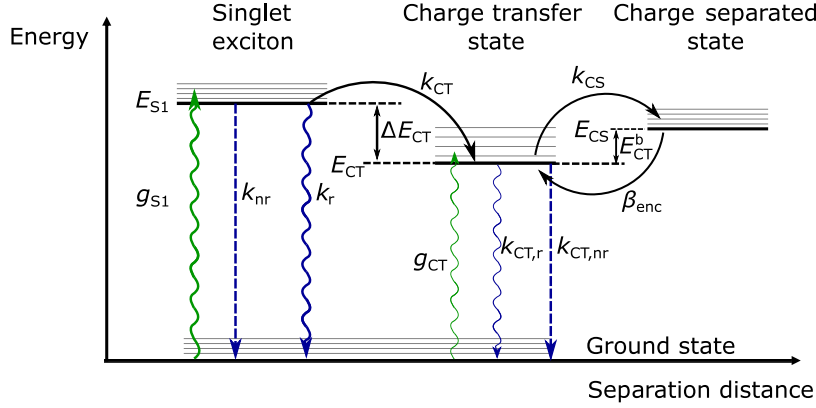


Figure 2.14: A simplified state diagram representing the most important generation and recombination processes mediated by singlet and charge transfer state (CT) excitons. The transitions from singlet to CT state to charge separated state represent electron transfer processes which increase the electron-hole separation distance in the exciton until electron and hole have overcome the electrostatic Coulomb forces and become free charge carriers.

the CS state energies. As mentioned earlier, E_{CT}^b is typically estimated to be between a few tens to 100 meV depending on the materials and techniques. To explain the, nonetheless, efficient charge separation from the CT state to the CS state, several mechanisms have been proposed based on the existence of entropy and an energy cascade between mixed and pure phases.^{69–71}

2.2.3 Free Charge Carrier Recombination

The recombination of electrons and holes, that do not originate from the same exciton, is called non-geminate recombination. Geminate recombination happens before the exciton dissociates into free charge carriers and was discussed in the previous section on charge generation. Once electrons and holes meet, the dominant recombination pathway depends on the energy levels of the photoactive semiconductor, the device layout and energetics, the temperature and applied voltage. Figure 2.15 demonstrates different non-geminate recombination mechanisms that are expected to be present in both inorganic and organic semiconductors.

Band-to-band recombination in the bulk is most probable for direct-bandgap inorganic semiconductors among the III-V compounds of the periodic table. If the oppositely charged carriers are statistically independent of each other, then carrier recombination is a random process depending on charge carrier densities n and p . At thermal equilibrium, the recombination rate is given by

$$R = \beta np, \quad (2.29)$$

where β is the bimolecular recombination rate constant, that is proportional to the thermal generation rate G_{th} via

$$G_{th} = \beta n_i^2. \quad (2.30)$$

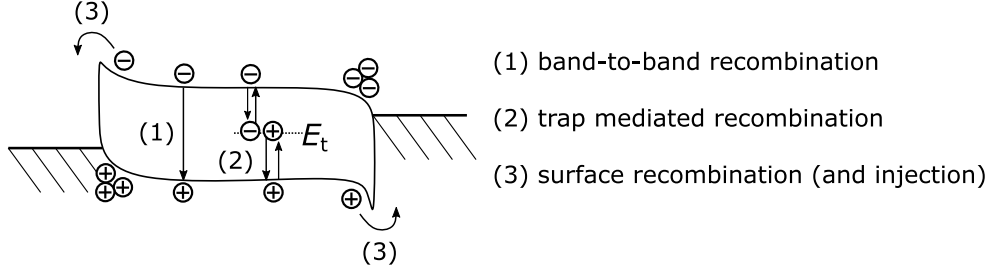


Figure 2.15: Different recombination pathways for free holes and electrons.

At thermal equilibrium, $np = n_i^2$ and hence $R = G_{\text{th}}$. The net transition rate U is then well approximated by

$$U = \beta(np - n_i^2), \quad (2.31)$$

assuming low level injection, where the number of excess carriers is negligible in comparison to majority carriers.

In neat, disordered organic semiconductors, the encounter of charge carriers in the bulk is limited by their low mobilities. In such low-mobility materials, $U = \beta_L(np - n_i^2)$, where β_L is the Langevin recombination rate constant depending on the hole and electron mobility, μ_h and μ_e , via

$$\beta_L = \frac{q(\mu_h + \mu_e)}{\epsilon_r \epsilon_0}, \quad (2.32)$$

where $\epsilon_0 \epsilon_r$ is the permittivity of the active layer. The limiting process in Langevin-type recombination is the diffusion of charge carriers to each other. In a donor-acceptor blend, the bimolecular recombination coefficient is reduced relative to Langevin recombination rate constant ($\beta < \beta_L$) expected for a neat organic semiconductor. That is because electrons and holes can only move in the respective acceptor and donor domains, which limits their encounter rate and thus lowers β .⁷² Moreover, upon encounter, electron and hole form a CT state exciton which can either recombine or re-dissociate into free charge carriers, while re-dissociation is expected to further decrease β relative to β_L .⁷³ The probability of CT state (re)dissociation into free charge carriers and recombination is described by the Onsager-Braun model as electric-field dependent processes.⁷⁴ However, there are doubts as to this model because of the random orientation of D:A interfaces with respect to the electric field direction. The generation-recombination dynamics of CT states therefore remain under debate.

For indirect-bandgap semiconductors such as Si and Ge, the dominant pathway is trap-assisted recombination described by Shockley, Read and Hall (SRH) in 1952.^{75–77} A schematic illustration of this type of recombination is drawn in Figure 2.15 showing a two-step process: First, an electron (or hole) is trapped by an energy state within the bandgap which is introduced through defects or impurities. Second, if a hole (or an electron) has previously occupied the same energy state, then electron and hole will recombine. The trap-assisted recombination rate constant β_{SRH} can be described by the competition of capture and release rates of holes or electrons from trap states with an energy E_t . For mid-gap trap states $E_t = E_i$ and

$$\beta_{\text{SRH}} = \frac{C_n C_p N_t}{C_n(n + n_1) + C_p(p + p_1)}, \quad (2.33)$$

where N_t is the trap density, C_n and C_p are the electron and hole capture coefficients, respectively. N_C and N_V are the effective DOS to be occupied by electrons and holes at kT . Furthermore, $n_1 = N_C \exp[(E_t - E_C)/kT]$ and $p_1 = N_V \exp[(E_V - E_t)/kT]$. In the case of trap state mediated recombination, $\beta = \beta_{\text{SRH}}$ and $U_{\text{SRH}} = \beta_{\text{SRH}}(np - n_i^2)$. According to SRH statistics, bulk traps with energy levels near the mid-gap are the most effective recombination centers.

In literature, the SRH model was previously applied to organic systems^{78–81} and perovskites^{82,83} to describe charge transport phenomena. Recently, mid-gap trap states were observed by different experimental techniques such as sensitive external quantum efficiency measurements⁸⁴, impedance spectroscopy⁸⁵ and intensity dependent photocurrent measurements⁸⁶.

The last non-geminate recombination type is surface recombination, which is the non-radiative recombination of free charge carriers at non-selective contacts as illustrated in Figure 2.15. This becomes particularly important for materials with low bulk recombination rates and high mobilities.⁸⁷ One way to overcome surface recombination is to design Ohmic contacts by adjusting the metal/semiconductor work function offset to block charge extraction at the “wrong” electrode (electrons at the anode, holes at the cathode), which is especially important under reverse bias. Another way is to employ truly charge-selective interlayers to prevent the charge diffusion to the “wrong” electrode.⁸⁸ However, contact design is complicated by a plethora of phenomena happening at the metal/organic interface like interface dipoles and Fermi level pinning.⁸⁹

2.2.4 Charge Transport

For a semiconductor, with both electrons and holes, the conductivity is given by

$$\sigma = q(n\mu_e + p\mu_h), \quad (2.34)$$

where μ_e and μ_h are the electron and hole mobilities, respectively, in units of $\text{cm}^2/(\text{V s})$. Since σ depends linearly on n and p , it can be drastically increased by doping, illumination and voltage bias, which will shift the Fermi level as shown in Section 2.2.1 by increasing

the charge carrier density. The charge carrier mobilities, μ_e and μ_h , are related to the average drift velocities v_d , reached by carriers under the applied electric field F , via

$$v_d = q(n\mu_e + p\mu_h)F. \quad (2.35)$$

In banded semiconductors, μ_e and μ_h are typically very high only being limited by phonon scattering or the presence of ionized impurities. For example, in silicon $\mu_e = 1450 \text{ cm}^2/(\text{V s})$ and $\mu_h = 450 \text{ cm}^2/(\text{V s})$. When scattering by phonons is predominant, the mobility decreases with increasing temperature according to $\mu \propto T^{-3/2}$ due to thermally activated phonon modes. On the other hand, when scattering at ionized impurities dominates the transport, the mobility increases with increasing temperature via $\mu \propto T^{3/2}$.⁵ This temperature dependence of μ is characteristic for band transport and it has been observed in inorganic crystalline semiconductors, but also in small organic molecules which can form perfect crystals, such as polyacenes.⁹⁰ Since for organic and inorganic crystalline materials at room temperature, phonon scattering is dominating the transport, an increase in mobility is observed with decreasing temperature. The mobility decreases, until at very low temperatures, no more charges are available to populate the conduction (or valence) band due to the temperature dependent occupancy described by the Fermi-Dirac distribution.

In disordered materials, the mobilities are typically orders of magnitude lower ($\mu = 10^{-2} \dots 10^1 \text{ cm}^2/(\text{V s})$).⁸ Due to the missing periodic lattice structure, charges are not free to move in bands, but regarded as localized on molecular sites. Moreover, the intrinsic charge carrier density in organic semiconductors is much lower than in crystalline inorganic semiconductors due to a higher bandgap in the range 2 eV to 3 eV making virtually no thermally activated charge carriers available. To describe the transport of localized charge carriers, hopping and tunnelling models are used as well as the concept of thermal activation to overcome a potential barrier. A combination of hopping and tunnelling, i.e., phonon-assisted tunnelling, from site i to site j is described by the Miller-Abrahams rate expression

$$v_{ij} = v_0 \exp(-2\alpha r_{ij}) \begin{cases} \exp\left(-\frac{E_j - E_i}{kT}\right) & \text{for } E_j > E_i \\ 1 & \text{for } E_j < E_i. \end{cases} \quad (2.36)$$

v_0 is the attempt-to-escape frequency, α and r_{ij} describe the electronic coupling and the distance between the sites i and site j , respectively, whereas E_i and E_j are their energy levels. The exponential term is a Boltzmann factor describing the thermal activation of the hopping process. In that case, the mobility increases with temperature as it is typically observed in organic disordered semiconductors. Note that two cases are distinguished: (i) for $E_j > E_i$, the rate is thermally activated; and (ii) for $E_j < E_i$, the rate is not impeded by the additional term. The problem of this model lies in the variety of intermolecular distances and undefined energetic landscape of the molecular sites in disordered semiconductors ($\Delta(E_j - E_i)$ inhomogeneous). In literature, the energetic landscape is widely assumed²⁷ to be a Gaussian-like DOS as described in Section 2.1.5.

This section describes the absorption coefficient lineshape broadening as a result of static disorder that is the Gaussian standard deviation.

A more sophisticated transport model can be described in the framework of Marcus theory which takes electron-phonon coupling into account in contrast to the Miller-Abrahams formalism. In Eq. 2.17 from Section 2.1.4, the Marcus rate k_{ij} was given for the photoexcitation from a singlet ground state i to the first excited singlet state j in the non-adiabatic, high-temperature limit. The same expression can be applied to electron transfer from molecule i with energy E_i to the molecule j with energy E_j . It is important to note that the Marcus rate has to be viewed in different limits, and thus can be applied to different electron transfer scenarios. In fact, the original description by Rudolph A. Marcus was formulated for electron transfer in a redox type reaction in solution.²⁴

2.3 Characterization of Organic Photodiodes

The primary task of a photodiode is to distinguish a measured optical signal from its background. Depending on the application, the optical signal may vary strongly in light power, wavelength or speed. To describe the performance of a photodiode in different scenarios, specific figures of merit were established including noise equivalent power, specific detectivity, bandwidth and frequency response. Depending on the application, one figure of merit may be more important than the other and sacrifices are made on one end to meet the expectations on the other end. For example, a high specific detectivity may be sacrificed for a higher speed, or the speed may be sacrificed for a large area device with a high power output. Underpinning all discussions on photodetection, is the role of dark current and noise current limiting the minimal detectable light power. In this section, the most important figures of merit of a photodiode are explained and performance limits of organic photodiodes are discussed in particular.

2.3.1 External Quantum Efficiency and Responsivity

Photodiodes are optimized to detect some part of the electromagnetic spectrum between X-Rays to Infrared radiation. The optical response window of a photodiode is characterised by the external quantum efficiency (EQE) and the spectral responsivity (R), that are closely related via

$$\text{EQE}(\lambda) = \frac{hc R(\lambda)}{q\lambda} \quad (2.37)$$

where λ is the wavelength in nm, h is the Planck constant, c is the velocity of light in vacuum and q is the elementary charge. R is given in units of A/W and therefore describes the photocurrent per incident unit optical power. The EQE describes the ratio of incident photons to extracted electrons and is in the range between 0 and 1 in the absence of photomultiplication. The EQE, as experimental quantity, is the product of the absorptance of the active layer A and the internal quantum efficiency (IQE)

$$\text{EQE}(\lambda) = A(\lambda) \times \text{IQE}(\lambda) \quad (2.38)$$

A and IQE also range somewhere between 0 and 1, but can not be measured directly. The IQE is the ratio of absorbed photons to extracted electrons and is given by $\text{IQE} = \eta_{\text{d,ex}}\eta_{\text{d,CT}}(F)\eta_{\text{coll}}(F)$, where $\eta_{\text{d,ex}}$ is the exciton dissociation efficiency, $\eta_{\text{d,CT}}(F)$ is the field-dependent CT state charge separation efficiency and η_{coll} is the charge collection efficiency. In literature, the charge generation efficiency $\eta_{\text{d,ex}}\eta_{\text{d,CT}}$ was shown to be excitation energy independent for conventional blends in efficient organic solar cells,^{49,51,91} although exemptions to the rule were demonstrated in exotic donor:acceptor blends.^{92,93} Moreover, for high enough internal fields, the charge generation efficiency approaches 1.^{94–97} η_{coll} strongly depends on the mobility of charge carriers, the morphology and thickness of the active layer and the energetics of the contacts. To maximize η_{coll} and to minimize the transit time of the charge carriers to

the electrodes, a reverse bias is applied to organic photodiodes. At large enough reverse bias, the IQE approaches 1, i.e., all photogenerated charge carriers are extracted at the contacts. More details were discussed in Section 2.2.3 and 2.2.4 on free charge carrier generation and charge transport, respectively. The absorptance A of the active layer is a function of the absorption coefficient α and depends on the optics of the multi-layer stack such as a photodiode. It can be said that $A = \tilde{f}\alpha d$, where \tilde{f} is a wavelength dependant correction factor for optical interference effects and d is the active layer film thickness. One way of obtaining A is to perform transfer matrix simulations as discussed in Section 2.1.1, which requires the knowledge of the optical constants of all layers in a multilayer stack that is the photodiode or the solar cell.

2.3.2 Current-Voltage Characteristics

The photocurrent density J_{ph} of a photodiode is the integral over the EQE and the irradiation spectrum of a light source (φ) over all energies:

$$J_{\text{ph}} = \int_0^\infty \text{EQE}(E) \varphi(E) dE. \quad (2.39)$$

φ is specific for the source of radiation, which can be the sun, an artificial light source such as a fluorescent lamp, or the thermal radiation of the surroundings. The thermal radiation of the surroundings at room temperature (at 300 K) is typically modelled by the black body radiation emitted into half sphere above the photodiodes, which is given by

$$\varphi_{\text{BB}}(E) = \frac{2h\pi E^2}{c^2 h^3} \exp\left(-\frac{E}{kT}\right). \quad (2.40)$$

q is the elemental charge, c is the speed of light, h is the Planck constant, k is the Boltzmann constant and T is the temperature. At thermal equilibrium, the dark current density can be calculated in analogy to Eq. 2.39 from

$$J_{0,\text{R}}(T) = \int_0^\infty \text{EQE}(E) \varphi_{\text{BB}}(T, E) dE. \quad (2.41)$$

$J_{0,\text{R}}(T)$ is called radiative dark saturation current density and it results from the detailed balance of absorption of thermal radiation and the emission via radiative recombination over the bandgap. $J_{0,\text{R}}(T)$ marks the lower thermodynamic limit of the dark current density of a photodiode. In an ideal photodiode, the current density in function of voltage is given by

$$J = J_{0,\text{R}}(T) \left[\exp\left(\frac{qV}{kT}\right) - 1 \right] - J_{\text{ph}} \quad (2.42)$$

as described by the Shockley diode equation. In the dark, $J_{\text{ph}} = 0$ and $J = J_{0,\text{R}}$ for large reverse bias. Under illumination and open-circuit conditions, ($J = 0$; $V = V_{\text{OC}}$), Eq. 2.42 can be rewritten as

$$V_{\text{OC}} = \frac{kT}{q} \ln\left(\frac{J_{\text{ph}}}{J_{0,\text{R}}} + 1\right). \quad (2.43)$$

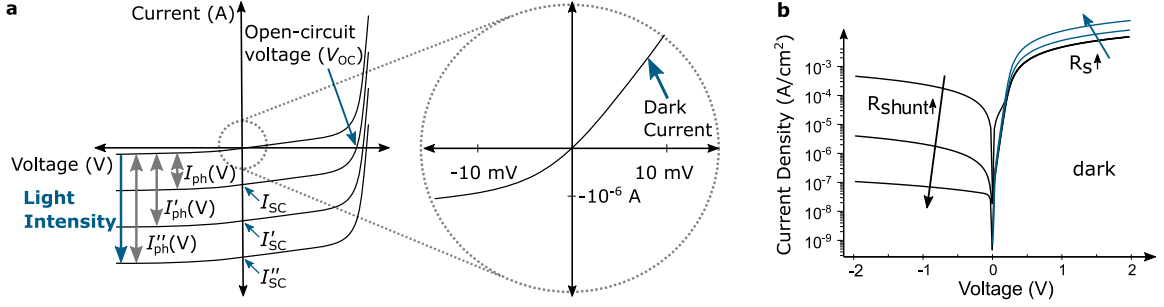


Figure 2.16: **a** An ideal photodiode produces a photocurrent I_{ph} that increases proportional to the incident light power (indicated by a blue arrow). Under illumination, I_{ph} at zero voltage equals the short-circuit current I_{SC} and the voltage at zero current flowing equals the open-circuit voltage V_{OC} . In the dark, the photodiode behaves like a Shockley diode as shown by the inset with a non-zero dark saturation current density in reverse bias. **b** The dark $J - V$ characteristics on a logarithmic scale show a strong dependence on shunt resistance R_{shunt} in reverse bias and dependence on series resistance R_s in forward bias.

Assuming only radiative generation-recombination over the bandgap, $V_{OC} = V_{OC,R}$. $V_{OC,R}$ is called the radiative V_{OC} limit and marks the upper thermodynamic limit of the open-circuit voltage. The difference between the experimental V_{OC} and $V_{OC,R}$ is the recombination loss, which is around 0.2 V in silicon photodiodes, but is typically between 0.4 V to 0.6 V in organic photodiodes.⁶² In organic photodiodes, the origin of such high V_{OC} losses is typically associated with non-radiative recombination.⁶² To account for the different non-idealities, the modified Shockley diode equation is written as

$$J = J_0(V, T) \left[\exp\left(\frac{q(V - JR_s)}{kT}\right) - 1 \right] + \frac{V - JR_s}{R_{shunt}} - J_{ph}, \quad (2.44)$$

where R_s is the series resistance and R_{shunt} is the shunt resistance. In Eq. 2.44, the dark saturation current $J_0(V, T)$ is no longer only on T -dependent, but also dependent on V . The origin of the voltage dependence lies in non-radiative recombination, i.e., $J_0(V, T) = J_{0,R}(T) + J_{0,NR}(V, T)$, where $J_{0,NR}$ is the non-radiative dark saturation current density. To account for the V -dependence of $J_{0,NR}$, often a diode ideality factor (n) is introduced, which deviates from unity ($J_0(V, T) \exp(qV/kT) \approx J_0(T) \exp(qV/nkT)$). Apart from band-to-band transitions, non-radiative recombination channels can be trap-mediated or related to surface effects as previously discussed in Section 2.2.3. In organic semiconductors, the absorption of trap states was detected via sensitively measured photothermal deflection spectroscopy^{98,99} as well as intensity dependent photocurrent measurements⁸⁶ for a large set of fullerene and non-fullerene blends. Recently, the effect of mid-gap trap states has also been observed in the sub-gap EQE⁸⁴ and by impedance spectroscopy.⁸⁵

Figure 2.16a illustrates the $I - V$ characteristics of a photodiodes under different light intensities. It is clear that the photocurrent I_{ph} increases with increasing light intensity. Note that the short circuit current I_{SC} equals I_{ph} at 0 V. Moreover, the photodiode produces a small dark current at voltages close to 0 V as indicated by the zoom to around ± 10 mV. Next, the effect of R_s and R_{shunt} on the dark $J - V$ characteristics are discussed with the help of Fig. 2.16b. To resolve small currents in reverse bias in comparison to forward bias, J (instead of I) is shown on a logarithmic

scale. R_s is the contact resistance associated with the bond between the cell and its wire leads, and the resistance of the semiconductor itself. It generally limits J for high currents in forward bias, but is negligible at reverse bias as shown in Figure 2.16. R_{shunt} typically dominates the $J - V$ curve at small forward bias and in the reverse bias. Since photodiodes are typically operated in reverse bias, the relative contribution of J_{shunt} to $J_0(V, T)$ determines the minimal detectable light power that produces a small photocurrent that equals the dark current. For organic photodiodes typically $J_0(V, T) \ll |J_{\text{shunt}}|$, where J_{shunt} arises from pinholes in the active layer, injection currents due to misaligned energy levels at the semiconductor/metal interface¹⁰⁰ and lateral currents¹⁰¹. Known strategies for reducing J_{shunt} include employing selective charge blocking layers, thick junctions and optimizing the device layout to decrease lateral leakage currents.

2.3.3 Sources of Noise

Noise describes spontaneous fluctuations of a current or voltage signal measured from a semiconductor device. Noise is typically quantified by the electrical power P that is dissipated over a resistor with resistance R . In the case of a time-variant current signal $i_{\text{noise}}(t)$, the power equals $P = \langle i_{\text{noise}}^2 \rangle \times R$, where $\langle i_{\text{noise}}^2 \rangle$ is the mean-square current. In the case of a time-variant voltage signal $v(t)$, that drops over a resistor R , the power equals $P = \langle v_{\text{noise}}^2 \rangle / R$. To extract more information about the signal, noise is typically characterized in the frequency domain as power spectral density (PSD) obtained from the Fourier transform of $i_{\text{noise}}(t)$ (or $v_{\text{noise}}(t)$) under consideration of the Parseval theorem. The PSD describes how the $\langle i_{\text{noise}}^2 \rangle$ (or $\langle v_{\text{noise}}^2 \rangle$) is distributed amongst the various frequency components in units of A^2/Hz (or V^2/Hz). From the unit, it is clear that the power is given per unit bandwidth (in Hz) in the frequency domain, which corresponds to a certain time interval (averaging time) of the measurement of $i_{\text{noise}}(t)$ (or $v_{\text{noise}}(t)$) in the time domain. Alternatively, the amplitude spectral density, which corresponds to the root-mean-square value $\sqrt{\langle i_{\text{noise}}^2 \rangle}$ in units of $\text{A}/\sqrt{\text{Hz}}$, can be used to characterize the noise.

Figure 2.17 illustrates the $\langle i_{\text{shot}}^2 \rangle$ spectrum of a semiconductor device as a function of frequency as it is obtained either from a direct measurement via a fast Fourier transform or swept super-heterodyne spectrum analyser. Alternatively, a fast Fourier transform can be applied to a measurement of $i_{\text{noise}}(t)$. Flicker noise comprises the dominant source of noise showing $1/f$ dependence at low frequencies up to the corner frequency f_c . The origin of Flicker noise is still under debate and no unifying theory for different materials and semiconductor devices exists. For $f > f_c$, shot noise and thermal noise dominate the spectrum. Shot noise is considered a frequency independent white noise for most devices, since the cut-off frequency is in the GHz regime which is rarely accessible with conventional device architecture and materials,^{102–104} and therefore is not explicitly mentioned in Fig. 2.17. Shot noise arises from the quantization of charge carried by electrons in a DC current, and constitutes

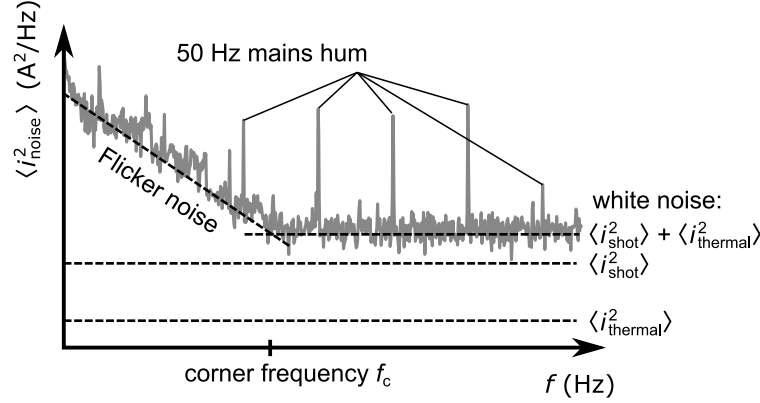


Figure 2.17: At frequencies f below the corner frequency f_c , the noise power spectral density $\langle i_{\text{noise}}^2 \rangle$ is dominated by the Flicker noise. For $f > f_c$, the sum of shot noise $\langle i_{\text{shot}}^2 \rangle$ and thermal noise $\langle i_{\text{thermal}}^2 \rangle$ dominate $\langle i_{\text{noise}}^2 \rangle$, which can be regarded as frequency independent white noise sources. In organic photodiodes at $V > 0$, $\langle i_{\text{shot}}^2 \rangle \gg \langle i_{\text{thermal}}^2 \rangle$. In practice, multiples of 50 Hz, that is mains supply frequency, are often observed in the noise power spectral density, but can be suppressed with electromagnetic shielding of the device under test.

the major noise source in most semiconductor devices that are operated under a voltage that is different to zero. The shot noise of a current density J is given by

$$\langle i_{\text{shot}}^2 \rangle = 2qJ\Delta f, \quad (2.45)$$

where Δf is the frequency bandwidth. Note, that shot noise is temperature independent. Thermal noise occurs in any semiconductor or semiconductor device and is caused by thermal fluctuations, which are an unavoidable source of noise. Herein, thermal agitation causes the occupation of the density of states to fluctuate giving rise to equilibrium current fluctuations in the external circuit – also at $V = 0$. Thermal noise is calculated as

$$\langle i_{\text{thermal}}^2 \rangle = \frac{4kT}{R_p} \Delta f, \quad (2.46)$$

where the parallel resistance R_p is given by

$$R_p = \left(\frac{dJ}{dV} \right)_{V=0}^{-1}. \quad (2.47)$$

For simplicity, it is often assumed that at frequencies above f_c , the total noise is given by the sum over shot and thermal noise,

$$\langle i_{\text{noise,total}}^2 \rangle = \langle i_{\text{shot}}^2 \rangle + \langle i_{\text{thermal}}^2 \rangle. \quad (2.48)$$

For photodiodes, it is important to look at contribution of shot noise and thermal at reverse bias voltage and zero voltage, since those constitute the typical operational bias. Assuming that charge injection can be neglected, the total dark current density is given by the sum of shunt current density J_{shunt} ($J_{\text{shunt}} = V/R_{\text{shunt}}$) and the ideal Shockley diode equation from Eq. 2.42 in the dark:

$$J = \frac{V}{R_{\text{shunt}}} + J_{0,R} \left(\exp \left[\frac{qV}{kT} \right] - 1 \right) \quad (2.49)$$

$J_{0,R}$ is the dark saturation current density of an ideal diode exhibiting no voltage dependence. First, shot noise of J from Eq. 2.49 is evaluated at $V = 0$ and $V \ll 0$. At $V = 0$, the net current density is zero ($J = 0$) and $\langle i_{\text{shot}}^2 \rangle = 0$. At $V \ll 0$, $\langle i_{\text{shot}}^2 \rangle = 2qJ_0\Delta f$, because J_{shunt} does not show shot noise. To calculate the thermal noise, R_P is calculated for J from Eq. 2.49, resulting in

$$\begin{aligned} R_P &= \left(\frac{dJ}{dV} \right)^{-1} \\ &= \left[\frac{1}{R_{\text{shunt}}} + \frac{qJ_{0,R}}{kT} e^{\frac{qV}{kT}} \right]^{-1} \end{aligned} \quad (2.50)$$

By replacing R_P in Eq. 2.46 with the expression obtained in Eq. 2.50, the thermal noise can be written as

$$\begin{aligned} \langle i_{\text{thermal}}^2 \rangle &= \frac{4kT}{R_P} \Delta f \\ &= \left[\frac{4kT}{R_{\text{shunt}}} + 4J_{0,R}q e^{\frac{qV}{kT}} \right] \Delta f \end{aligned} \quad (2.51)$$

with

$$\begin{aligned} \langle i_{\text{thermal}}^2 \rangle &= \frac{4kT}{R_{\text{shunt}}} \Delta f + 4J_{0,R}q \Delta f \quad \text{at } V = 0 \\ \langle i_{\text{thermal}}^2 \rangle &= \frac{4kT}{R_{\text{shunt}}} \Delta f \quad \text{at } V \ll 0. \end{aligned} \quad (2.52)$$

For narrow-gap blends the contribution of $4J_{0,R}q\Delta f$, arising from thermally activated band-to-band recombination, is expected to gain importance¹⁰⁵, since the overlap integral between the EQE and black body radiation spectrum increases when decreasing the bandgap.

2.3.4 Specific Detectivity and Noise Equivalent Power

The dominant figure of merit for a photodetector is the specific detectivity D^* in units of Jones (1 Jones = 1 cm $\sqrt{\text{Hz}}$ /W). D^* is proportional to the square root of the area (A) and the inverse of the noise equivalent power (NEP).

$$D^* = \frac{\sqrt{A\Delta f}}{\text{NEP}} \quad (2.53)$$

The NEP describes a light power that produces a signal that is so small that it can no longer be distinguished from the noise spectral density measured in a bandwidth of 1 Hz. The unit of NEP is therefore W. Sometimes NEP is also given in units of W/ $\sqrt{\text{Hz}}$, which makes Δf redundant in Eq. 2.53. The NEP is obtained directly from extrapolating the linear relationship between photocurrent response and light power down to the noise current. Alternatively, D^* can be obtained from R according to

$$D^* = \frac{R\sqrt{A}}{\sqrt{\langle i_{\text{noise}}^2 \rangle}}, \quad (2.54)$$

where it is assumed that R decreases linearly with optical power. As discussed in Section 2.3.5, the relationship between photocurrent response and light power can deviate from linearity in the presence of traps. In those system, D^* is better inferred from the NEP (see Eq. 2.53) rather than from R and the measured noise current.

Eq. 2.54 can be used to calculate a theoretical D^* in the limit of different noise sources. The upper D^* limit is D_{BLIP}^* , where BLIP stands for the background limited infrared photodetector. In this case, the only source of noise is the shot noise of the thermal radiation of the background due to the discrete nature of incident photons. To find an expression for D_{BLIP}^* for a photodetector with the bandgap E_g , one assumes an ideal photoresponse, where

$$\text{EQE} = \begin{cases} 0 & \text{if } E < E_g \\ 1 & \text{if } E \geq E_g. \end{cases} \quad (2.55)$$

In a real photodetector, the photoresponse is never step-like due to the energetic and static disorder inducing sub-gap absorption as discussed in Section 2.1.5. In thermal equilibrium, the absorption and emission of thermal radiation results in a dark current $J_{0,\text{R}}$. The photodiode is said to operate in the radiative limit as previously discussed in Section 2.3.2. $J_{0,\text{R}}$ is the integral over the EQE and the temperature dependent black-body radiation (see Eq. 2.40). For a step-like EQE, the analytic expression for $J_{0,\text{R}}$ reads

$$J_{0,\text{R}} = \frac{2\pi q}{c^2 h^3} E_g^2 kT e^{-\frac{E_g}{kT}}, \quad (2.56)$$

where q is the elemental charge, c is the speed of light, h is the Planck constant, k is the Boltzmann constant and T is the temperature. Next, assuming that only the shot noise of $J_{0,\text{R}}$ ($= 2qJ_{0,\text{R}}\Delta f$) contributes to the total noise current, D_{BLIP}^* can be calculated at any temperature T using the expression from R according to Equation 2.54 and $J_{0,\text{R}}$ from Eq. 2.45.

$$D_{\text{BLIP}}^* = \frac{R\sqrt{A}}{\sqrt{2qJ_{0,\text{R}}\Delta f}}. \quad (2.57)$$

2.3.5 Linear Dynamic Range

The linear dynamic range (LDR) is the range over which the responsivity R remains constant for different light intensities. Here, the light intensity is described by the physical quantity of irradiance (E_e) in units of W/cm^2 . For imaging, a large LDR allows differentiation over a wide range of brightness levels. The LDR is experimentally obtained by stepwise attenuation of the light source and subsequent current readings on a spectrum analyser or a lock-in amplifier. The LDR should be determined from the double logarithmic plot of photocurrent (I_{ph}) as a function of E_e as shown in Fig. 2.18. A slope that equals 1 indicates a constant R . As shown in Fig. 2.18, the LDR extends

from the deviation point at high irradiance ($E_{e,\max}$) to the deviation point at low irradiance ($E_{e,\min}$). Consequently, the LDR is defined by

$$\text{LDR} = 20 \log \frac{E_{e,\max}}{E_{e,\min}} \quad (2.58)$$

in units of decibel (dB). From the extrapolation of the LDR down to $\sqrt{\langle i_{\text{noise}}^2 \rangle}$ in units of $\text{A}/\sqrt{\text{Hz}}$, the NEP is determined. Note that this definition of the LDR applies to double logarithmic plot of I_{ph} in function of E_e . For a plot of electrical power P ($P \propto I_{\text{ph}}^2$) in function of E_e , the LDR is defined as $\text{LDR} = 10 \log [E_{e,\max}/E_{e,\min}]$.

At high irradiance, the deviation from linearity is often caused by the onset of bimolecular recombination (where recombination is quadratically proportional to the carrier density) or the impact of high series resistance including non-ohmic contacts.^{80,106,107} At low irradiance, a super-linear slope was previously observed due to trap-limited gain.^{108,109} In Fig. 2.18, the black line indicates an ideal LDR with slope 1, while the red line indicate a non-ideal LDR with a sub-linear slope in the high and a super-linear slope low irradiance limit. Assuming a slope of 1 in the low irradiance limit of the red curve would overestimate the NEP, while the true NEP should consider the super-linear behaviour as shown with dashed lines in Fig. 2.18.

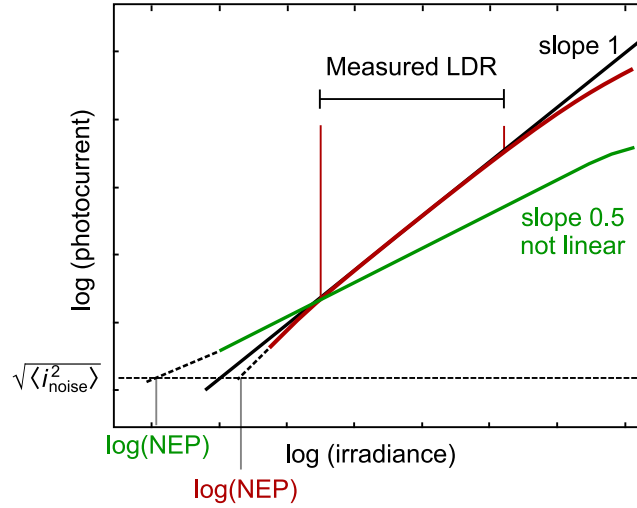


Figure 2.18: Schematic illustration of intensity dependent photocurrent measurements on a log-log plot from which the linear dynamic range (LDR) and the noise equivalent power (NEP) are determined as indicated. The black lines indicates a perfectly linear LDR with a slope of 1, i.e. a constant responsivity R . Non-idealities include a super-linear slope at low irradiance due to traps as well as a sub-linear slope at high intensities due to bimolecular recombination and series resistance. For photodiodes based on photomultiplication, the slope is sometimes 0.5 as indicated by the green line, and a LDR is extracted erroneously despite a non-constant R .

Moreover, there are examples in literature, where the photocurrent is a non-linear function throughout the whole intensity range, hence, the R changes with irradiance. This is often observed for photodiodes based on photomultiplication, where the photocurrent as a function of irradiance on a log-log scale describes a linear function with a slope of 0.5¹¹⁰. Such an example is demonstrated in Fig. 2.18 by a green line. In that case, the LDR is non-existent. For the two cases of non-ideal LDR demonstrated in Fig. 2.18 an estimate of D^* from the R derived Eq. 2.54 would result in a wrong value. The better way of obtaining D^* is to measure the LDR for different light intensities – including the low intensity regime above the noise floor – and then infer the NEP from the extrapolation of the LDR down to $\sqrt{\langle i_{\text{noise}}^2 \rangle}$.

2.3.6 Photodetector Speed

The speed of a photodetector is usually given as the frequency at which the output power has decreased by half its maximum value, hence decreased by -3 dB. The so-called -3 dB cut-off frequency ($f_{-3\text{dB}}$) can be directly estimated from the Bode plot that is obtained with the help of a lock-in amplifier or a network analyser showing the output power of the photodiode as a function of frequency. Another experimental method is to measure the transient photocurrent. In this method, the photodetector is illuminated by a short light pulse and the photocurrent response in function of time is measured with an oscilloscope. From the Fourier Transform of the transient photocurrent signal, a Bode plot can be calculated and $f_{-3\text{dB}}$ can be estimated.

Depending on the application, different photodetectors speeds are required ranging from roughly 100 Hz for imaging applications up to the sub-GHz regime for optical telecommunication. Organic photodiodes routinely reach a response speed of kHz regime (except for photodiodes based on trap-induced photomultiplication) and can reach all the way to 420 MHz in the visible.¹¹¹ Several bandwidth limiting processes are known – each associated with an individual time constant. Typical processes include: (i) transit or drift of charge carriers under an applied electric field; (ii) diffusion of excitons; (iii) trapping and detrapping of charge carriers at interfaces or defects and (iv) capacitive charging and discharging.

Diffusion is a slow process and should be eliminated if possible. In literature on bulk heterojunction, it was shown that the diffusion process of excitons is fast enough such that it will not limit the bandwidth.¹¹² However, in bilayers, where the donor:acceptor interface area is reduced to the junction interface, excitons need to travel longer distances in order to separate and, hence, the photodetector speed becomes diffusion limited.¹¹³

Trapping and detrapping times are especially important at low irradiances in the nW/cm^2 regime, when the majority of photogenerated carriers are required to fill the traps. Consequently, the capture and emission rates of those carriers limit the charge extraction and hence reduce the frequency bandwidth.¹¹⁴ In organic photodiodes based on trap-assisted photomultiplication, the frequency bandwidth is typically below 100 Hz even for higher light intensities due to the slow trap dynamics that are a prerequisite for photogeneration in this type of devices.^{110,115}

Most often, the bandwidth of an organic photodetectors is either transit limited or RC limited, where R is the load resistance and C is the capacitance of the photodetector. Using a dielectric constant of $\varepsilon = 3$ to describe an organic semiconductor, the RC limited bandwidth of the photodetector can be estimated from

$$f_{RC} = \frac{1}{2\pi RC} = \frac{d}{2\pi R_L \varepsilon \varepsilon_0 A} \quad (2.59)$$

to be roughly 6 MHz. R_L is the standard load impedance of 50Ω (as for the network analyser or oscilloscope), d is the layer thickness of around 200 nm, A the photoactive area of 4 mm^2 and the dielectric constant of vacuum is $8.85 \times 10^{-14} \text{ F/cm}$. Note that the capacitance C is given by $C = \varepsilon \varepsilon_0 A/d$. The RC limited bandwidth increases linearly with the layer thickness d due to a decrease in C . Moreover, the RC time constant τ is often mentioned in literature, which is related to the RC limited bandwidth via

$$f_{RC} = \frac{1}{2\pi RC} = \frac{1}{2\pi \tau}. \quad (2.60)$$

The transit limited bandwidth f_{tr} is inversely proportional to d , since an increase in layer thickness leads to a longer transit time t_{tr} via

$$t_{tr} = \frac{d^2}{\mu V}, \quad (2.61)$$

where μ is the carrier mobility. t_{tr} decreases with increasing reverse bias voltage, which is why high-speed photodetectors are typically operated below -0.5 V applied voltage. The carrier transit time limited bandwidth f_{tr} is given by

$$f_{tr} = \frac{0.35}{t_{tr}}. \quad (2.62)$$

The experimental frequency response, characterized by $f_{-3\text{dB}}$, is limited by the slowest process, which can be estimated from

$$f_{-3\text{dB}} = \sqrt{\frac{1}{1/f_{tr}^2 + 1/f_{RC}^2}}. \quad (2.63)$$

Note that reducing the organic layer thickness increases f_{tr} , but it also makes the photodetector more prone to RC limitations due to the direct proportionality between f_{RC} and d (see Eq. 2.59). For a device with a typical active layer thickness of 100 nm to 300 nm, RC limitations can be overcome by lowering the device area. In that case, the transit times of the slower carrier (either electrons or holes in acceptor and donor phase, respectively) will limit the device bandwidth. A common strategy to increase the bandwidth is to use high mobility D:A blends with balanced electron and holes mobilities. In thick junctions devices, the optical field maximum is located much closer to the transparent top contact than the reflective bottom contact. In that case, the

carriers, that have to travel the longer distance to the reflective bottom contact for extraction, will limit the bandwidth irrespective of being the slower or faster species.¹¹⁶

2.4 Organic Near-infrared Photodiodes

In the field of light detection, there exists a variety of absorber materials and photon-to-electron conversion mechanisms. In this chapter, typical photosensing mechanisms used in organic photodiodes are discussed – in particular for energies in the sub-gap range, where the sub-gap states and interference effects play an important role. To this end, the design of the device stack is discussed and how it determines the optical response window, the operational speed and the dark current. Challenges associated with the different device types are shown and comparisons to inorganic photodetectors are drawn.

2.4.1 Organic Semiconductors for Photodetection

Photodiodes are often characterized by the position and the width of the optical response window within the electromagnetic spectrum. This operational window is both a function of the absorption coefficient of the photoactive material and the overall device architecture. Organic semiconductors are seen as particularly promising for the near-infrared (NIR) spectral range between 750 nm to 1700 nm. Notable fields of applications include optical telecommunication (1300 nm to 1550 nm), light detection and ranging (LIDAR) control systems for automotive imaging (905 nm and 1550 nm) and spectroscopy, e.g. for water with characteristic absorption peaks at 960 nm and 1460 nm. For the aforementioned applications, narrowband photoresponse is required, which poses additional complexity on design and function.

Organic semiconductors typically show a strong absorption coefficient and a tunable bandgap by means of chemical structure modifications. As discussed in Section 2.1, a common strategy to achieve a redshift of the photoresponse is to increase the conjugation length of the π -system and to add electron-donating groups to decrease the HOMO-LUMO bandgap. Doing so, optical bandgaps up to 1500 nm were previously demonstrated.^{6,117–119} Besides the tunable photoresponse, organic semiconductors can be incorporated into flexible form factor geometries, promise extremely low cost and low embodied energy manufacturing from earth abundant materials. This is particularly important for use in low-cost photodetectors produced en masse such as wearable devices.

The material properties of organic semiconductors can be viewed as complimentary to the conventional inorganic semiconductors: The ubiquitous silicon (Si) photodiodes show a weak broadband absorption up to 1100 nm, which is not suitable for the NIR. Conventional lower bandgap semiconductors, such as indium gallium arsenide, mercury cadmium telluride or lead sulphide, deliver excellent device performances in the NIR, but typically contain rare or toxic materials and are costly given their increased device complexity. For imaging purposes, conventional sensors have a limited resolution, related to the fact that the photoactive layer is mounted via wire-bonded electrical connections onto the silicon read-out integrated circuitry (ROIC).¹²⁰ This limits the smallest pixel pitch to approximately 10 μm since a very precise alignment between the ROIC and the active layer is required. To allow downscaling of the pixel

size, an ongoing endeavour focuses on directly growing photoactive layers on the ROIC. However, device breakdown upon temperature fluctuations is often observed due to the difference in thermal expansion coefficients between the active layer and the ROIC or the electrical interconnects.¹²¹ Wavelength selectivity in conventional narrowgap semiconductors is typically achieved by addition of optical filters and dichroic prisms, which increases device complexity and poses extra limits on the spatial resolution.¹²²

Using submicron thick, strongly absorbing organic semiconductors, it is possible to decrease the pixel pitch to the diffraction limit of NIR light of a couple of microns¹²³ via monolithic integration.⁷ Solution processing, combined with the fact that organic semiconductors are less brittle and more resistant to internal thermal stress, enables deposition of organic active layers directly on the ROIC, thereby very much simplifying device fabrication and lowering costs. Using the naturally small bandwidth of some organic semiconductors, or electro-optical device concepts such as charge collection narrowing (CCN) or micro-cavities, narrowband gap photodetection can be achieved with organic semiconductors without the need of additional optical filters. In the following, the device architecture of conventional bulk heterojunction type organic photodiodes will be discussed, followed by the concepts of CCN, micro-cavities and finally photomultiplication, which has shown promising results in literature for achieving high specific detectivities in the VIS and NIR.

2.4.2 Bulk Heterojunction Organic Photodiodes

In the past decade, advances in the field of organic solar cells have strongly benefited the field of organic photodiodes. This includes the development of organic semiconductors with high absorption coefficients and charge carrier mobilities, as well as their processing conditions leading up to the bulk heterojunction (BHJ), which comprises the active layer of the modern organic solar cells and photodiodes with record efficiencies. In organic photodiodes, with a simple device architecture resembling that of organic solar cells, the BHJ is sandwiched between charge selective transport layers, and a top and a bottom contact in a vertically stacked device architecture. A schematic representation of an organic photodiode with a solar cell type device architecture is shown in Fig. 2.19a. In early stages, planar junctions, similar to the inorganic *pn*-junctions, were fabricated using organic semiconductors. However, the short exciton diffusion length in organic semiconductors decreased the maximum achievable internal quantum efficiency, which is why the planar junction was later abandoned for the BHJ for reasons discussed in Section 2.2.2. During device fabrication, a BHJ is formed on top of the charge transport layer either by spin-coating D and A from a single solution or via co-evaporation (small molecules; not solution processable) in a vacuum chamber. An ongoing endeavour is to find the right processing conditions for emerging non-fullerene acceptor blends to form a BHJ morphology that promotes efficient charge generation and charge extraction. Given that non-fullerene acceptors are small molecules, it was shown that they tend to form larger crystalline domains^{124,125} than previously observed in fullerene blends, which is expected to increase the exciton diffusion length. In efficient solution-processed organic

photodetectors, additives such as diiodooctane (DIO) are used to promote the formation of a more favourable BHJ morphology.¹²⁶ The charge selective transport layers adjacent to the photoactive layer comprise an electron transport layer (ETL) and hole transport layer (HTL) with characteristic thicknesses below 30 nm. ETL and HTL prevent the hole and electron extraction at the wrong contact, respectively. Typical ETLs are BCP⁽¹⁾, ZnO⁽²⁾ and BPhen⁽³⁾, while typical HTLs are PEDOT:PSS⁽⁴⁾ and MoO₃⁽⁵⁾. In vacuum-processed organic photodiodes, thicker transport layer are routinely evaporated such as neat C₆₀ with thicknesses up to 100 nm, which acts as an efficient ETL decreasing the dark current. Moreover, doped transport layers are often used to adjust the energy barriers at the contacts and to reduce ohmic losses through increased conductivity. Doping in organic semiconductors can be achieved by co-evaporation of small quantities of molecules with either a low ionization potential acting as *n*-dopants or molecules with strong electron affinity acting as *p*-dopants. Finally, the photodiode requires two metal contacts for charge extraction of which one contact has to be at least semitransparent for the light to enter the device. As transparent contact, ITO⁽⁶⁾ on glass is used almost exclusively in organic semiconductors, while the other contact is typically either silver or aluminium.

A conventional solar cell type architecture with an active layer thickness of around 100 nm delivers a broadband response primarily in the visible (VIS) as schematically shown in the EQE spectrum in Fig. 2.19b. As discussed in Section 2.1, there is sub-gap absorption which results in a low-energy shoulder to the EQE, but can have different spectral lineshapes depending on the absorption of sub-gap states and optical interference effects. Using this type of photovoltaic device architecture, specific detectivities of D^* have been demonstrated between 10^{12} to 10^{13} Jones, which is comparable to the D^* of the silicon *pn*-type photodiode.^{127,128} By decreasing the bandgap of the organic semiconductor, the broadband absorption can be redshifted up to 1500 nm. However, for wavelengths above 1400 nm, D^* is typically limited to below 10^{10} Jones due to a lack of suitable absorber materials.^{6,117–119}

⁽¹⁾bathocuproine

⁽²⁾zinc oxide

⁽³⁾4,7-diphenyl-1,10-phenanthroline

⁽⁴⁾poly(3,4-ethylenedioxythiophene) polystyrene sulfonate

⁽⁵⁾molybdenum trioxide

⁽⁶⁾indium tin oxide

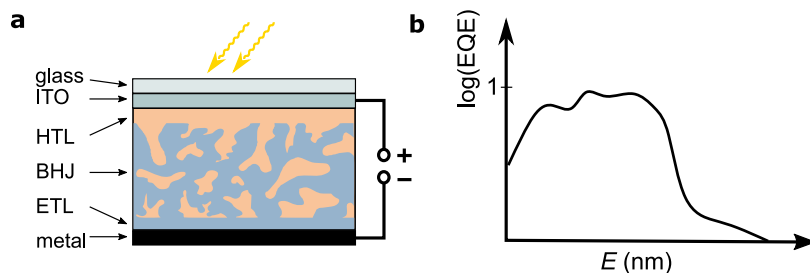


Figure 2.19: **a** Schematic illustration of an organic photodiode with a solar cell like device architecture. The photodiode comprises a vertical stack of indium tin oxide (ITO) as the top contact, a hole transport layer (HTL), a bulk heterojunction (BHJ) active layer, an electron transport layer (ETL) and a bottom metal contact. **b** The photoresponse of the photodiode can be described by the external quantum efficiency (EQE) spectrum for which $\text{EQE} \leq 1$. On the logarithmic scale a sub-gap EQE contribution can often be observed comprising charge transfer absorption and/or trap state absorption.

2.4.3 Organic Photodetectors with Charge Collection Narrowing

For applications such as imaging or spectroscopy, wavelength-selective photodetection or color discrimination is required. One important concept to achieve a narrowband photoresponse is charge collection narrowing (CCN). In literature, a tunable photoresponse window with full width at half maximum (FWHM) of around 90 nm was demonstrated at 940 nm with a D^* of 5×10^{12} Jones at -1 V.¹²⁹ The device architecture is similar to a solar cell type photodiode, but it comprises a thick BHJ ($\approx 2 \mu\text{m}$) as the active layer and an additional ETL of thermally evaporated C_{60} . A schematic representation of the device architecture is shown in Fig. 2.20a. According to the Lambert-Beer law discussed in Section 2.1, the transmission of a thin-film with the thickness d decays exponentially with $\exp[-\alpha(\lambda)d]$, where $\alpha(\lambda)$ is the wavelength dependent absorption coefficient of the active layer. Upon illumination, short wavelength photons, for which high α is typically high in organic semiconductors, are absorbed close to the transparent ITO contact in the photoactive layer and result in surface generation of charge carriers with high recombination losses. Long wavelength photons, for which α is typically lower in organic semiconductors, can penetrate deeper into the active layer resulting in more homogeneous photogeneration with less recombination. As a result, only electrons generated from long wavelength photons will be collected efficiently due to the shorter transit times. The thickness of the photoactive layer is adjusted such that charge collection is only efficient for photons with energies just above the bandgap. Since photon absorption below the bandgap decreases exponentially with energy, a narrowband response arises that is centred around the absorption onset as shown in Fig. 2.20b. By tuning the active layer thickness with respect to the bandgap of the BHJ, narrowband red, green, and blue photodetectors were realized without the use of external colour filters. Moreover, response speeds in the sub-MHz regime have been demonstrated, which were limited by the slowest carrier transit time in the thick junction.¹¹⁶

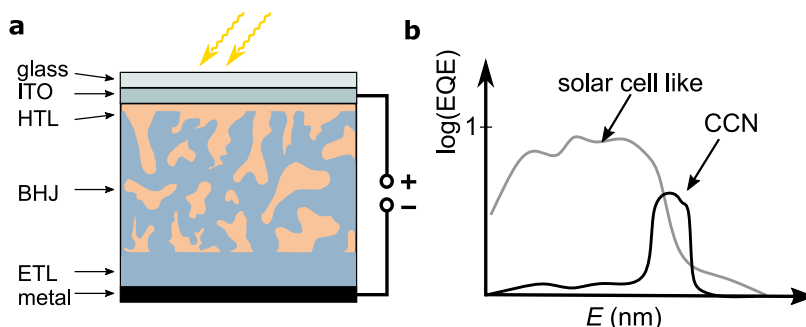


Figure 2.20: **a** Schematic illustration of an organic photodiode with charge collection narrowing (CCN). The photodiode comprises a vertical stack of indium tin oxide (ITO) as the top contact, a hole transport layer (HTL), a bulk heterojunction (BHJ) active layer (micron thick), an electron transport layer (ETL) and a bottom metal contact. **b** The photoresponse of a CCN type photodiode is a narrow band (FWHM between 50 nm to 100 nm)^{129, 130} centered around the EQE onset of an equivalent photovoltaic type photodiode with a thin active layer (≈ 100 nm).

2.4.4 Micro-cavity Enhanced Organic Photodetectors

Another method to achieve narrowband photodetection with FWHM of 50 nm and below¹⁶ is to employ an optical micro-cavity. The main difference to a photodiode with a solar cell like device architecture presented earlier is an additional semitransparent top contact. The incoming light is partially trapped in between the electrodes resulting in optical interference with an electric field maximum at the so-called resonance wavelength. The resonance wavelength and peak intensity depend on the absorption coefficient and the effective cavity thickness as described in Section 2.1. For an efficient optical micro-cavity, the electric field maximum at the resonance wavelength has to be located within the photoactive layer. This is achieved by either using optical spacers¹⁴ as indicated in Fig. 2.21a, which are ideally both charge selective as well as transparent to the resonance wavelength, or through tuning the active layer thickness¹³¹. This optimization of thickness and optical constants of each layer requires optical transfer-matrix simulations. Moreover, the absorption coefficient at the resonance wavelength should be relatively low ($\approx 10^3 \text{ cm}^{-1}$) for a high quality optical cavity to achieve amplification at the resonance wavelength. For that reason, optical cavities have proven particularly successful in combination with weak CT state absorption. In this regard, cavity enhanced photodetectors with a maximum D^* of around 10^{13} Jones at 910 nm and 0 V were demonstrated, as well as the most red-shifted narrowband photodiode at 1680 nm with D^* of around 10^8 Jones at 0 V.¹³¹ The advantages of this method in comparison to the earlier presented CCN method are faster response time, as the active layer can be relatively thin (< 500 nm). In vacuum-processed cavity-enhanced photodiodes, a thin active layer (≈ 25 nm) and doped interlayers are used as optical spacers enabling fast charge collection for a response speeds up to 68 MHz.¹³² In a solution-processed cavity-enhanced photodiodes, response speeds of around 1 MHz for a narrowband photodiode with an active layer thickness of 440 nm operating at 910 nm were demonstrated.¹³¹

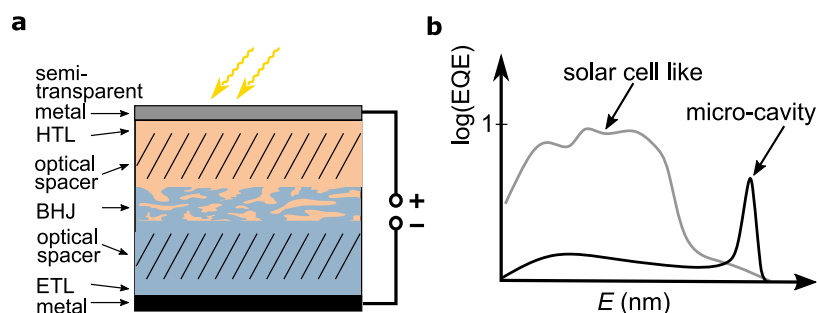


Figure 2.21: **a** Schematic illustration of a micro-cavity enhanced organic photodiode. The micro-cavity comprises a semitransparent top electrode, a hole transport layer (HTL), a bulk heterojunction (BHJ) active layer, an electron transport layer (ETL) and a fully reflective bottom contact. The HTL and ETL also act as optical spacers controlling the spatial distribution of the optical field. **b** The ideal photoresponse of a cavity-enhanced NIR photodetector is an ultra-narrow Lorentzian shaped resonance peak with FWHM < 30 nm in the spectral range of charge transfer absorption.

As a disadvantage, the respective devices often comprise a significant above-gap EQE contribution, which requires the use of external filters. Moreover, optical micro-cavities can be difficult to design and to fabricate due to the thin metal layer on top, additional interlayers and the optical simulations required. Moreover, the above-gap α of most organic semiconductors is too high to be used in efficient cavity-enhanced photodiodes.

2.4.5 Organic Photodetectors with Photomultiplication

Another literature reported working principle of organic photodetectors is trap-assisted photomultiplication. Similar to established inorganic devices, such as photomultiplier tubes and avalanche photodiodes, in photomultiplication type photodetectors, one photon can result in multiple electrons, hence $\text{EQE} > 1$. To do so, nanoparticles (such as cadmium telluride or zinc oxide) are blended into a BHJ matrix¹⁰ as illustrated in Fig. 2.22a or an interfacial layer^{133,134} is introduced. Both methods will create traps for one type of charge carrier. Upon illumination, the photogenerated carriers of one type are trapped close to the contact, hence accumulated, and the electrical field of those carriers causes band bending at the contact enabling carriers with the opposite charge to be injected via tunnelling across the injection barrier under applied reverse bias. The EQE increases with applied reverse bias as indicated in Fig. 2.22b on a logarithmic scale reaching to a maximum reported value of around 74000 % for voltages as high as -20 V at 600 nm.¹³⁵ In this same study, the dark current increases strongly with applied reverse bias to -0.01 A/cm². As a consequence, despite the high EQE, D^* reaches only modest values of 2×10^{12} Jones. Some other studies seem to combine an extremely high EQE with a low dark current reaching D^* up to 10^{14} Jones,^{130,136} however, there is clearly a trade-off between the EQE and dark current that needs further clarification.¹¹⁵ A clear disadvantage of photomultiplication type photodiodes is the limited response speed of below 1 kHz¹³³ due to the slow trap dynamics. Moreover, non-linearities of the responsivity are often observed at low light intensities for systems with high trap densities.

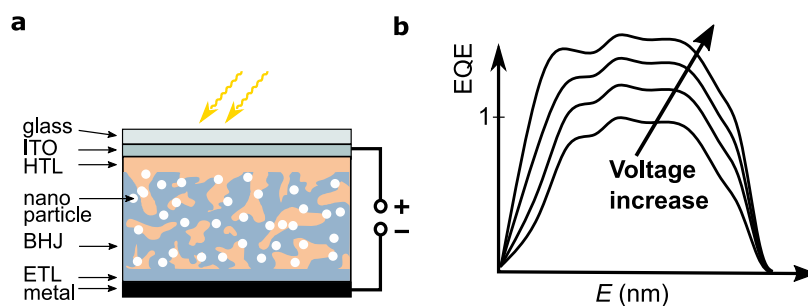


Figure 2.22: **a** Schematic illustration of a possible photodiode device architecture using trap-assisted photomultiplication. The photodiode comprises a transparent top electrode, a hole transport layer (HTL), a bulk heterojunction (BHJ) active layer with added nanoparticles (white spheres) creating charge selective trap state, an electron transport layer (ETL) and a fully reflective bottom contact. **b** For a device architecture as shown in (a), a broadband photoresponse in the VIS spectral range is expected. By applying large reverse bias, the EQE can be increased by multiple orders of magnitude. However, this often increases the dark current to a similar extent.

Chapter 3

Experimental Methods

This chapter introduces the main experimental methods used in the research presented in this thesis. At the beginning, all organic materials are listed as well as their processing conditions used in the course of this thesis. Next, the fabrication of organic solar cells and photodetectors is explained including partially solution-processed and fully thermally evaporated devices. Finally, the different electrical and optical characterization methods for organic solar cells and photodiodes are explained.

3.1 Materials

Table 3.1 to 3.3 show the materials used in the work described in this thesis, including their full chemical name and supplier. Electron-donating (donors) polymers and small molecules are shown in Table 3.1. Electron-accepting molecules (fullerenes and non-fullerene acceptors) are shown in Table 3.2. Materials used as either hole or electron transport layer from solution processing are shown in Table 3.3.

Material	Full Name	Supplier
PTTBAI	poly[(thieno[3,2-b]thiophene)-alt-(7,14-bis(4-(2-octyldodecyl)thiophen-2-yl)diindolo[3,2,1-de:3',2',1'-ij][1,5]naphthyridine-6,13-dione)]	Hasselt University
PBTQ(OD)	poly[(thiophene)-alt-(6,7-bis(5-(2-hexyldecyl)thiophen-2-yl)-4,9-di(thiophen-2-yl)-[1,2,5]thiadiazolo[3,4-g]quinoxaline)]	Hasselt University
PTTQ(HD)	poly[(benzene)-alt-(6,7-bis(5-(2-octyldodecyl)thiophen-2-yl)-4,9-di(thiophen-2-yl)-[1,2,5]thiadiazolo[3,4-g]quinoxaline)]	Hasselt University
PTTQn(HD)	4,9-dibromo-6,7-bis(5-(2-hexyldecyl)thiophen-2-yl)-[1,2,5]thiadiazolo[3,4-g]quinoxaline	Hasselt University
D1*	2,2',6,6'-tetraphenyl-4,4'-bipyranlydene	IAPP [†]
D2*	2,2',6,6'-tetra-p-tolyl-4,4'-bipyranlydene	IAPP [†]
D3*	2,2',6,6'-tetrathienyl-4,4'-bipyranlydene	IAPP [†]
D4*	2,2',6,6'-tetra-(2-methylthienyl)-4,4'-bipyranlydene	IAPP [†]
D5*	2,2',6,6'-tetraphenyl-4,4'-bithiopyranlydene	IAPP [†]
D6*	2,2',6,6'-tetra-p-tolyl-4,4'-bithiopyranlydene	IAPP [†]
D7*	2,2',6,6'-tetrathienyl-4,4'-bithiopyranlydene	IAPP [†]
D8*	2,2',6,6'-tetra-(2-methylthienyl)-4,4'-bithiopyranlydene	IAPP [†]
PCDTBT	Poly[N-9'-heptadecanyle-2,7-carbazole-alt-5,5-(4',7'-di-2-thienyl-2',1',3'-benzothiadiazole)]	Sigma-Aldrich & Ossila
BQR	benzodithiophene-quaterthiophene-rhodanine	University of Melbourne
PM6	poly[(2,6-(4,8-bis(5-(2-ethylhexyl-3-fluoro)thiophen-2-yl)-benzo[1,2-b:4,5-b']dithiophene))-alt-(5,5-(1',3'-di-2-thienyl-5',7'-bis(2-ethylhexyl)benzo[1',2'-c:4',5'-c']dithiophene-4,8-dione))]	Zhi-yan (Nanjing) Inc
m-MTDATA	4,4',4''-tris[(3-methylphenyl)phenylamino]triphenylamine	Ossila
PBDB-T	poly[(2,6-(4,8-bis(5-(2-ethylhexyl)thiophen-2-yl)-benzo[1,2-b:4,5-b']dithiophene))-alt-(5,5-(1',3'-di-2-thienyl-5',7'-bis(2-ethylhexyl)benzo[1',2'-c:4',5'-c']dithiophene-4,8-dione))]	Zhi-yan (Nanjing) Inc.
PTB7-Th	poly[4,8-bis(5-(2-ethylhexyl)thiophen-2-yl)benzo[1,2-b:4,5-b']dithiophene-2,6-diyl-alt-(4-(2-ethylhexyl)-3-fluorothieno[3,4-b]thiophene-)-2-carboxylate-2,6-diyl]	Zhi-yan (Nanjing) Inc.
EH-IDTBR	5,5'-[[4,4,9,9-tetrakis(2-ethylhexyl)-4,9-dihydro-s-indaceno[1,2-b:5,6-b']dithiophene-2,7-diyl]bis(2,1,3-benzothiadiazole-7,4-diylmethylidene)]bis[3-ethyl-2-thioxo-4-thiazolidinone]	Solarmer (Beijing)
PBTTT	poly[2,5-bis(3-tetradecylthiophen-2-yl)thieno[3,2-b]thiophene]	Sigma-Aldrich

Table 3.1: Donor materials used throughout the work described in this thesis. * Small molecules deposited from vacuum. [†] Dresden Integrated Center for Applied Physics and Photonic Materials.

Material	Full Name	Supplier
PC ₇₀ BM	[6,6]-phenyl-C71-butyric acid methyl ester	Sigma-Aldrich
C ₆₀	buckminsterfullerene	CreaPhys
ITIC	3,9-bis(2-methylene-(3-(1,1-dicyanomethylene)-indanone))-5,5,11,11-tetrakis(4-hexylphenyl)-dithieno[2,3-d:2',3'-d']-s-indaceno[1,2-b:5,6-b']dithiophene	Zhi-yan (Nanjing) Inc
IT-4F	3,9-bis(2-methylene-(3-(1,1-dicyanomethylene)-6,7-difluoro)-indanone))-5,5,11,11-tetrakis(4-hexylphenyl)-dithieno[2,3-d:2',3'-d']-s-indaceno[1,2-b:5,6-b']dithiophene	Zhi-yan (Nanjing) Inc
Y6	2,2'-((2Z,2'Z)-((12,13-bis(2-ethylhexyl)-3,9-diundecyl-12,13-dihydro-[1,2,5]thiadiazolo[3,4-e]thieno[2'',3'':4',5']thieno[2',3':4,5]pyrrolo[3,2-g]thieno[2',3':4,5]thieno[3,2-b]indole-2,10-diyl)bis(methanylylidene))bis(5,6-difluoro-3-oxo-2,3-dihydro-1H-indene-2,1-diylidene))dimalononitrile	Zhi-yan (Nanjing) Inc

Table 3.2: Acceptor Materials used throughout the work described in this thesis.

Material	Full Name	Supplier
PEDOT:PSS	poly(3,4-ethylenedioxythiophene) polystyrene sulfonate	Heraeus
ZnO	Precursor for ZnO: zinc acetate dihydrate	Sigma Aldrich
PEIE	Polyethylenimine ethoxylated	Sigma Aldrich
BPhen	4,7-diphenyl-1,10-phenanthroline	Lumtux

Table 3.3: Solution processed hole and electron transport materials used throughout the work described in this thesis.

3.2 Device Fabrication

3.2.1 Solution Processed Devices

Commercial ITO coated glass substrates from Ossila (100 nm ITO, sheet resistivity $20 \Omega/\square$) were used for the studies conducted in this thesis. Figure 3.1a shows a bare ITO coated glass substrate as purchased from Ossila and Figure 3.1b illustrates an example of a organic solar cell (without encapsulation glass on top). Each substrate is designed to contain eight pixels (also called “devices”) with an active area of 0.04 cm^2 each, as illustrated in Figure 3.1c. Prior to the deposition of the organic layers, the bare ITO substrates were cleaned in an aqueous solution of Alconox at 60°C , followed by an ultrasonic bath in deionize water, acetone and isopropanol. The cleaned substrates were dried with nitrogen, followed by a UV/O₃ treatment (Ossila, L2002A2-UK).

Solar cells were fabricated with either a conventional architecture ITO/PEDOT:PSS/active layer/Ca/Al or inverted architecture ITO/ZnO/active layer/MoO₃/Ag. For the conventional device architecture, a 30 nm-thick layer of PEDOT:PSS was spin-coated at 6000 rpm for 30 s onto precleaned ITO substrates and annealed at 155°C for 15 min. For the inverted device architecture, a solution of 200 mg of zinc acetate dihydrate in 2-methoxyethanol (2 ml) and ethanolamine (56 μl) was prepared and stirred overnight under ambient conditions. 30 nm of ZnO thin film formed upon spin-coating the solution at 4000 rpm onto the precleaned ITO substrates followed by thermal annealing at 200°C for 60 min. The active layer was deposited on top of PEDOT:PSS or ZnO via solution processing as described in Table 3.4 under

nitrogen atmosphere (<1 ppm O_2 and H_2O) in the LC150 Glovebox (LC Technology Solutions Inc). In the next step, the substrates were transferred into the glove box with an integrated evaporator (Kurt J. Lesker NANO 36TM). For the conventional device architecture, 20 nm of calcium (Ca) and 100 nm of Aluminium (Al) were thermally evaporated at around 10^{-6} mbar pressure. For the inverted device architecture, 7 nm of MoO_3 and 100 nm of Ag were thermally evaporated at a similar pressure.

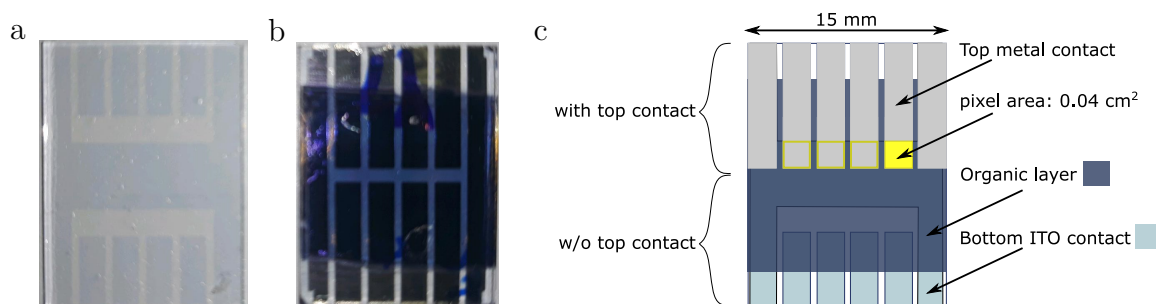


Figure 3.1: **a** Image of a bare ITO coated glass substrate from Ossila. **b** Image of a solution processed organic solar cell build on top of the ITO substrate from (a). **c** Sketch of the organic solar cell with a single device (one pixel) marked in yellow with a total number of eight devices. The device area of 0.04 cm^2 is defined by the geometrical overlap of the top metal electrode (Ag or Al, marked in grey) the active layer (marked in blue) and the bottom ITO contact (marked in light blue).

Device Architecture	Active Layer Processing Conditions	Chapter
ITO/PEDOT:PSS/ BQR:PC ₇₀ BM /Ca/Al	BQR and PC ₇₀ BM were dissolved in toluene (24 mg/ml) with a donor:acceptor mass ratio of 1:1 and stirred at 60 °C for 3 hours.	6 (†)
ITO/ZnO/m- MTDATA:PC ₇₀ BM /MoO ₃ /Ag	Equimolar solutions of PC ₇₀ BM and m-MTDATA in dichloromethane (DCM) with a concentration of 19.4 mmol/mg were prepared. To obtain a series of solutions with different molar ratios of m-MTDATA to PC ₇₀ BM (5 mol%, 1 mol%, 0.1 mol% and 0 mol%), 50 μ L, 10 μ L, 1 μ L and 0 μ L of m-MTDATA in DCM were added to 1 ml of PC ₇₀ BM in DCM. The solutions were spin-coated at a spin rate of 800 rpm to get an active layer thickness of around 90 nm.	6 (†)
ITO/ZnO/PM6:Y6 /MoO ₃ /Ag	PM6:Y6 was dissolved in CF solution (14 mg/ml with 0.5 vol.% CN) with a D:A ratio of 1:1.2. The solution was spin-coated (3000 rpm) on ZnO and thermally annealed at 110 °C for 10 min to form a 100 nm thick film.	6 (*)
ITO/ZnO/ PM6:ITIC /MoO ₃ /Ag	PM6:ITIC was dissolved in CB solution (18 mg/ml) with 0.5 vol.% DIO) with a D:A ratio of 1:1, and spin-coated (1000 rpm) on ZnO to form a 100 nm thick film. The active layers were further treated with thermal annealing at 100 °C for 10 min.	6 (*)
ITO/ZnO/ PBDB-T:EH- IDTBR/MoO ₃ /Ag	PBDB-T:EH-IDTBR was dissolved in CB solution (14 mg/ml) with a donor:acceptor ratio of 1:1, and spin-coated (800 rpm) on ZnO to form a 100 nm thick film.	6 (*)
ITO/ZnO/PBDB- T:ITIC /MoO ₃ /Ag	PBDB-T:ITIC was dissolved in CB solution (14 mg/ml with 0.5 vol.% DIO) with a donor:acceptor ratio of 1:1, and spin-coated (800 rpm) on ZnO to form a 100 nm thick film. The active layers were further treated with thermal annealing at 100 °C for 10 min.	6 (*)
ITO/ZnO/PTB7- Th:ITIC /MoO ₃ /Ag	PTB7-Th:ITIC was dissolved in CB solution (14 mg/ml with 1 vol.% DIO) with a donor:acceptor ratio of 1:1.4, and spin-coated (1000 rpm) on ZnO to form a 100 nm thick film.	6 (*)
ITO/ZnO/PBDB- T:IT-4F /MoO ₃ /Ag	PBDB-T:IT-4F was dissolved in CB solution (14 mg/ml with 0.5 vol.% DIO) with a donor:acceptor ratio of 1:1, and spin-coated (800 rpm) on ZnO to form a 100 nm thick film. The active layers were further treated with thermal annealing at 100 °C for 10 min.	6 (*)
ITO/ZnO/PBDB- T:PC ₇₀ BM /MoO ₃ /Ag	PBDB-T:PC ₇₀ BM was dissolved in CB solution (14 mg/ml with 3 vol.% DIO) with a donor:acceptor ratio of 1:1.4, and spin-coated (1000 rpm) on ZnO to form a 100 nm thick film.	6 (*)
ITO/ZnO/ ITIC/MoO ₃ /Ag	ITIC was dissolved in chloroform solution (10 mg/ml) and spin-coated on ZnO (2000 rpm) to form a 70 nm thick film.	6 (*)

Table 3.4: Device fabrication process, reference to the chapter in which the relevant device results are described. * Devices were fabricated by Dr. Wei Li. † Devices were fabricated by Dr. Nasim Zarrabi.

3.2 SOLUTION PROCESSED DEVICES

Device Architecture	Active Layer Processing Conditions	Chapter
ITO/ZnO/IT-4F/MoO ₃ /Ag	IT-4F was dissolved in chloroform solution (10 mg/ml) and spin-coated on ZnO (2000 rpm) to form a 70 nm thick film.	6 (§)
ITO/ZnO/PBDB-T/MoO ₃ /Ag	PBDB-T was dissolved in chloroform solution (10 mg/ml) and spin-coated on ZnO (3000 rpm) to form a 70 nm thick film	6 (§)
ITO/ZnO/Y6/MoO ₃ /Ag	Y6 was dissolved in chloroform solution (16 mg/ml) and spin-coated on ZnO (3000 rpm) to form a 700 nm thick film.	6 (§)
ITO/ZnO/PEIE*/PTTBAI:PC ₇₀ BM/MoO ₃ /Ag	A solution of PTTBAI and PC ₇₀ BM (ratio 1:3, 64 mg/ml) was prepared in o-dichlorobenzene and stirred overnight at 60 °C. Upon addition of 7 vol.% of DIO, the solution was spin-coated (1500 rpm for 250 nm, 800 rpm for 450 nm). The active layer was left to dry overnight before metal deposition.	7&8 (†)
ITO/ZnO/PEIE*/PBTQ(OD):PC ₇₀ BM/MoO ₃ /Ag	A solution of PBTQ(OD) and PC ₇₀ BM (ratio 1:3, 48 mg/ml) was prepared in o-dichlorobenzene and stirred overnight at 60 °C. Upon addition of 3 vol.% of DIO, the solution was spin-coated (1100 rpm for 140 nm, 700 rpm for 410 nm). The active layer was left to dry overnight before metal deposition.	7&8 (†)
ITO/ZnO/PEIE*/PTTQ(HD):PC ₇₀ BM/MoO ₃ /Ag	A solution of PTTQ(HD) and PC ₇₀ BM (ratio 1:3, 32 mg/ml) was prepared in chloroform and stirred overnight at 60 °C. Upon addition of 3 vol.% of DIO, the solution was spin-coated (700 rpm for 250 nm). The active layer was left to dry overnight before metal deposition.	7&8 (†)
ITO/ZnO/PEIE*/PTTQn(HD):PC ₇₀ BM/MoO ₃ /Ag	A solution of PTTQn(HD) and PC ₇₀ BM (ratio 1:3, 40 mg/ml) was prepared in o-dichlorobenzene and stirred overnight at 60 °C. Upon addition of 3 vol.% of DIO, the solution was spin-coated (700 rpm for 130 nm, 500 rpm for 310 nm). The active layer was left to dry overnight before metal deposition.	7&8 (†)
ITO/ZnO/PBTTT:PC ₇₀ BM/MoO ₃ /Ag	PBTTT and PC ₇₀ BM were mixed in a weight ratio of 1:4 and dissolved in chloroform:1,2-dichlorobenzene (6:4 volume ratio). The solution was stirred overnight, filtered through a 0.2 µm PTFE filter in the cold and spin-coated at 65 °C for 60 s. For film thicknesses between 100 and 200 nm, the concentration of the solution was chosen to be 32 mg/ml and the spin speed was varied between 1000 and 3000 rpm. For layer thicknesses below 100 nm, the same solution was diluted to 20 mg/ml and the spin speed varied between 1000 and 1500 rpm.	4
ITO/ZnO/PBDB-T:PC ₇₀ BM/MoO ₃ /Ag	PBDB-T and ITIC were mixed in a weight ratio of 1:1 and dissolved in chlorobenzene at 50 °C overnight to form a 20 mg/ml solution. 0.5 vol.% of DIO was added prior to spin-coating, while keeping the solution at 50 °C throughout the deposition process. Film thicknesses between 60 and 375 nm were obtained by varying the spin speed between 400 and 2700 rpm and subsequent thermal annealing at 160 °C for 10 min.	4

Table 3.5: Device fabrication process and reference to the chapter in which the relevant device results are described. *PEIE interlayers were spin-coated from a solution of PEIE (0.1 ml, 35-40 wt% PEIE in H₂O, Merck) in isopropanol (35 ml). § Devices were fabricated by Dr. Wei Li. † Devices were fabricated by Dr. Sam Gielen.

3.2.2 Thermally Evaporated Devices

The solar cells and photodetectors presented in Chapter 5 are were fabricated in a commercial evaporation tool (Kurt J. Lesker company) under typical pressures of $p = 10^{-9}$ to 10^{-7} mbar.⁽¹⁾ The solar cells had the device architecture: ITO (90 nm)/MoO₃ (2 nm)/active layer (50 nm)/BPhen (8 nm)/Al (100 nm). The active layer comprised a blend of around 5 weight%donor (D) diluted in the acceptor C₆₀. The donors used for this worked were small molecules from the bipyranlydene family as listed in Table 3.1. This dilution was achieved by thermal co-evaporation of D and C₆₀. To compare with the solar cell architecture, a series of narrowband photodetectors with the same active layers was fabricated comprising a fully reflective top Ag contact (100 nm) and semitransparent bottom Ag contact (25 nm). The device layout is sketched in Figure 3.2. The transport layers were varied in thickness to tune the cavity resonance, plus, interlayers were employed for an improved contact and to reduce the dark current. Layer sequences and thicknesses of the photodetectors are documented in Appendix A.1. To avoid exposure to ambient conditions, the organic part of the device was covered by a small glass substrate that is glued on top.

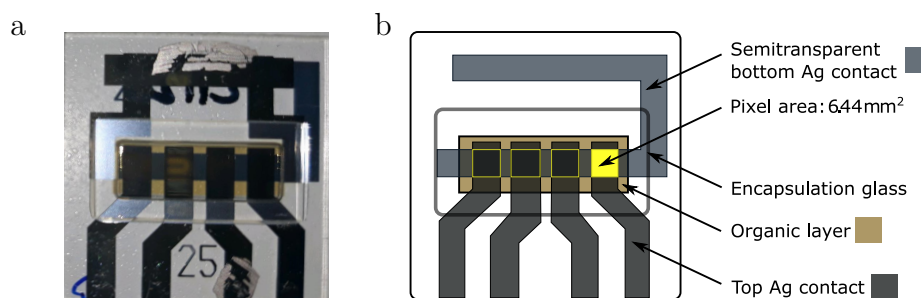


Figure 3.2: **a** Image of a thermally evaporated photodetector fabricated with a semitransparent bottom electrode, a fully reflective top electrode and encapsulation glass glued on top. **b** Sketch of layout of the photodetector from (a). One of four devices (or pixels) with an active area of 6.44 mm^2 is marked in yellow.

3.3 Spectroscopic Ellipsometry

The optical constants and film thicknesses of spin-coated films were determined experimentally by spectroscopic ellipsometry using the J.A. Woollam M-2000 ellipsometer in the wavelength range from 370 to 1700 nm. The samples comprised a single layer of material spin-coated from solution on either quartz glass or silicon substrates of with typical film thicknesses between 100 and 300 nm. In the experiment, linearly polarized light is directed onto the sample at typically three angles (65° , 70° and 75°) in three subsequent measurements. The light beam reflected off the sample changes its polarization state to elliptical, which can be expressed by the complex reflectance ρ defining the ratio between the reflectance coefficient r_p (electric field

⁽¹⁾at the Dresden Integrated Center for Applied Physics and Photonic Materials with the project being led by Dr. Bernhard Siegmund and Dr. Johannes Benduhn

amplitude oriented parallel to the plane of incident) and the reflectance coefficient r_s (electric field amplitude oriented in perpendicular to the plane of incident).

$$\rho = \frac{r_p}{r_s} = \tan(\Psi) e^{-i\Delta}. \quad (3.1)$$

An alternative way to describe the relative change in polarization state is to use $\tan(\Psi)$ as the ratio of the s- and p-polarized field amplitudes and Δ as the corresponding ratio of the phases. From the experimental quantities Ψ and Δ , the film thickness and optical constants are obtained via optical modelling – here performed using the CompleteEASE 5.23 software. To do so, a layer model is constructed containing (i) the substrate with known thickness and optical constants, and (ii) the studied thin film with a first thickness estimate. A model fitting to the experimental data is initially performed in the so-called Cauchy regime (the sub-bandgap wavelength range where absorption in organic semiconductor thin films is negligible) to estimate the film thickness based on optical interference originating from reflectance at the substrate/sample and sample/air interfaces. The fitting is then expanded to energies above the band gap using either a B-spline or general oscillator model to obtain the optical constants. Since ellipsometry only measures the relative change from incident to reflected light and no absolute quantities, it is relatively insensitive to light scattering and fluctuations, and requires no standard sample or reference beam. The limitations of ellipsometry for the characterization of organic semiconductors are associated with inhomogeneous and anisotropic films and high surface roughness. For such films, it is often impossible to find an appropriate optical model to fit the experimental data.

3.4 Light Current-Voltage Characterization

The light $I - V$ characteristics were measured with an Ossila Solar Cell $I - V$ Test System in combination with the Oriel LCS-100 TM (model 94011A) solar cell simulator. The illumination was chosen to be 1 sun ($= 100 \text{ mW/cm}^2$) and calibrated against a Newport calibrated reference cell (model 91150 V, series number 2087). The illumination mask area is 0.256 cm^2 applied to a solar cell with a pixel area of 0.04 cm^2 .

3.5 Dark Current-Voltage Characterization

The dark $I - V$ characteristics were measured with a Keithley Lambda 2450 source meter with the device mounted in an electrically shielded sample holder (Linkam LTS420 thermal stage) to decrease the electrical pick-up noise allowing to measure currents of around 10^{-12} A for organic photodetectors low intrinsic electrical noise. A typical $I - V$ measurement was conducted with a step size of 0.05 V starting from 0 V to -2 V in reverse bias direction, and from 0 to 1 V in forward bias direction. For temperature dependent dark $I - V$ measurements, the organic photodetectors were mounted in the Janis CCR12 cryogenic probe station. Encapsulation of the devices under test (DUT)

was omitted to avoid encapsulation-induced degradation of the sample under operational chamber pressures of 10^{-5} to 10^{-6} mbar. The probe station cools the sample container by compressing helium gas in a closed Gifford McMahon cycle and subsequently allows expansion, during which time heat is extracted from the heat exchangers cooling the sample. In consequence, the temperature of the sample can be set between 15 K to 330 K using the Lake Shore 336 temperature controller.

3.6 External Quantum Efficiency Measurements

A Perkin Elmer UV/VIS/IR spectrometer (LAMBDA 950) with an integrated Universal Reflectance Unit was used as a source for monochromatic light. In the spectrophotometer, the light of a tungsten halogen lamp is split into monochromatic light by a diffraction grating resulting in full-width-of-half-maximum of only 0.05 nm in the VIS and 0.20 nm in the IR as well as low stray light content and high wavelength reproducibility. The output light was chopped at 273 Hz using the MC2000B chopper system from Thorlabs and focused by a lens onto the DUT that was held under short circuit conditions in a Linkam LTS420 thermal stage. The photocurrent of the DUT was amplified by a low noise current amplifier (Femto DLPCA-200) and converted into a voltage signal, which was then detected with the lock-in amplifier (Stanford SR860). The lock-in amplifier was set to the reference frequency of 273 Hz by connecting it to the chopper system. On the lock-in amplifier, an averaging time (time per wavelength step) of up to 300 s was used for detecting wavelengths above 1500 nm, but typically 3 s for wavelengths below. For uncorrelated, frequency-independent noise sources, increasing the averaging time leads to a decrease of the noise floor by the square root of the number of averaged samples (i.e. number of measurements taken). In frequency space, this is equivalent to decreasing the bandwidth of the measurement. A voltage bias can be optionally applied to the DUT via the shield of the BNC input connector of the current amplifier by manually switching from ground to the amplifier-internal potentiometer (variable from -10 V to 10 V). NIST-calibrated 818-UV/DB silicon and 818-IR/DB germanium photodetectors from Newport were used as a calibration references for the wavelength range of 350 nm to 1100 nm and 780 nm to 1800 nm, respectively. In the wavelength range between 1800 nm to 2400 nm, the S148C photodetector from Thorlabs was used as a calibration reference. The measurement setup is schematically shown in Figure 3.3.

In the EQE measurement, low light intensities are detected by suppressing the optical and electrical noise sources of the measurement setup such that one is only limited by the electrical noise of the DUT. The optical noise sources include stray light and harmonics of the light source, and ambient light sources. The commercial Perkin Elmer UV/VIS/IR spectrometer (LAMBDA 950) was industrially optimized to exhibit low optical noise by using system integrated optics. Moreover, the lock-in amplifier extracts primarily the signal with the reference frequency hence suppresses optical noise from the lamp or ambient light with other frequencies. Lastly, covering the sample holder and dimming the ambient lights has proven to prevent the low noise current amplifier from overloading at the highest gain. Ambient electrical noise sources (50 Hz mains hum and overtones,

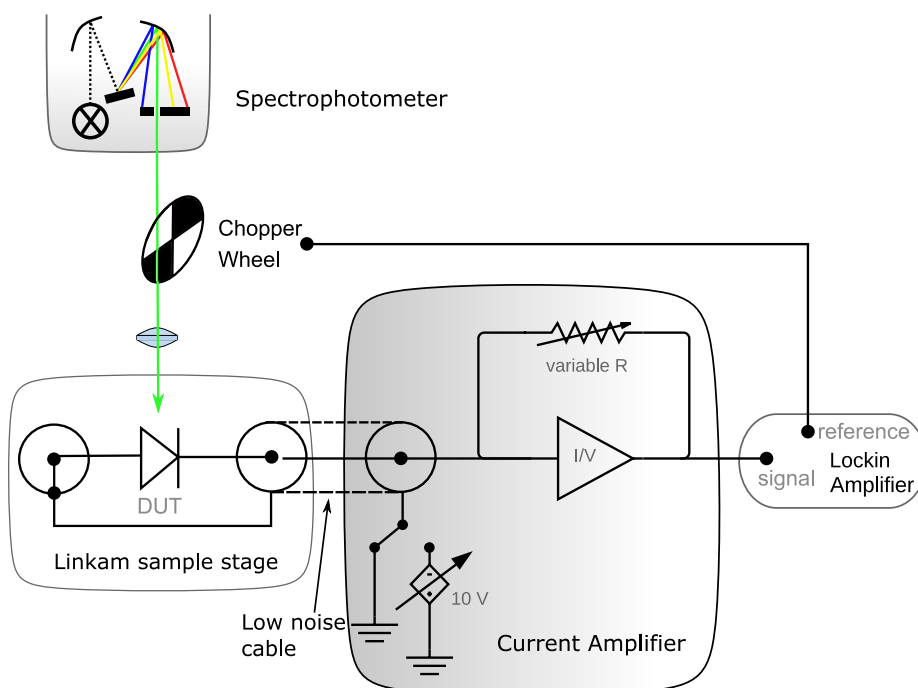


Figure 3.3: Schematic drawing of the external quantum efficiency measurement setup. Monochromatic light from the spectrophotometer is chopped and focused by a lens onto the DUT that is held under short-circuit condition. Reverse bias up to -10 V can be applied on the shield via the input connector of the current amplifier. The photocurrent is amplified choosing different gain settings from 10^4 V/A to 10^9 V/A and converted to photovoltage that is read out by the lock-in amplifier at the set reference frequency.

high voltage wires, power adapters) were strongly reduced by electromagnetic shielding of the DUT in the Linkam LTS420 thermal stage and connecting it via triaxial cables (or low-noise cables from CAB-LN1 Femto line) to the current amplifier.

For temperature dependent external quantum efficiency (EQE) measurements on the organic photodetectors from Chapter 6, the Linkam sample stage was set to -120 °C to 60 °C by the Linkam T96 temperature controller in combination with an LNP96 liquid nitrogen pump. The measurements on a single sample were performed subsequently on the same day to ensure reproducible settings between different temperatures (e.g., sample remained in the sample holder, same calibration file and constant gain setting on the current amplifier during one measurement). In the study described in Chapter 6, a commercial amorphous silicon thin film solar cell from TRONY with the part number sc80125s-8 was used as an exemplary inorganic test device to study its temperature dependent EQE. The solar module was cut into a smaller piece, placed into the Linkam sample stage and its top and bottom contacts were connected by the read-out pins of the sample holder.

3.7 Electrical Noise Measurements

The intrinsic electrical noise of the DUT was measured under short-circuit conditions in the electromagnetically shielded Linkam LTS420 thermal stage in the dark as shown in Figure 3.4. The anode and cathode of the DUT are electrically connected to the core and the shield of one BNC output, respectively, which connects via triaxial cables (or

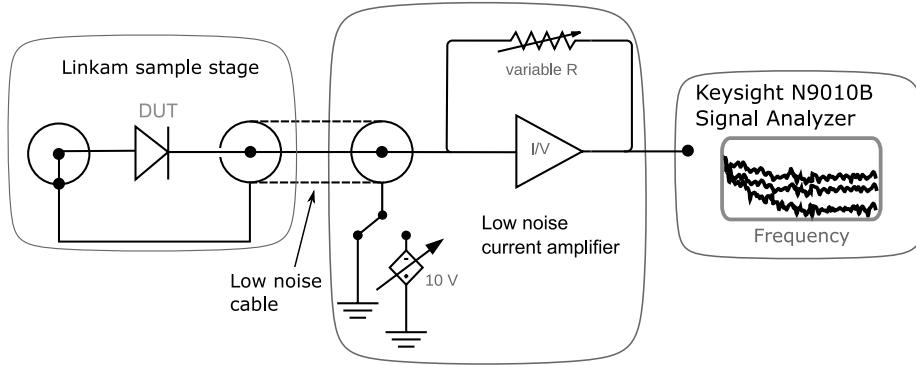


Figure 3.4: To obtain the electrical noise voltage of the DUT, it is placed in an electrically shielded sample holder (Linkam LTS420 thermal stage), which is then connected via low-noise BNC cables to the low-noise current amplifier (Femto DLPCA-200). The current of the DUT is amplified at a given gain converting it to a voltage signal that is fed into the spectrum analyser (Keysight N9010B Signal Analyser), which extracts the voltage noise in function of frequency.

low-noise BNC cables from the CAB-LN1 Femto line) to the BNC input connector of the Femto DLPCA-200 current amplifier. A voltage bias can be optionally applied to the DUT via the shield of the BNC input connector of the current amplifier by manually switching from ground to the amplifier-internal potentiometer (variable from -10 V to 10 V). The noise current of the DUT was amplified using a Femto DLPCA-200 low-noise current amplifier and converted to a voltage signal. The voltage signal was then fed into the Keysight N9010B Signal Analyser (spectrum analyser) with the resolution bandwidth (RBW) set to 1 Hz .

A spectrum analyser measures the magnitude of an input signal versus frequency within the frequency span of the instrument. Depending on the frequency and RBW, the operational mode of the spectrum analyser switches automatically between swept-mode or Fast-Fourier-Transform (FFT) mode. In this work, the frequency span was dictated by the specifications of the low noise current amplifier, i.e., the higher the gain, the lower the frequency span. At the maximum gain of 10^9 V/A , the upper cut-off frequency is at around 1.1 kHz . For such low frequency spans, the spectrum analyser switches to FFT mode, where a time domain voltage signal is recorded and the mathematical FFT operation is performed to calculate the spectral component of the signal. For higher frequency spans, e.g. radio-frequencies, the spectrum analyser switches to swept-mode, where it operates like a lock-in amplifier that sweeps the full frequency range at a given RBW using its internal local oscillator as reference. The input signal of the spectrum analyser comprised the output voltage of the low-noise amplifier. The respective voltage noise was obtained by the spectrum analyser in units of $\text{V}/\sqrt{\text{Hz}}$. The units reflect that signal noise depends on the RBW.

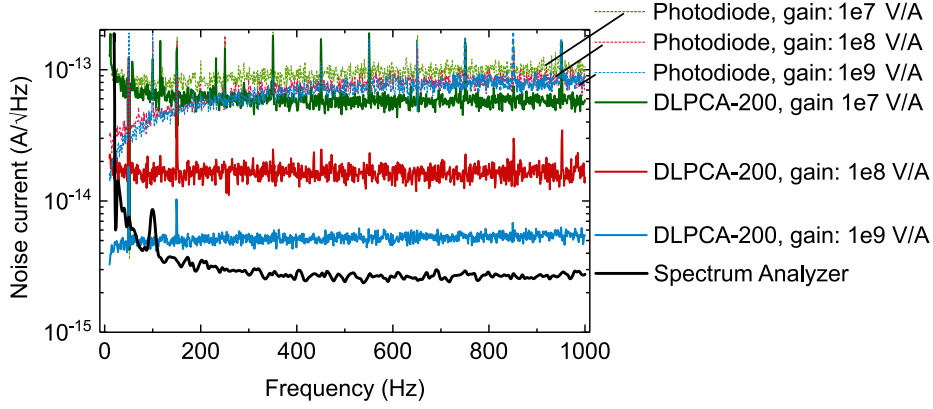


Figure 3.5: Experimental noise currents obtained for the spectrum analyser (Keysight N9010B Signal Analyser; black line), the low-noise current amplifier (Femto DLCPA-200) at different gain settings (blue line: 10^9 V/A; red line: 10^8 V/A; green line: 10^7 V/A) and lastly the full measurement setup including spectrum analyser, current amplifier and DUT at different gain settings (blue dashed line: 10^9 V/A; red dashed line: 10^8 V/A; green dashed line: 10^7 V/A). To measure the internal electrical noise of the spectrum analyser, its input BNC connector was connected to a 50Ω terminator to omit electrical pick-up noise.

After taking into account the gain of the current amplifier in units of V/A, the noise voltage on the spectrum analyser is converted to noise current in units of $\text{A}/\sqrt{\text{Hz}}$. To measure the electrical noise of the DUT, it is important that the electrical noise of the apparatus is below the electrical noise of the DUT. As an example, Figure 3.5 illustrates the noise current of the DUT and the current amplifier at different gain settings, and the internal electrical noise of the spectrum analyser as obtained from the root-mean-square noise current at frequencies between 800 kHz to 1000 kHz. The DUT has an electrical noise current of around $80 \text{ fA}/\sqrt{\text{Hz}}$, which was measured using either a gain of 10^9 V/A or 10^8 V/A on the current amplifier. For such high gain, the electrical noise of the current amplifier is well below the one of the DUT. However, at a gain of 10^7 V/A, its internal electrical noise current increased to $43 \text{ fA}/\sqrt{\text{Hz}}$, and, hence, the measured noise current of the DUT increases to roughly $100 \text{ fA}/\sqrt{\text{Hz}}$. It is therefore important to use the highest gain on the current amplifier without overloading the spectrum analyser or current amplifier.

3.8 Linear Dynamic Range

To perform light-intensity dependent characterization of the photodiodes, i.e., to obtain the linear dynamic range (LDR) and the noise equivalent power (NEP), the electrical noise measurement setup was upgraded by a laser source (Oxxius L6Cc laser) and a waveform generator (Keysight 33600 A series). The Oxxius L6Cc laser can generate light at 405, 520, 638, 785 and 940 nm. In this work, it was typically modulated by the waveform generator in the sub-kHz regime at 520 nm. Modulation frequencies, that are multiples of 50 Hz, were avoided to suppress electrical pick-up noise from the mains. Prior to measuring the LDR of the DUT, its oscillating photocurrent was monitored on the oscilloscope and the modulation settings (DC voltage offset and peak-to-peak voltage) on the waveform generator were adjusted to

drive the laser between 0 V and 5 V. This resulted in an oscillating light power between its minimal and maximal output power with a RMS power of around 10 mW. Ideally, the photocurrent describes a clean sinusoidal waveform in time without clipping, which could otherwise lead to high-frequency noise artefacts measured with the spectrum analyser.

To record the photocurrent response over light powers spanning 13 orders of magnitude, optical filters were used including the continuous filter wheel within the Oxxius L6Cc laser box that can attenuate the light power by 4 orders of magnitude. After internal attenuation, the laser light is guided through an optical fibre from the laser box to the external set of Neutral-density (ND) filters from Thorlabs arranged in a filter wheel. Among an unfiltered position, the filter wheel contains nine ND filters with increasing optical density (OD) from 1 to 9. In the filter wheel, the light is out-coupled, attenuated by a maximum of 9 orders of magnitude, focused by a movable optical lens and coupled into the second optical fibre that guides the light either to the reference photodetector for calibration or the DUT. The light power was calibrated against the Femto OE-300-SI photoreceiver with a NEP of $8 \text{ fW}/\sqrt{\text{Hz}}$ at the responsivity maximum at 900 nm and an electrical noise current of $10 \text{ fA}/\sqrt{\text{Hz}}$ at the highest gain setting (lowest noise floor). Note that the RBW of this measurement was set to 10 Hz.

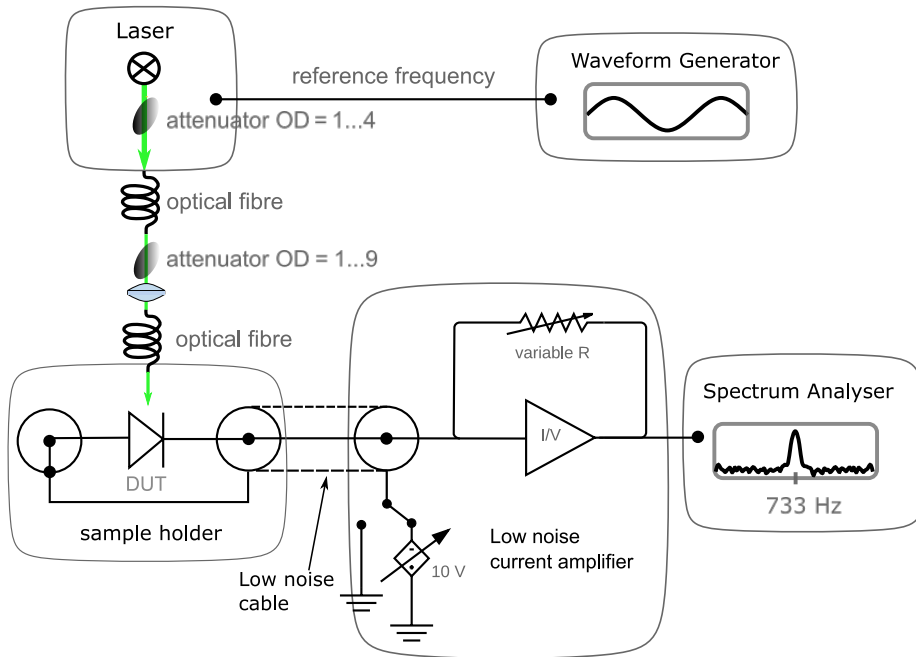


Figure 3.6: Sketch of the experimental setup used to performed light-intensity photodetector characterization, including the electrical noise measurement setup upgraded by a laser source (Oxxius L6Cc laser) and a waveform generator (Keysight 33600 A series). The light intensity of the laser can be attenuated over 13 orders of magnitude using the laser internal continuous attenuation wheel and external ND filters. The sample is kept in the electrically shielded sample holder (Linkam LTS420 thermal stage) under short circuit conditions. The laser is modulated by a waveform generator (Keysight 33600 A series) at a reference frequency at which the spectrum analyser detects the photovoltage signal.

At the reference frequency f_{ref} , the spectrum analyser records the absolute voltage magnitude, whereas at frequencies $f < f_{\text{ref}} - \text{RBW}/2$ and $f > f_{\text{ref}} + \text{RBW}/2$, the voltage noise of the measurement setup is displayed. In analogy to the electrical noise measurements, the measured voltage signal was recorded and converted into a current signal by taking into account the gain in units of V/A on the current amplifier. Figure 3.7 illustrates how the photocurrent at $f_{\text{ref}} = 980$ Hz decreases by one order of magnitude with increasing the OD filter from 1 to 9. For OD=5 to OD=9, the same gain on the current amplifier was used, resulting in the same current noise at frequency below and above f_{ref} . At OD=8, the photocurrent signal has an amplitude of only 20 fA, while it can no longer be discerned from the current noise current at OD=9.

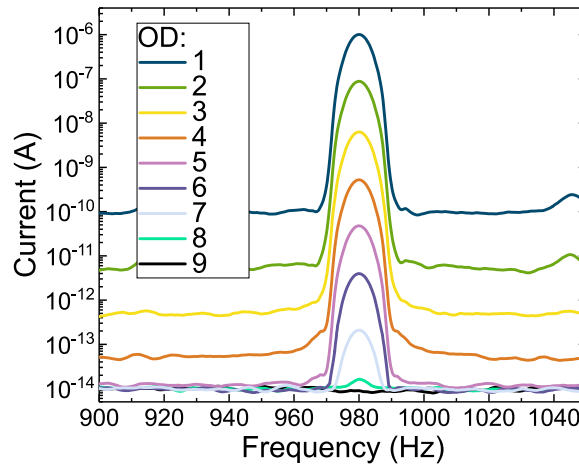


Figure 3.7: Photocurrent in function of frequency from a DUT that is excited by a laser source modulated at 980 Hz. The peak intensity decreases with each attenuation step until the current signal can no longer be distinguished from the current noise of the DUT in the dark (black line). The RBW of the measurement comprised 10 Hz.

3.9 Frequency Response

To measure the frequency response of the DUT, the electrical noise measurement setup was upgraded to include a laser source (Oxxius L6Cc laser) and a network analyser (Keysight E5071C ENA Vector Network Analyser) as shown in Figure 3.8. A network analyser acts both as source signal and as receiver, and can therefore probe relative changes of amplitude and phase between output and input signal. The results are transmission measurements (transmission coefficient, insertion loss, gain), reflection measurements (reflection coefficient, return loss), impedance and the scattering parameters (S_{11} , S_{12} , S_{21} , S_{22}). In this work, the network analyser was used in transmission mode. In such as mode, it generates waveforms over a set range of frequencies, which modulate the laser source that excites the DUT. The photocurrent of the DUT is amplified by the low noise current amplifier (Femto DLPCA-200) and converted to a voltage signal that is the input to the network analyser. The network analyser then displays the relative response (power ratio) of input to output in function of frequency in units of decibel (dB). The maximum of the relative response is normalized to 0 dB, and hence the frequency where the relative response has decreased by 50 % is the -3 dB cut-off-frequency f_c .

To successfully record the full frequency response of the DUT, following aspects were considered: First, the intensity of the modulated light must be within the LDR of the DUT. The light intensity of the laser was attenuated using its internal attenuator wheel as illustrated in Figure 3.8. Second, the photocurrent of the DUT should describe a clean sinusoidal waveform in time without clipping, which could otherwise lead to high-frequency artefacts in the frequency response spectrum. Prior to measuring the frequency response of the DUT, its photocurrent was therefore measured at a constant frequency below f_c with an oscilloscope and the modulation settings (DC voltage offset and peak-to-peak voltage) on the network analyser were adjusted to drive the laser between 0 V and 5 V, which resulted in an oscillating light power between its minimal and maximal output power. Third, the DUT must be the “slowest” component of the experimental setup, i.e., show the lowest f_c . f_c of the Oxxius L6Cc laser at a wavelength of 520 nm was determined to be around 955 kHz and the f_c of the Femto DLPCA-200 low noise current amplifier is 500 kHz according to the user manual. For photodiodes faster than 500 kHz, the amplifier was omitted and the signal of the DUT directly fed into the network analyser without amplification.

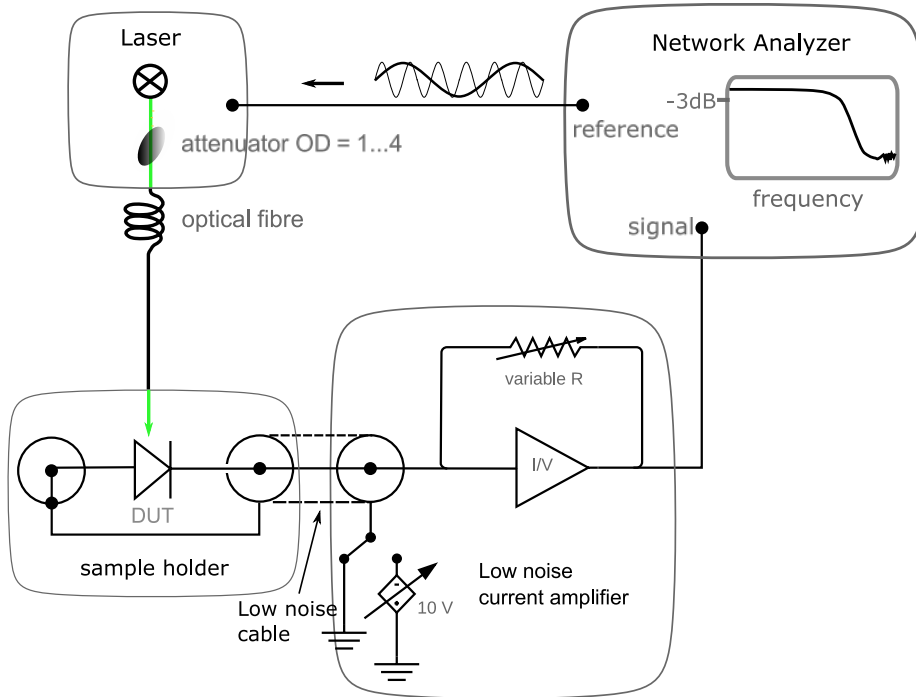


Figure 3.8: Sketch of the experimental setup to measure frequency response comprising the electrical noise measurement setup upgraded by a laser source (Oxxius L6Cc laser) and a network analyser (Keysight E5071C ENA Vector Network Analyser). The network analyser generates an (oscillating) voltage output that modulates the laser subsequently at different frequencies typically increasing between continuous wave illumination up to 1 MHz. The light intensity of the laser can be attenuated by its internal attenuator to be within the LDR of the DUT. The DUT is kept in the electrically shielded sample holder (Linkam LTS420 thermal stage) under short circuit conditions. Upon illumination, the photocurrent of the DUT is amplified at a given gain converting it to a voltage signal that is fed into the network analyser, which displays the relative input to output power ratio in units of dB and in function of frequency.

Chapter 4

Determining Subgap Absorption Coefficients

*Energy states below the bandgap of a semiconductor, such as trap states or charge transfer states in organic semiconductor donor-acceptor blends, can contribute to light absorption. Due to their low number density or ultra-small absorption cross-section, the absorption coefficient (α) of these states is challenging to measure using conventional transmission and reflection spectroscopy. As an alternative, the external quantum efficiency (EQE) of photovoltaic devices is often used as a representative of α , where the spectral line shape of the EQE is assumed to follow α of the active layer material. In this chapter, the work is presented which shows that the sub-bandgap EQE is subject to thickness dependent low finesse cavity effects within the device – making this assumption questionable. A better estimate for α is obtained when EQE spectra of photodiodes with different active layer thickness t are fitted simultaneously for one α using an iterative transfer matrix method. Herein, α is determined to an accuracy of 10^{-2} cm^{-1} in the sub-gap spectral range of two exemplary D:A blends often used in high efficiency organic solar cells. It is found that in photodiode with a non-fullerene containing active layer, the interference-induced t -dependence of EQE is more pronounced due to the large refractive index of this material system. These results indicate that one cannot directly relate the sub-gap EQE spectra to the sub-gap α without performing appropriate optical simulations. This is particularly important in systems with larger refractive indices such as non-fullerene blends. A summary of the work presented in this chapter was published by the authors in *Advanced Optical Materials* in 2019. C. Kaiser fabricated the devices, performed the experiments and optical simulations. S. Zeiske developed the experimental EQE setup, and P. Meredith and A. Armin conceptualized the idea and provided the leadership of this project.*

C. Kaiser, S. Zeiske, P. Meredith, A. Armin, *Determining Ultralow Absorption Coefficients of Organic Semiconductors from the Sub-Bandgap Photovoltaic External Quantum Efficiency*, *Adv. Opt. Mater.* **8**, 1901542 (2019).

4.1 Experimental Sub-gap Absorption Coefficient

For photon energies ($h\nu$) above the bandgap (E_g), the absorption coefficient α is often determined through transmission and reflection spectrophotometry or spectroscopic ellipsometry, which gives the complex reflective index. The same experimental techniques become very challenging when applied to the sub-bandgap optical constants, particularly because for $h\nu < E_g$ the absorptance is typically orders of magnitude weaker than for $h\nu > E_g$. Precise sub-bandgap optical constants are, however, crucial for modelling a variety of semiconductor devices operating at energies below the bandgap such as near-infrared photodetectors^{14,137} or light emitting exciplex LEDs.¹³⁸ In addition, the spectral line shape of α for $h\nu < E_g$ is indicative of a variety of phenomena such as structural disorder and charge transfer absorption in organic semiconductors as shown in Section 2.1. Disorder-induced and charge transfer state absorptions are related to loss mechanisms in organic solar cells, and have been studied extensively to improve solar cell efficiencies.^{139–141}

Given the considerable interest in the sub-bandgap α , sensitive methods of measuring it have been developed. This includes photothermal deflection (PDS) spectroscopy as a powerful technique for measuring α down to 0.001 cm^{-1} in the best case, but more commonly down to 1 cm^{-1} in condensed matter phases.^{45–47,98} Similar to ellipsometry, PDS requires the preparation of single layer samples. Another technique is Fourier Transform Photocurrent Spectroscopy (FTPS) that is based on recording the photocurrent action spectrum using a Fourier Transform Infrared spectrometer. FTPS is often used to determine low energy trap states in inorganic semiconductors.^{142,143} One should note that photocurrent-based methods may be more sensitive than PDS but can only probe the absorptance of the photocurrent-generating species. In amorphous silicon, it has been shown that FTPS systematically underestimates the optical absorptance for $h\nu < 1.4 \text{ eV}$ when compared with PDS.^{144,145} Similar to FTPS, the external quantum efficiency (EQE) is another photocurrent-based method commonly used to characterize the photocurrent response of solar cells and photodetectors over the visible (VIS) and near-infrared (NIR) spectral range. The EQE is the product of absorptance of the active layer as a function of wavelength $A(\lambda)$ and the internal quantum efficiency (IQE), such that

$$\text{EQE}(\lambda) = A(\lambda) \times \text{IQE} \quad (4.1)$$

As a consequence of eq. 4.1, the spectral line shape of the EQE must be directly translatable to $A(\lambda)$ assuming that the IQE does not feature any substantial energy dependence. The latter assumption has been proven in technologically relevant high efficiency systems such as efficient bulk heterojunction^{49–51,91} and perovskite¹⁴⁶ solar cells. Nevertheless, examples for donor-acceptor (D:A) systems with an excitation energy dependent IQE have been shown recently.^{92,93} If the spectral line shape of the EQE changes with applied bias, the IQE is not spectrally flat and $A(\lambda)$ can be more precisely inferred from the EQE measured at the largest possible bias to ensure photocurrent saturation.^{92,147}

Assuming an excitation energy independent IQE, $A(\lambda)$ can be obtained from the spectral line-shape of the EQE. $A(\lambda)$ is a property of a multi-layer stack device such as a solar cell or a photodetector. To infer α of the active layer from $A(\lambda)$, an optically thin active layer with $\alpha t \ll 1$ (layer thickness t) is often assumed with negligible cavity effects. Herein, it is assumed that $A \approx 2\alpha t$ for $h\nu < E_g$.^{91,131,148,149} Therefore the spectral line shape of the EQE should follow α via $A(\lambda)$. However, the assumption of $A \approx 2\alpha t$ is invalid in the presence of electrodes as the device forms a low-finesse cavity with an associated t -dependence. The well-known cavity effects are typically observed as pronounced interference fringes in the above-gap EQE (where $\alpha t \approx 1$) but can have a similar effect on the sub-gap EQE. The prominence of these cavity effects depends primarily on the relative difference between the individual layer refractive indices and can be simulated using the so-called transfer matrix model which was introduced in Section 2.1.1.

4.2 Optical Constants from Spectroscopic Ellipsometry

Optical constants comprise the attenuation coefficient κ and the refractive index n , where α is related to κ via $\alpha = 2\pi\kappa / \lambda$. In optical simulations, κ is often used as an input parameter instead of α . To investigate ultra-low α in the sub-gap region, PBTTT:PC₇₁BM (1:4) and PBDB-T:ITIC (1:1) were chosen as model material systems. PBTTT:PC₇₁BM is known for its extended sub-gap EQE shoulder due to charge transfer state (CT) absorption,¹⁵⁰ while PBDB-T:ITIC shows a narrow CT state-related EQE contribution that is barely distinguishable from the above-gap EQE caused by singlet excitons.¹⁴⁹ First, the optical constants were obtained from single layer samples of spin-coated material with thicknesses ranging between 100 nm to 400 nm on both glass and silicon substrates. Ellipsometry is considered as an indirect method for obtaining the optical constants, as it measures the polarization parameters $\tan \Psi(\lambda)$ and $\cos \Delta(\lambda)$, which are then globally fitted for t and n in the transparent region between 1200 nm to 1600 nm ($\kappa \approx 0$, i.e., the Cauchy region). Thereafter, n and κ are fitted stepwise over the entire spectrum with fixed t . Figure 5.1 shows the optical constants obtained for PBDB-T:ITIC and PBTTT:PC₇₁BM, which were determined in good agreement between the experimental data and the mathematical model (mean-squared error < 15) as well as high reproducibility between samples in the VIS spectral range. The dashed lines in Figure 5.1 indicate the sensitivity limit for determining κ , which roughly corresponds to the bandgap energy beyond which this method is not applicable to κ (as seen from the divergence of κ for different t). At the same time, the relative change in n with t in the Cauchy regime compared to κ is insignificant, as n lacks spectral features and converges to a constant value around 2. In summary, n was used as obtained from ellipsometry for transfer matrix simulations in the entire spectral range but dismissed κ for wavelengths beyond the dashed lines illustrated in Figure 5.1. Furthermore, the optical constants of indium tin oxide (ITO), MoO₃ and ZnO were determined experimentally, while for Ag tabulated data was

used.¹⁵¹ As a next step, electrically inverted photovoltaic cells with the structure ITO (105 nm) / ZnO (37 nm) / active layer / MoO₃ (7 nm) / Ag (130 nm) were fabricated with different active layer thicknesses (PBDB-T:ITIC: 60, 132, 215, 375 nm and PBTTT:PC₇₁BM: 60, 81, 110, 140, 190 nm).

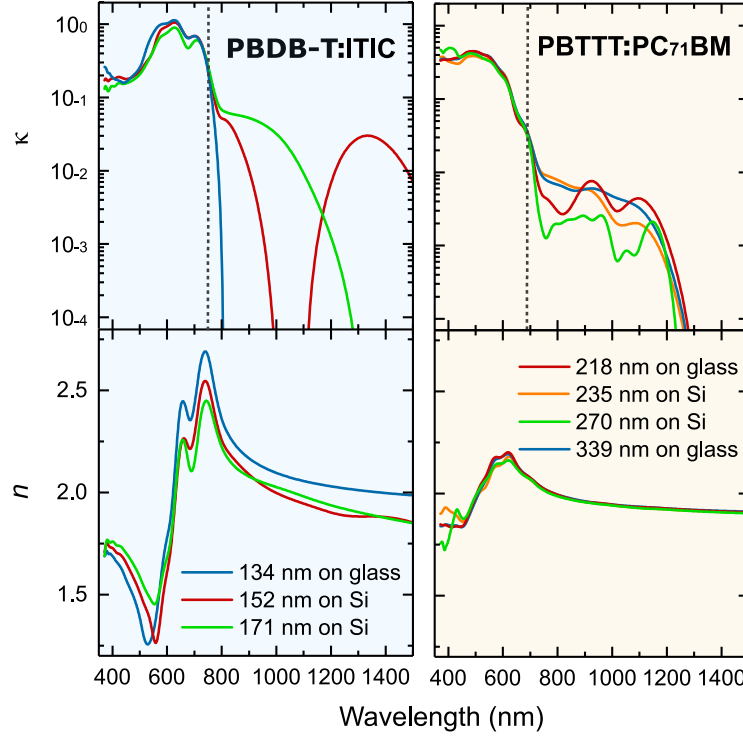


Figure 4.1: Spectroscopic ellipsometry obtained refractive indices n and κ of PBTTT:PC₇₁BM and PBDB-T:ITIC on silicon (Si) and glass with the respective layer thicknesses as shown. Dashed lines highlight the sensitivity limit in κ of the ellipsometric technique. PBDB-T:ITIC shows a significantly larger dispersion in n compared to PBTTT:PC₇₁BM.

4.3 Numerical Sub-gap Absorption Coefficient

The EQE spectra are used in the procedure depicted in the process flowchart of Figure 4.2 to obtain ultra-low α . The numerical basis for this process is the Nelder-Mead simplex algorithm that minimizes a non-linear and constrained objective function.¹⁵² Importantly, the presented method does not depend on the algorithm used for the minimization. Other derivative-free algorithms like the Brent's method or Powell's conjugate direction method can also be employed.¹⁵³ To numerically determine the κ , two steps were followed as shown in Figure 4.2a and 2c: (i) Estimation of the precise active layer thickness for the single device (defined as the 'pixel') and (ii) calculation of κ under consideration of the preoptimized t . First, $A(\lambda)$ of each device is modelled by the transfer matrix method. The experimental input data required for the modelling comprise the measured active layer thickness t_{measured} and the optical constants in the VIS spectral range that is from 400 nm to 600 nm for PBTTT:PC₇₁BM and 400 nm to 700 nm for PBDB-T:ITIC.

Thereafter, IQE_{VIS} and the mean (IQE_{mean}) are obtained using eq. 4.1. From the

4.3 NUMERICAL SUB-GAP ABSORPTION COEFFICIENT

active layer	t_{measured} in nm	$t_{\text{simulated}}$ in nm
PBTTT:PC ₇₁ BM	70	60
	80	81
	120	110
	130	140
	200	190
PBDB-T:ITIC	50	60
	142	132
	205	215
	385	375

Table 4.1: Active layer thickness t of devices with either PBTTT:PC₇₁BM or PBDB-T:ITIC. The numerical thickness $t_{\text{simulated}}$ is obtained using a numerical fitting procedure that varies the thickness between ± 10 nm around the measured thickness t_{measured} . The fit aims to optimize $t_{\text{simulated}}$ by reducing the deviations of the simulated IQE of the device from its mean, since the IQE is in good approximation spectrally flat.

available ellipsometric constants, values were chosen that resulted in the minimum deviations of the IQE_{VIS} from its mean. The IQE of one exemplary PBDB-T:ITIC device (375 nm active layer layer) is depicted in Figure 4.2b showing a deviation of the IQE of no more than 13 % from its mean. Such deviations can be caused by thickness variations over the device area which are common for solution-processed layers and could even be seen with the naked eye for the 210 nm PBTTT:PC₇₁BM device. For that reason, t was preoptimized within 10 nm boundaries around the experimental thickness t_{measured} . To do so, the absorptance A' was calculated from the IQE_{mean} as $A' = \text{EQE} \times \text{IQE}_{\text{mean}}^{-1}$. Figure 4.2b shows that the absolute difference between A' and A is largest where the IQE deviates most from its mean. To match A' to A , t is numerically varied to minimize the function $(A - A')^2/A$. In the case of $A = A'$, IQE_{VIS} would be spectrally flat, which is impossible to achieve given the experimental errors and uncertainties related to optical constants and thicknesses of other device layers. Nevertheless, the IQE spectra remains approximately flat within these unavoidable errors. IQE spectra of the devices under investigation are shown in Figure 4.3-4.4.

The experimental and the simulated $t_{\text{simulated}}$ of all the investigated devices are shown in Table 4.1. Once the optimized $t_{\text{simulated}}$ and IQE_{mean} for all devices are obtained, the absorption spectra below the bandgap can be estimated by $A'' = \text{EQE} \times \text{IQE}_{\text{mean}}^{-1}$ using the experimental EQE over the full spectral range. Importantly, A'' is now a matrix containing the estimated absorptance of all devices. Figure 4.2c shows the process of numerically obtaining κ . The fixed input comprises the absorption matrix A'' , the experimental α at the last wavelength within the VIS spectral range $\kappa(\lambda_{m-1})$, the α n over the full spectral range, and the numerically obtained t . The optimization of κ proceeds wavelength by wavelength starting from the λ_m , where λ_{m-1} is the last wavelength within the VIS spectral range. At λ_m , the transfer matrix calculates A''' using $\kappa(\lambda_{m-1})$ as the initial guess of α . To further match A''' to $A''(\lambda_m)$, the κ is varied between 0 and $\kappa(\lambda_{m-1}) + \kappa(\lambda_{m-1})/10$ with the goal to minimize the function $(A''(\lambda_m) - A''')^2/A''(\lambda_m)$. Once a predefined number of iterations has been exceeded, $\kappa(\lambda_m)$ is fixed and the algorithm proceeds to the next wavelength λ_{m+1} choosing $\kappa(\lambda_m)$ as the initial estimate for fitting $\kappa(\lambda_{m+1})$.

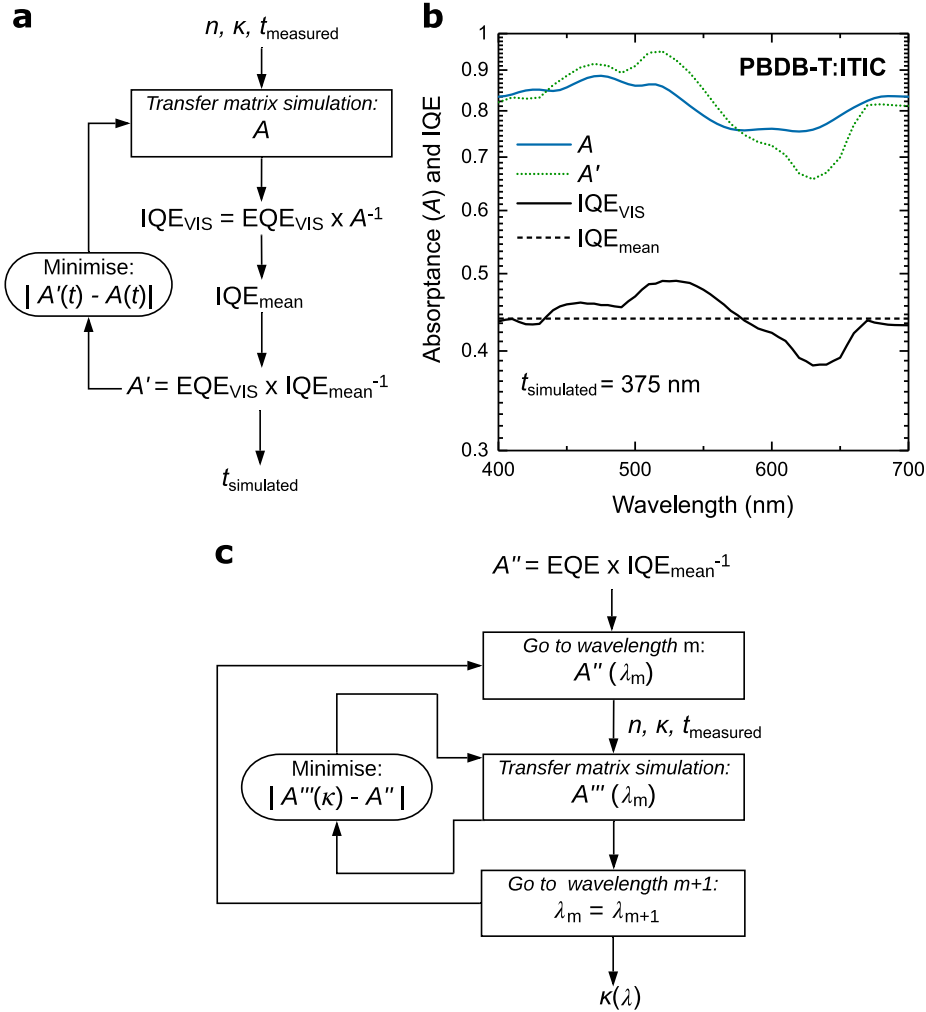


Figure 4.2: Process flow for obtaining ultra-low α ($= 2\pi\kappa/\lambda$) in the weakly absorbing spectral range using numerical optimization. **a,b** The active layer thickness t is optimized such that the difference between A and A' in the visible spectral range is minimal resulting in a spectrally flat IQE_{VIS} . **c** From the mean of the IQE and sensitively measured sub-bandgap EQE, an absorptance matrix A'' for several t is calculated. Using the preoptimized t , κ is numerically obtained by recursive simulation of the active layer absorptance $A'''(\lambda_m)$ for all t at one wavelength with the goal to fit A'' .

spectrum	t_{measured} in nm	E_{CT} in eV	λ_{CT} in meV
α	-	1.155	162.7
EQE	60	1.175	152.9
	81	1.181	134.4
	110	1.150	182.5
	140	1.158	150.8
	190	-	-

Table 4.2: Charge transfer energy (E_{CT}) and reorganization energy (λ_{CT}) of PBTtT:PC₇₁BM obtained from a Gaussian fit to the low-energy part of α or the experimental external quantum efficiency (EQE) spectra. The Gaussian fit to the EQE of the 190 nm thick device was not reliable and therefore excluded. E_{CT} and λ_{CT} extracted as fit-parameter from the EQE spectra show negligible deviation from the values extracted from the α given an estimated fit-error of $\pm 10 \text{ meV}$ and $\pm 20 \text{ meV}$ for E_{CT} and λ_{CT} , respectively.

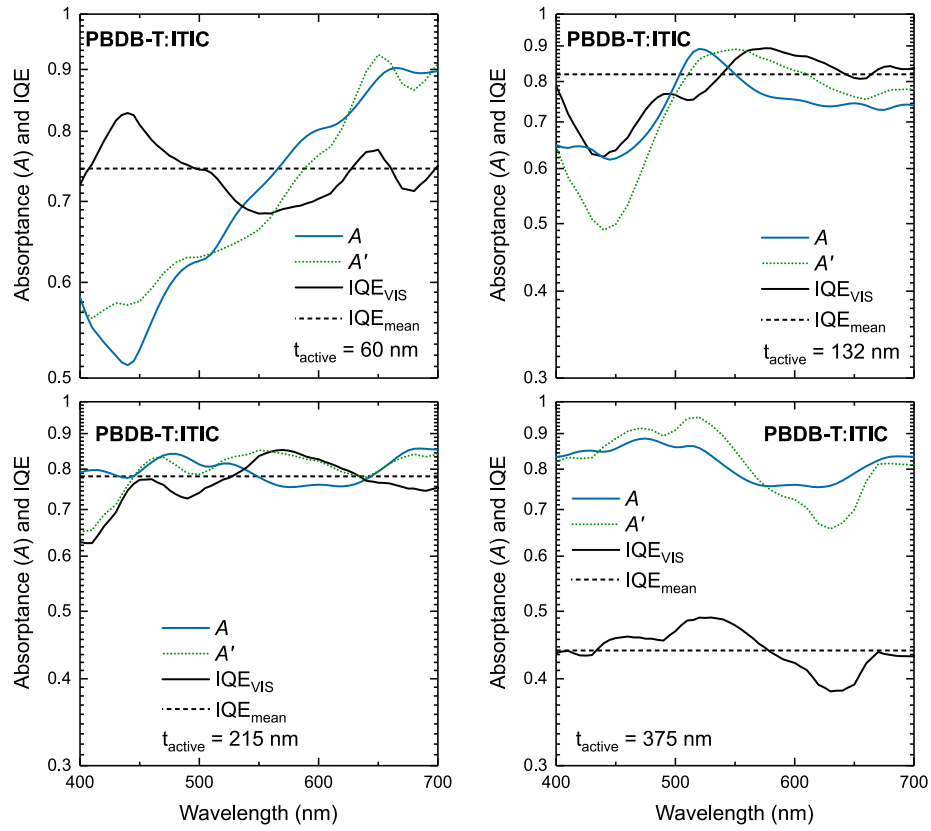


Figure 4.3: Simulated active layer absorption, IQE and the mean of the IQE (IQE_{mean}) of devices with the structure ITO (109 nm) / ZnO (37 nm) / PBDB-T:ITIC (60 – 400 nm) / MoO₃ (7 nm) / Ag (130 nm). A corresponds to the absorption calculated by the transfer matrix using the experimentally obtained optical constants. A' corresponds to the absorptance calculated as $A' = EQE \times IQE_{mean}^{-1}$.

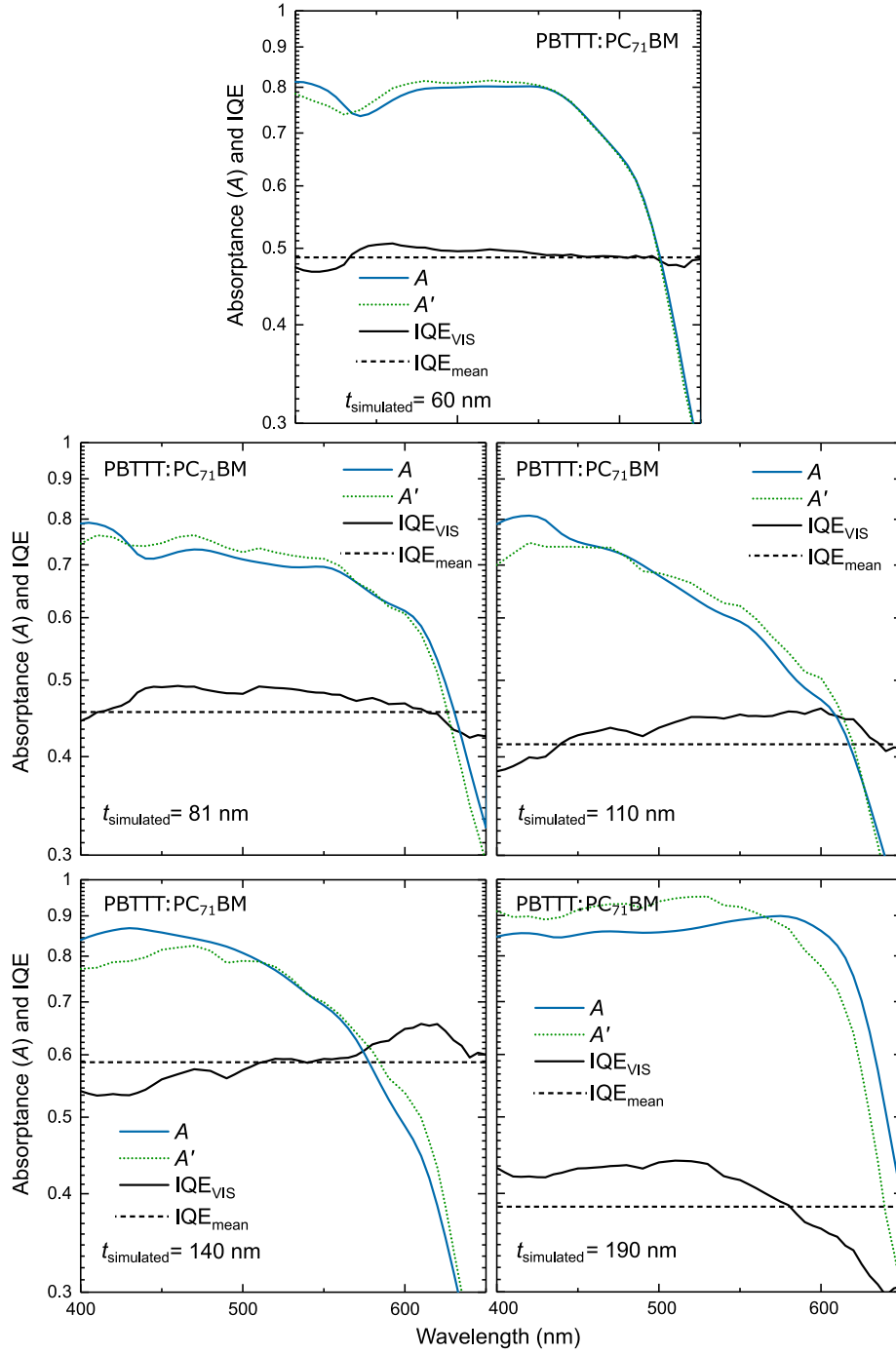


Figure 4.4: Simulated active layer absorbance, IQE and the mean of the IQE (IQE_{mean}) of a device with the structure ITO (109 nm) / ZnO (37 nm) / PBTTT:PC₇₁BM (60 – 190 nm) / MoO₃ (7 nm) / Ag (130 nm). A corresponds to the absorbance calculated by the transfer matrix using the experimentally obtained optical constants. A' corresponds to the absorbance calculated as $A' = EQE \times IQE_{mean}^{-1}$.

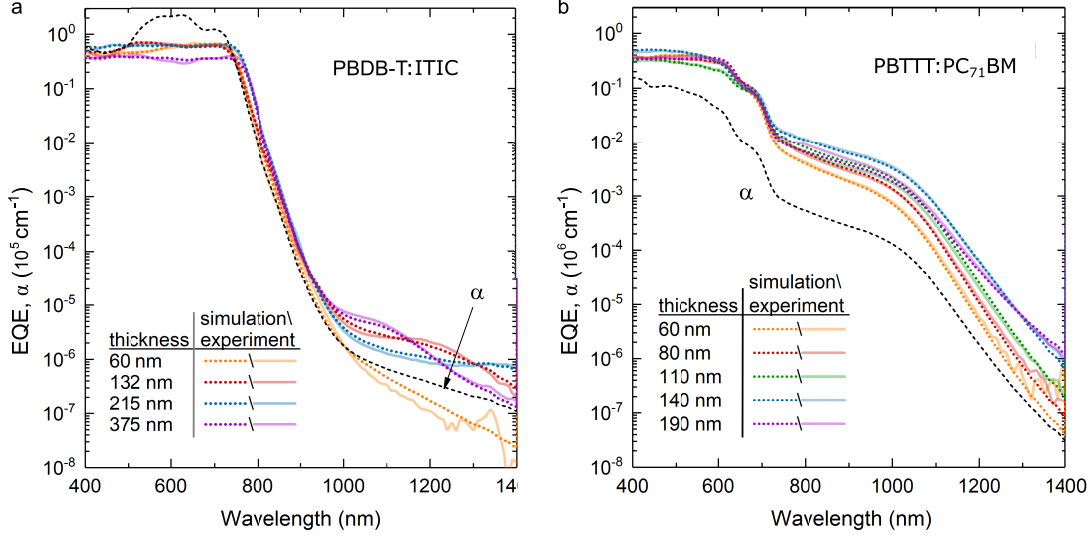


Figure 4.5: α (dashed black lines) of PBDB-T:ITIC (a) and PBTTT:PC₇₁BM (b) comprising ellipsometric data for above-gap and numerical data for sub-bandgap absorption. Using α in a conventional transfer matrix simulation, the active layer absorptance was calculated and scaled by IQE_{mean} to obtain the simulated EQE (dotted lines). The thickness-dependence of the sub-bandgap EQE is clearly reproduced in the simulation validating the numerical α as well as indicating that the commonly used assumption $A \approx 2\alpha t$ is only true for a subset of thicknesses.

4.4 External Quantum Efficiency Simulations

A computer code for computational method explained in the previous Section 4.3 is provided in an online repository with exemplar data.¹⁵⁴ This method is applicable to a single or more devices of different t . However, experimental inaccuracies t_{measured} and small deviations from the flat IQE assumption will have a large impact on the numerically obtained α if only one device is considered. Therefore, it will be more accurate to numerically fit devices with different t . From the globally obtained α , the active layer absorptance can be simulated and then scaled by IQE_{mean} to obtain the EQE. It is important to consider that electronic effects, such as the charge collection imbalance of thick junctions, are not considered in the optical model. Figure 4.5a and b illustrate α , the experimental EQE (EQE_{exp}) and simulated EQE (EQE_{sim}) spectra of PBDB-T:ITIC and PBTTT:PC₇₁BM. The agreement between simulation and experiment for different active layer t was quantified by calculating the relative percentage difference. EQE_{sim} is typically within 40 % deviation around the absolute EQE_{exp} despite the simulation covering 7 orders of magnitude. Consequently, the EQE_{sim} spectra follow the t -induced spectral line shape of the EQE_{exp} spectra.

From a Gaussian fit to the α of PBTTT:PC₇₁BM, a charge transfer energy (E_{CT}) of 1.16 eV and a reorganization energy λ_{CT} of the D:A complex of 163 meV were determined as shown in Figure 4.6. E_{CT} of PBTTT:PC₆₁BM was previously reported to be 1.15 eV in a thin solar cell, where the active layer absorptance A in the device was approximated by $A \approx 2\alpha t$.¹³¹ As both E_{CT} values are in excellent agreement, a Gaussian fit was performed on EQE_{exp} spectra for different t under the assumption of $A \approx 2\alpha t$. The 190 nm PBTTT:PC₇₁BM device could not be reliably fitted, but other devices with active layer thicknesses of 60, 81, 110 and 140 nm resulted in E_{CT} and λ values ranging from 1.15 eV to 1.18 eV and 143 meV to 186 meV, respectively (see

Table 4.2). Given the dependence of the fit parameters on the chosen fitting range, an uncertainty of ± 10 meV for E_{CT} and ± 20 meV for λ_{CT} is estimated. To conclude this phase of the analysis, the assumption of $A \approx 2\alpha t$ leads to an insignificant error in determining E_{CT} and λ_{CT} for the material system PBTTT:PC₇₁BM for $t < 190$ nm. For PBDB-T:ITIC devices, the t -dependent EQE features in the spectral range above 1000 nm were identified as resonances of the device acting as a low-finesse cavity. To eliminate the possible effect of higher order harmonics derived from the illumination system, the EQE of the 190 nm device was remeasured with long-pass filters placed in front of the sample. No significant changes in the EQE were observed as depicted in Figure 4.8. It should be noted that the recorded EQE spectra are all above the electrical noise level of the apparatus as shown in Figure 4.8. In Figure 4.5a and b, the numerically obtained α is scaled to compare its spectral line shape to the EQE spectra of devices with different active layer t .

The assumption $A \approx 2\alpha t$, according to which the spectral line shape of α follows A and therefore the EQE, is not applicable to any PBDB-T:ITIC device without greatly over- or underestimating α . To find the t at which this assumption is valid, A was simulated using the conventional transfer matrix method over a broad range of t (see Figure 4.7). For PBDB-T:ITIC, the best fit was obtained for t between 130 nm to 170 nm, however, the assumption clearly fails for other t . This is mainly caused by a strong dispersion of n for PBDB-T:ITIC (see refractive indices in Figure 4.3). The strong dispersion arises from the high α and its sharp bandgap resulting in larger Cauchy factors. Consequently, interference effects are more pronounced in PBDB-T:ITIC than in PBTTT:PC₇₁BM devices, which presumably also applies to other non-fullerene containing systems with similarly large α . For PBTTT:PC₇₁BM, $A \approx \alpha t$ can give a better estimate for the numerical α over a wide range of t . At the same time, the change in t between 60 nm to 150 nm also affects the spectral line shape of the simulated absorptance. From these two examples, it becomes clear that active layer t plays a significant role in the observed spectral line shape of the EQE and care must be taken to not mistake material properties with device properties.

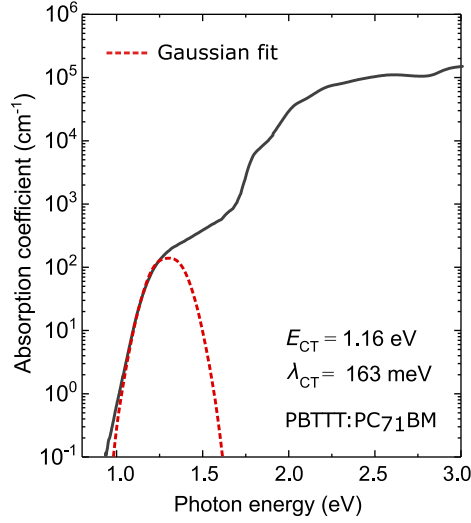


Figure 4.6: α of PBTTT:PC₇₁BM inferred from the ellipsometric extinction coefficient in the VIS spectral range and the numerical extinction coefficient in the sub-bandgap range. It is known that PBTTT:PC₇₁BM exhibits a strongly redshifted CT absorption leading to a sub-bandgap EQE shoulder. The low energy part of α was fit by a Gaussian-like function to extract the charge transfer energy (E_{CT}) and the reorganization energy (λ). A charge transfer energy (E_{CT}) of 1.15 eV has already been reported in literature¹³¹ for PBTTT:PC₆₁BM.

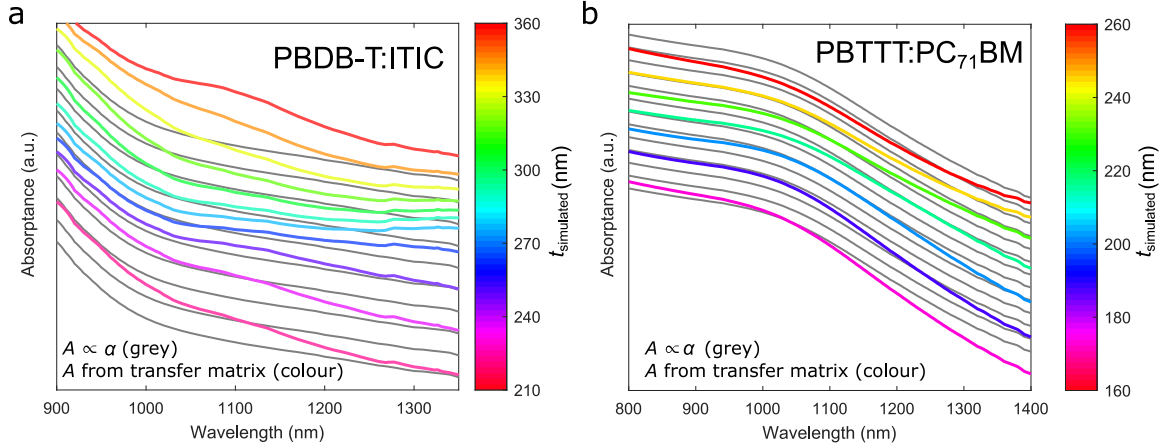


Figure 4.7: Sub-bandgap spectral line shape of the active layer absorbance for different $t_{\text{simulated}}$ in devices with PBDB-T:ITIC (a) and PBTTT:PC₇₁BM (b). Coloured lines represent the simulated absorbance obtained from the transfer matrix method and the numerical α . Grey lines represent the absorbance obtained by assuming $A \approx 2\alpha t$ for a subset for different $t_{\text{simulated}}$.

4.5 Absorption of Trap States

The α spectra of PBDB-T:ITIC shown in Figure 4.5a further indicate a broad absorption feature between 1000 nm to 1400 nm with an ultra-low α of 0.1 cm^{-1} to 0.01 cm^{-1} . According to the empirically established relation $E_{CT} \approx qV_{OC} + 0.6 \text{ eV}$, E_{CT} of PBDB-T:ITIC is expected to be at around 1.5 eV. This has been experimentally shown^{149,155} and can be observed in Figure 4.5 as a shoulder in the α spectrum at 800 nm. The corresponding Gaussian-distributed absorbance of CT states occurs at much higher energies than the observed tail states. Importantly, the ability to determine α between 0.1 cm^{-1} to 0.01 cm^{-1} , allows one to observe ultra-weak optical transitions that are typically associated with defect absorption in this spectral range.^{144,145,156} Moreover, the tail of α observed here can be easily fitted by an

exponential function. Similar to FTPS measurements, the presented method determines exclusively photocurrent-generating trap states. Therefore, it possibly underestimates the α in the spectral range of defect absorption. However, the thus obtained “effective α ” is advantageous for modelling solely photocurrent-based devices like solar cells and photodetectors, and to perform detailed balance analysis to determine the open circuit voltage of the solar cells and thermodynamic limit of the detectivity of the photodetectors.

4.6 Noise Equivalent External Quantum Efficiency

Using the presented method, the sensitivity to α depends solely on the ability to measure small photocurrents in the weakly absorbing spectral region. Figure 4.8a shows the EQE of PBDB-T:ITIC cells measured up to 1700 nm. Depending on the device noise current and measurement integration time, the noise floor is reached at different wavelengths, but always above 1400 nm. In Figure 4.8b, the current response of a 105 nm thick PBDB-T:ITIC device in the dark is depicted as the noise-equivalent EQE of the measurement system utilized in this work. Presumably, it is possible to obtain α values down to 0.001 cm^{-1} , if the device noise can be decreased via, for example, increasing the shunt resistances (i.e., lowering the thermal noise). Importantly, this α is only valid for charge-generating states. Another limitation of this method concerns finding the accurate optical constants via spectroscopic ellipsometry needed to determine the IQE. Anisotropy or thickness dependent morphology as well as birefringent optical properties can be very difficult to model. Moreover, it has been reported that some material systems show an excitation energy dependent IQE.^{49,92} In that case the sub-bandgap IQE cannot be inferred from the above bandgap IQE making the method presented here not applicable. However, if the experimental EQE spectra for several thicknesses can be simulated reliably, the numerical α is valid for the material system under investigation and hence the assumption of an energy independent IQE applies.

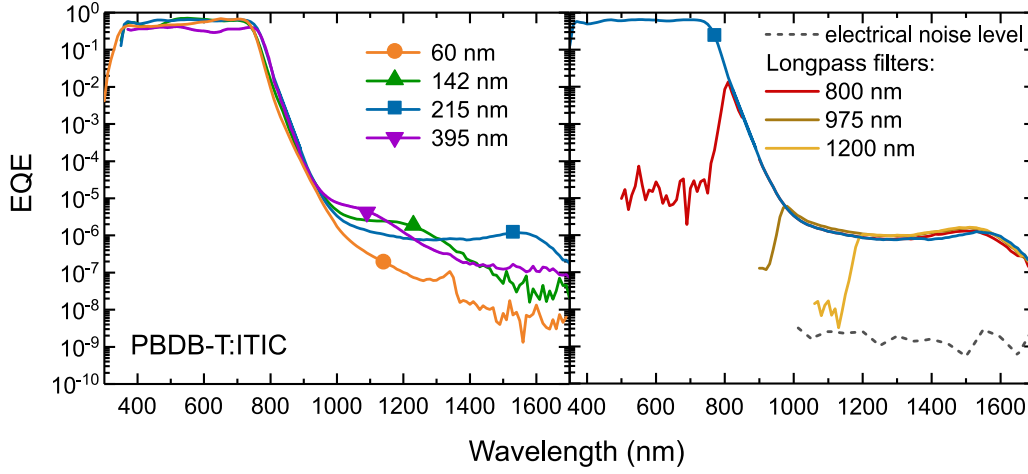


Figure 4.8: **a** EQE spectra measured for PBDB-T:ITIC devices showing optical interference fringes as the result of the device acting as a low-finesse cavity for wavelengths above 1000 nm. **b** EQE of the PBDB-T:ITIC device with a 215 nm active layer. Different longpass filters were placed in front of sample to eliminate higher incident light order harmonics. The noise-equivalent EQE of a 105 nm thick PBDB-T:ITIC cell was recorded by fully blocking the light beam.

4.7 Conclusions

To summarize this chapter, a numerical and experimental approach was presented to determine ultra-small α of sub-gap states from EQE and applied it to organic semiconductors-based solar cells. Due to non-negligible cavity effects, the spectral shape of the sub-bandgap EQE is influenced by interference fringes that are greater when the refractive index is more dispersive as exemplified with the PBDB-T:ITIC system. The t -dependent EQE spectra of PBDB-T:ITIC and PBTTT:PC₇₁BM devices were accurately predicted when modelling the device using the as-obtained α . While E_{CT} of the PBTTT:PC₇₁BM was determined as previously reported, sub-bandgap states were observed for the PBDB-T:ITIC blend, which are most likely linked to photocurrent generating trap states. The method presented here refines how to obtain α from EQE spectra while offering a novel way to study sub-bandgap absorption with relatively low experimental overhead.

Chapter 5

Manipulating the Charge Transfer Absorption for Narrowband Light Detection in the Near-Infrared

Charge generation and recombination processes at interfaces between electron donating (donor, D) and accepting molecules (acceptor, A) are mediated by intermolecular charge-transfer (CT) states. Since organic photovoltaic and photo-detecting devices rely on D:A interfaces, an understanding of the molecular and morphological aspects governing CT state properties is crucial. The work presented in this chapter illustrates how molecular structure and energy levels within a family of bipyranilidene based donor molecules affect the line-shape of the CT absorption cross-section of a D:C₆₀ blend. The molecule 2,2',6,6'-tetra-(2-methylthienyl)-4,4'-bithiopyranilidene is identified to have the strongest CT absorption peak combined with a strongly redshifted CT shoulder, which is exploited by fabricating near-infrared, cavity enhanced narrowband detectors. The photodetectors cover an impressive wavelength range from 810 nm to 1665 nm with line-widths between 30 to 50 nm. This chapter is written based on a collaborative work between (i) Swansea University, (ii) Dresden Integrated Center for Applied Physics and Photonic Materials (IAPP) and Institute for Applied Physics, (iii) Center for Advancing Electronics Dresden and (iv) Instituut voor Materiaalonderzoek (IMO) published in Chemistry of Materials in 2019. C. Kaiser performed optical simulations, cyclic voltammetry measurements, electro-optical measurements of the NIR photodetectors and drafted the manuscript. K. S. Schellhammer and F. Ortmann provided results of a theoretical study via density functional theory and the respective interpretation. J. Benduhn and B. Siegmund fabricated the photodiodes. C. Kaiser, O. Zeika and M. Tropicano synthesized the D materials. K. Vandewal and B. Siegmund conceptualized the idea of this project. K. Vandewal, P. Meredith and A. Armin provided the overall leadership of this project.

C. Kaiser, K. S. Schellhammer, J. Benduhn, B. Siegmund, M. Tropicano, O. Zeika, F. Ortmann, P. Meredith, A. Armin, K. Vandewal, *Manipulating the Charge Transfer Absorption for Narrowband Light Detection in the Near-Infrared*, Chem. Mater. **31**, 9325 (2019).

5.1 Bispyranylidenes for Near-Infrared Detection

To achieve near-infrared (NIR) detection, one strategy is to use D:A blends with a pronounced charge transfer (CT) absorption in the NIR and to optically amplify this absorption by using a micro-cavity device architecture as discussed in Section 2.4.4.¹⁴ The key advantage of these photodetectors is the extended detection range far beyond the absorption onset of the neat organic materials. By blending the donor 2,2',6,6'-tetraphenyl-4,4'-bipyranilidene (D1) with C₆₀, Siegmund et al. achieved a photodetection window extending from 810 nm up to 1550 nm, while the wavelengths corresponding to the absorption onsets of neat C₆₀ and D1 are below 700 nm. The authors concluded that new D:C₆₀ blends with a stronger and more redshifted CT absorption would improve the next generation of these photodetectors. This chapter investigates a new series of molecules (D1 to D8, see all molecular structures in Figure 5.1) that was synthesized⁽¹⁾ with the goal to improve the characteristics of CT absorption based NIR photodetectors. The synthesis was conducted according to two main strategies: First, the bipyranilidene core of the literature-known molecule D1 was substituted with sulfur. This substitution was inspired by increased conductivities of pressed powder or single crystals of the neat donors D5 and D6 or their CT complexes with the acceptor 7,7,8,8-tetracyanoquinodimethane (TCNQ) as compared to their oxygen analogues D1 and D2, indicating improved charge transport properties.^{157–159} Second, side chains with higher electron-donating strength than phenyl were introduced to extend the wavelength range of CT absorption further into the NIR, as it is known that E_{CT} scales with the energy difference between the HOMO of the donor and the LUMO of the acceptor.^{158–161}

To showcase the influence of the CT state manipulation, a series of fully vacuum-deposited photodetectors was fabricated⁽¹⁾. For the active layer, D8 and C₆₀ were co-evaporated from vacuum to form the active layer. Moreover, a complicated planar stack of charge selective interlayers, including doped layers, was evaporated to tune the resonance wavelength and reduce the dark current, thus, improving the specific detectivity (D^*) of the photodetector. The exact device architectures are depicted in Appendix A.1. A comparison of photodetectors with D1 and D8 shows that photodetectors employing D8 have an increased external quantum efficiency (EQE) over the entire spectral region of CT absorption with the strongest enhancement around the CT state absorption onset. As a result, their photoresponse window was increased by 100 nm reaching 1665 nm, while a narrow spectral line width of only 50 nm was observed for the most redshifted sensor. Molecules with a bipyranilidene core such as D1 and D5 are known as strong donors when combined with fullerenes. Moreover, they are known to show reversible double oxidation at low potentials, which was previously measured⁽¹⁾ via cyclic voltammetry (CV). The CV measurements are shown in Appendix A.1. Herein, relatively high energies for the first and second oxidation ranging between 0.1 eV to 0.4 eV can be observed. These results were reproduced by density functional theory simulations (DFT) as presented in Appendix A.2. Since the

⁽¹⁾at the Dresden Integrated Center for Applied Physics and Photonic Materials (IAPP)

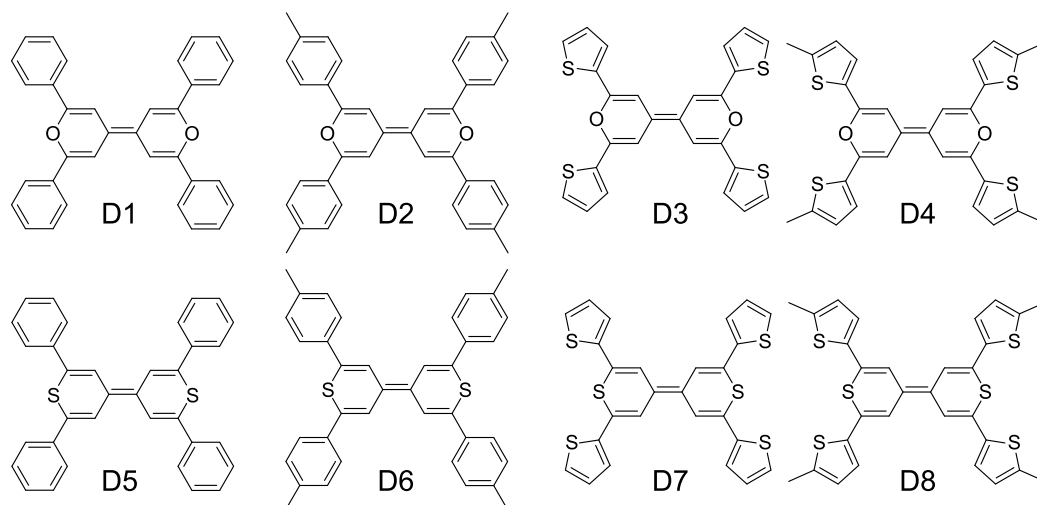


Figure 5.1: Chemical structures of the donor materials used in this chapter.

HOMO energy levels are particularly important for the expected E_{CT} values (see Chapter 2.1.6), DFT calculations were used to visualize the ground state conformations and the extension of the HOMO orbital lobes. It was concluded that sulfur in the bipyranthiylene core leads to a larger orbital extension in out-of-plane direction for the molecules D5-D8. Moreover, multiple rotamers can be observed that lie close in energy. Oxygen in the bipyranylidene core, in contrast, leads to more conformational planarity and less orbital extension in out-of-plane direction as visualized in Appendix A.3 and A.4. As a result, the calculated and experimentally determined HOMO levels of oxygen substituted bipyranylidenes are generally lower in energy than for the sulfur substituted bipyranthilenes (cf. Figure A.2 in the Appendix), which is expected to lower E_{CT} .

5.2 Spectral Line-shape of the External Quantum Efficiency

As a next step, the effect of the structural modifications on the device performance is investigated with the help of simple solar cells employing the D:C₆₀ blends as active layer. Note, that CT absorption is too weak to be detected directly by conventional optical spectroscopy, thus, photocurrent measurements were employed. The solar cells were fabricated using thermal evaporation under ultra-high vacuum, where D:C₆₀ blend represents the active layer in the device stack: ITO (90 nm) / MoO₃ (2 nm) / D:C₆₀ (50 nm) / BPhen (8 nm) / Al (100 nm). The donor was diluted at around 5 wt% in the C₆₀ acceptor matrix, allowing the change in device performance to be regarded solely as the result of structural modification of the donor.

Figure 5.2a compares the EQE and IQE spectra of D1:C₆₀ and D8:C₆₀. The substitution of oxygen by sulfur in the pyranthiylene core of the donor leads to an increase of the EQE by roughly 1 order of magnitude in the spectral region of CT absorption. To elucidate the effect of molecular structure on the EQE, one has to distinguish contributions from the IQE and the absorbance (A) to the EQE

($\text{EQE} = A \times \text{IQE}$). To estimate the IQE in this region, the EQE spectra were determined under reverse bias voltage (0 V to -3.5 V) as shown in Figure 5.3.^{92,147} As the reverse bias increases, charge collection and charge dissociation efficiencies improve (η_{col} and η_{diss} , respectively) until the photocurrent saturates at -3.5 V. In that case, the IQE is approximately 1 ($\text{IQE} = \eta_{\text{col}} \times \eta_{\text{diss}}$) and therefore the active layer A can be estimated from the EQE. Consequently, the “IQE” at different bias can be estimated by dividing the EQE spectra at different bias by A ($\approx \text{EQE}$ at -3.5 V). “IQE” spectra at different voltages are shown in Figure 5.4. Note that, as the absolute voltage bias increases, the voltage-dependent shot noise is increasing as well and can therefore limit sensitivity of the EQE and IQE for wavelengths above 1500 nm. The IQE spectra at 0 V are presented in Figure 5.2a showing a minor energy dependence of 2 % to 12 % in the case of D1, and 17 % to 5 % in the case of D8. This confirms the excitation energy independence (spectral flatness) of the IQE can be assumed in those systems in good approximation. The same assumption was validated for the two systems PBTTT:PC₇₁BM and PBDB-T:ITIC Chapter 4, however, it is often debated in literature.^{49–51,91–93} As the bias increases, the spectral flatness of the IQE increased for all investigated blends as shown in Figure 5.4.

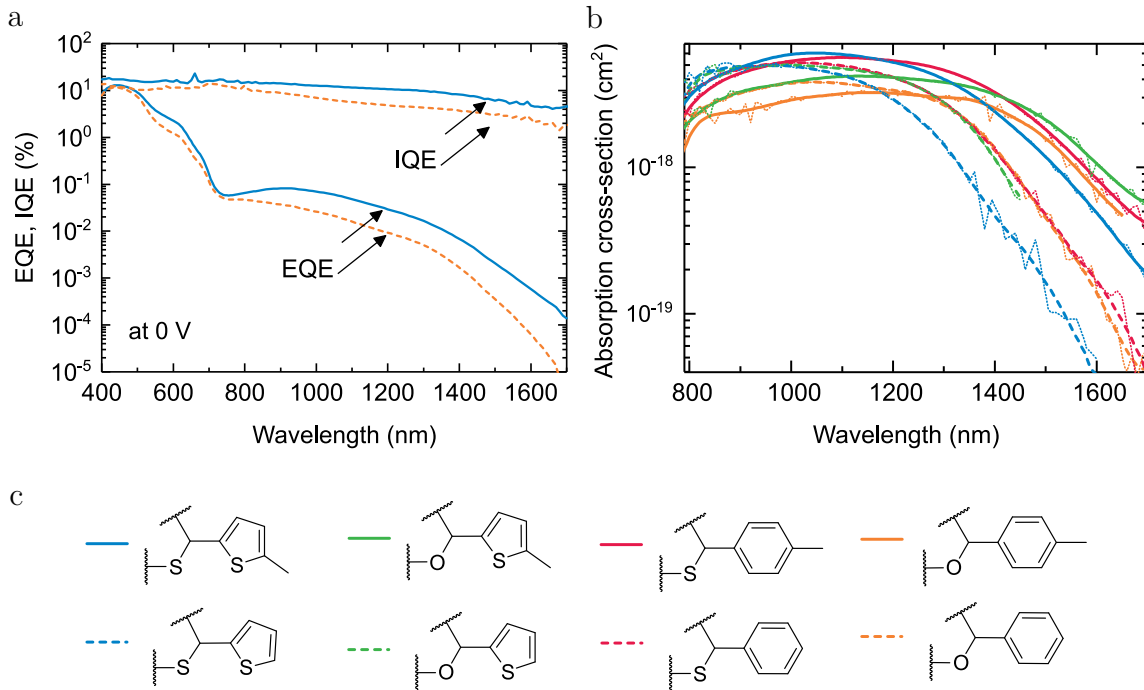


Figure 5.2: **a** EQE spectra of D8:C₆₀ (solid line) and D1:C₆₀ (dashed line) measured under short-circuit condition. The IQE spectra under short circuit condition were estimated as the ratio of the EQE at zero bias and saturated EQE at -3.5 V in reverse bias. **b** CT state absorption cross-sections σ_{CT} of all D:C₆₀ blends as calculated from the absorption coefficient spectra. The latter were obtained from the saturated EQE spectra under reverse bias. Solid lines represent methylated donors and dashed lines nonmethylated donors. **c** Characteristic molecular features of the donor molecules, where solid lines represent methylated compounds and dashed lines nonmethylated compounds.

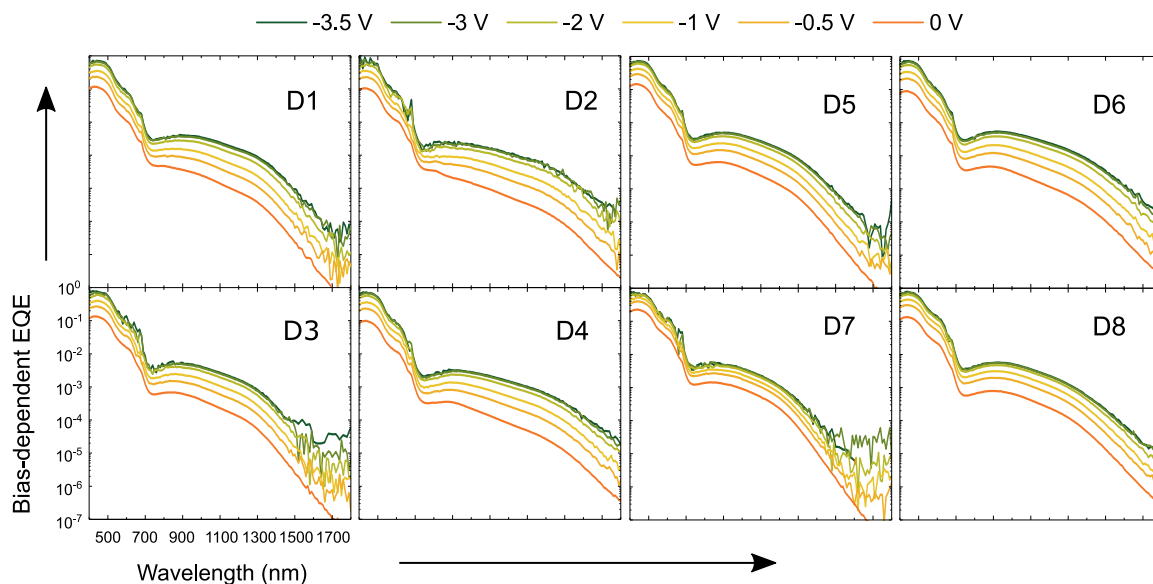


Figure 5.3: EQE of the D:C₆₀ solar cells containing the donor materials D1 to D8 under reverse bias ranging from 0 V to -3.5 V.

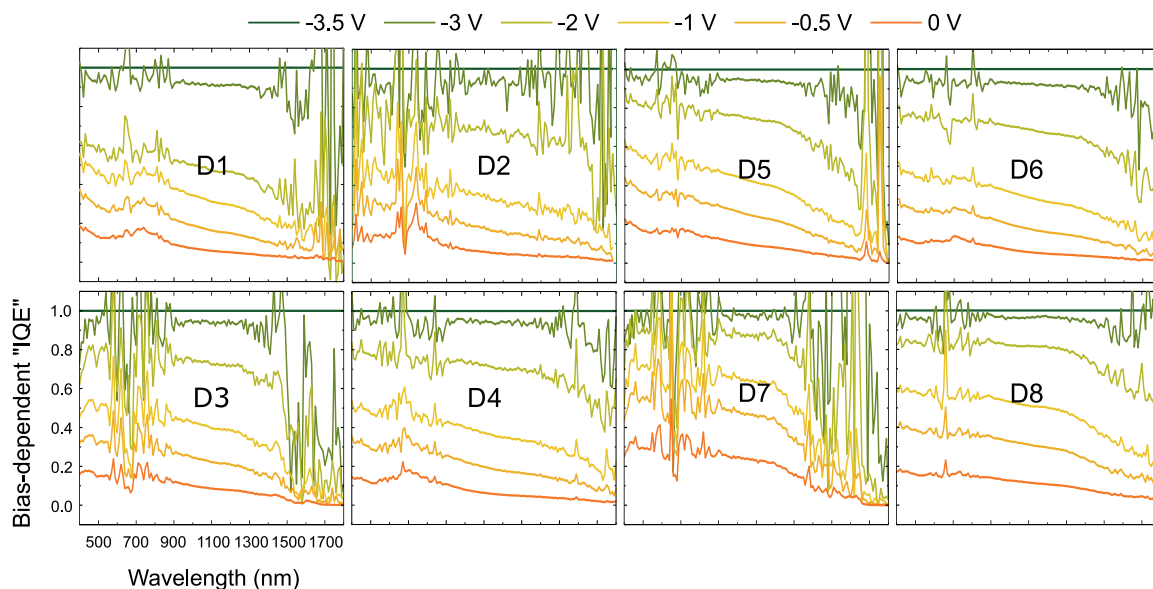


Figure 5.4: Calculated “IQE” of D:C₆₀ photodiodes under reverse bias ranging from 0 V to -3.5 V. The IQE was approximated by dividing the experimental EQE by EQE(-3.5 V), since $A \approx \text{EQE}(-3.5 \text{ V})$ and $\text{IQE} = \text{EQE}/A$. Measurement limitations, caused by either a low light intensity in the visible spectral range or by the voltage-dependent shot noise, make it impossible to obtain a smooth EQE under applied bias.

To confirm the obtained IQE at 0 V in the visible spectral range by a second method, transfer matrix simulations were performed for wavelengths between 425 and 520 nm, where only C₆₀ absorbs and the unknown optical constants of the donor materials can be neglected. The simulated absorbance of the active layer was then used to calculate the IQE. The IQE values at 0 V and the respective standard deviations obtained from both methods (EQE under reverse bias – method “S”; and transfer matrix simulations – method “T”) are compared in Figure 5.5 for the same spectral range showing good agreement. As illustrated in Figure 5.2a, the photodiode with D8 shows both an increased EQE and IQE in comparison to D1. At 1600 nm, the difference in IQE is roughly 2-fold, whereas the EQE is approximately 9 times higher for the photodiode with D8. Therefore, the improvement in EQE for D8 is predominantly the result of a stronger charge transfer absorption rather than an improvement in the IQE. It is worth mentioning that the moderate increase in IQE is likely caused by an increase of the charge carrier mobility of the D8:C₆₀ blend. In literature, sulfur substitution in the bipyranlydene core has led to higher conductivity of the D5:TCNQ over the D1:TCNQ blend. Similarly, an increase of the IQE to 18 % was observed for the D5:C₆₀ blend in comparison to 14 % for the oxygen analogue blend D1:C₆₀ (cf. Figure 5.5). As a next step, the absorption coefficient α of each D:C₆₀ blend is estimated from the active layer absorbance A (\approx EQE at -3.5 V). Using the Beer–Lambert law, it is often assumed^{131, 148, 149} that $A \approx 2\alpha d$, where d is active layer thickness. In Chapter 4, it was shown that even sub-bandgap absorption can be influenced by low-finesse cavity effects so that A does not necessarily follow the spectral line shape of α . Using the optical simulation methods presented earlier, α was determined from the EQE at -3.5 V taking those interference effects into account. To further obtain the absorption cross-section from α , the number density of CT states is estimated as the number density of the donor molecules. In diluted D:A blends, aggregation effects of the donor are absent,^{131, 149} and hence each donor molecule is involved in CT complexation with C₆₀. Figure 5.2b shows how the line shape of the absorption cross-section depends on the core and side-chain substitution.

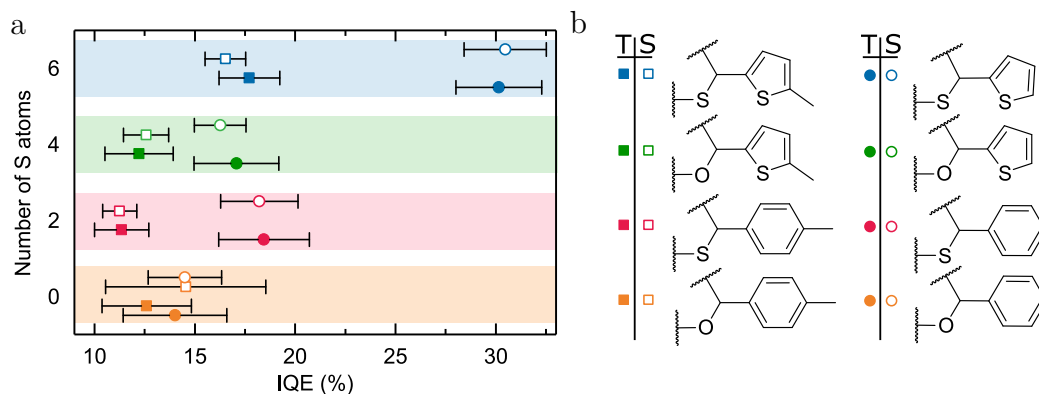


Figure 5.5: **a** The IQE and its standard deviation for photodiodes using the D:C₆₀ blends as photoactive layer. **b** Characteristic features of the donor molecules used in the active layer blends with C₆₀. Filled and hollow markers represent the IQE obtained by two independent methods (methods T and S). The IQE corresponding to filled markers was determined from the experimental EQE (method S) and the simulated absorption of the active layer using the transfer matrix method (method T).

5.3 Influence of Substitution on Charge Transfer Absorption

The CT absorption spectra can be quantitatively characterized by E_{CT} , the oscillator strength f_σ , and the reorganization energy λ_{DA} of the D:A complex, which are depicted in Figure 5.6. Those parameters are extracted by fitting a Gaussian to the low energy part of the absorption cross-section spectra using Eq. 5.1,

$$\sigma(E)E = \frac{f_\sigma}{\sqrt{4\pi\lambda_{DA}k_BT}} \exp \frac{-(E_{CT} + \lambda_{DA} - E)^2}{4\lambda_{DA}k_BT} \quad (5.1)$$

$E_{CT} + \lambda_{DA}$ is the energy at the peak position of the low energy Gaussian and is used to quantify the redshift upon molecular functionalisation. More details on the Gaussian fit are given in Section 2.1.4. The reorganization energy λ_{DA} equals the energy required to rearrange the nuclei of D, A, and their chemical environment for an intermolecular charge transfer to occur. f_σ correlates with the electronic coupling between D and A in the CT state.¹⁶² In disagreement with the stabilization of the HOMO of the neat donor upon sulfur substitution in the core, no systematic increase in E_{CT} was observed (cf. Figure 5.6a). Figure 5.6b shows that the core substitution with sulfur increases the oscillator strength f_σ . It appears that the increased orbital features of the donor molecules and the related extension of the orbital perpendicular to the π -system increase the overlap between the HOMO of the donor and the LUMO of the acceptor as previously described.¹⁶³ Therefore, core substitution results in a beneficial increase of f_σ , making the donors D5:D8 potentially superior to the donors D1:D4 for achieving higher responsivity when used in cavity-enhanced photodetectors. Moreover, a systematic increase in the reorganization energies λ_{DA} upon substitution with sulfur was observed. This can only be partially explained by a stronger localization of the HOMO. Estimations of λ_{DA} from single molecule DFT calculations give much smaller values. The larger λ_{DA} for molecules D5:D8 might be related to the presence of different donor rotamers being energetically accessible at room temperature. The availability of

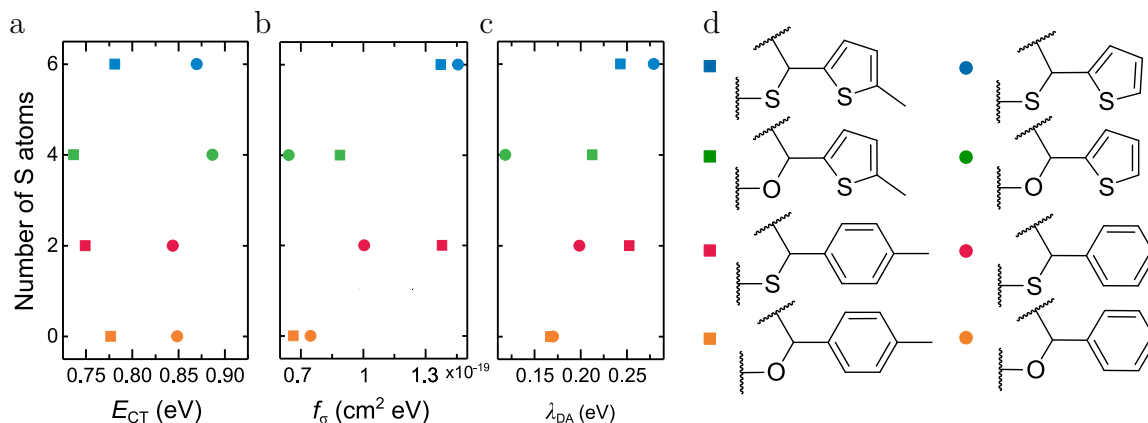


Figure 5.6: CT state energy E_{CT} (a), oscillator strength f_σ (b) and reorganization energy λ_{DA} (c) as a function of the donor molecular structure with increasing sulfur substitution from bottom to top for all investigated D:C₆₀ blends. **d** Characteristic molecular features of the D molecules, where squares represent methylated donors and circles nonmethylated donors.

multiple local energetic minima at the donor interface could lead to a broadening of the low-energy CT band edge independent of intramolecular reorganization effects. Side-chain substitution in the form of methylated thienyl or phenyl groups decreases E_{CT} and thus redshifts σ_{CT} . In this case, methyl groups increase the π -electron density without influencing the rotation of the outer phenyl or thienyl rings. In summary, the D:C₆₀ blends with the donors D6 and D8 combine the strong redshift of methylated compounds together with a high oscillator strength f_{σ} of the sulfur substituted donor materials.

5.4 Cavity Enhanced Near-Infrared Detectors

D8 was further processed in a new generation of cavity-enhanced NIR photodetectors based on CT absorption. The photodetectors comprise a photoactive blend which is sandwiched between a fully reflective (100 nm) and a semireflective (25 nm) silver electrode. Transparent doped layers were employed as optical spacers to push the D8:C₆₀ layer into the optical field maximum of the microcavity device. In this way, CT absorption is amplified within a narrow spectral range. The optimal cavity length was estimated with the help of transfer matrix simulations such that the resonance wavelengths of the photodetectors span the entire CT absorption band of D8:C₆₀ (see Figure 5.7). The EQE maxima within the photodetector series follow the line shape of the respective photodiode's EQE which exhibits minimal interference effects. As depicted in Figure 5.2a, using D8 leads to an overall increase of the EQE as compared to the previously used D1 by Siegmund et al.¹⁴ While the photodetectors perform equally well at 800 nm, the EQE of the novel photodetector series declines slower toward longer wavelengths. At 1600 nm, the EQE has improved by approximately a factor of 9, while the IQE has only increased by a factor of 2. The majority of EQE improvement is therefore the result of an improved absorption of the active layer. Given the overall

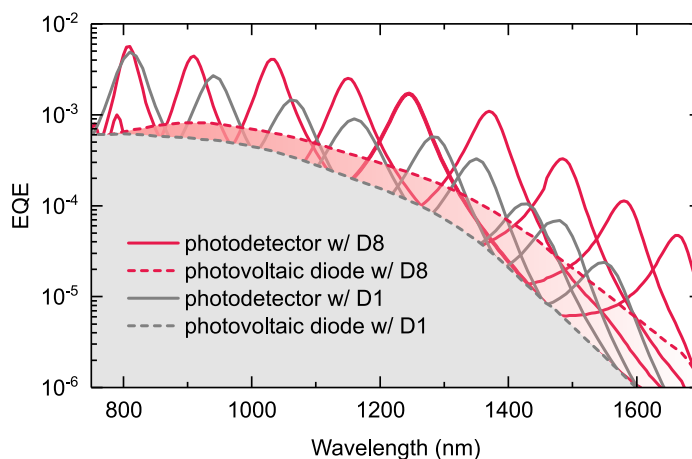


Figure 5.7: EQE of solar cells with minimal interference (dashed lines) and cavity enhanced photodetectors (solid lines) using D1 (gray) and D8 (red). The photodetector lines represent devices of different active layer or transport layer thicknesses leading to one characteristic cavity peak for each device. The photodetector series with D8 shows a higher peak-EQE toward long wavelengths, which is the result of increased redshift and increased CT absorption.

higher EQE of the new series and its redshift by 100 nm, the new photodetector series covers the NIR between 810 nm to 1665 nm. Line widths of only 50 nm and a quality factor Q of 33 are observed at 1665 nm, as well as narrower resonances with line widths of 38 nm and $Q \approx 24$ for more blueshifted resonances (see Lorentz fit to the EQE in Figure 5.8). This most redshifted photodetector settles among the highest detection wavelength obtained for organic sensors so far.¹⁴⁹ As the ultimate measure for the photodetector performance, the specific detectivity D^* (in units of $\text{cm}\sqrt{\text{Hz}}/\text{W}$) is determined from the EQE and the noise current i_{noise} (in units of $\text{A}/\sqrt{\text{Hz}}$) at 1 kHz of three representative photodetector with resonances at 908 nm, 1150 nm and 1665 nm. As previously discussed in Section 2.3.4, D^* takes into account the device area (A) and the electrical bandwidth (B) of the noise measurement.

$$D^* = \frac{e\lambda\sqrt{AB}EQE}{hc i_{\text{noise}}} \quad (5.2)$$

i_{noise} was measured as the noise spectral density of the photodetectors in the dark from the Fourier transform of the current versus time as shown in Figure 5.9. At frequencies below 200 Hz, the photodetector's noise is dominated by flicker noise that is strongly frequency dependent. D^* was therefore evaluated from the noise current at 1 kHz, where the noise current is the least affected by flicker noise, but still within the bandwidth of the preamplifier. At zero bias and 1 kHz, the photodetectors have typically a low noise floor, ranging between 30 fA/ $\sqrt{\text{Hz}}$ to 100 fA/ $\sqrt{\text{Hz}}$ that is valid up to the -3 dB cutoff frequency of the detector. The photodetector at 1150 nm has the lowest noise floor with remarkable 30 fA/ $\sqrt{\text{Hz}}$ and shows the highest D^* in the order of $2 \times 10^{10} \text{ cm}\sqrt{\text{Hz}}/\text{W}$. The most redshifted detector at 1665 nm has a D^* of $3 \times 10^8 \text{ cm}\sqrt{\text{Hz}}/\text{W}$.

In the next step, D^* was evaluated at 0.5 V reverse bias. As apparent from Figure 5.9, the devices show different voltage dependence of the noise current under applied bias. As expected, the noise level increases with applied bias, as the shot noise component becomes dominant. At the same time, the EQE increases under applied reverse bias as previously shown. To account for the voltage dependence of the EQE, the ratio of the photocurrent response with and without bias is taken as obtained in voltage-dependent EQE measurements from Figure 5.3.

The detector at 908 nm, with the thinnest active layer (25 nm), demonstrates the highest increase in the noise current by 2 orders of magnitude under 0.5 V reverse bias. This leads to a drop in D^* to $6 \times 10^9 \text{ cm}\sqrt{\text{Hz}}/\text{W}$. The detector with the detection wavelength of 1150 nm has a 75 nm thick active layer and shows almost no increase in the noise current under applied bias. This leads to a 2-fold increase of the D^* to $4 \times 10^{10} \text{ cm}\sqrt{\text{Hz}}/\text{W}$ as the result of improved collection efficiency under applied bias.

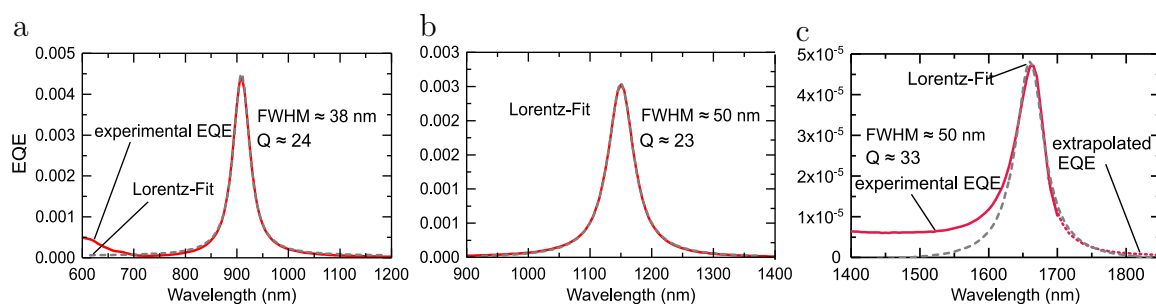


Figure 5.8: Linewidth (FWHM) of representative photodetectors at 908 nm (a), 1150 nm (b) and 1665 nm (c) determined by a Lorentz-fit to the resonance mode. Quality factor Q determined as center frequency divided by FWHM. To fit the EQE of the resonance peak at 1665 nm beyond 1700 nm without being limited by the wavelength range of the sensitive EQE measurement, the experimental EQE is extrapolated to wavelengths between 1700 nm to 1850 nm.

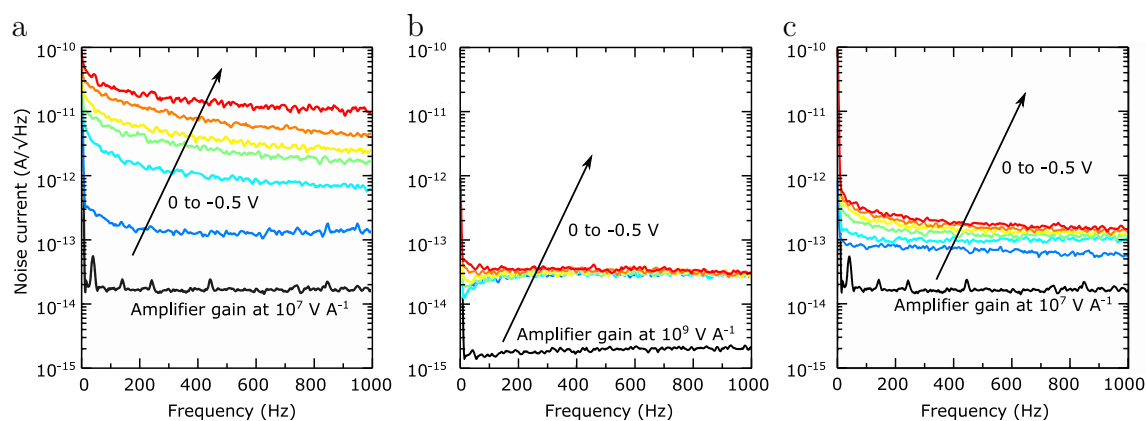


Figure 5.9: Voltage dependent noise current spectral density of photodetectors with resonances at 908 nm (a), 1150 nm (b) and 1665 nm (c). The black line shows the noise floor of the preamplifier used either at 10⁹ V/A or 10⁷ V/A gain.

5.5 Conclusions

Molecule D1 is known as a promising material for application in cavity enhanced narrowband NIR light detectors due to the formation of a broad and severely redshifted CT absorption when combined with C₆₀, covering almost the full NIR spectral region. In this chapter, results have been presented showing that targeted modifications to this molecule can further increase and redshift the CT absorption. On the one hand, core functionalization has led to an increased out-of-plane extension of the HOMO which presumably expands the overlap with the LUMO of the acceptor, and thus, the CT state oscillator strength is increased. On the other hand, methylation of the side chains destabilized the HOMO and redshifted the CT absorption by 100 nm. The donor material 2,2',6,6'-tetra-(2-methylthienyl)-4,4'-bithiopyranylidene combines an increased CT absorption strength with one of the largest redshifts observed. Cavity-enhanced NIR photodetectors using this new donor show an operational window of 810 nm to 1665 nm and a line width of only 50 nm for one of longest wavelength detecting organic photodiodes reported so far.

Chapter 6

Universal Urbach Rule for Organic Semiconductors

In crystalline semiconductors, absorption onset sharpness is characterized by temperature-dependent Urbach energies. These energies quantify the static, structural disorder causing localized exponential-tail states, and dynamic disorder from electron-phonon scattering. Applicability of this exponential-tail model to disordered solids has been long debated. Nonetheless, exponential fittings are routinely applied to sub-gap absorption analysis of organic semiconductors. In this chapter, the sub-gap spectral line-shapes of organic semiconductors and their blends are discussed with the help of temperature-dependent quantum efficiency measurements. The sub-gap absorption coefficient in the spectral range of singlet exciton absorption is found to be universally dominated by thermal broadening at low photon energies. The associated Urbach energy equals the thermal energy, regardless of static disorder. This is consistent with absorptions obtained from a convolution of Gaussian density of excitonic states weighted by Boltzmann-like thermally activated optical transitions. A simple model is presented that explains absorption line-shapes of disordered systems, and a strategy to determine the excitonic disorder energy is provided. This chapter elaborates on the meaning of the Urbach energy in molecular solids and relates the photo-physics to static disorder, crucial for optimizing organic solar cells for which a new radiative open-circuit voltage limit is presented. A summary of the work in this chapter was published by the authors in Nature Communications in 2021. C. Kaiser and A. Armin designed the experiments. C. Kaiser performed most measurements, analyzed the data, and performed optical modeling. O. J. Sandberg developed the theoretical model. O. J. Sandberg and A. Armin conceptualized the idea. C. Kaiser, O. J. Sandberg and A. Armin interpreted the data. N. Zarrabi assisted with external quantum efficiency measurements. W. Li fabricated the devices. A. Armin and P. Meredith provided the overall leadership of the project.

C. Kaiser, O. J. Sandberg, N. Zarrabi, W. Li, P. Meredith, A. Armin *A Universal Urbach Rule for Disordered Organic Semiconductors*, Nat. Commun. **12**, 3988 (2021).

6.1 Disorder Induced Broadening of the Sub-gap Absorption Coefficient

Depending on their energetic disorder, semiconductors tend to absorb more or less light at photon energies below the bandgap (sub-gap absorption). In the case of inorganic semiconductors, the absorption coefficient (α) often displays an exponential tail below the bands. These so-called Urbach tails increase their broadening with temperature T .²⁸ The sub-gap α generally follows the expression

$$\alpha(E, T) \propto \exp\left(\frac{E - E_{\text{on}}(T)}{E_{\text{U}}(T)}\right), \quad (6.1)$$

where E is the photon energy, E_{on} is the energy onset of the tail and $E_{\text{U}}(T)$ is the Urbach energy quantifying the total energetic disorder of the system. Depending on the semiconductor, E_{U} generally varies between 10 meV to 100 meV at room temperature.^{29,33–35} In banded semiconductors, it has been suggested that $E_{\text{U}}(T) = E_{\text{U,D}}(T) + E_{\text{U,S}}$, where $E_{\text{U,D}}(T)$ is a temperature-dependent dynamical disorder term related to the thermal occupation of phonon states,^{34,164} while $E_{\text{U,S}}$ is the width of the assumed exponential distribution of sub-gap states induced by static disorder.¹⁶⁵ However, a unifying theory describing the density of states and their absorption leading to Urbach tails for materials of different chemical bonding and morphology is still lacking.^{36,166}

In non-excitonic amorphous semiconductors, the definition of a clear bandgap edge is often difficult due to large static disorder inducing sub-gap broadening. Organic semiconductors, which are excitonic and partially amorphous, display even more complex sub-gap features including intermolecular hybrid charge transfer (CT) states in technologically-relevant blends of electron donors (donor, D) and acceptors (acceptor, A), excitonic features¹⁶⁷ and trap states⁸⁴. CT states give rise to light absorption with Gaussian sub-gap spectral line-shapes. This has been attributed to intermolecular D:A transitions described by non-adiabatic Marcus theory⁴¹ or its extensions^{42,74,140,168}. More details are provided in Section 2.1.4 Whether a similar description applies for sub-gap absorption by intramolecular excitons is unclear. With the rise of NFA semiconductors with small energetic offset relative to donors¹⁶⁹, the lack of CT state sub-gap spectral features in D:A blends has led to the increased usage of Urbach energies to understand disorder and sub-gap photo-physics. As a rule of thumb, it has been assumed that low Urbach energies are indicative of lower static disorder and hence expected to result in higher performance such as reduced charge recombination and higher charge carrier mobilities in a photovoltaic device.^{170–172} More details on static disorder are provided in Section 2.1.5. Due to the complex and often convoluted spectral features in sub-gap light absorption of organic semiconductors, however, the Urbach energy carries significant ambiguity. Moreover, a long-standing debate^{27,139,173} on the distribution of density of states (DOS) defining the static disorder in organic semiconductors has been revived: Does the DOS follow a Gaussian or an exponential distribution? With no doubt, the origin of the static

disorder is of great importance for the classification and future development of organic semiconductors and their electro-optical properties. However, it has remained unclear how this important figure-of-merit relates to the Urbach energy.

6.2 Definition of the Apparent Urbach Energy

The spectral line shape of α and the absorbance A in the sub-gap tail are generally related via a modified Beer-Lambert law, $A = \tilde{f}\alpha d$, where d is the thickness of the active layer and \tilde{f} is an energy-dependent correction factor accounting for optical interference.^{174, 175} For optically thin films with layer thicknesses of 100 nm to 150 nm, \tilde{f} is often assumed to be close to 1 (negligible optical interference effects). Moreover, it has been shown for efficient D:A systems that the internal quantum efficiency (IQE) is generally excitation energy independent, hence $\text{EQE} \propto A$ and the spectral line shape of the EQE follows α .^{49–51, 91} Based on this underlying premise, EQE measurements have been frequently employed in the past to determine E_U . However, a previous lack of sensitivity in the EQE measurements has led to speculative assumptions about the spectral range of trap state absorptions, exponential tails and associated E_U in organic semiconductors. By choosing a small fitting range, exponential fits can be forced on to EQE spectra resulting in rather arbitrary E_U dependent on the spectral range of the fitting. More insight can instead be gained from the apparent Urbach energy (E_U^{app}) here defined as:

$$E_U^{\text{app}}(E) = \left[\frac{d \ln(\text{EQE})}{dE} \right]^{-1} \quad (6.2)$$

For a true exponential tail of the form Eq. 6.2, E_U^{app} is constant in the sub-gap spectral region and given by E_U .

6.3 Apparent Urbach Energy Spectra

Figure 6.1 shows the EQE and E_U^{app} for a wide range of organic semiconductor D:A blends. The material systems studied here can be generally grouped according to the D:A energy offset or, in other words, the difference between the CT state energy E_{CT} and the optical bandgap E_{opt} . Here, E_{opt} is typically equal to the local exciton (LE) energy of the lower-bandgap component (D or A). Large offset systems, such as PCDTBT:PC₇₁BM, BQR:PC₇₁BM and PBDB-T:PC₇₁BM (Figure 6.1a), show three distinct spectral ranges for energies below the gap: (i) mid-gap trap state absorption at energies below 1.2 eV, (ii) CT state absorption in the mid-range (≈ 1.2 eV to 1.5 eV) and (iii) LE absorption above 1.5 eV. For mid-gap and CT state absorption, Gaussian-shaped EQE features were observed as previously⁸⁴ reported in literature. The EQE associated with CT states and mid-gap states were routinely fitted in accordance with the standard Marcus charge-transfer formalism. The associated EQEs

are given by $\text{EQE}_{\text{CT}}(E) = g(E, E_{\text{CT}}, \lambda_{\text{CT}}, f_{\text{CT}})$ and $\text{EQE}_{\text{t}}(E) = g(E, E_{\text{t}}, \lambda_{\text{t}}, f_{\text{t}})$ for CT and mid-gap state absorption, respectively, where

$$g(E, E_j, \lambda_j, f_j) = f_j E^{-1} (4\pi\lambda_j kT)^{-1/2} \exp\left(-\frac{(E_j + \lambda_j - E)^2}{4\lambda_j kT}\right). \quad (6.3)$$

Here, f_j , E_j and λ_j are fitting parameters. Because of the Gaussian line-shape, the corresponding $E_{\text{U}}^{\text{app}}$ in the spectral range of CT absorption is expected to be strongly energy-dependent and given by $E_{\text{U}}^{\text{app}} \approx 2kT\lambda_{\text{CT}}/(E_{\text{CT}} + \lambda_{\text{CT}} - E)$; this is highlighted by the black solid line in Figure 6.1a. Here, E_{CT} and λ_{CT} , as obtained from the Gaussian fits, are to be considered the effective energy and reorganization energy of CT states which includes the effect of static disorder^{42, 74} as described in more detail in Section 2.1.5 on the Marcus theory. At higher energies corresponding to the sub-gap LE absorption regime, in turn, $E_{\text{U}}^{\text{app}}$ has a narrow parabolic shape with a sharp minimum at roughly 40 meV to 50 meV for the large offset blends.

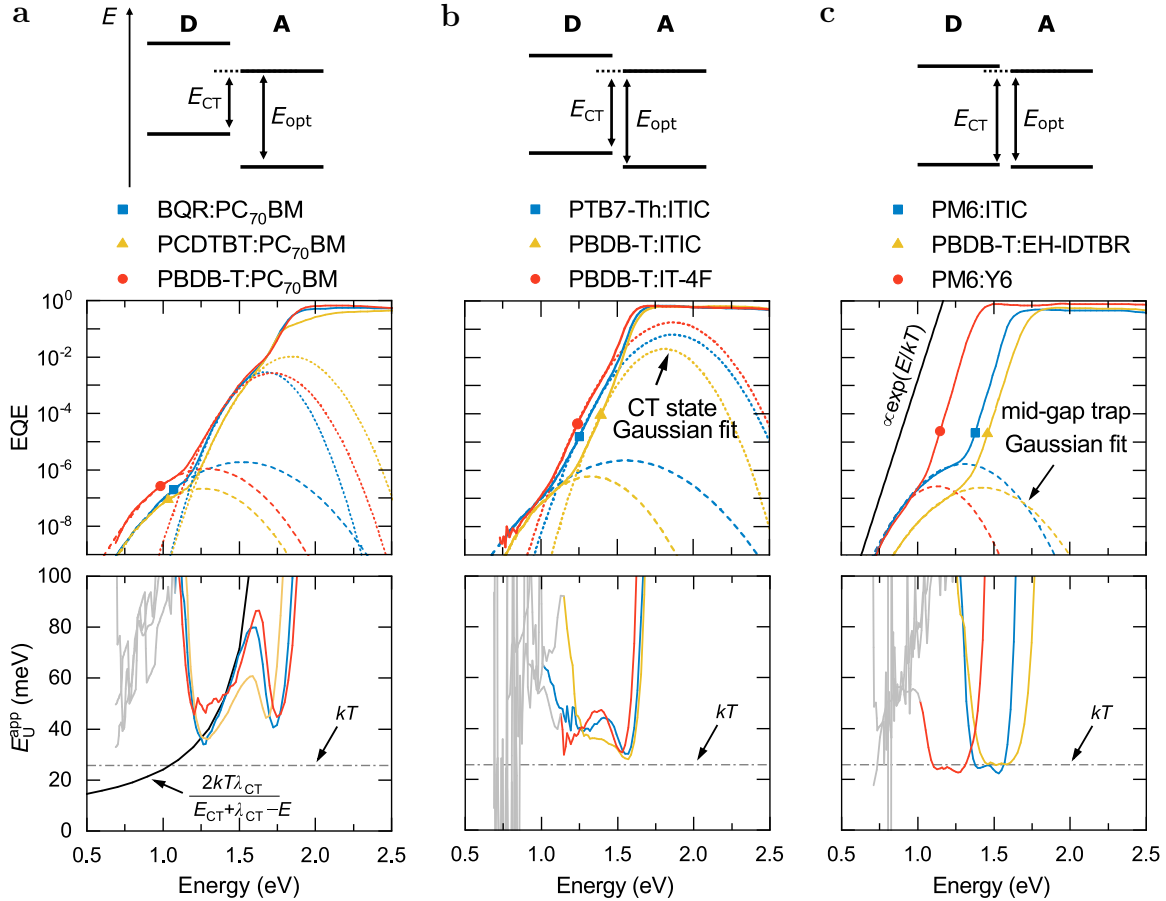


Figure 6.1: EQE and $E_{\text{U}}^{\text{app}}$ for organic D:A blends with different energetic offsets between E_{CT} and E_{opt} . Schematic illustration of the energetic offset ($E_{\text{opt}} - E_{\text{CT}}$) decreasing from left to right. Gaussian fits in the spectral range of CT state and trap state absorption were performed where possible. For low offset blends PM6:Y6, PM6:ITIC and PBDB-T:EH-IDTBR, the EQE tail has the form $\exp(E/kT)$, and $E_{\text{U}}^{\text{app}}$ roughly equals kT in the spectral range that is dominated by the absorption of the acceptor. For large offset material systems, such as BQR:PC₇₁BM, PBDB-T:PC₇₁BM and PCDTBT:PC₇₁BM, $E_{\text{U}}^{\text{app}}$ shows a $E_{\text{U}}^{\text{app}} \approx 2kT\lambda_{\text{CT}}/(E_{\text{CT}} + \lambda_{\text{CT}} - E)$ dependence in the spectral range of CT absorption.

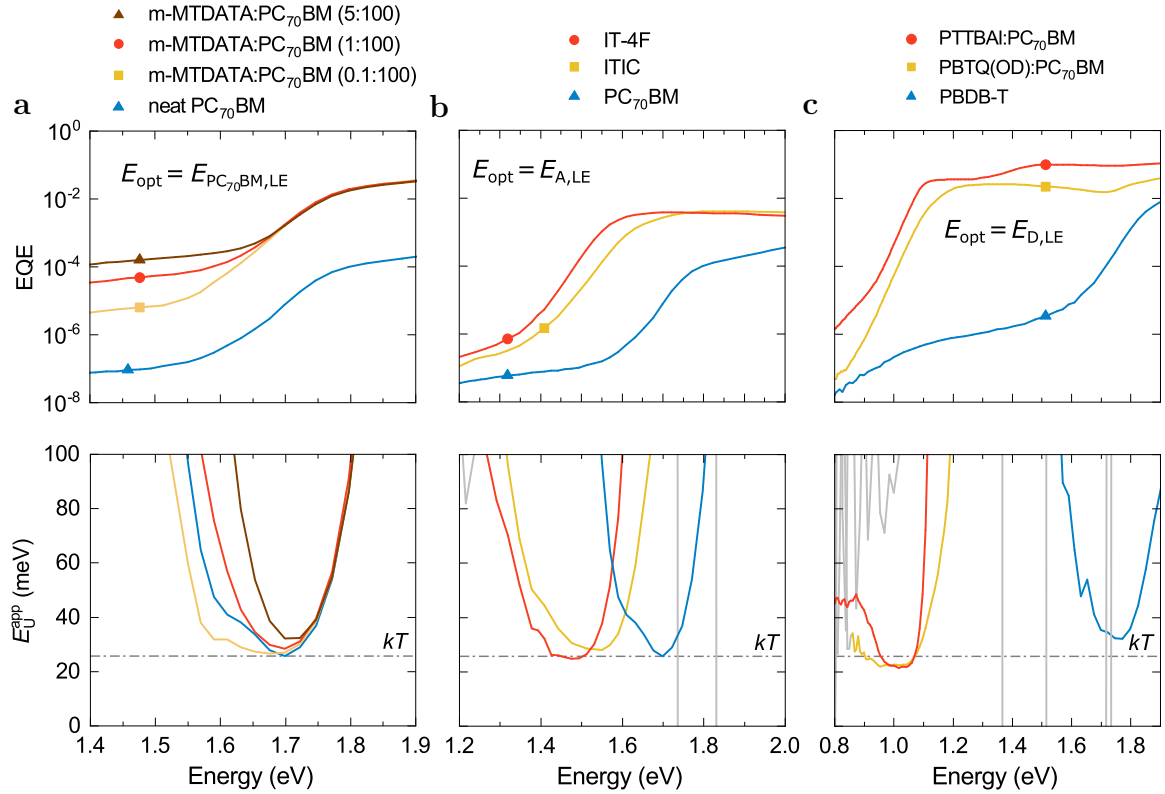


Figure 6.2: **a** EQE and E_U^{app} for a series of m-MTDATA sensitized PC₇₁BM solar cells. The widest energy range over which E_U^{app} equals kT was observed for 0.1 mol% m-MTDATA in PC₇₁BM due to improved exciton dissociation in comparison to neat PC₇₁BM. Examples for EQE tails partially dominated by **b**, the neat donor absorption or by **c**, the neat acceptor absorption hence showing $E_U^{\text{app}} \approx kT$ in some parts of the spectrum. EQE spectra of PTTBAI:PC₇₁BM and PBTQ(OD):PC₇₁BM were taken from literature.¹⁷⁶

The EQE and E_U^{app} of blends with a smaller offset between E_{CT} and E_{opt} (PTB7-Th:ITIC, PBDB-T:ITIC and PBDB-T:IT-4F) are shown in Figure 6.1b. In this case, the Gaussian CT state line-shape is barely recognizable, and the α tail in the spectral range of LEs is visible over a wider spectral range. While E_U^{app} retains its parabolic shape in the LE sub-gap absorption regime, because of the wider range, the minimum value of E_U^{app} is significantly reduced to values close to kT . Finally, the EQE and E_U^{app} of blends in low-offset D:NFA systems (PM6:Y6, PM6:ITIC and PBDB-T:EH-IDTBR) are shown in Figure 6.1c. In these blends, the CT state absorption can no longer be discerned from the EQE spectra. Instead, the α tail in the spectral range of LEs remains dominant down to the energy range of mid-gap state excitation. In this limit, the E_U^{app} in the LE-dominated sub-gap absorption range finally saturates and reaches a broad plateau where $E_U^{\text{app}} \approx kT$.

The above experimental observation for low offset D:NFA systems suggests the presence of an intramolecular sub-gap absorption regime where $\alpha \propto \exp(E/kT)$, but that its spectroscopic observation is obstructed by CT absorption in systems with larger offsets. To further clarify this, neat D or A systems without an intermolecular CT absorption were investigated as shown in Figure 6.2. In the case of neat PC₇₁BM, a narrow spectral range where $E_U^{\text{app}} \approx kT$ can be identified (see Figure 6.2a). This is consistent with photothermal deflection spectroscopy results¹⁵⁰ of neat PC₆₁BM, confirming the underlying assumption that the spectral line shape of the EQE follows α

in the sub-gap. In PC₇₁BM, the spectral range where $E_U^{\text{app}} \approx kT$ is limited by deep trap-state absorption at low energies, while the poor exciton dissociation in the neat phase (translating into a low IQE) strongly reduces the EQE range at higher energies. However, the spectral range where $E_U^{\text{app}} \approx kT$ can be increased by adding 0.1 mol% of the wide-gap donor m-MTDATA, resulting in enhanced exciton dissociation. Since m-MTDATA:PC₇₁BM is characterized by a low E_{CT} , the LE tail of PC₇₁BM can be clearly distinguished from CT states as shown in Figure 6.2a. By further increasing the donor content, the CT state absorption increases and the parabolic shape of E_U^{app} emerges. This explains the parabolic shapes seen for large offset systems in Figure 6.1a, which appear when the α tail in the spectral range of LE absorption becomes convoluted with CT state absorption. This is further supported by results shown in Figure 6.2b for neat NFA devices comprising ITIC and IT-4F active layers, respectively. Here again, exponentially decaying α tail regions with $E_U^{\text{app}} \approx kT$ were observed.

To check if $E_U^{\text{app}} \approx kT$ is also true for donor materials has proven more challenging, since the neat donor absorption is often convoluted with deep trap-state absorption. This convolution effectively increases E_U^{app} above kT as shown for PBDB-T in Figure 6.2c, where $E_U^{\text{app}} \approx 30$ meV. The problem can be circumvented by using narrow-gap polymer donors such as PBTQ(OD) or PTTBAI, which show strongly redshifted EQE spectra when blended with PC₇₁BM as previously reported.¹⁷⁶ As shown in Figure 6.2c, E_U^{app} is around 22 meV in this case. While deviations of the type $E_U^{\text{app}} > kT + 10$ meV are due to the presence of other absorbing species like CT states or deep trap states, small deviations of E_U^{app} around kT are likely caused by optical interference in the solar cell.^{174,177}

6.4 Influence of Optical Interference on the Apparent Urbach Energy

To demonstrate the presence of optical interference, PM6:ITIC and PM6:Y6 based solar cells were fabricated with different active layer thicknesses. Figure 6.3 illustrates the EQE and E_U^{app} spectra of a series of PM6:ITIC and PM6:Y6 solar cells showing weak thickness dependence of the sub-gap features. In the spectral range of LE absorption, E_U^{app} varies between $kT + 2.3$ meV to $kT - 5.8$ meV. The interference pattern depends on the optical constants of the different layers in the thin-film stack and their thicknesses. In optimized solar cells with minimal parasitic absorption, the active layer is the predominant absorber contribution to the photocurrent spectrum. Based on the optical constants of the full stack, optical transfer-matrix simulations can determine the absorptance of the active layer, which equals the EQE in the absence of any spectral dependence of the IQE. For the optical simulation, a perfectly exponential sub-gap absorption-coefficient was assumed with $E_U^{\text{app}} = kT$ for $E < 1.55$ eV, while for $E > 1.55$ eV the experimental above-gap absorption coefficient of a 200 nm thick PM6:ITIC film on silicon is used and its refractive index as determined from spectroscopic ellipsometry over the entire wavelength range. This hypothetical absorption coefficient is shown in Figure 6.4a. By changing the layer thickness of

PM6:ITIC in the simulation, the spectral line-shape of the absorptance changes as demonstrated by the spectrum of E_U^{app} in Figure 6.4b. In the experiment, $E_U^{\text{app}} \approx kT$ was observed between 1.6 and 1.3 eV. In this spectral range, the simulated E_U^{app} shows deviations of +1 to -2 meV around kT , while discontinuities around 1.55 eV are due to the manual stitching of the experimental and fictional sub-gap absorption coefficient. As shown earlier, the fluctuation in the experimental $E_U^{\text{app}} = kT$ for PM6:ITIC devices lies in between +3 to -3 meV and are therefore very close to the simulated deviations.

6.4 INFLUENCE OF OPTICAL INTERFERENCE ON THE APPARENT URBACH ENERGY

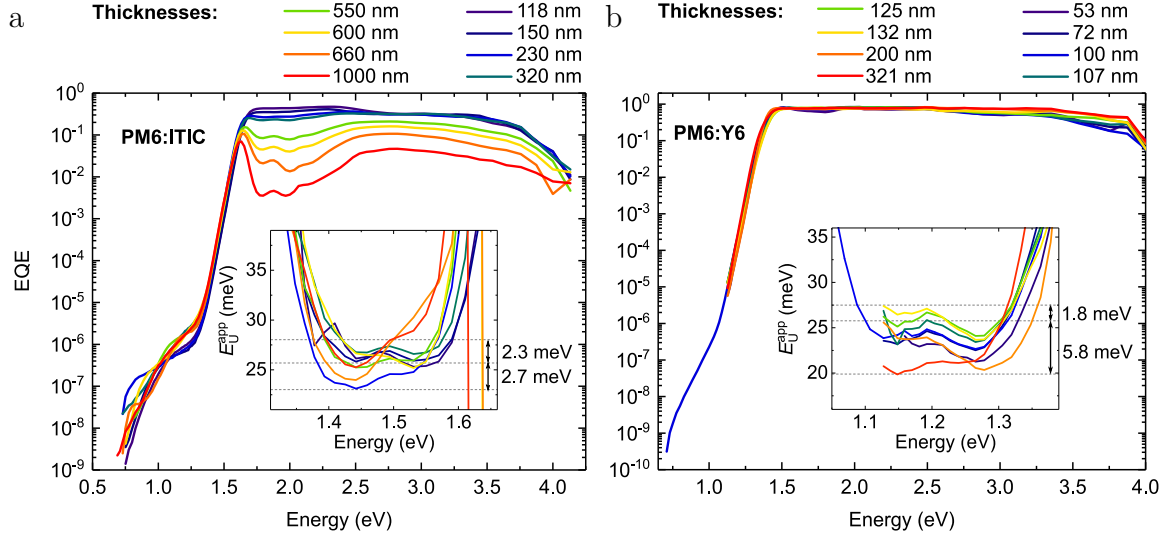


Figure 6.3: For different active layer thicknesses, nearly exponential EQE tails are observed for PM6:ITIC (a) and PM6:Y6 (b) based solar cells in the spectral range of sub-gap LE absorption (i.e., $1.4 \text{ eV} < E < 1.6 \text{ eV}$ for PM6:ITIC and $1.1 \text{ eV} < E < 1.3 \text{ eV}$ for PM6:Y6). In this spectral range, E_U^{app} is close to kT for all thicknesses of PM6:ITIC and PM6:Y6 as shown in the inset (a) and (b), respectively. Small deviations from kT can be attributed to weak optical cavity effects.

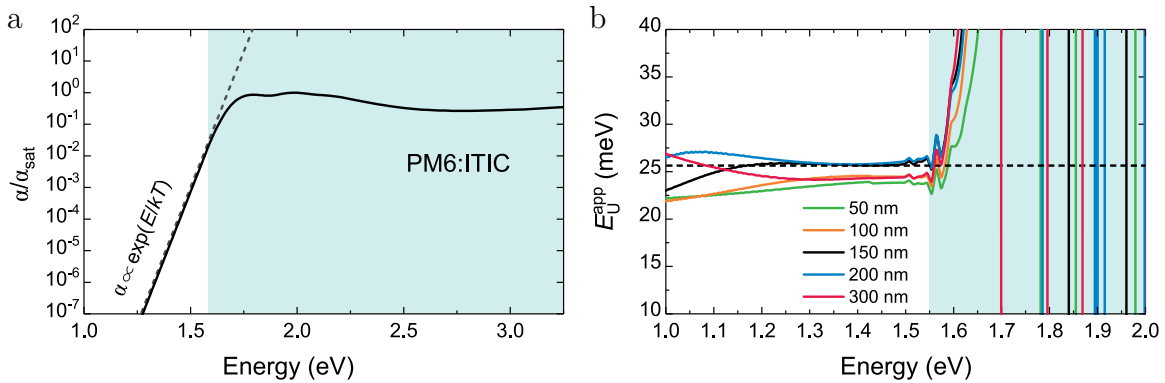


Figure 6.4: **a** Absorption coefficient (α) used in transfer-matrix simulations to calculate the absorbance of the active layer (device architecture ITO (100 nm)/ZnO (30 nm)/active layer/MoO₃ (8 nm)/Ag (100 nm)). **b** Sub-gap E_U^{app} for different active layer thicknesses (50 to 300 nm) showing energy and thickness dependence within $+1/-2 \text{ meV}$ range around kT for $1.3 \text{ eV} < E < 1.6 \text{ eV}$. Optical cavity effects, included in the transfer-matrix simulation, are thus expected to cause spectral dependence of E_U^{app} in a real device.

6.5 Temperature-dependent External Quantum Efficiency

To verify that the exponential α tails in the spectral range of LEs are characterized by $E_U^{\text{app}} \approx kT$, T -dependent EQE measurements were performed on PBDB-T:EH-IDTBR, PM6:Y6 and PM6:ITIC, and the neat materials IT-4F and Y6. Figure 6.5a shows the normalized EQE and the respective E_U^{app} spectra of three representative systems: PBDB-T:EH-IDTBR, PM6:Y6 and IT-4F. The remaining material systems are provided in Appendix B.1. Depending on T , two different regimes can be distinguished in the sub-gap absorption tail: At high T , E_U^{app} spectra show a T -dependent plateau only influenced by interference effects and the shift in the absorption onset. At low T , however, the E_U^{app} spectra generally attain a parabolic shape suggesting that the LE tail becomes convoluted with CT and/or mid-gap states. The thermal activation of the exponential α tail is then finally illustrated in Figure 6.5b where E_U^{app} at a constant energy in the plateau region is shown as a function of kT for the systems studied. It was found that E_U^{app} at higher temperature is linear and equals $kT \pm 2.5$ meV, where the offset arises from interference effects. At lower T , E_U^{app} eventually deviates from linearity, as the spectral shape is increasingly affected by other absorbing species. For example, the low-energy tail of the CT absorption may emerge at low T owing to its distinctly different T -dependence compared to LE absorption.⁴⁴ Moreover, the absorption of trap states is expected to play a role as well, while little is yet known about their spectral broadening as a function of T .

For comparison, T -dependent EQE spectra were experimentally obtained for a commercial a-Si:H thin-film solar cell as shown in Figure 6.6. In banded semiconductors such as a-Si:H, the total energetic disorder is $E_U(T) = E_{U,D}(T) + E_{U,S}$ consistent with the presence of an exponential DOS of tail states (defined by the associated width $E_{U,S}$). In Figure 6.3b, two regimes can be distinguished for a-Si:H comprising the low-temperature saturation of E_U to $E_U(0) \approx 40$ meV and thermal activation at higher temperatures with an offset of roughly 21 meV from kT in agreement with previous reports.^{178–180} In contrast, for the organic semiconductor systems in Figure 6.3b, an extrapolation to $T = 0$ implies that $E_{U,S} \approx 0$, suggesting the lack of an exponential tail state distribution in these systems. These observations raise the question why excitons in organic semiconductors follow $\alpha \propto \exp(E/kT)$ resulting in $E_U^{\text{app}} \approx kT$ and what is the role of static disorder in shaping the E_U^{app} spectra.

6.6 Modelling the Sub-gap Absorption Coefficient

In the context of Marcus formalism for non-adiabatic charge transfer in the high-temperature limit, the presence of $E_U^{\text{app}} \approx kT$ in the spectral range of LE absorption may be rationalized in terms of non-equal potential energy surfaces for the excited state and the ground state. By assuming a significantly more diffuse or delocalized excited state, compared to the strongly localized ground state, a much smaller reorganization energy is obtained for the excited state in comparison to the

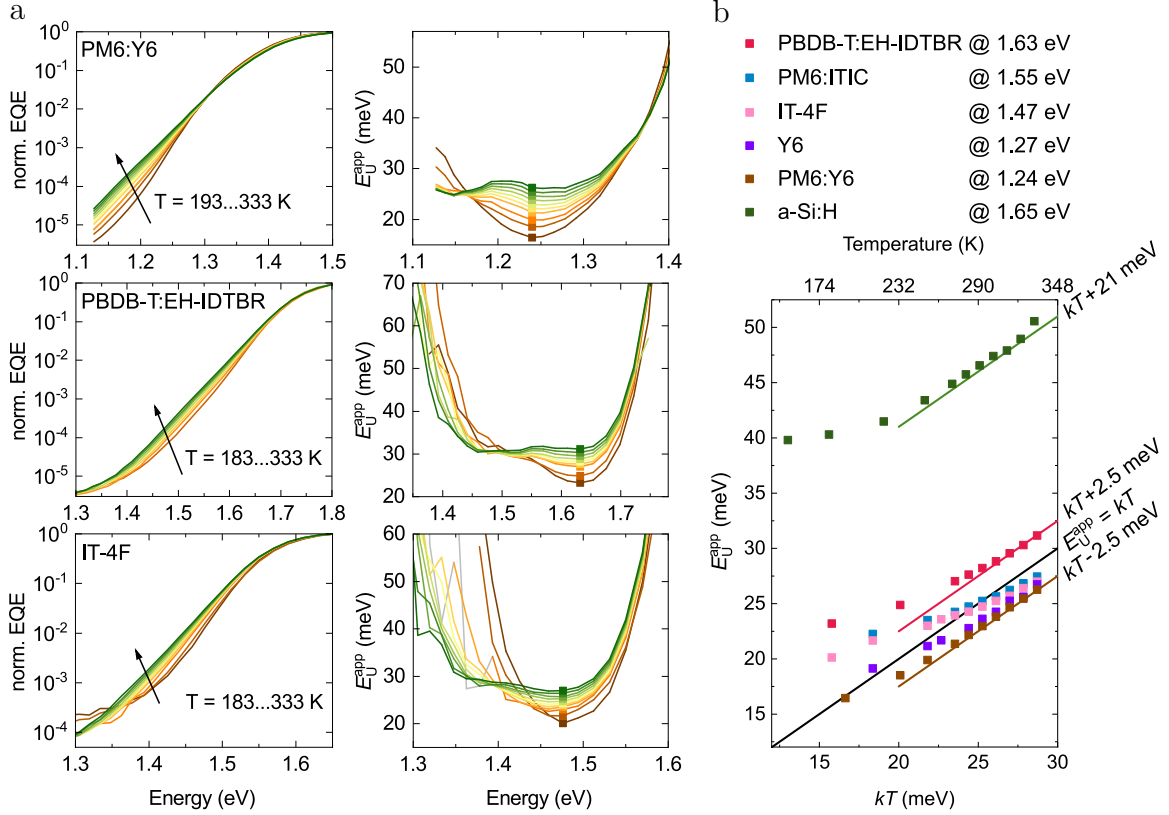


Figure 6.5: **a** Normalized sub-gap EQE and E_U^{app} spectra of inverted PM6:Y6, PBDB-T:EH-IDTBR and neat IT-4F solar cells at different temperatures. Independent of temperature, E_U^{app} spectra show a local minimum (solid markers) at a constant energy within the spectral range dominated by exciton absorption. **b** Minimum E_U^{app} as a function of kT for all tested materials systems including a commercial a-Si:H thin-film solar cell.

ground state.^{181–183} In this limit, it is expected that $\alpha_{\text{LE}}(E) \approx \alpha_{\text{sat}} \exp[(E - E'_{\text{opt}})/kT]$ for $E < E'_{\text{opt}}$ in the case of a singlemode transition with an associated optical gap E'_{opt} . Here, α_{sat} includes a $1/E$ dependence, however, the sub-gap spectral line-shape is dominated by the Boltzmann factor. For above-gap absorption $E > E_{\text{opt}}$, it is assumed that $\alpha_{\text{LE}}(E) \approx \alpha_{\text{sat}}$. This simplification of $\alpha_{\text{LE}}(E)$ for a singlemode absorption essentially follows a Miller-Abrahams (MA) type charge-transfer formalism, sometimes used to describe exciton migration¹⁸⁴, but more commonly used for charge transport¹⁸⁵ in organic semiconductors. More details on the Marcus theory in the case of unequal reorganization energy resulting in the singlemode α_{LE} are provided in Appendix B.2.

To calculate the multimode α_{LE} , the static disorder of excitons in the bulk has to be considered via a DOS given by $g_{\text{DOS}}(E'_{\text{opt}})$. The total absorption coefficient is then calculated by integrating over all absorbing sites with the energy E'_{opt} and the absorption coefficient $\alpha_{\text{LE}}(E, E'_{\text{opt}})$ in the form

$$\alpha_{\text{LE}}(E) = \int \alpha_{\text{LE}}(E, E'_{\text{opt}}) g_{\text{DOS}}(E'_{\text{opt}}) dE'_{\text{opt}}. \quad (6.4)$$

In disordered organic semiconductors, the energetic distribution of E'_{opt} is often assumed to be Gaussian (centred around E_{opt}), with a width σ_s describing the Gaussian

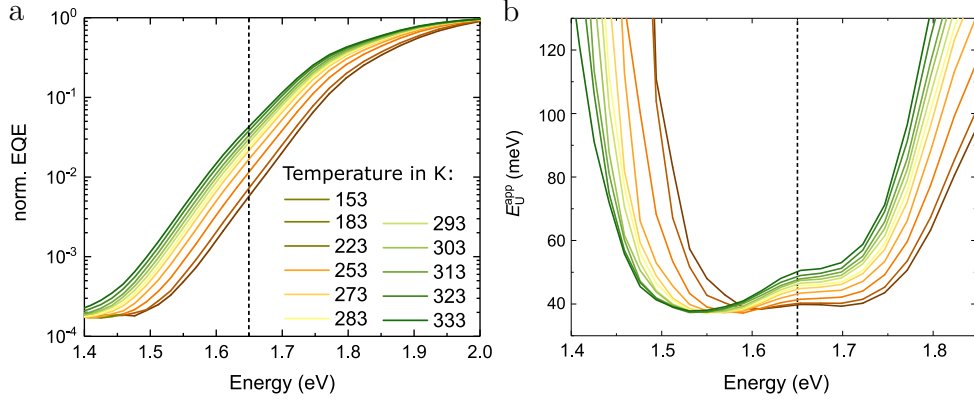


Figure 6.6: **a** Normalized sub-gap EQE of a commercial a-Si:H solar cell at different temperatures. **b** Apparent Urbach energy E_U^{app} as calculated from the sub-gap EQE. The dashed line indicates the energy at which energy E_U^{app} was evaluated.

energetic disorder. In banded crystalline semiconductors, the so-called tail states below the bands caused by static disorder, are often modelled based upon an exponentially distributed DOS with the width W . The expressions for the Gaussian and exponential DOS were previously discussed in Eq. 2.18 and Eq. 2.19, respectively, in Section 2.1.5 on static disorder. For an exponential DOS, it is assumed that there are no tail states for $E'_{\text{opt}} > E_{\text{opt}}$ and hence the upper bound is E_{opt} . Solving the integral in Eq. 6.4 for an exponential tail DOS with the width W , the associated absorption coefficient reads

$$\alpha(E) = \alpha_{\text{sat}} \exp\left(\frac{E - E_{\text{opt}}}{W}\right) \left[\frac{1 - \exp\left(\frac{E - E_{\text{opt}}}{kT} - \frac{E - E_{\text{opt}}}{W}\right)}{\frac{W}{kT} - 1} + 1 \right]. \quad (6.5)$$

It is clear that Eq. 6.5 is dominated by the exponent and hence $\alpha(E)$ follows an exponential decay, where $E_U^{\text{app}} = W$ as shown in Figure 6.7. This was indeed not observed in the experiments. For a Gaussian DOS, in turn, the associated absorption coefficient reads

$$\frac{\alpha_{\text{LE}}(E)}{\alpha_{\text{sat}}} = \frac{1}{2} \left\{ \exp\left(\frac{E - E_{\text{opt}} + \frac{\sigma_s^2}{2kT}}{kT}\right) \left[1 - \text{erf}\left(\frac{E - E_{\text{opt}} + \frac{\sigma_s^2}{kT}}{\sigma_s \sqrt{2}}\right) \right] + \text{erf}\left(\frac{E - E_{\text{opt}}}{\sigma_s \sqrt{2}}\right) + 1 \right\}, \quad (6.6)$$

where σ_s is the standard deviation of the Gaussian DOS and E_{opt} is the associated mean exciton energy. Since E_{opt} corresponds to the optical gap, it is determined by the first excited singlet state of either donor ($E_{\text{opt}} = E_{\text{D,LE}}$) or acceptor ($E_{\text{opt}} = E_{\text{A,LE}}$) in a blend. At $E \ll E_{\text{opt}}$, Eq. 6.6 reduces to the exponential part and E_U^{app} therefore equals kT . For $E \geq E_{\text{opt}}$, the error functions govern the spectral shape at the absorption edge as demonstrated in Figure 6.10. To bring this part of the analysis to a conclusion, assuming a MA-type singlemode absorption coefficient (arising from Marcus theory with unequal potential for ground state and excited state), and a Gaussian DOS is in accordance with the experimental observations that $E_U^{\text{app}} = kT$ at $E \ll E_{\text{opt}}$. To validate Eq. 6.6, T -dependent EQE spectra of neat Y6 and IT-4F were simulated as

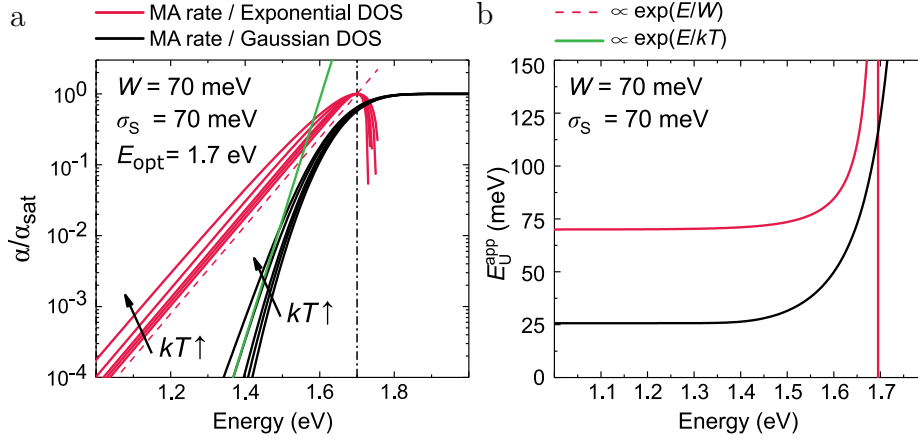


Figure 6.7: Calculated absorption coefficient based on MA-type rate constants normalized to α_{sat} . **a** α derived for an exponential DOS (red lines; normalized at $E = E_{\text{opt}}$) and for a Gaussian DOS (black lines) at kT between 13 to 30 meV. The green line is a guideline for the eye illustrating a function that is proportional to $\exp(E/kT)$. **b** α derived from the MA-type rate constant using an exponential DOS showing that $E_{\text{U}}^{\text{app}} = W$ in the limit $E \gg E_{\text{opt}}$.

demonstrated in Figure 6.8a. Using neat materials avoids the influences of CT states in the low-energy tail although trap states are always present at lower energies. In consequence, σ_s was estimated to 47.0 ± 0.7 meV for Y6 and 35.0 ± 2.6 meV for IT-4F as illustrated in Figure 6.9. More fittings on room temperature EQE spectra of other material systems are shown in the Figure 6.10. For blend systems, the full experimental sub-gap EQE can be reconstructed assuming $\alpha(E) = \alpha_{\text{LE}}(E) + \alpha_{\text{CT}}(E) + \alpha_{\text{t}}(E)$ constituting the exponentially decaying α_{LE} according to Eq. 6.6 and the sum of two Gaussian functions (CT states and deep trap states; see Eq. 6.3). In Figure 6.8b, the model for PBDB-T:PC₇₁BM is demonstrated using the parameters $E_{\text{opt}} = 1.89$ eV and $\sigma_s = 60$ meV. PBDB-T:PC₇₁BM belongs to the group of blends for which $E_{\text{CT}} \ll E_{\text{opt}}$ with $E_{\text{CT}} - E_{\text{opt}} \approx 0.45$ eV. Nevertheless, the simplified model reproduces the strong spectral dependence of the experimental $E_{\text{U}}^{\text{app}}$, including the parabolic behaviour in the LE absorption dominated spectral range. On the other hand, by keeping all other parameters constant while increasing E_{CT} with respect to E_{opt} , the emergence of the $E_{\text{U}}^{\text{app}} = kT$ plateau at around 1.6 ± 0.1 eV can be reproduced.

In the absence of CT states, the above model predicts three sub-gap regimes of the $\alpha_{\text{LE}}(E)$ based on the dominant disorder mechanism as illustrated in Figure 6.8c. For photon energies close to the gap ($E > E_{\text{opt}} - \sigma_s^2/kT$), $E_{\text{U}}^{\text{app}}$ is dominated by Gaussian static disorder. In this regime, the absorption resembles a Gaussian-like shape, where the steepness close to the gap is determined by σ_s , causing a redshift of the effective energy gap with increasing σ_s . While $E_{\text{U}}^{\text{app}}$ does not directly represent σ_s at any energy, a positive correlation between $E_{\text{U}}^{\text{app}}$ and σ_s is observed in this regime Figure 6.11. A closer inspection suggests that $E_{\text{U}}^{\text{app}}$ is strongly energy dependent in this regime, scaling with σ_s as $E_{\text{U}}^{\text{app}}(E) \approx 2\sigma_s^2 / (E_{\text{X}} - E)$, for $\sigma_s < 4kT$, where E_{X} is a constant independent of E . This explains the previously reported correlation between morphological disorder and $E_{\text{U}}^{\text{app}}$ close to the absorption onset.^{171, 186–188}

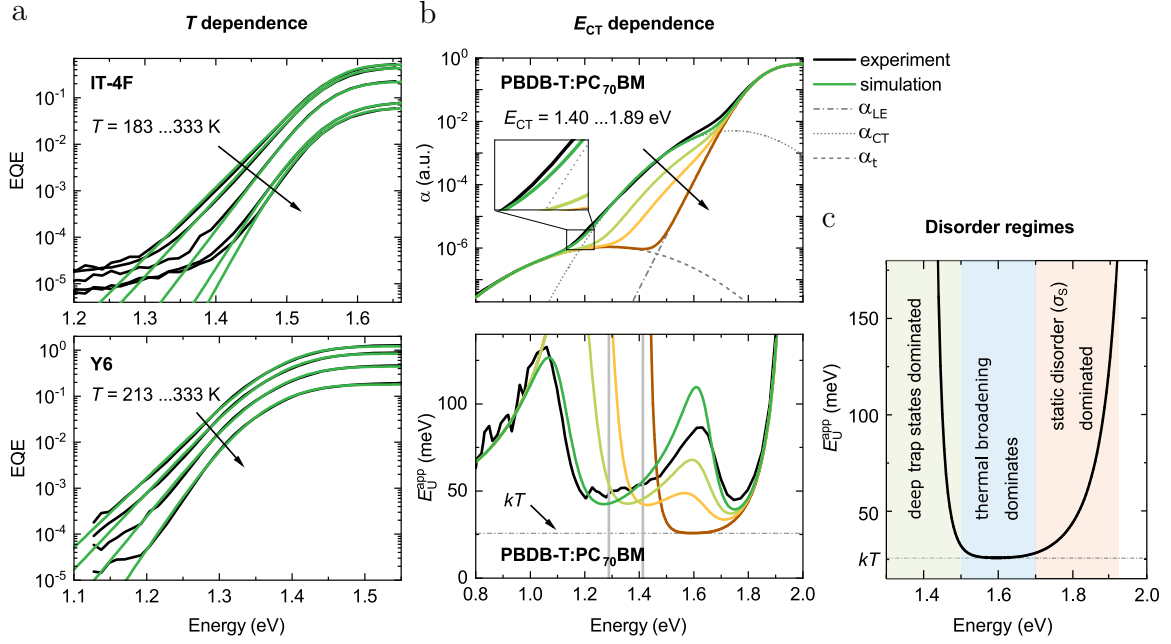


Figure 6.8: The sub-bandgap EQE as a function of T (a) and E_{CT} (b). Experimental (black lines) and simulated (green lines) sub-gap EQE spectra of IT-4F and Y6. The line-shape of the experimental sub-gap EQE of PBDB-T:PC₇₁BM can be described as the sum of LE absorption, CT state absorption, and trap state absorption: $\alpha = \alpha_{LE} + \alpha_{CT} + \alpha_t$, with α_{LE} given by Eq. 6.6 ($E_{opt} = 1.89$ eV, $\sigma_s = 60$ meV), while α_{CT} and α_t are determined from their respective Gaussian fits. In the experiment, E_U^{app} is well above kT , since $E_{opt} - E_{CT} > 0.3$ eV. Increasing E_{CT} in the simulation results in $E_U^{app} \rightarrow kT$ between 1.5 eV to 1.7 eV. c Schematic representation of the disorder regimes dominating α in the absence of CT absorption comprising (i) static disorder σ_s close to the band edge, (ii) thermal broadening, where $E_U^{app} = kT$, and (iii) deep trap state absorption well below the gap.

For $E < E_{opt} - \frac{\sigma_s^2}{kT}$, however, the exponential term in Eq. 6.6 eventually starts to dominate the spectral line shape of α_{LE} . In this regime, the sub-gap absorption of LEs is dominated by thermal broadening with $E_U^{app} \rightarrow kT$, thus becoming independent of σ_s . The transition between the static disorder dominated and the thermal broadening dominated regime depends on σ_s and the temperature. This was simulated for the two cases $\sigma_s = 70$ meV and $\sigma_s = 100$ meV as shown in Figure 6.11: For $\sigma_s = 70$ meV, E_U^{app} reaches kT at $\alpha(E)$ values 3 to 4 orders of magnitudes below α_{sat} , while this is 6 orders below α_{sat} for $\sigma_s = 100$ meV at room temperature. Finally, at energies well below the optical gap, $\alpha(E)$ eventually becomes dominated by deep trap state absorption, resulting in an artificial increase in E_U^{app} and a concomitant deviation from $E_U^{app} = kT$. Deep trap state absorption is typically observed 6 orders of magnitude below α_{sat} limiting the spectral range dominated by thermal broadening.

Based on these considerations, it is assumed that it is possible to observe $E_U^{app} \approx kT$ only when $\sigma_s < 100$ meV (see Figure 6.11). Other conditions that must be met are: (i) the neat phase absorption of one component is spectrally separated from the other neat phase absorption, as well as from the CT states and trap states; (ii) the dynamic range of the EQE (or α) measurement is sufficiently wide to measure photocurrent at wavelengths well below the absorption onset of the neat material ($E < E_{opt} - \frac{\sigma_s^2}{kT}$); and (iii) optical cavity effects are not significant. Exponential sub-gap EQE spectra previously reported in literature for BHJs often do not fulfill these requirements, explaining reported Urbach energies much larger than kT .

6.6 MODELLING THE SUB-GAP ABSORPTION COEFFICIENT

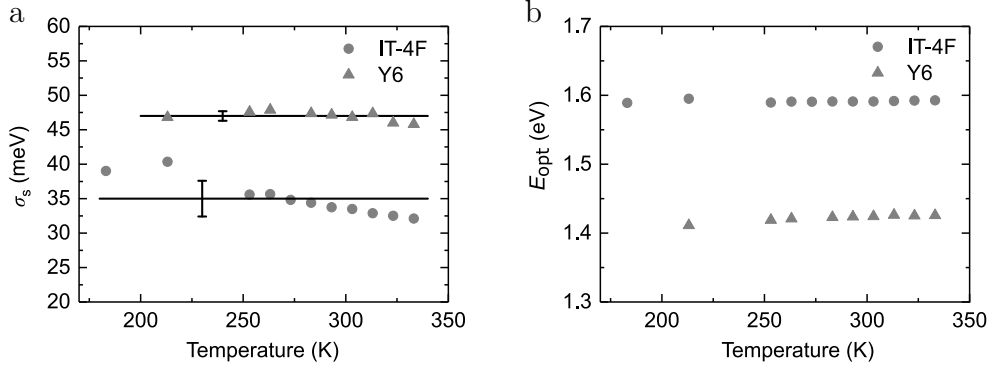


Figure 6.9: **a** Static disorder σ_s and **b** the exciton bandgap energy E_{opt} obtained as fit parameters from the simulated sub-gap absorption coefficient.

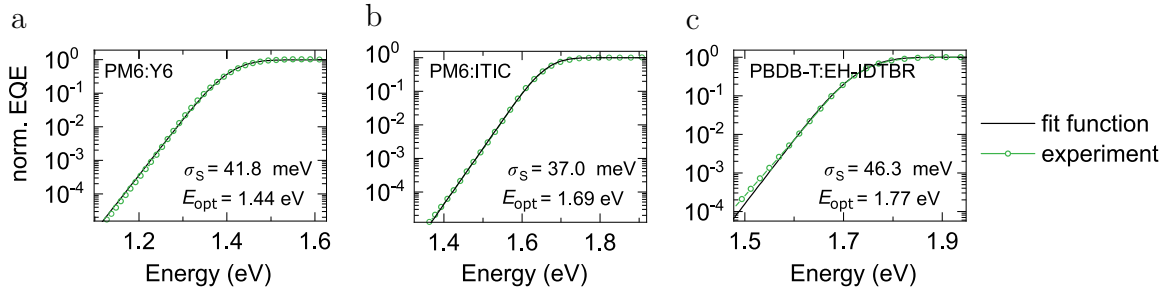


Figure 6.10: Normalized experimental (green lines) and simulated (black lines) EQE spectra measured at 303 K for the low-offset system D:A systems PM6:Y6 (a), PM6:ITIC (b) and PBDB-T:EH-IDTBR (c). Static disorder σ_s and the exciton band gap energy E_{opt} were obtained as fit parameters.

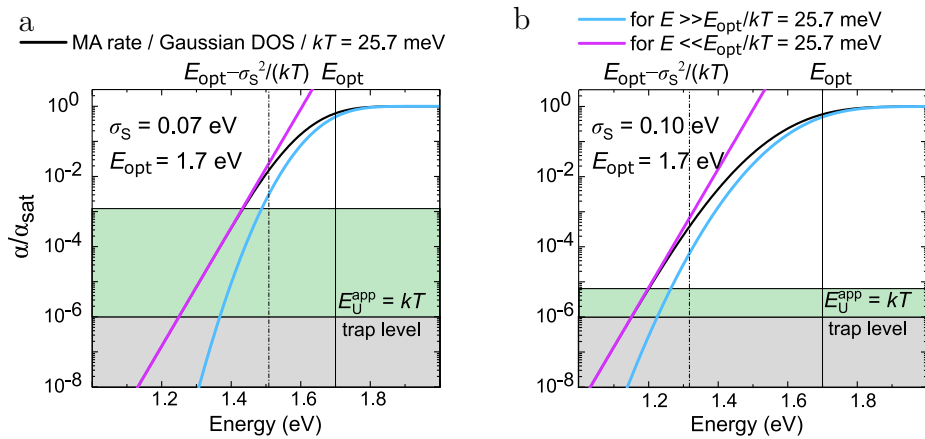


Figure 6.11: Absorption coefficient derived for MA-type rate and Gaussian DOS characterized by $E_{opt} = 1.7$ eV and $\sigma_s = 0.07$ eV (a) and $\sigma_s = 0.1$ eV (b) at room temperature. Purple and green colours indicate α in the limit of $E \ll E_{opt}$ and $E \gg E_{opt}$, respectively. For $E \ll E_{opt}$, α converges to an exponential function with a slope described by $E_U^{app} = kT$. For $E \gg E_{opt}$, α converges to 1 if normalized to α_{sat} . The larger σ_s , the more sensitive the EQE measurement must be to show that $E_U^{app} = kT$ at low energies. Roughly 6 to 7 orders of magnitude below α_{sat} , deep trap state absorption typically dominates the spectrum as shown experimentally. Hence, $E_U^{app} = kT$ cannot be observed experimentally for $\sigma_s \geq 0.1$ eV.

Importantly, the E_U^{app} spectra introduced here do not suffer from the short fitting ranges of previous of E_U measurements. In contrast, it was shown that an exponential distribution of tail states cannot explain the sub-gap spectral line-shape associated with singlet absorption, nor CT or trap state absorption in organic semiconductors.

6.7 Radiative Open-Circuit Voltage Losses

The presence of sub-gap absorption is known to induce radiative recombination losses additional to those predicted by Shockley and Queisser (SQ) approach. While the short-circuit current density (J_{SC}) remains largely unaffected, the presence of sub-gap absorption mainly translates into enhanced losses in the open-circuit voltage (V_{OC}). In general, the V_{OC} can be expressed as $V_{\text{OC}} = V_{\text{OC}}^{\text{SQ}} - \Delta V_{\text{OC}}^{\text{RAD}} - \Delta V_{\text{OC}}^{\text{NR}}$, where $V_{\text{OC}}^{\text{SQ}}$ represents the upper thermodynamic limit of the V_{OC} based on the SQ model, assuming perfect above-gap absorption and no sub-gap absorption. Furthermore, $\Delta V_{\text{OC}}^{\text{RAD}} = V_{\text{OC}}^{\text{SQ}} - V_{\text{OC}}^{\text{RAD}}$ is the radiative loss induced by sub-gap absorption, while $\Delta V_{\text{OC}}^{\text{NR}} = V_{\text{OC}}^{\text{RAD}} - V_{\text{OC}}$ is the non-radiative loss. Here, $V_{\text{OC}}^{\text{RAD}}$ is the radiative limit of the V_{OC} corresponding to the expected V_{OC} in the absence of non-radiative losses. In accordance with detailed balance, it is expected that $V_{\text{OC}}^{\text{RAD}} = kT/q \ln \left(\frac{J_{\text{SC}}}{J_0^{\text{RAD}}} + 1 \right)$, where $J_{\text{SC}} = q \int_0^\infty \text{EQE}(E) \phi_{\text{sun}}(E) dE$ and $J_0^{\text{RAD}} = q \int_0^\infty \text{EQE}(E) \phi_{\text{BB}}(E) dE$ is the dark saturation current density in the radiative limit; q is the elementary charge and ϕ_{sun} (ϕ_{BB}) the solar spectrum (black body spectrum).¹⁸⁹ The SQ limit ($V_{\text{OC}}^{\text{RAD}} = V_{\text{OC}}^{\text{SQ}}$) corresponds to the case when $\text{EQE} = 1$ for $E > E_{\text{opt}}$, while $\text{EQE} = 0$ for $E < E_{\text{opt}}$. Note that because of the different ideality factors, the contribution from deep trap states will be negligible under 1 sun conditions, as reported previously.⁸⁴

As shown in the above text, in low offset systems such as state-of-the-art NFA-based blends (or neat material systems), the CT absorption is mostly overshadowed by the stronger NFA absorption (or is absent). In such systems the sub-gap absorption tail is dominated by excitons ($\alpha = \alpha_{\text{LE}}$). The expected radiative limit $V_{\text{OC}}^{\text{RAD}}$ set by excitons can be calculated by assuming $\text{EQE} = \text{EQE}_{\text{max}} \times (\alpha_{\text{LE}} \alpha_{\text{sat}})$, with α_{LE} given by Eq. 6.6. The concomitant radiative loss $\Delta V_{\text{OC}}^{\text{RAD}}$, arising from the imperfect spectral line shape of α_{LE} (leading to deviations from the ideal box-like EQE shape), is shown in Figure 6.12a at different E_{opt} and σ_s . As shown, the voltage loss $\Delta V_{\text{OC}}^{\text{RAD}}$ increases with increasing σ_s . For example, when $\sigma_s = 100$ meV, $\Delta V_{\text{OC}}^{\text{RAD}}$ is larger than 0.2 V. Furthermore, at large σ_s , the voltage loss becomes more prominent at larger E_{opt} . Those losses are caused by a drastic increase in J_0^{RAD} , while J_{SC} is essentially unchanged. As σ_s is reduced, in turn, $\Delta V_{\text{OC}}^{\text{RAD}}$ is correspondingly decreased. For small static disorder (i.e., small σ_s), an analytical approximation relating $\Delta V_{\text{OC}}^{\text{RAD}}$ and σ_s can be obtained as

$$q\Delta V_{\text{OC}}^{\text{RAD}} \approx \frac{\sigma_s^2}{2kT} + kT \ln \left(\frac{E_{\text{opt}}}{3kT} \left[1 - \left(\frac{\sigma_s^2}{2E_{\text{opt}}kT} \right) \right]^3 \right). \quad (6.7)$$

A good agreement between Eq. 6.7, as indicated by the dashed lines in Figure 6.12a, and the full simulation was indeed obtained for small σ_s . Importantly, even in the limit of vanishing static disorder, $\sigma_s \rightarrow 0$, a voltage loss ΔV_{OC}^{RAD} of roughly 70 meV to 80 meV is expected due to non-vanishing sub-gap absorption induced by thermal broadening. Based on the E_{opt} and σ_s extracted (Figure 6.10) for the low-offset D:A systems PM6:Y6 ($E_{opt} = 1.44$ eV, $\sigma_s = 42$ meV), PM6:ITIC ($E_{opt} = 1.69$ eV, $\sigma_s = 37$ meV) and PBDB-T:EH-IDTBR ($E_{opt} = 1.77$ eV, $\sigma_s = 46$ meV), the radiative voltage loss induced by sub-gap absorption can be estimated. Subsequently, ΔV_{OC}^{RAD} is 108 mV for PM6:Y6, 107 mV for PM6:ITIC and 120 mV for PBDB-T:EH-IDTBR. In the absence of CT absorption, the corresponding would-be ΔV_{OC}^{RAD} for PBDB-T:PC₇₁BM is 150 mV.

Finally, Figure 6.12b shows the corresponding effect of σ_s on the radiative limit of the PCE, assuming $\text{EQE}_{max} = 1$ (and ideal charge collection). Compared to the SQ limit of the PCE (indicated by black solid line), the presence of the sub-gap absorption results in a PCE peak loss of around 1.5 % for $\sigma_s = 0$. For $\sigma_s \neq 0$, the radiative PCE limit is further lowered, with the PCE peak decreasing with increasing σ_s . Hence, to minimize ΔV_{OC}^{RAD} , and thus maximize PCE, it is important to minimize σ_s . However, an unavoidable radiative loss, relative to the SQ limit, will still be present due to thermal broadening. Based on those findings, this loss is inherent to all organic solar cells, and needs to be taken into account in low offset systems where excitons dominate the sub-gap absorption.

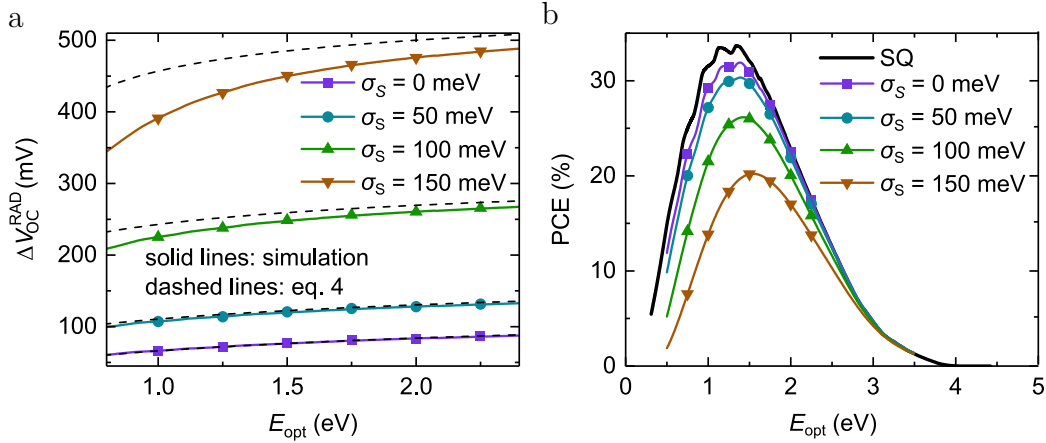


Figure 6.12: The radiative V_{OC} loss induced by sub-gap absorption and associated radiative PCE limit of low-offset D:A solar cells. **a** The radiative voltage loss ΔV_{OC}^{RAD} as a function of the optical bandgap for varying degree of Gaussian static disorder σ_s , assuming the sub-gap absorption dominated by LEs as per eq. 3 (solid lines with symbols). The corresponding analytical approximation (Eq. 6.7) is represented by the dashed lines. **b** The corresponding radiative PCE limit based on Eq. 6.6, assuming $\text{EQE}_{max} = 1$ and ideal charge collection, is shown (solid lines with symbols). For comparison, the SQ limit, representing the ideal case with no sub-gap absorption, is included as indicated by the black solid line. The PCE decreases with respect to the SQ limit as σ_s increases. The SQ limit is not expected to be reached even for vanishing σ_s due to the thermal broadening.

6.8 Conclusions

In summary, the exciton sub-gap absorption in organic semiconductors is dominated by Gaussian static disorder near the onset, while thermal broadening dominates at lower photon energies. Furthermore, for a large number of organic semiconductors, the

Urbach energy in the sub-gap absorption regime is dominated by thermal broadening that equals the thermal energy kT within the variations caused by the optical interference. While exponential absorption tails have been previously observed mainly in non-fullerene systems, it is shown that this property is universal for organic semiconductors and consistent with a Gaussian density of excitonic states undergoing Boltzmann-like thermally activated optical transitions. The static disorder is shown to arise from the width of the Gaussian DOS and to broaden the absorption onset at energies close to the optical gap. Using a model for the sub-gap excitonic absorption tail, it is possible to discriminate spectral regimes dominated by static disorder (where the Urbach energy is strongly dependent on the energy) and thermal broadening ($E_U = kT$), as well as to reproduce the temperature dependence of absorption coefficient due to excitons. This modified view of the sub-gap absorption coefficient in disordered organic semiconductors clarifies a long-standing debate concerning the shape of the DOS and the relevance of an Urbach description in these important and intriguing materials.

Chapter 7

Intrinsic Detectivity Limits of Organic Near-Infrared Detectors

Organic photodetectors (OPDs) with a performance comparable to that of conventional inorganic ones have recently been demonstrated for the visible regime. However, near-infrared photodetection has proven to be challenging. To date, the true potential of organic semiconductors in this spectral range (800 to 2500 nm) remains largely unexplored. In this chapter, it is shown that the main factor limiting the specific detectivity (D^) is non-radiative recombination, which is also known to be the main contributor to open-circuit voltage losses. The relation between open-circuit voltage, dark and noise current is demonstrated using four bulk heterojunction devices based on narrow-gap donor polymers. Their maximum achievable D^* is calculated alongside a large set of devices to demonstrate an intrinsic upper limit of D^* as a function of the optical gap. It is concluded that OPDs have the potential to be a useful technology up to 2000 nm, given that high external quantum efficiencies can be maintained at these low photon energies. The following chapter is written based upon a collaborative work of the authors published in Advanced Materials in 2020. S. Gielen fabricated the photodiodes. S. Gielen and C. Kaiser performed the device characterisation and data analysis. S. Gielen and F. Verstraeten synthesized the low-gap donor materials. P. Verstappen and W. Maes provided leadership on topics of material synthesis and characterisation. J. Kublitski, J. Benduhn and D. Spoltore supported this project with IV data and electroluminescent external quantum efficiency spectra of other low-gap organic OPDs. P. Meredith, A. Armin, K. Vandewal provided the overall leadership to this project.*

S. Gielen, C. Kaiser, F. Verstraeten, J. Kublitski, J. Benduhn, D. Spoltore, P. Verstappen, W. Maes, P. Meredith, A. Armin, K. Vandewal, *Intrinsic Detectivity Limits of Organic Near-Infrared Photodetectors*, Adv. Mater. **32**, 2003818 (2020).

7.1 Current-Voltage Characteristics of Narrow-gap Photodiodes

In the work detailed in this chapter, four different NIR-photoactive narrow-gap donor polymers were investigated in a photodiode architecture. The donor polymers comprise PTTBAI, PBTQ(OD), PTTQn(HD) and PTTQ(HD) with the chemical structures depicted in Figure 7.1a. D:A blends with PC₇₁BM as acceptor A formed the active layer of photodiodes with the structure: glass/ITO/ZnO-PEIE/active layer/MoO₃/Ag. Using cyclic voltammetry (CV), their frontier orbital energy levels were estimated as illustrated in Figure 7.1b. Moreover, solution and thin-film absorbance spectra were recorded via an optical spectrophotometer as reproduced in Appendix C.1. Absorbance spectra suggest low optical gaps for the studied polymers (< 1.5 eV), whereas CV estimates the effective bandgaps (E_{CT}) of the organic D:A blends between 0.81 and 1.12 eV. Consequently, the photodiodes show open-circuit voltages between 0.12 and 0.44 V measured under high intensity radiation (100 mW/cm) in accordance to the previously reported linear relationship between E_{CT} and V_{OC} .⁶² For such low effective gaps, it is expected that the dark saturation current I_0 becomes comparable or higher than the shunt current I_{shunt} , which typically dominates the dark current I in organic D:A blends optimized for photovoltaic applications.

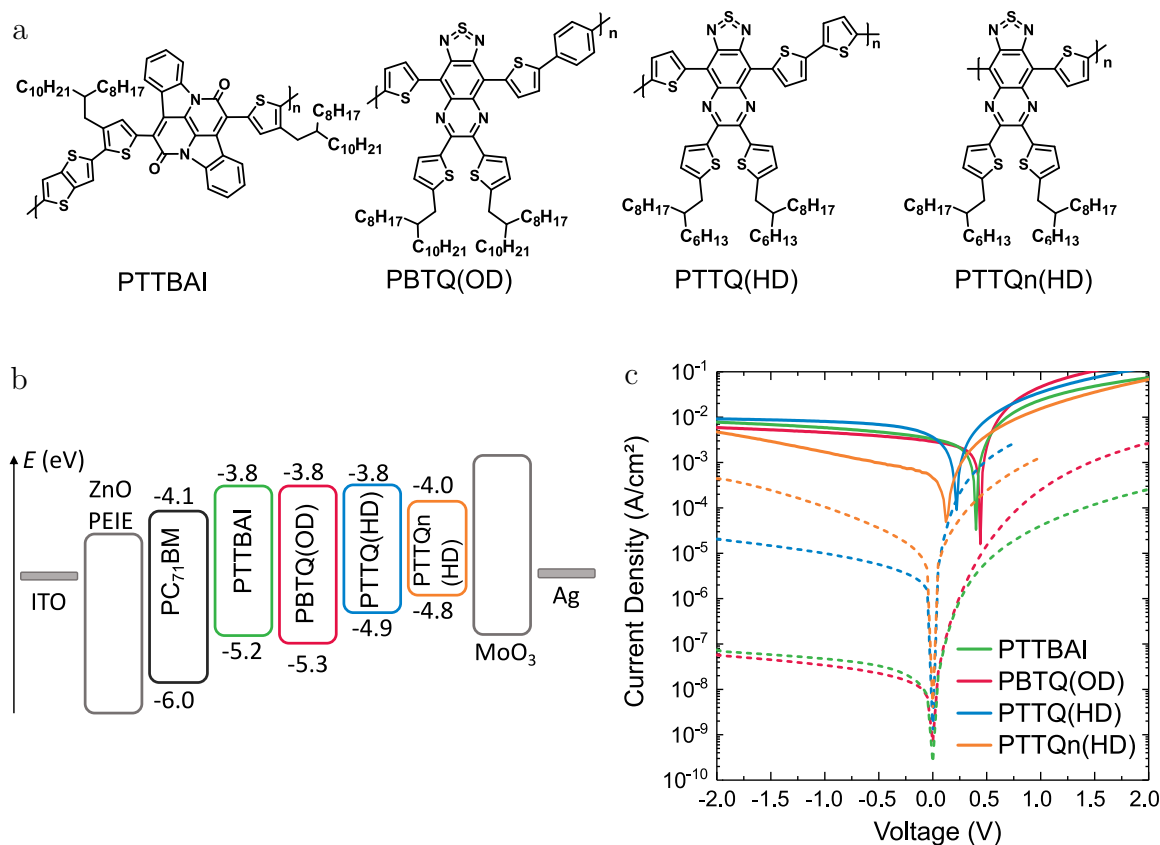


Figure 7.1: **a** Chemical structures of the four NIR absorbing donor polymers. **b** Energy level diagram displaying the different layers used in the inverted OPD device stack. The frontier orbital energy levels are estimated by CV. **c** J/V curves for the OPD devices (solid lines: light current under 1 sun illumination; dashed lines: dark current).

7.1 CURRENT-VOLTAGE CHARACTERISTICS OF NARROW-GAP PHOTODIODES

Assuming that the dark current in the narrow-gap photodiodes can be described as the sum of Shockley diode equation (band-to-band recombination) and shunt current (parasitic leakage in the bulk), a fit to the dark $J - V$ curves (see Figure 7.1c) was attempted using

$$I_D = I_0 \left[e^{\frac{qV}{kT}} - 1 \right] + I_{\text{shunt}} \quad (7.1)$$

and returning I_0 (and R_{shunt}) as a fit parameter. Importantly, in Chapter 8 it will be shown that not band-to-band recombinations are the dominant recombination, but recombination via mid-gap traps. Therein, temperature dependent $J - V$ measurements prove that the thermal activation energy equals half the bandgap at small reverse bias, and hence, I_{shunt} can be neglected at $V \leq -0.1$ V. Note that for a band-to-band recombination dominated process, the thermal activation energy would equal exactly bandgap energy. Irrespective of the dominant recombination process, the experimental V_{OC} differs at maximum 0.06 V from the calculated V_{OC} using the fit parameter I_0 . Table 7.1 displays the obtained fit parameters, as well as the experimental and calculated V_{OC} . If $I_D \approx I_0$ at sufficiently low reverse bias, the V_{OC} and the ratio I_{SC}/I_D are expected to be logarithmically related according to

$$V_{\text{OC}} = \frac{kT}{q} \ln \left[\frac{I_{\text{SC}}}{I_0} + 1 \right], \quad (7.2)$$

which is obtained from the Shockley diode in the dark and at $V = V_{\text{OC}}$ neglecting parasitic currents (see Chapter 2.3.2 for reference). Indeed, a linear relation between V_{OC} (at $V_{\text{OC}} < 0.25$ V) and I_{SC}/I_D on a semi-logarithmic scale was observed for the studied narrow-gap D:A blends and a large set of literature-reported blends as shown in Figure 7.2. A list with the literature-reported D:A blends and the respective data set is provided in Appendix C.3. Since I_D can only be $I_D \geq I_0$, the points in Figure 7.2a are either very close to the intrinsic limit, i.e., within the experimental error, or well above, but cannot be significantly below. For $V_{\text{OC}} < 0.25$ V, the experimentally measured dark current is limited to $I_D < 25 I_0$. For higher voltages, I_{SC}/I_D increasingly deviates from the intrinsic limit, due to the increasing contribution of I_{shunt} . For $V_{\text{OC}} = 1$ V, I_D is typically 12 orders of magnitude higher than I_0 . Note that the I_D used in Figure 7.2a was evaluated at -0.1 V for all D:A blends to reduce the influence of additional shunt currents. However, if devices are not fully optimized, and hence show some leakage, I_{SC}/I_D cannot be close to the intrinsic limit set by the V_{OC} .

Table 7.1: Device performance parameters for the photodiodes with the studied narrow-gap D:A blends. R_{shunt} , I_0 were obtained from the fits to the experimental dark currents in reverse bias using Eq. 7.1 under the assumption of band-to-band recombination is the dark recombination mechanism. I_{SC} is the experimental photocurrent under short-circuit conditions. The V_{OC} was calculated via Eq. 7.2 showing only small offset from the experimental V_{OC} .

Material	R_{shunt} in Ω	I_0 in A	I_{SC} in A	experimental V_{OC} in V	calculated V_{OC} in V
PTTBAI	7.90e8	3.42e-10	2.90e-4	0.40	0.35
PBTQ(OD)	1.07e9	2.90e-10	2.20e-4	0.44	0.35
PTTQ(HD)	3.37e6	4.49e-8	3.40e-4	0.22	0.23
PTTQN(HD)	4.54e5	3.78e-8	4.00e-5	0.12	0.18

In agreement with previous literature, a linear relationship between E_{CT} and I_D was observed, but only for $E_{CT} < 0.9$ eV, as shown in Figure 7.2b. This agrees with V_{OC} values up to 0.25 V, since the offset observed between the V_{OC} and the E_{CT}/q in organic D:A blends is typically around 0.6 V to 0.7 V. From the trend shown in Figure 7.2b, the minimum achievable I_D can be estimated for a given material system with known E_{CT} . Moreover, it confirms that the fitting procedure of extracting I_0 from I_D is reasonable only in the case of low E_{CT} blends. From the above it is clear that the lowest achievable dark current, I_0 , at reverse voltages is set by the V_{OC} . Devices with an E_{CT} and an optical gap smaller than 0.9 eV (≈ 1380 nm) approach this limit.

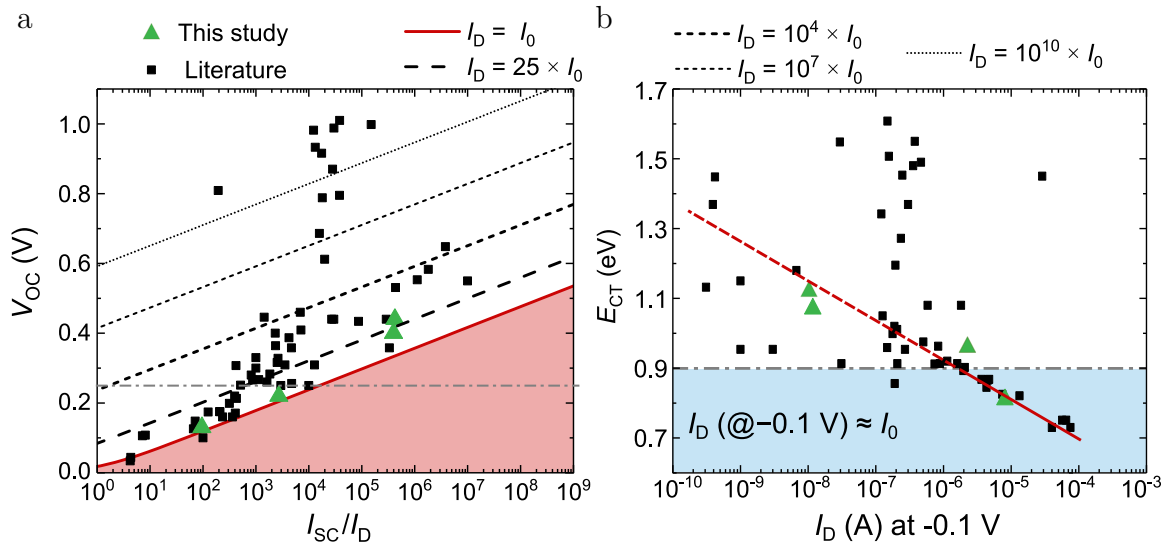


Figure 7.2: **a** Experimental V_{OC} as a function of the ratio I_{SC} to I_D on a semi-logarithmic scale. The green symbols represent the narrow-gap D:A blends and the respective devices, while the black symbols represent a set of literature reported D:A blends (all fullerene-based devices, additional information in Appendix C.3). The red solid line marks the lower thermodynamic limit of the dark current. **b** E_{CT} as a function of I_D (at -0.1 V) for the devices studied in this work (green symbols) and some reported D:A blends (black symbols). For devices with $E_{CT} < 0.9$ eV, I_D is close to I_0 if the device structure is optimized. The red solid line marks the region in which $I_D(-0.1 \text{ V}) \approx I_0$. In the region of the red dashed line, no correlation between E_{CT} and $I_D(-0.1 \text{ V})$ was found.

7.2 Specific Detectivity of Narrow-gap Photodiodes

As presented earlier in Section 2.3.4, the specific detectivity D^* is either obtained from the ratio of responsivity (R) to noise current (i_{noise}) according to

$$D^* = \frac{R\sqrt{A\Delta f}}{i_{\text{noise}}}, \quad (7.3)$$

or directly from the noise equivalent power (NEP) via

$$D^* = \frac{\sqrt{A\Delta f}}{\text{NEP}}. \quad (7.4)$$

D^* is always normalized to the square root of the area (A) multiplied by the bandwidth (Δf).¹⁹⁰ So far, it was shown in this chapter that for a given E_{CT} and V_{OC} , there is a theoretical upper limit for the ratio $I_{\text{SC}}/I_{\text{D}}$ that decreases with decreasing E_{CT} and V_{OC} . Known factors, preventing the V_{OC} being closer to the optical gap in organic D:A blends, will also affect the maximum achievable D^* . One can arrive to the same conclusion analytically when expressing R by the ratio I_{SC}/I_0 as shown in the following. In the radiative limit, the photocurrent I_{SC} is described as

$$I_{\text{SC,R}} = q \int_{E_{\text{g}}}^{\infty} \text{EQE}_{\text{PV}}(E) \phi_{\text{sun}}(E) dE, \quad (7.5)$$

where $\phi_{\text{sun}}(E)$ is the solar spectrum. Since $\text{EQE}_{\text{PV}} = RE/q$, the responsivity can be expressed as

$$R(E) = \frac{I_{\text{SC,R}}(E)}{dE} \frac{1}{\phi_{\text{sun}}(E)E}. \quad (7.6)$$

In accordance to Eq. 7.3, the D^* can be written as

$$D^*(E) = \frac{I_{\text{SC,R}}(E)}{dE} \frac{\sqrt{A\Delta f}}{q\phi_{\text{sun}}(E)E} \times (i_{\text{noise}})^{-1}. \quad (7.7)$$

For a resolution bandwidth Δf of 1 Hz and assuming that shot noise component is the dominant noise contribution, i.e. $i_{\text{noise}} = \sqrt{2qI_0}$, Eq. 7.8 can be rewritten as

$$D^*(E) = \frac{I_{\text{SC,R}}(E)}{dE} \frac{\sqrt{A}}{q\phi_{\text{sun}}(E)E} \times (2qI_0)^{-0.5}. \quad (7.8)$$

$dI_{\text{SC,R}}(E)/d(E)$ equals the photocurrent measured under illumination with a laser source that emits at a photon energy E with intensity $\phi_{\text{sun}}(E)$. According to Eq. 7.8, D^* is proportional to $I_{\text{SC}}/\sqrt{I_0}$. To obtain D^* according to Eq. 7.3, R is first calculated from the experimental EQE_{PV} according to $R = \text{EQE}_{\text{PV}} \times \lambda/1240$. As an example, Figure 7.3a shows the responsivity spectrum of the PTTQ(HD) based photodiode under 0 V, and -1 V and -2 V reverse bias. As expected, R increases with applied

reverse bias due to improving charge collection and charge dissociation efficiencies. Moreover, the experimental i_{noise} spectra are measured with the spectrum analyser and reproduced in Figure 7.3b for the same photodiode. It is shown that, independent of the voltage, i_{noise} increases strongly for frequencies below 200 Hz. Since most commercial photodetectors are operated at a couple kHz up to MHz regime (while avoiding flicker noise dominated frequencies), it is useful to consider an experimental frequency range between 1 kHz to 3 kHz. The upper frequency limit is typically imposed by the bandwidth of the low-noise current amplifier at a specific gain setting. The voltage dependence of i_{noise} shown in Figure 7.3b will be discussed later on in the text.

Next, the experimental D^* is determined from the experimental R and i_{noise} using Eq. 7.3. This method assumes that the current response of the device will decrease linearly with light power until it vanishes in the current noise. To verify this assumption, D^* is also calculated from the NEP according to Eq. 7.4 as a second method for experimentally obtaining D^* . Herein, the light power of a 520 nm laser diode is gradually decreased, while measuring the respective photocurrent as described in Section 3.8. A graphical representation is shown in Figure 7.4a and b of the photodiodes PTTBAI:PC₇₁BM and PBTQ(OD):PC₇₁BM, respectively, demonstrating a linear dynamic range of 180 dB for the PBTQ(OD) photodiode. D^* from the NEP and from the R are compared in Figure 7.4c and d at 0 V applied bias. Herein, both methods for obtaining D^* were found to be in good agreement differing only by a factor of 1.6 and 2.6 for PBTQ(OD) and PTTBAI, respectively.

To calculate the upper limit of D^* , i_{noise} was regarded as the root-mean-square (RMS) value over its most dominant components in the high-frequency limit, namely shot (i_{shot}) and thermal noise (i_{thermal}):

$$i_{\text{total}} = \sqrt{\langle i_{\text{shot}}^2 \rangle + \langle i_{\text{thermal}}^2 \rangle}. \quad (7.9)$$

i_{shot} and i_{thermal} can be calculated for any current I , since they reflect random fluctuation of I in time around its mean value and show no frequency dependence. The thermal noise depends on the resistance, R' , of the device via $i_{\text{thermal}} = \sqrt{4\Delta f kT/R'}$

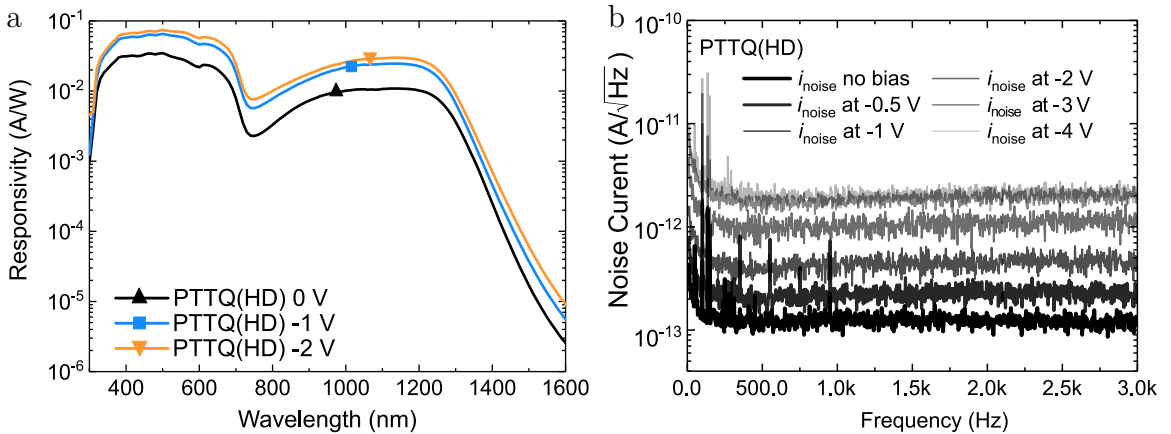


Figure 7.3: **a** Spectral responsivity of the PTTQ(HD):PC₇₁BM photodiode at 0, −1 and −2 V applied voltage. **b** Measured noise current as a function of the frequency and applied reverse bias for the PTTQ(HD):PC₇₁BM based photodiode.

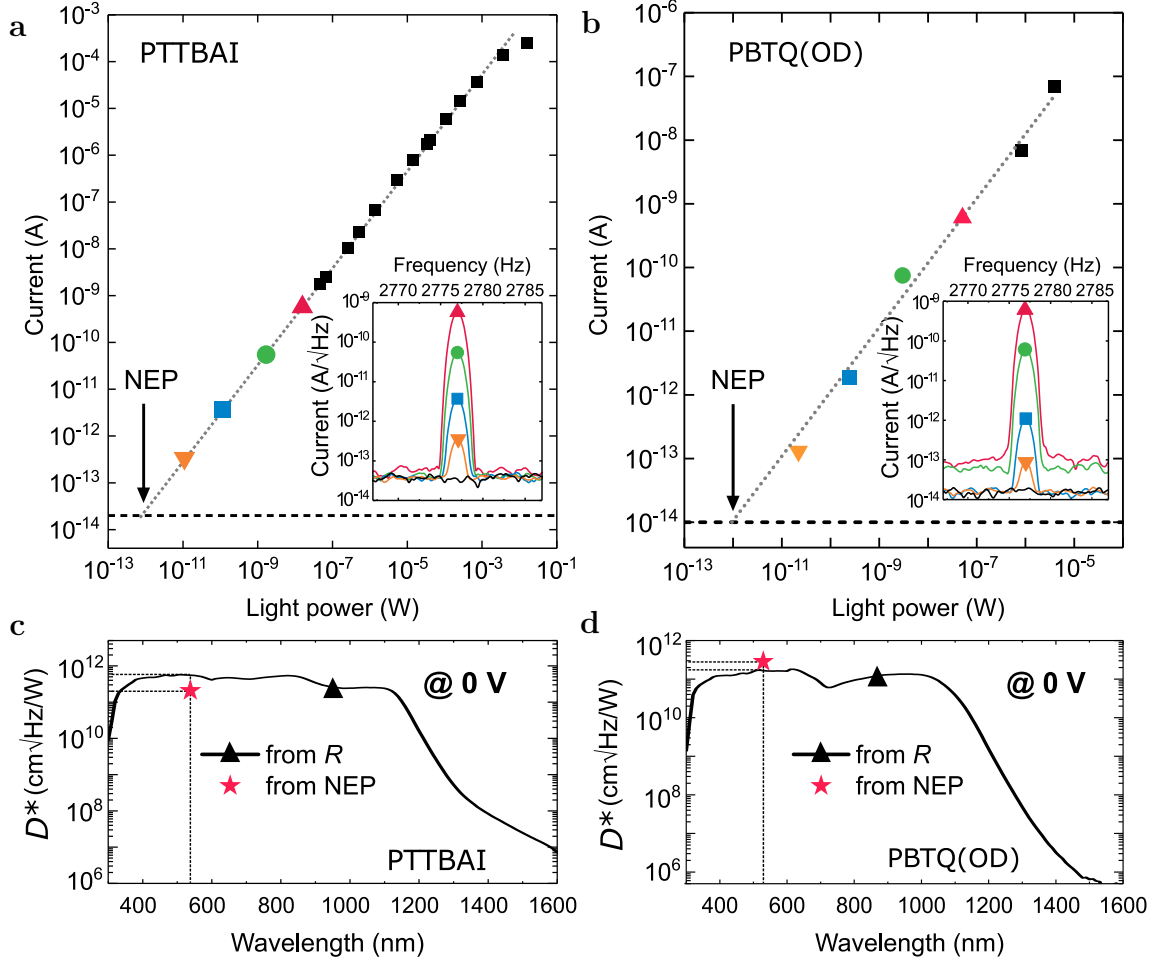


Figure 7.4: Linear dynamic range (photocurrent in function of light intensity) measured at 1 Hz bandwidth and 0 V voltage for the PTTBAI (a) and PBTQ(OD) (b) based photodiodes. Extrapolation of the LDR into the noise floor marks the NEP from which D^* was obtained at 0 V bias. The different colours mark different light intensities for which the current response as a function of frequency is shown in the inset. The frequency at the maximum response is incident with the modulation frequency of the laser diode. D^* obtained from the NEP and the R photodiodes are in good agreement for the PTTBAI (c) and PBTQ(OD) (d) based photodiodes.

and therefore shows no voltage dependence. The shot noise scales with the signal magnitude via $i_{\text{shot}} = \sqrt{2q\Delta f I}$ and therefore shows strong voltage dependence.⁵ More information on the different sources of noise is provided in Section 2.3.3. The total i_{noise} can now be calculated in two limits: (i) $I = I_0$, representing the lower theoretical limit of i_{noise} , and (ii) $I = I_D$, as often performed in literature in the absence of experimental noise current measurements. Figure 7.5 illustrates the calculated noise currents for all narrow-gap photodiodes as a function of voltage alongside the average value of the experimental noise current in the frequency range between 1 and 3 kHz. Note that the thermal noise is independent of whether $I = I_0$ or $I = I_D$ is assumed, however, it is the dominant noise source at low reverse voltage (typically for $|V| < 0.1$ V). Moreover, the experimental noise current is mostly above the calculated one, since Eq. 7.9 does not account for all noise sources (which are known to exist but not well described) and experimental limitations imposed by the amplifier noise. Consequently, the experimental D^* is expected to be lower than the calculated one according to Eq. 7.3.

In the next step, D^* was calculated at -2 V in the two limits: (i) $I = I_0$, which marks the upper thermodynamic limit, and (ii) assuming $I = I_D$, as often performed in literature^{118,191}. Figure 7.6 shows that at -2 V, the experimental D^* and the calculated D^* assuming $I = I_D$ are typically in good agreement (less than a factor 2 difference) except for the PTTQn(HD) based photodiode, where the difference is a factor 20. At the same time, it can be seen that the measured noise current increases much faster with reverse bias than expected from the shot noise component of I_D (cf. Figure 7.5). In conclusion, three out of material narrow-gap photodiode had an optimized device architecture and work close to the upper thermodynamic limit of D^* imposed by the active layer blend and its V_{OC} . For those photodiodes, D^* calculated from the shot noise component of I_D represents a sufficient approximation for the experimental D^* obtained from the measured noise current and responsivity, or from the NEP.

7.2 SPECIFIC DETECTIVITY OF NARROW-GAP PHOTODIODES

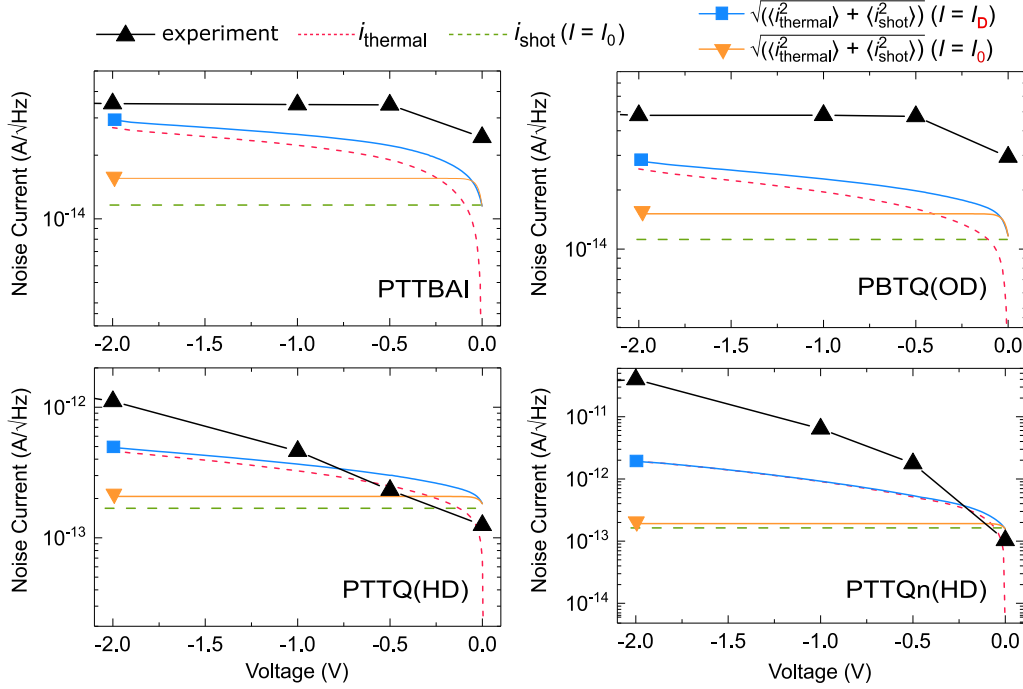


Figure 7.5: Experimental and calculated noise for the narrow-gap photodiodes as a function of voltage. The experimental noise current (black marker) is the RMS noise current at frequencies between 1 kHz to 3 kHz. The noise current calculated from the measured dark current (blue marker) or from the dark saturation current (orange marker). Below -1.0 V, the total calculated noise current is dominated by shot noise (red dashed line), and above -0.1 V by thermal noise (green dashed line).

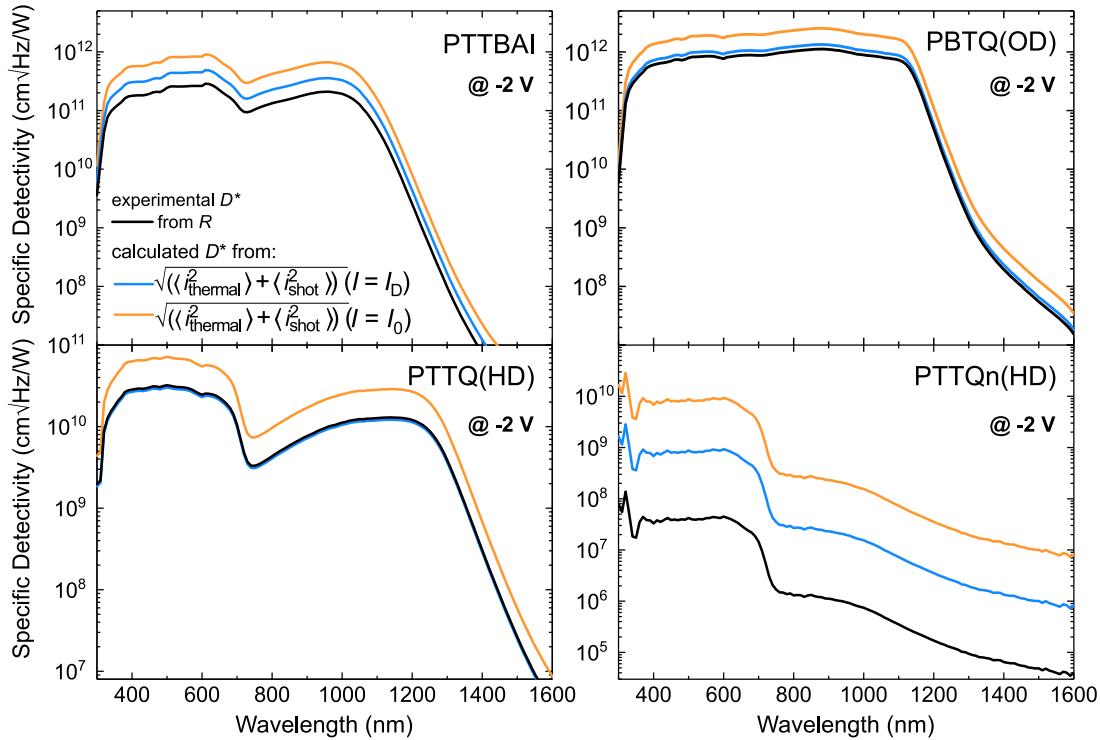


Figure 7.6: Experimental and calculated specific detectivity (D^*) for the studied narrow-gap photodiodes evaluated at -2 V. Experimental D^* obtained from the measured noise spectral density and the responsivity R at -2 V. Calculated D^* in the two limits $I = I_0$ and $I = I_D$, assuming that the total noise current can be described by the RMS value of shot noise and thermal noise.

7.3 Intrinsic Non-radiative Voltage Losses

As discussed in Section 2.3.2, the dark saturation current I_0 is comprised of a radiative and a non-radiative component $I_0 = I_{0,R} + I_{0,NR}$. $I_{0,R}$ can be calculated via

$$I_{0,R} = q \int_0^\infty \text{EQEPV}(E) \phi_{\text{BB}}(E) dE. \quad (7.10)$$

$\phi_{\text{BB}}(E)$ is the temperature dependent black body spectrum as discussed in Section 2.3.4. In the radiative limit ($I_0 = I_{0,R}$), the upper limit of the V_{OC} ($V_{\text{OC},R}$) is obtained via Eq. 7.2. The difference between $V_{\text{OC},R}$ and the experimental V_{OC} equals the non-radiative voltage losses ($V_{\text{OC},NR} = V_{\text{OC},R} - V_{\text{OC}}$). Figure 7.7a shows $\Delta V_{\text{OC},NR}$ for a large set of D:A blends with different E_{CT} , including the devices studied here. Clearly, $\Delta V_{\text{OC},NR}$ depends on E_{CT} . An increase of $\Delta V_{\text{OC},NR}$ by 300 mV is observed when E_{CT} decreases from 1.6 to 0.8 eV. As a next step, $I_{0,NR}$ was obtained from $\Delta V_{\text{OC},NR}$ via

$$\Delta V_{\text{OC},NR} = kT/q \ln(\text{EQE}_{\text{EL}}^{-1}) \quad (7.11)$$

where $\text{EQE}_{\text{EL}}^{-1} = (I_{0,R} + I_{0,NR})/I_{0,R}$.^{148,192} Table 7.2 summarizes the device parameters related to non-radiative losses for the devices studied in this work. Since $I_{0,NR} \gg I_{0,R}$, the dark saturation current will be dominated by the non-radiative recombination current and it can be assumed that $I_0 = I_{0,NR}$.

Next, the effect of $I_{0,NR}$ on the D^* is studied in comparison to a background limited infrared photodetector (BLIP), which was discussed in Section 2.3.4. Figure 7.7b shows D^* of a BLIP at 300 K for different optical gap energies corresponding to wavelengths up to 2 μm . By lowering the optical gap, D^* decreases down to 5×10^{13} Jones at 2 μm , which marks the thermodynamic limit of D^* for any type of photodetector without photo-multiplicative gain ($\text{EQEPV} \leq 1$). For organic D:A blends, the EQEPV is below 1 and has a strong spectral dependence as well as sub-gap features, which will increase $I_{0,R}$ in comparison to the step-like EQEPV example and hence decrease D^* . As deduced earlier from the V_{OC} losses, the total dark saturation current is dominated by the non-radiative component $I_{0,NR}$. A realistic upper limit for the achievable D^* for organic NIR OPDs can therefore be obtained by considering $I_{0,NR}$ and a box-shaped EQEPV that is 1 for energies above E_{CT} . First, $I_{0,NR}$ is considered to be independent of E_{CT} and thus constant across the spectrum and corresponding to realistic EQE_{EL} values between 10^{-3} to 10^{-9} . As shown in Figure 7.7b, D^* decreases by one order of magnitude across the spectrum for a decrease of EQE_{EL} by two orders of magnitude (corresponding to an increase of $I_{0,NR}$ by two orders).

In literature, high frequency molecular vibrations were previously identified as the source of the rather large non-radiative decay rates in organic D:A blends,⁶² explaining the experimentally observed dependence of $I_{0,NR}$ on E_{CT} . Below, three different cases for $\Delta V_{\text{OC},NR}$ as a function of E_{CT} are distinguished: (i) a model-based lower limit for $\Delta V_{\text{OC},NR}$ reported by Azzouzi et al.,¹⁴⁸ (ii) an empirical lower limit for $\Delta V_{\text{OC},NR}$ reported by Benduhn et al.,⁶² and (iii) an average value for $\Delta V_{\text{OC},NR}$ as a function of E_{CT} as observed in this work. While case (i) predicts an upper limit for D^* to about

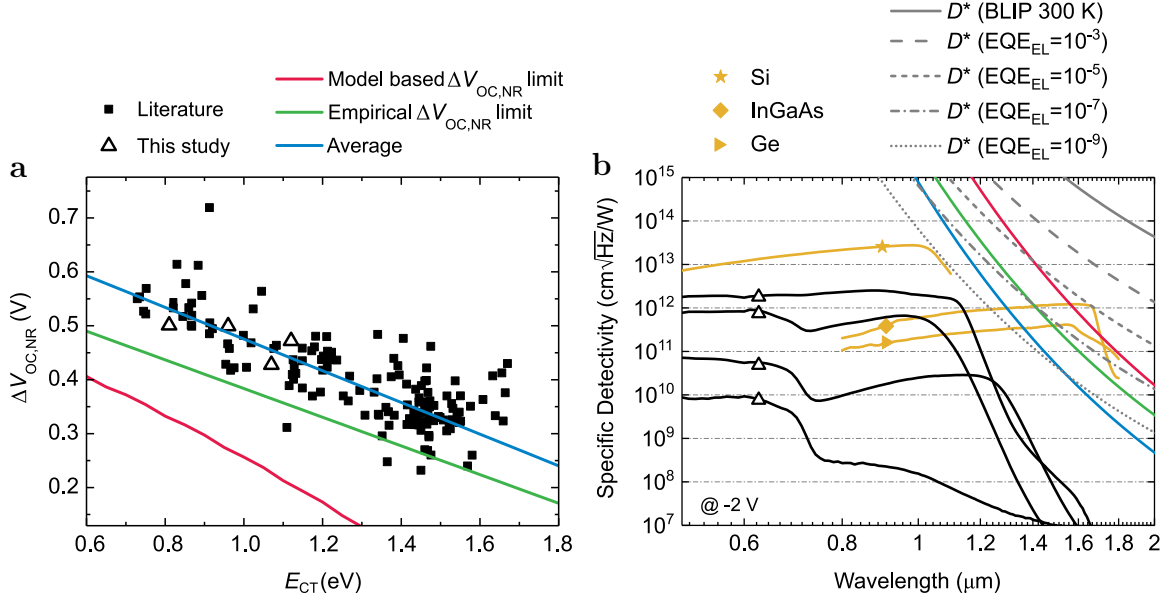


Figure 7.7: **a** $\Delta V_{OC,NR}$ as a function of E_{CT} for D:PC₇₁BM blends studied in this work (hollow triangles) and literature reported D:A blends (black squares) which are reproduced in Appendix C.3.⁶² The red line represents a model based lower limit¹⁴⁸ (Azzouzi et al.), the green line shows a previously reported (Benduhn et al.) empirical lower limit⁶² to $\Delta V_{OC,NR}$ and the blue line shows an average value for $\Delta V_{OC,NR}$ as observed in this study.⁶² **b** Specific detectivity as a function of wavelength. The black lines with hollow triangles represent the D^* for D:PC₇₁BM blends studied in this work. The upper limit of the D^* is calculated for different contributions of non-radiative recombination currents (represented as EQE_{EL} values according to Eq. 7.11) to the dark current ranging from zero (solid grey line: BLIP at 300 K) to very high ($\text{EQE}_{EL} = 10^{-9}$). The coloured lines represent the upper limit of the D^* determined from the models used in (a). The D^* of commercial photodiodes¹⁹³ (orange lines) are added for comparison.

10^{10} Jones at $2\mu\text{m}$, the empirical and average cases (ii) and (iii) predict that OPDs based on materials with similar recombination properties, as the ones studied here, will typically not reach more than 10^9 Jones at $2\mu\text{m}$. At the same time, D^* is expected to reach a respectable 10^{12} Jones at 1500 nm if the EQE_{PV} can approach 1. This value is comparable to commercial InGaAs detectors and even surpasses commercial Ge detectors (Figure 7.7).¹⁹³ Importantly, the upper limit of D^* decreases significantly faster for models where $I_{0,NR}$ is dependent on E_{CT} than if it is not. Hence, further red-shifting the absorption to the mid-infrared ($2\mu\text{m}$ to $10\mu\text{m}$) in OPDs is not expected to be useful, as it seems impossible to compete with inorganic alternatives. Nonetheless, OPDs remain a viable alternative for the NIR regime up to $2\mu\text{m}$, given that EQE_{PV} values approaching 1 can be achieved at such low gaps with a steep EQE_{PV} tail onset. To increase D^* to the theoretical maximum for NIR organic

Table 7.2: Device performance parameters for the photodiodes with the studied donor materials. ^{a)} Calculated from Eq. 7.10; ^{b)} Calculated from $\text{EQE}_{EL}^{-1} = (I_{0,R} + I_{0,NR})/I_{0,R}$; ^{c)} Calculated from Eq. 7.11; ^{d)} E_{CT} values obtained from the intercept of the reduced EQE_{PV} and EL spectrum (see Appendix C.4).

Material	V_{OC} in V	$I_{0,R}$ ^{a)} in A	EQE_{EL} ^{b)}	$\Delta V_{OC,NR}$ ^{c)} in V	E_{CT} ^{d)} in eV
PTTBAI	0.40	5.59e-16	6.54e-8	0.42	1.07
PBTQ(OD)	0.44	8.54e-17	1.18e-8	0.47	1.12
PTTQ(HD)	0.22	4.60e-15	4.10e-9	0.49	0.96
PTTQN(HD)	0.12	3.65e-15	3.86e-9	0.49	0.81

photodiodes, as indicated by the red curve in Figure 7.7b, one should find a way to decrease $\Delta V_{OC,NR}$ while maintaining the NIR absorption. A reasonable pathway could be the use of NFA materials as these are known to yield lower non-radiative V_{OC} losses.^{194,195} A hurdle to overcome is to find a well-performing combination of a NIR-photoactive donor and NFA, as only a selected group of donor materials tend to work well with the best non-fullerene acceptors produced to date.¹⁹⁶

7.4 Conclusion

In this chapter, a study to determine the intrinsic limit of the specific detectivity of near-infrared organic photodiodes was detailed. The open-circuit voltage of photodiodes with narrow-gap polymer:PC₇₁BM blends was related to the dark current, noise current and specific detectivity. For devices with open-circuit voltages up to 0.25 V, corresponding to effective and optical gaps lower than 0.9 eV, the experimental dark current approaches its theoretical limit. Above 0.25 V, the deviation increases with increasing open-circuit voltage. Moreover, it is observed that the upper limit for the D^* of NIR OPDs is predominantly limited by non-radiative losses, effectively decreasing D^* by 3 to 4 orders of magnitude in comparison to the BLIP for perfectly radiative materials. This allowed calculation of an intrinsic upper limit for D^* of 10^{12} and 10^{10} Jones at 1500 nm and 2000 nm, respectively. The applicability of OPDs to the NIR region above 2 μm seems therefore negligible and future research should focus on reducing voltage losses, in which NFAs will likely play an important role.

Chapter 8

Mid-gap Trap State Mediated Dark Current in Organic Photodiodes

In the last chapter, results are shown which describe that in narrow-gap organic blends for near-infrared detection the dark saturation current is not overshadowed by shunt current, as it is usually the case in organic donor:acceptor blends for photovoltaic applications. This in turns allows the charge transfer state energy to be studied in relation to the dark saturation current and therefore to deduce an upper specific detectivity limit as a function of the charge transfer energy. From the experimental open-circuit voltage, the dominant source of recombination was determined to be non-radiative, however, the origin of the dark current magnitude remained unclear as it was still orders of magnitude higher than expected for thermally excited band-to-band transitions. The work presented in this chapter shows how the lower limit of the dark current is given by recombination via mid-gap trap states. This new insight is generated from temperature dependent dark current measurements of narrow-gap photodiodes for the near-infrared using the same materials as in Chapter 7. Based on Shockley-Read-Hall statistics, a diode equation is derived which can be used to determine an upper limit for the specific detectivity and to explain the general trend observed for the light to dark current ratio as a function of the experimental open-circuit voltage for a series of organic photodiodes. This chapter presents a summary of the work submitted for publication in July 2021, which is currently still under review at time of thesis submission. C. Kaiser and A. Armin designed the experiments. C. Kaiser performed most measurements, analyzed the data, and performed optical modeling. O. J. Sandberg developed the theoretical model and assisted in data analysis. O. J. Sandberg and A. Armin conceptualized the idea. W. Maes provided the materials. S. Gielen assisted with device fabrication. S. Zeiske performed the IPC measurements. K. Vandewal, A. Armin and P. Meredith provided the overall leadership of the project.

8.1 External Quantum Efficiency of Narrow-gap Photodiodes

Three of the four narrow-bandgap polymers presented in Chapter 7 were used to fabricate D:PC₇₁BM photodiodes with different active layer thicknesses. The molecular structures are shown in Figure 8.1a and the respective External Quantum Efficiency (EQE) spectra are shown in Figure 8.1b on a logarithmic scale, illustrating the bandgap edges and the sub-gap spectral range being strongly affected by optical interference. The HOMO (highest occupied molecular orbital) and LUMO (lowest unoccupied molecular orbital) energy levels of the narrow-gap donor materials were previously reported in Chapter 7 and are repeated in Figure 8.1b for completeness.

The EQE measurements were performed down to approximately 0.5 eV (≈ 2500 nm) over a dynamic range of 90 dB. For PBTQ(OD):PC₇₁BM and PTTQ(HD):PC₇₁BM, the spectral range of PC₇₁BM absorption above 1.65 eV (≈ 750 nm) can be clearly distinguished from the narrow-gap polymer absorption at lower energies. Four orders of magnitude below the above-gap EQE, organic semiconductors generally show trap state absorption as discussed in Chapter 6 for conventional D:A blends with corresponding to effective bandgaps of 1.3 eV and above. Charge transfer and mid-gap trap state absorption features at sub-gap energies⁸⁴ can be fitted with Gaussian functions to obtain the CT state energy (E_{CT}) and the mid-gap trap state energy (E_t) unless overshadowed by interference effects. In the narrow-gap blends, E_{CT} is expected to be very close to the singlet exciton energy ($E_{SE,D}$) of the neat donor polymer, where E_{CT} can be estimated from the gap between donor HOMO and acceptor LUMO, while $E_{SE,D}$ can likewise be estimated from the HOMO-LUMO gap of the donor. Based on the experimental CV energy levels (depicted as insets in Figure 8.1b), similar offsets of approximately 0.3 eV between E_{CT} and $E_{SE,D}$ are found for all of the narrow-gap D:PC₇₁BM blends. Combined with the intrinsically low oscillator strength of CT absorption, the CT absorption shoulder is expected to be masked by the donor singlet exciton absorption. Moreover, the absorption of mid-gap trap states cannot be experimentally discerned from the EQE of the narrow-gap systems, likely because the respective energies are outside the energy range of the experimental apparatus.

From the EQE spectra it is possible to calculate the thermodynamic limit of J_0 , namely the radiative dark saturation current $J_{0,R}$, via detailed balance¹⁸⁹ as described in Section 2.3.2:

$$J_{0,R} = q \int_0^\infty \text{EQE}(E) \phi_{BB}(E) dE, \quad (8.1)$$

where $\phi_{BB}(E)$ is the temperature dependent black body spectrum. In practice, the reliable evaluation of Eq. 8.2 is limited by the upper and lower integration bounds set by the experimental apparatus thus providing a lower limit of $J_{0,R}$. The calculated $J_{0,R}$ is demonstrated in Figure 8.2b, where, for example, the narrow-gap blend PTTBAI:PC₇₁BM is characterized by $J_{0,R} = 3.1 \times 10^{-16}$ A/cm². This is to be compared to the corresponding experimental J_D value of $J_D(-0.1 \text{ V}) = 7.8 \times 10^{-9}$ A/cm², measured at -0.1 V, where J_{shunt} is expected to be

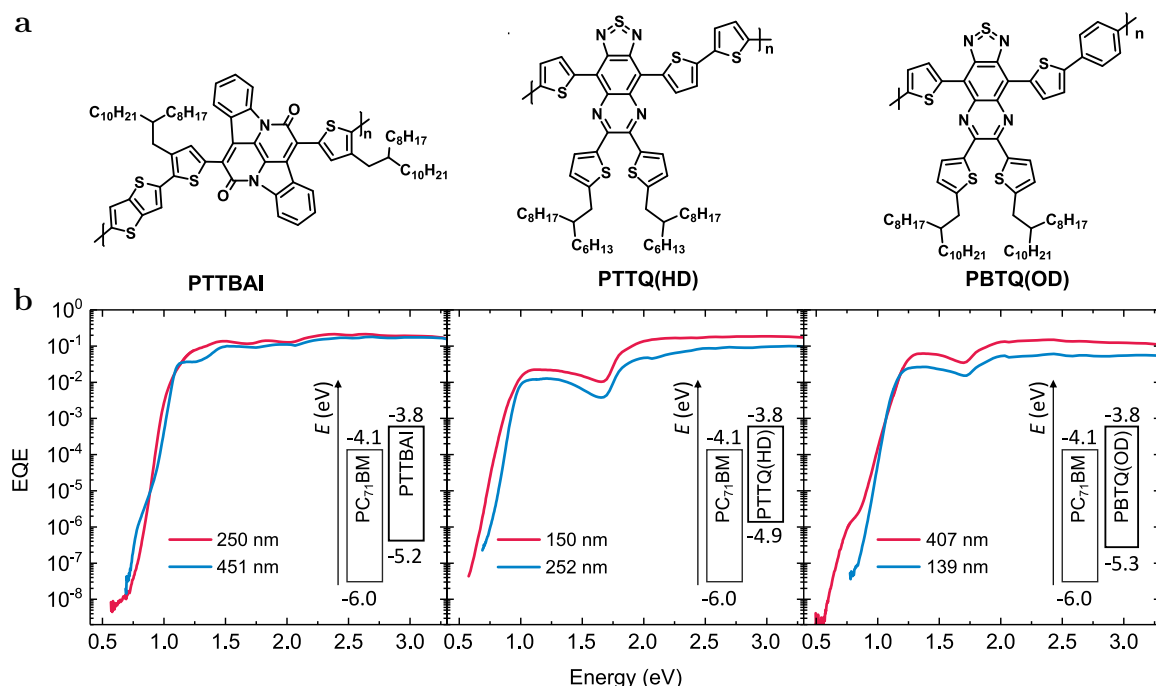


Figure 8.1: **a** Molecules structures of the narrow-gap donor polymers used. **b** Sensitive measured EQE spectra of narrow-gap D:PC₇₁BM photodiodes for two different active layer thicknesses demonstrating optical interference. Frontier molecular orbital energy levels as previously obtained from cyclic voltammetry for PBTQ(OD), PTTBAI and PTTQ(HD) are shown as insets.

minimal. Hence, even when the EQE in the spectral range of mid-gap trap states is included down to 0.6 eV, the calculated $J_{0,R}$ is still 6 to 7 orders of magnitude below the experimental J_D at low reverse bias. This high offset between $J_{0,R}$ and J_D is commonly observed in organic photodiodes, but underlying reasons are still debated. Provided that the contribution from shunt currents is small at this voltage, the dark saturation current density is found to be strongly dominated by non-radiative generation-recombination mechanisms. In Chapter 7, it was shown that for the same narrow-gap D:PC₇₁BM blends studied here, the experimental J_D at low bias voltages, i.e. -0.1 V, is barely influenced by J_{shunt} , hence $J_D(-0.1 \text{ V}) \approx J_0$. It was further suggested that for narrow-gap blends, $J_D(-0.1 \text{ V})$ decreases exponentially with increasing E_{CT} .

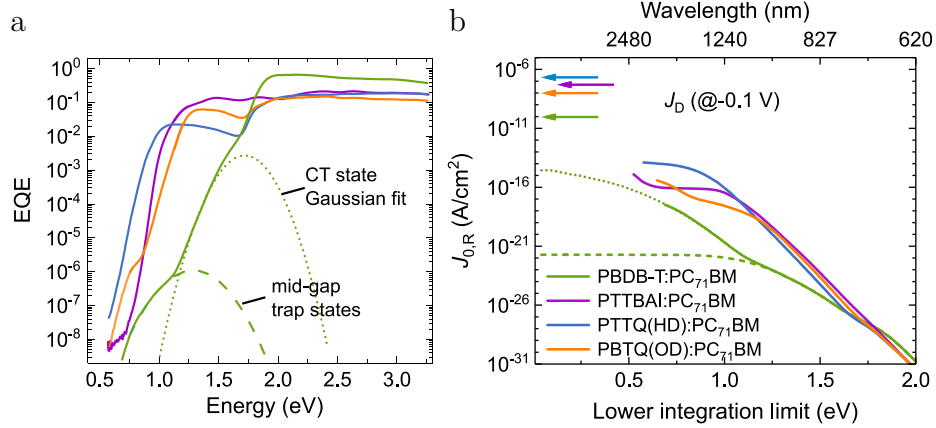


Figure 8.2: **a** Sub-gap EQE including a conventional wide-gap blend PBDB-T:PC₇₁BM with CT and trap state absorption features. **b** Radiative saturation current density $J_{0,R}$ calculated from detailed balance showing strong dependence on the low-energy EQE shoulder. The lower integration bound E_{\min} is often extended beyond the experimental limit (here E_{\min} is between 0.5 to 0.6 eV) by a Gaussian fit to the CT state (dashed green line) and mid-gap trap state (dotted green line) absorption features, as shown for PBDB-T:PC₇₁BM. The experimental $J_D(-0.1\text{ V})$ is typically 6-7 orders of magnitude above the calculated $J_{0,R}$ when $E_{\min} = 0.6\text{ eV}$.

8.2 Temperature Dependent Dark Current Measurements

To gain more insight into the dominant, non-radiative recombination mechanism behind J_0 , temperature dependent $J - V$ measurements were conducted. Assuming that $J_D(-0.1\text{ V}) \approx J_0$, noting that the dark saturation current density takes the form $J_0 = J_{00} \exp(-E_a/kT)$, the corresponding activation energy E_a may be determined. Here, E_a equals the effective energy barrier of the dominating thermal excitation process in the dark, while J_{00} is a prefactor. For a CT state mediated band-to-band generation-recombination process, $E_a = E_{CT}$, while for a mid-gap state mediated generation-recombination process, $E_a \approx E_{CT}/2$ is expected. Figure 8.3a shows $J_D(-0.1\text{ V})$ as a function of $1/kT$ in the so-called Arrhenius plots for the different D:PC₇₁BM blends and device thicknesses. It was found that the voltage sweep direction and the input impedance of the source measure unit can have an impact on the $J - V$ curve, in particular at low current levels near voltages around $V = 0$. Therefore, the current was measured continuously under applied bias while changing temperature to ensure that trapped charge carriers have sufficient time to be released and reach the electrodes. To minimize the effects of shunts (high reverse bias) and noise (voltages near zero), however, the current was measured at -0.1 V . As shown in Figure 8.3a, the natural logarithm of J_D at (-0.1 V) is linearly dependent on $1/kT$ for temperatures above 260 K. For temperatures below 260 K, deviations from linearity are either caused by the inability to measure currents below 10^{-12} A or the dominance of other current channels such as J_{shunt} or surface recombination with weaker temperature dependences. In the high temperature limit, PTTBAI:PC₇₁BM (and PBTQ(OD):PC₇₁BM) photodiodes at two different active layer thickness show similar E_a with a difference of only 0.08 eV (and 0.02 eV) between the two thicknesses. Figure 8.3b shows the obtained E_a as a function of several energy level gaps (E_g).

8.2 TEMPERATURE DEPENDENT DARK CURRENT MEASUREMENTS

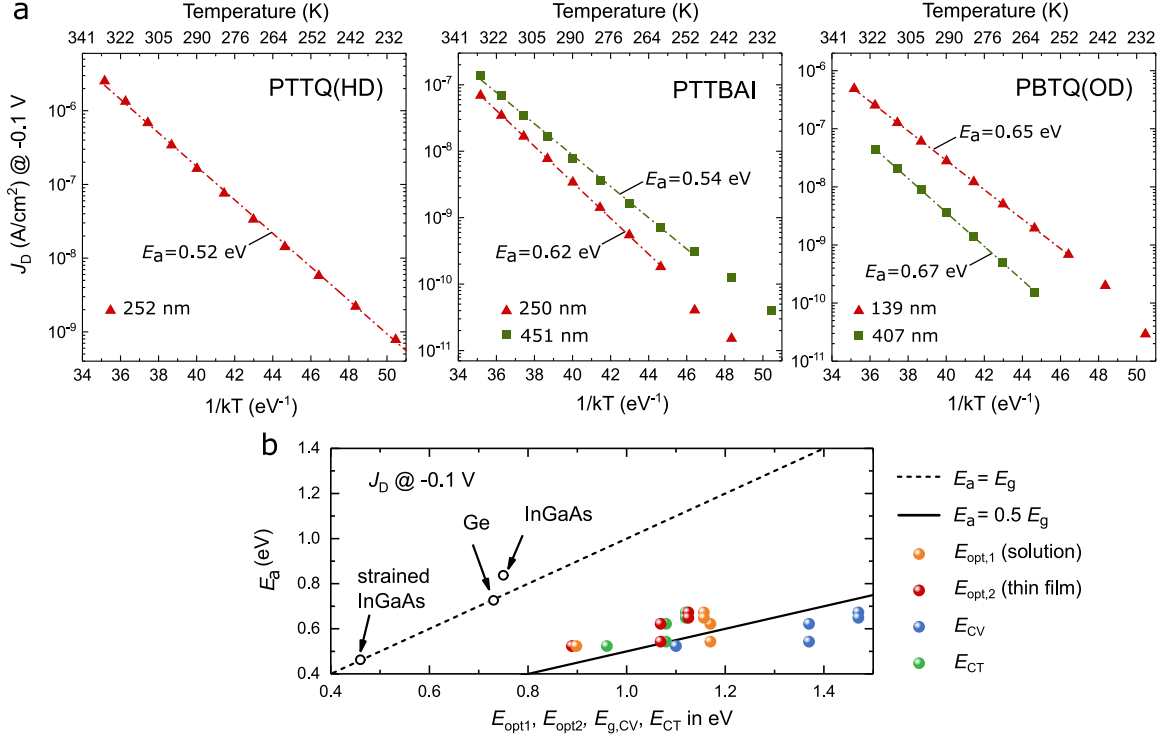


Figure 8.3: Extracting E_a from temperature dependent $J - V$ measurements. **a** The natural logarithm of $J_D(-0.1 \text{ V})$ in function of $1/kT$ can be fitted by a linear function with slope E_a for temperatures above 260 K ($1/kT < 45 \text{ eV}^{-1}$). The narrow-gap D:PC₇₁BM photodiodes, where D is PTTQ(HD), PTTBAI or PBTQ(OD), were fabricated with typically two different active layer thicknesses (green and red points). **b** For narrow-gap organic D:PC₇₁BM blends, $E_a \approx 0.5 E_g$ whereas for commercial inorganic photodiodes, $E_a \approx E_g$. The bandgap was obtained from the optical gap $E_{opt,1}$ from (i) solution absorption and $E_{opt,2}$, (ii) thin film absorption of the neat donor film, (iii) the electronic bandgap E_{CV} from cyclic voltammetry and (iv) E_{CT} from the blend as the intercept of the measured EQEPV and calculated EQEEL.

In addition, the optical gap from thin-film absorption of the neat donor ($E_{opt,2}$) and E_{CT} as the intercept of the measured EQEPV and calculated EQEEL of the photodiodes are included as shown in Appendix C.3. The solution and thin film absorption spectra are given in Appendix C.1. Moreover, the electronic bandgap E_{CV} from cyclic voltammetry and the optical gap from solution absorption of the neat donor ($E_{opt,1}$) are included. Despite the known uncertainties^{50,53} of obtaining the correct bandgap energy, the general correlation is $E_a \approx 0.5 E_g$ was observed for all narrow-gap organic D:A blends. Those results are compared to temperature dependent $J - V$ measurements of three commercial NIR photodetectors comprising germanium (Ge), strained and unstrained indium gallium arsenide (InGaAs). For the organic semiconductors, Figure 8.4a shows the $J - V$ characteristics of PBTQ(OD):PC₇₁BM and PTTBAI:PC₇₁BM photodiodes at temperatures between 260 K to 330 K, while Figure 8.3b displays the Arrhenius plots of the dark current at different voltages. For small reverse bias, E_a equals half the bandgap energy. For the inorganic semiconductors, the $J - V$ characteristics are depicted in Figure 8.5a and the Arrhenius plots in Figure 8.5b illustrating that E_a equals the bandgap energy, as expected. Herein, E_a of the inorganic semiconductors was taken from the responsivity spectra provided by the manufacturer.

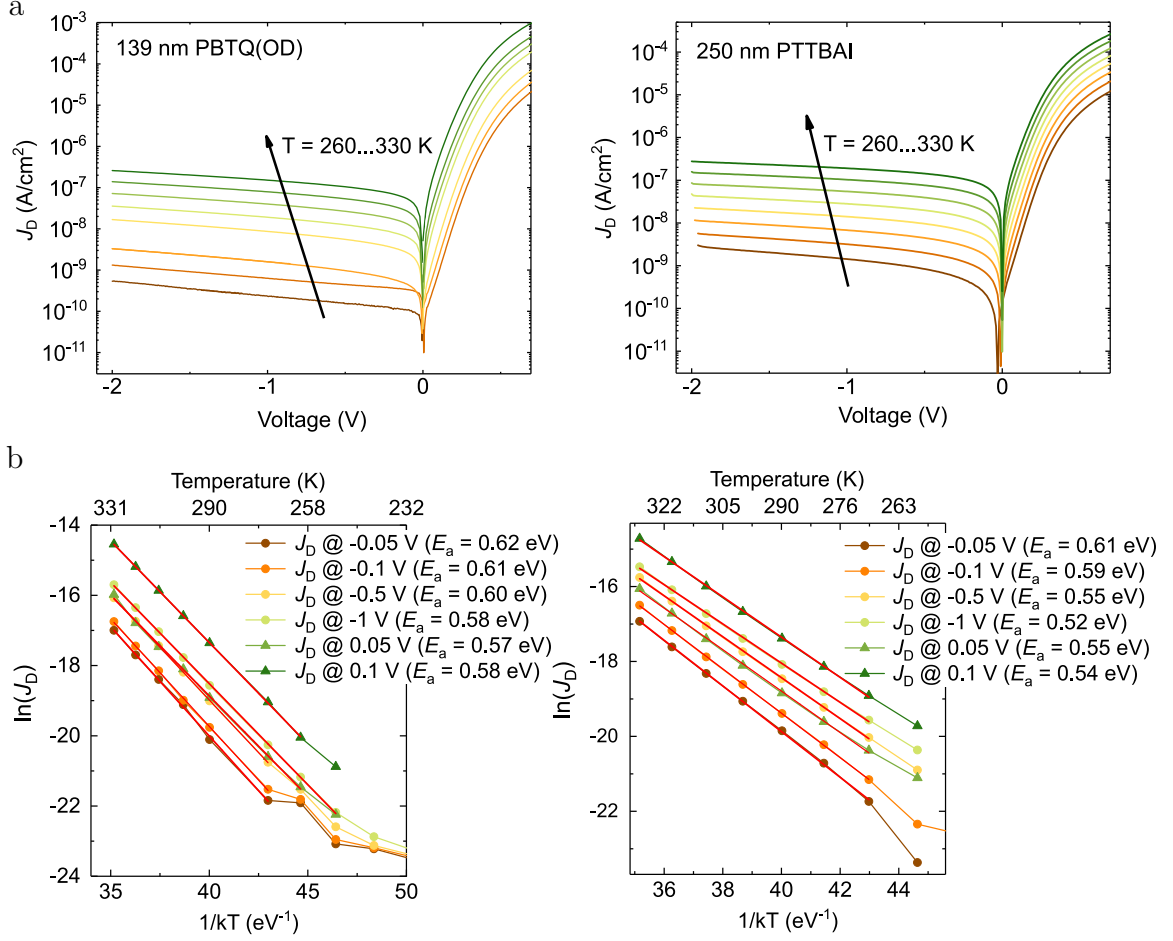


Figure 8.4: Temperature dependent dark $J - V$ characteristics and Arrhenius plots of J_D at different voltages for the PBTQ(OD):PC₇₁BM (a) and the PTTBAI:PC₇₁BM (a) photodiode. $E_a(V)$ is largest for $V = 0.05$ V and decreases for larger reverse bias or in forward bias by up to 0.09 eV for PTTBAI:PC₇₁BM.

8.3 New Diode Equation based on Shockley-Read-Hall

The observation that E_a equals half of the related bandgap energy for the organic semiconductor blends suggests that the dark saturation current in these systems is mediated by generation and recombination via mid-gap trap states in reverse bias. In general, the dark saturation current can be expressed by the sum of the components related to band-to-band recombination (J_0^{bb}) and mid-gap state mediated recombination (J_0^{SRH}) currents:

$$J_0(V) = J_0^{bb} + J_0^{SRH}(V) + J_0^{inj}(V) \quad (8.2)$$

where, for completeness, additional injection current components were included J_0^{inj} that are related to surface generation-recombination at the electrodes. In organic semiconductor blends, the band-to-band component is expected to be independent of voltage, following $J_0^{bb} \propto \exp(-E_{CT}/kT)$. The activation energy of J_0^{inj} , on the other hand, is expected to be predominantly given by the injection barrier of minority

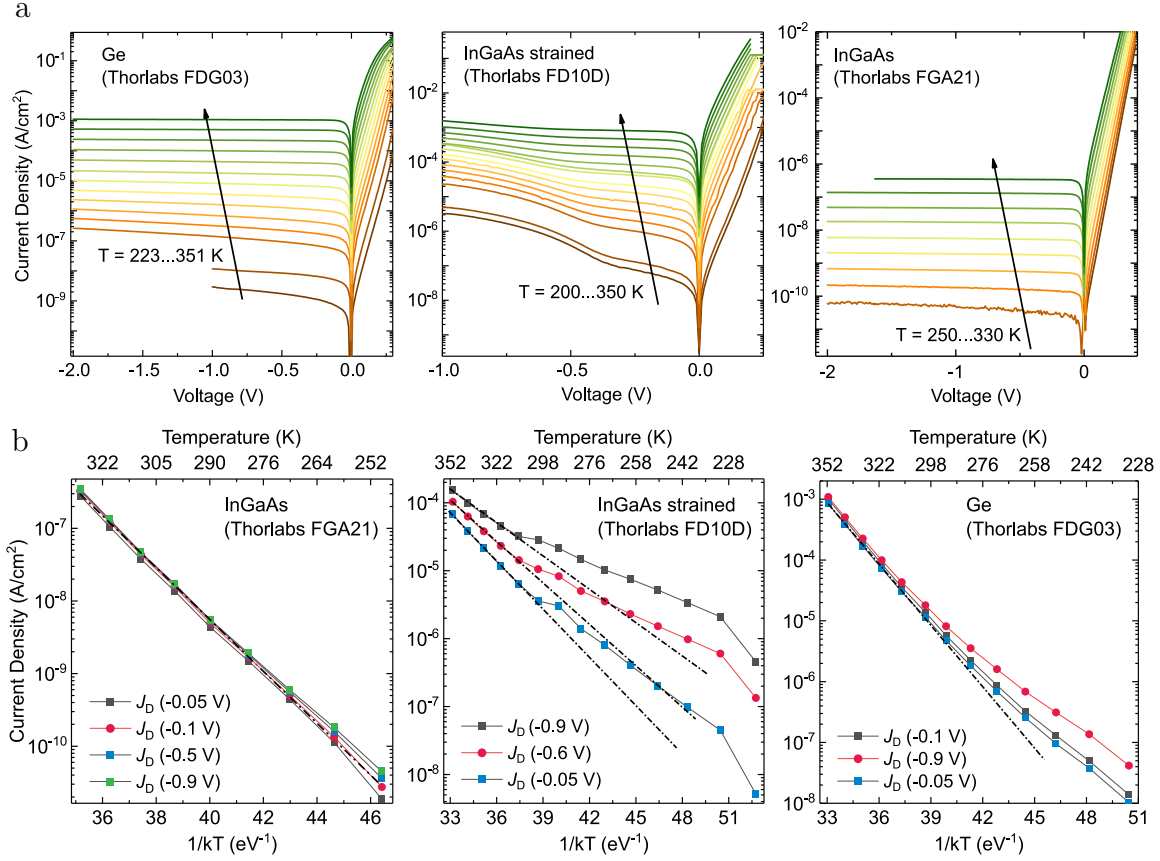


Figure 8.5: **a** Dark current as a function of temperature for three commercial IR photodetectors. Note that the strong voltage dependence of J_D (V) of the strained InGaAs photodiode at low temperatures was previously attributed to recombination via trap mediated tunneling.¹⁹⁷ **b** Arrhenius plot of J_D at different voltages for three commercial IR photodetectors.

carriers at the electrodes.⁸⁸ Given that $E_a \approx E_{CT}/2$, the results point towards $J_0(V) \approx J_0^{SRH}(V)$.

In order to evaluate the voltage dependence of $J_0^{SRH}(V)$, an analytical expression of the related dark current was derived for organic photodiodes based upon Shockley-Read-Hall (SRH) statistics (see the Appendix C.4):

$$J_0^{SRH}(V) \approx J_{0,SRH} \frac{2kT}{q[V_{bi} - V]} \times \ln \left[\frac{1 + 2B \exp\left(\frac{-qV}{2kT}\right)}{1 + 2B \exp\left(\frac{-qV_{bi}}{2kT}\right)} \right] \quad (8.3)$$

where V_{bi} is the built-in voltage, while $J_{0,SRH}$ and B are related to the SRH lifetimes and trap energies for holes and electrons. For mid-gap trap states, it was assumed that $J_{0,SRH} = qdN_0 \exp(-E_g/(2kT))/\tau_{SRH}$, where d is the active layer thickness, N_0 is the available density of states for free charge carriers, and $\tau_{SRH} = \tau_n + \tau_p$ is the effective SRH lifetime, whereas $B = (\sqrt{\tau_n \tau_p} + \sqrt{\tau_p \tau_n})/2$. Here, τ_n and τ_p are the SRH lifetime for electrons and holes, respectively. The corresponding trap-mediated dark recombination current can be expressed as $J_{SRH}(V) = J_0^{SRH}(V)[\exp(qV/kT) - 1]$. In forward bias, near flat-band conditions ($V \approx V_{bi}$), this current density simplifies as $J_{SRH}(V) \approx 2BJ_{0,SRH} \exp(qV/2kT)$, consistent with an ideality factor of 2. In reverse bias, in turn, it was assumed that $J_{SRH}(V) \approx J_{0,SRH}V/[V_{bi} - V]$, saturating to

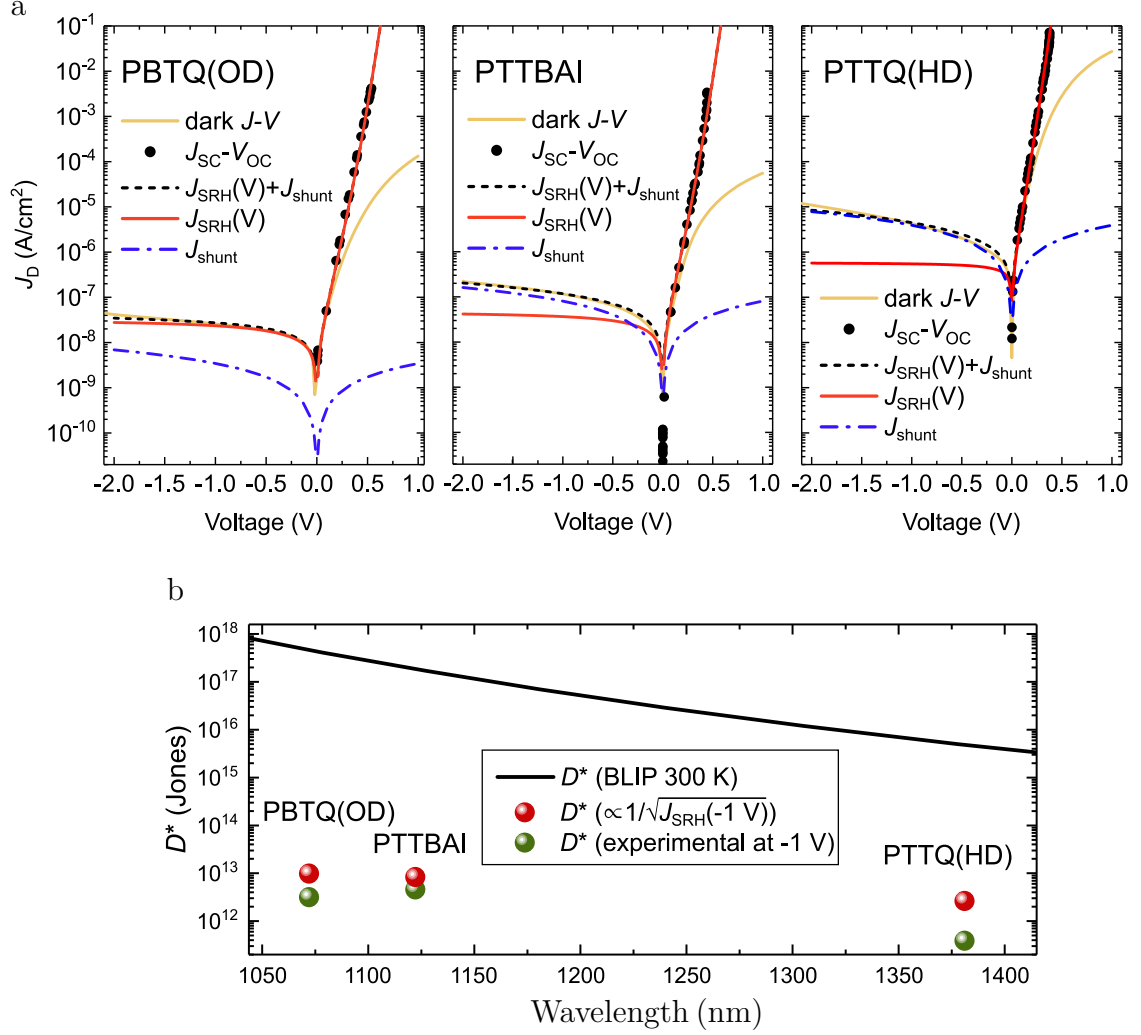


Figure 8.6: Experimental dark $J-V$ characteristics and upper D^* limit. **a** Deconvolution of the experimental dark $J-V$ curves of narrow-gap D:PC₇₁BM photodiodes into mid-gap trap mediated J_{SRH} and J_{shunt} . Forward bias is taken from $J_{SC}-V_{OC}$ measurements to avoid series resistance. **b** D^* approximated from i_{shot} of J_{SRH} at -1 V and the experimental noise current spectrum at -1 V. BLIP is the Background Limited Infrared Performance.

$J_{SRH}(V) \rightarrow J_{0,SRH}$ at large reverse bias. Note that the derived SRH-mediated dark recombination current density presents an excellent and analytically tractable approximation for the expression originally proposed by Sah et al. describing the recombination current.⁷⁷

In accordance with Eq. 8.3, it is expected that the dark saturation current to depend on the voltage. However, the experimental dark current in forward bias quickly becomes limited by the series resistance and/or transport limitations at voltages above 0.2 V in narrow-gap blends. To overcome these resistive limitations and thus obtain a more accurate estimate for $J_{SRH}(V)$, light intensity dependent J_{SC} and V_{OC} measurements were performed. Here, V_{OC} is the open-circuit voltage at which the total current under illumination is zero, $J(V_{OC}) = -J_{SC} + J_D(V_{OC}) = 0$, while J_{SC} is the short-circuit current density being proportional to the light intensity. Hence, since $J_D(V_{OC}) = J_{SC}$, by varying the light intensity and plotting the related J_{SC} as a function of V_{OC} , the dark $J-V$ in the forward bias can be reproduced, but without the

effect of transport limitations or series resistance (since $J = 0$).¹⁹⁸ The experimental dark $J - V$ characteristics along with the associated $J_{\text{SC}} - V_{\text{OC}}$ plots are shown in Figure 8.6 for the PTTBAI:PC₇₁BM, PBTQ(OD):PC₇₁BM and PTTQ(HD):PC₇₁BM photodiodes.

A good fit of the dark $J - V$ in reverse bias and the $J_{\text{SC}} - V_{\text{OC}}$ plot in forward bias was obtained for all systems using $J_{\text{D}} = J_0^{\text{SRH}}(V) \exp [(qV/kT) - 1]$ with J_0^{SRH} given by Eq. 8.3 and assuming $B = 1$. These results further corroborate the assertion that the dark saturation current is dominated by bulk processes mediated via mid-gap trap states. The corresponding $J_{0,\text{SRH}}$ values as extracted from the fits are shown in Tab. 8.1, allowing for the effective SRH lifetimes τ_{SRH} to be calculated. Assuming a typical value of $1 \times 10^{20} \text{ cm}^{-3}$ for N_0 , it was found that τ_{SRH} for PTTBAI, PBTQ(OD) and PTTQHD to be 0.3, 0.1 and 1 μs , respectively. Note that J_0^{bb} from the band-to-band recombination converges to values much lower than $J_0^{\text{SRH}}(V)$ and hence, can be neglected in reverse and forward bias. In contrast, $J_{\text{shunt}}(V)$ dominates the dark $J - V$ at high reverse bias. This is demonstrated, first, in the dark $J - V$ fits in Figure 8.6a and, secondly, in Figure 8.4, where $E_{\text{a}}(V)$ is shown to decrease with increasing reverse bias. For example, $E_{\text{a}}(-1 \text{ V}) = E_{\text{CT}}/2 - 0.09 \text{ eV}$ for PTTBAI and $E_{\text{a}}(-1 \text{ V}) = E_{\text{CT}}/2 - 0.04 \text{ eV}$ for PBTQ(OD). It can be concluded that $J_{\text{D}} \approx J_0^{\text{SRH}}$ holds true, at least for small voltages close to zero, including $V = -0.1 \text{ V}$.

Table 8.1: Fit parameters $J_{0,\text{SRH}}$, R_{shunt} and V_{bi} extracted from the experimental dark $J - V$ curves in reverse bias and $J_{\text{SC}} - V_{\text{OC}}$ in forward bias using Eq. 8.3 under the assumption that $B = 1$. Experimental V_{OC} from light $J - V$ measurements under 1 sun illumination. τ_{SRH} calculated from $J_{0,\text{SRH}}$ via $\tau_{\text{SRH}} = qdN_0 \exp(-E_{\text{g}}/(2kT))/J_{0,\text{SRH}}$.

Material	V_{OC} in V	$J_{0,\text{SRH}}$ in A/cm ²	R_{shunt} in Ω/cm^2	V_{bi} in V	τ_{SRH} in μs
PTTBAI	0.44	4.88e-8	1.2e7	0.38	0.31
PBTQ(OD)	0.40	3.35e-8	2.9e8	0.49	0.11
PTTQ(HD)	0.27	5.91e-7	2.5e5	0.10	1.20

8.4 New Specific Detectivity Limit based on Shockley-Read-Hall Recombination

Based on the above findings, a new efficiency limit for organic BHJ photodiodes is obtained as follows. The performance of a photodetector is given by the specific detectivity $D^* = R\sqrt{A\Delta f} \times (i_{\text{noise}})^{-1}$, where R is the responsivity, i_{noise} is the measured noise current and Δf is the frequency bandwidth. In organic electronics, i_{noise} can be well approximated by its shot noise component i_{shot} at small bias. i_{shot} of any signal S is $i_{\text{shot}} = \sqrt{2qS\Delta f}$. Then, assuming absorber materials that are dominated by recombination via mid-gap trap states, the lower limit of D^* corresponding to EQE = 1 for $E \geq E_{\text{a}}$ and EQE = 0 for $E \leq E_{\text{a}}$ (i.e. R of an ideal photodiode) can be approximated by $D^* = R[2qJ_{\text{SRH}}(V)]^{-1/2}$. Figure 8.6b compares this calculated D^* at -1 V with the experimental D^* previously obtained in Chapter 7

from the measured noise current at -1 V and 3 kHz. The experimental D^* is generally close to the calculated D^* with a maximum offset of roughly 1 order of magnitude for PTTQ(HD):PC₇₁BM. From the fit shown in Figure 8.6a, PTTQ(HD):PC₇₁BM has the largest relative contribution of J_{shunt} to the total J_D at -1 V, which can be the origin of the relatively high experimental noise current. To improve D^* for this particular system, J_{shunt} should be decreased. Known strategies for reducing J_{shunt} include employing selective charge blocking layers, thick junctions and optimizing the device layout to decrease lateral leakage currents.

Furthermore, since photodetectors are generally operated under reverse bias, the voltage and V_{bi} dependence of J_{SRH} must be considered when calculating the expected noise current or analysing experimental noise measurements. At 0 V, the net current is zero, but i_{thermal} of J_{SRH} and J^{bb} are non-zero. It is assumed that the total dark current density is given by

$$J = \frac{V}{R_{\text{shunt}}} + J_0^{\text{bb}} \left[e^{\frac{qV}{kT}} - 1 \right] + J_0^{\text{SRH}} \left[e^{\frac{qV}{kT}} - 1 \right], \quad (8.4)$$

where J_0^{SRH} is given by Eq. 8.3. The thermal noise reads

$$\langle i_{\text{thermal}}^2 \rangle = \frac{4kT}{R_P} \Delta f, \quad (8.5)$$

where R_P is the parallel resistance given by $R_P = dV/dJ$. More details on the thermal noise are given in Chapter 2.3.3. The thermal noise of the dark current density from Eq. 8.4 can be written as

$$\langle i_{\text{thermal}}^2 \rangle = 4kT\Delta f \times \left[\frac{1}{R_{\text{shunt}}} + \frac{J_0^{\text{bb}}q}{kT} + \frac{2J_{0,\text{SRH}}}{V_{\text{bi}}} \times \ln \left\{ \frac{1 + 2B}{1 + 2Be^{\frac{-qV_{\text{bi}}}{2kT}}} \right\} \right]. \quad (8.6)$$

The factor in Eq. 8.6, that includes the natural logarithm, was introduced due to J_{SRH} . For i_{thermal} at $V = 0$, Eq. 8.6 is reobtained and hence, $i_{\text{thermal}}(J_{\text{SRH}}) > i_{\text{thermal}}(J^{\text{bb}})$. In reverse bias for $V \ll 0$, $R_P = dV/dJ = R_{\text{shunt}}$ and $\langle i_{\text{thermal}}^2 \rangle = 4kT\Delta f \times (R_{\text{shunt}})^{-1}$.

i_{shot} of J_{SRH} increases with voltage, while i_{shot} of J^{bb} is expected to increase with increasing reverse bias until $J^{\text{bb}} \approx J_0^{\text{bb}}$ for $V \ll 0$. In contrast, due to the voltage dependence of J_0^{SRH} , a stronger voltage dependence at small reverse bias is expected when recombination via mid-gap state dominates. The voltage dependence of $J_{0,\text{SRH}}$ is determined by the magnitude of V_{bi} , i.e., $J_0^{\text{SRH}}(V) \approx J_{0,\text{SRH}}$ is reached for higher voltages, when the effective V_{bi} is high. However, the total i_{shot} in the limit $V \ll 0$ must be the sum over band-to-band recombination and SRH recombination via mid-gap trap states, hence, $\langle i_{\text{shot}}^2 \rangle = 2(J_0^{\text{bb}} + J_{0,\text{SRH}})q\Delta f$.

8.5 Open-circuit Voltage in the Limit of Shockley-Read-Hall Recombination

Based on Eq. 8.3, the dark saturation current density exhibits distinctly different voltage dependence in forward and reverse bias when trap-mediated SRH recombination dominates. The principal voltage dependence of $J_0^{\text{SRH}}(V)$ in the forward bias is of the form $J_0^{\text{SRH}}(V) \propto \exp(-qV/2kT)$, while $J_0^{\text{SRH}}(V)$ saturates to a constant value for voltages far into the reverse bias. Therefore, the ratio between the dark saturation current densities in the forward bias, at a voltage V_F , and in the reverse bias, at a voltage V_R , scales presumably as $J_0^{\text{SRH}}(V_F)/J_0^{\text{SRH}}(V_R) \propto \exp(-qV_F/2kT)$. This is in contrast to the case when band-to-band recombination dominates the dark saturation current, where J_0 is typically independent of the voltage and $J_0^{\text{SRH}}(V_F)/J_0^{\text{SRH}}(V_R) = 1$. Hence, $J_0^{\text{SRH}}(V_F)/J_0^{\text{SRH}}(V_R)$ may be used as a proxy for the dominant recombination mechanism. To reliably determine $J_0(V_F)/J_0(V_R)$, the influence of resistive effects needs to be avoided. To this end, the J_{SC} vs V_{OC} data set is used, allowing for the corresponding dark current density in forward bias ($V_F = V_{\text{OC}}$) to be obtained via $J_{\text{D}}(V_{\text{OC}}) = J_{\text{SC}}$. Subsequently, the ratio between the dark saturation current densities in forward and reverse bias can be calculated via

$$\frac{J_{\text{SC}}}{|J_{\text{D}}(V_{\text{R}})|} = \frac{J_0(V_{\text{OC}})}{J_0(V_{\text{R}})} \times \left[\exp\left(\frac{qV_{\text{OC}}}{kT}\right) - 1 \right], \quad (8.7)$$

for $V_{\text{R}} < -3kT/q$, noting that the dark current density is approximately given by $J_{\text{D}}(V_{\text{R}}) \approx -J_0(V_{\text{R}})$ in the reverse bias. To minimize the J_{shunt} contribution to the total J_{D} in the reverse bias, J_{D} is evaluated at $V_{\text{R}} = -0.1 \text{ V}$. In Figure 8.7a, the experimentally-obtained $J_{\text{SC}}/|J_{\text{D}}(V_{\text{R}})|$ is shown as a function of V_{OC} for the narrow-gap photodiodes investigated in this work (closed symbols), alongside other photodiodes described in Appendix C.2 assuming $V_{\text{R}} = -0.1 \text{ V}$. The theoretical limit, as expected based on Eq. 8.7, when band-to-band recombination dominates the dark saturation current, i.e., $J_0(V_{\text{OC}})/J_0(V_{\text{R}}) = 1$, is indicated by the red line in Figure 8.7. Most photodiodes are generally well below this limit, consistent with previous findings described in Chapter 7. The theoretical behaviour, expected for SRH recombination via mid-gap states dominating the dark saturation current, is indicated by the black line for the case $V_{\text{OC}} \rightarrow V_{\text{bi}}$ when $J_0^{\text{SRH}}(V_{\text{OC}}) \rightarrow 2J_{0,\text{SRH}} \exp(-qV_{\text{OC}}/2kT)$ in Eq. 8.3. Comparing with the experimental data, it can be seen that the general trend is indeed consistent with SRH recombination via mid-gap traps dominating J_0 in narrow-gap systems where $V_{\text{OC}} < 0.7 \text{ V}$. This is further corroborated by the experimentally obtained $J_0(V_{\text{OC}})/J_0(V_{\text{R}})$, estimated using Eq. 8.7 in Figure 8.7b, showing that narrow-gap systems follow the trend predicted by mid-gap state mediated recombination. Note that the scatter around the black line can be partly attributed to the fact that $V_{\text{OC}} \neq V_{\text{bi}}$ in general, and a weak additional voltage dependence is thus expected in accordance with Eq. 8.3. For systems with relatively wide gaps ($V_{\text{OC}} > 0.7 \text{ V}$), in turn, a deviation from the trend is seen. However, such a deviation is to be expected considering that the V_{OC} increases linearly with the effective bandgap

E_{CT} (independent of whether band-to-band or SRH recombination dominates at open-circuit). Subsequently, high V_{OC} blends are characterized by very low J_0 levels, with $J_D(V_R)$ inevitably becoming dominated by parasitic shunts (J_{shunt}), overshadowing the true J_0 in these systems.

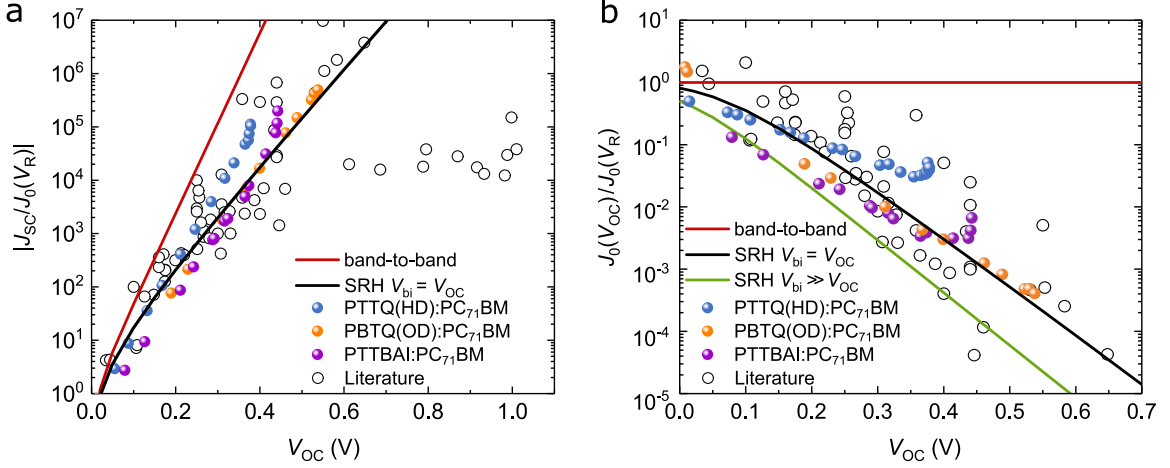


Figure 8.7: General trend in performance metrics of narrow-gap photodiodes dominated by SRH recombination. Calculated ratio of J_{SC} to $J_0(V_R)$ (a) and calculated ratio of $J_0(V_{OC})$ to $J_0(V_R)$ (b) plotted as a function of V_{OC} on a semi-logarithmic scale, where $J_0(V_R) \approx J_D(V_R)$ and $V_R = -0.1$ V for all fullerene-based devices (empty circles, data in Appendix C.2). Blue, orange and purple circles represent $J_{SC} - V_{OC}$ data of the studied narrow-gap photodiodes at different light intensities. Red lines represent an analytical limit taking only into account band-to-band recombination. Black and green lines show the theoretical limits of SRH recombination via mid-gap trap states, where $V_{bi} = V_{OC}$ and $V_{bi} \gg V_{OC}$, respectively.

8.6 Conclusions

In this chapter, a detailed study was presented on the origin of the dark current in organic photodiodes for the near-infrared. Specifically, the temperature dependent dark $J - V$ measurements were utilized on narrow-gap organic semiconductor blend photodiodes to show that the thermal activation of the dark current at small reverse bias equals half the bandgap, i.e., $E_a \approx 0.5 E_g$. The dominant dark recombination mechanism is therefore mid-gap trap mediated. A new expression for the dark current mediated by mid-gap trap states using SRH statistics was derived. In this new expression, the dark saturation current J_0^{SRH} is voltage dependent and therefore can strongly affect the reverse bias dark current and its shot noise depending on the built-in voltage. In this light, a revised upper limit of D^* for the studied narrow-gap blends was calculated based on J_0^{SRH} that was obtained from a fit to the dark $J - V$ characteristics. Lastly, it is shown that for a large set of narrow-gap organic photodiodes, the J_{SC} to $J_D(-0.1$ V) ratio as a function of voltage roughly describes a trend expected when considering SRH recombination via mid-gap trap states.

Chapter 9

Conclusions and Outlook

9.1 Conclusions

Organic semiconductors possess promising optoelectronic properties that are in many ways complementary to conventional inorganic semiconductors. New applications for photodiodes are constantly emerging, such as the internet of things and wearable electronics that demand different mechanical and optoelectronic properties from those provided by conventional inorganic devices. In this thesis, an extensive body of work has been described which seeks to explore the sub-gap states in organic semiconductors. An emphasis is laid on how sub-gap states affect the dependence of dark current and D^* of organic photodiodes on the active layer thickness and energetics of donor and acceptor.

In Chapter 4, it is shown that optical interference imposes additional spectral features onto the sub-gap EQE depending on the thickness of the organic layers in the photodiode and their optical constants. These spectral features are convoluted with the absorption features of CT states right below the absorption onset as well as the mid-gap trap states at the low-energy range of the measured EQE spectra. Using a novel, iterative approach to the conventional optical transfer matrix simulation, the ultra-low sub-gap absorption coefficient ($\alpha(\lambda)$) is extracted from a set of experimental EQE spectra for two conventional organic semiconductor blends (PBDB-T:ITIC and PBTTT:PC₇₁BM). From the interference-free $\alpha(\lambda)$ the characteristic absorption features can be studied providing insights about the energy of the states, their energetic disorder and the oscillator strength of the optical transition. It is further observed that the low-offset blend PBDB-T:ITIC in comparison to the large offset system PBTTT:PC₇₁BM shows more pronounced interference effects presumably because of the greater dispersion in the refractive index which is characteristic for the low-offset non-fullerene blends. This becomes very clear in the sub-gap range, where distinct interference fringes are observed for photodiodes with increased active layer thicknesses. Consequently, the often made assumption for optically thin films, i.e., that the EQE follows the spectral lineshape of $\alpha(\lambda)$, is misleading – in particular for the emerging low-offset non-fullerene blends.

Bearing this in mind, the work described in Chapter 5 shows how the sub-gap EQE spectral lineshape can be manipulated by changing the energetics of the donor:acceptor (D:A) blend. Notably, a series of vacuum-deposited organic photodiodes was fabricated, where the donor is strongly diluted in the acceptor C₆₀. For the donor material, a series of molecules from the same family of bipyranilidenes was used, characterized by a relatively high energy of the highest occupied molecular orbital

(HOMO). In the resulting D:A blend, the offset between the HOMO of the donor and the lowest unoccupied molecular orbital (LUMO) of the acceptor C₆₀ is low, resulting in low charge transfer (CT) energy (E_{CT}) which correlates with this HOMO-LUMO offset. Given a strong $\alpha(\lambda)$ in the spectral range of CT absorption and the low E_{CT} , a broad sub-gap EQE shoulder was observed for the respective D:C₆₀ photodiodes. By substituting the side-chains and the backbone of the bipyranilidene molecules with more electron-donating functional groups and atoms, respectively, not only the HOMO energy was increased as expected, but that also E_{CT} was decreased confirming the linear relationship between the intermolecular HOMO-LUMO offset and E_{CT} . For the D:C₆₀ blend with the lowest E_{CT} and largest α in the spectral range of CT absorption, a series of cavity-enhanced near-infrared (NIR) photodetectors was fabricated with an operational window from 810 nm to 1665 nm and a line width of only 50 nm for one of longest wavelength detecting organic sensors reported so far.

Working with a large series of organic D:A blends, a general pattern for the sub-gap EQE becomes apparent, which was the topic of Chapter 6: While for the fullerene containing blends, the CT absorption dominates the sub-gap EQE at energies close to the absorption onset, low offset blends with non-fullerene acceptors do not show CT absorption. Instead, the latter show an exponentially decaying EQE tail related to the singlet exciton absorption of either donor or acceptor depending on the lowest bandgap component. Within the deviations expected from optical interference, this excitonic sub-gap EQE can be characterized by a slope for which the apparent Urbach energy E_U^{app} equals the thermal energy kT . Temperature dependent measurements confirmed that the sub-gap excitonic EQE is thermally activated. An analytical model describing α was developed that is consistent with a Gaussian density of excitonic states undergoing Boltzmann-like thermally activated optical transitions. At energies close to the absorption onset, the model predicts a spectral range, where the broadening only depends on the static disorder (standard deviation of the Gaussian density of states) and E_U^{app} becomes strongly energy dependent. At the low-energy end of the EQE spectrum, the Gaussian absorption features of mid-gap trap states were observed with a trap energy E_t that is half E_{CT} . The universally observed Urbach tails in low-offset organic semiconductors, as well as the mid-gap trap states, present an unavoidable radiative losses, which lower the maximum achievable D^* in comparison to the background limited infrared photodetector with an ideal step-like EQE.

In Chapter 7 and 8 of this thesis, the dark current of narrow-gap D:A photodiodes was related to the effective bandgap energy E_{CT} . Narrow-gap donor polymers were blended with PC₇₁BM to fabricate a series of narrow-gap, solution processable organic photodiodes with different bandgaps. For those narrow-gap photodiodes, I_D shows almost ideal diode behaviour, with an ideality factor (n) close to 1 and a small voltage dependence in reverse bias. This is in contrast to large bandgap photodiodes used for VIS photodetection (e.g. solar cells) that often have large I_{shunt} contribution and $n > 1.5$. It was first assumed that for those devices, the dark saturation current I_0 is at least comparable to I_{shunt} in magnitude in reverse bias, hence, $I_0 \approx I_D$ at -0.1 V. It was further found that within this series of investigated polymer photodiodes and for other literature known narrow-gap photodiodes, the ratio of the short-circuit current I_{SC} to

$I_D(-0.1\text{ V})$ is exponentially dependent on V_{OC} . At the same time, I_0 must be dominated by non-radiative recombination, since radiative band-to-band recombination cannot explain the high losses observed between the experimental V_{OC} and the radiative V_{OC} limit. In Chapter 7, this general trend between I_0 and the bandgap was used to calculate an expected D^* limit for organic photodiodes that are predominantly limited by non-radiative losses in comparison to the background limited infrared photodetection for perfectly radiative materials. As a consequence, the intrinsic upper limit of D^* is 10^{12} and 10^{10} Jones at 1500 and 2000 nm, respectively. In Chapter 8, the temperature dependence of I_0 in those narrow-gap photodiodes was further investigated to clarify the dominant mechanism for dark current generation. It was shown that the thermal activation energy E_a of I_0 equals E_t , hence half of E_{CT} . The dominant dark recombination mechanism is therefore mid-gap trap mediated and not band-to-band recombination via CT states as often assumed in literature. This experimental observation is in alignment with the spectroscopic observation of mid-gap trap states in the sub-gap EQE of higher bandgap blends. A new analytical expression for the dark current was derived, which is the result of charge generation-recombination via mid-gap trap states using Shockley-Read-Hall (SRH) statistics. In this expression, the dark saturation current depends on the built-in voltage (V_{bi}) and the voltage bias, which affects the shot noise limit of D^* at operational conditions. Moreover, a revised thermal noise limit at zero voltage was derived for mid-gap trap mediated I_0 that is higher than I_0 expected from band-to-band recombination. And lastly, the general trend between I_{SC} to $I_D(-0.1\text{ V})$ and the V_{OC} is revised in Chapter 8 showing that a large number of narrow-bandgap devices are better described assuming the analytical expression of I_0 based on SRH recombination via mid-gap trap states in the limit of $V_{OC} \approx V_{bi}$.

9.2 Outlook

In Chapter 4, the presence of strong interference effects in organics thin-film stacks was described as well as a method to obtain an interference free sub-gap α . Going forward in the research on organic semiconductors, it will be important to decouple optical phenomena related to the device stack from that of material properties – especially in the field of non-fullerene acceptors. First, this will allow the study of the true α in the spectral range of sub-gap state absorption. Second, a deeper understanding of interference in particular materials may be utilized to manipulate optical effects either to reduce radiative losses or to fabricate high quality resonators for cavity-enhanced photodetectors.

The findings in Chapter 6 show that organic, low-offset organic semiconductors are characterized by exponentially decaying Urbach tails. From the analytically derived expression for the sub-gap α , the static disorder was extracted for a limited number of materials. In follow-up experiments, the relationship between the extracted static disorder and other characteristics of the photoactive material such as bandgap, morphology or processing conditions should be investigated with the goal to establish

general trends. This may provide a roadmap to lower static disorder, which is detrimental for many device applications.

From the work described in Chapter 8, it becomes clear that non-radiative recombination via mid-gap trap states contributes strongly to the large dark current observed in organic photodiodes. The origin of non-radiative losses is a hot topic in both the organic solar cells and the photodetector community. To reduce non-radiative losses means to increase the maximum achievable open-circuit voltage as well as to increase the D^* of organic photodiodes closer to the radiative limit of photodetection. In the next step, it is therefore crucial to study the origin of mid-gap trap states. Two experimentally available platforms were identified in the work described in this thesis, which are the interference-free, sub-gap EQE spectra as well as the dark current of narrow-gap blends. Using the EQE spectra, it is possible to study the reorganization energy and the oscillator strength as a function of bandgap, morphology, processing conditions. Using dark current measurements of narrow-gap photodiodes, the contribution of I_0 in relation to I_{shunt} should be further investigated for different materials and active layer thicknesses. As an advantage, optical interference does not play a role in dark current measurements. Notably, the influence of I_{shunt} is known to decrease with increasing thickness. Recently, some non-fullerene D:A acceptor blends were demonstrated to combine high layer thickness with high charge collection efficiencies^{199,200} and/or to reduce dark current leading to specific detectivities on the order of 10^{12} to 10^{13} Jones for the wavelengths below 1000 nm.^{201–203} At the same time, research on non-fullerene photodiodes for the NIR is still in its infancy. Non-fullerene acceptors have typically a photoresponse up to 1000 nm and this spectral range is likely to be extended further into the NIR through chemical modifications. Moreover, electro-optical effects like charge collection narrowing and optical micro-cavities have yet to be reevaluated for those new materials.

Appendix A

Manipulating the Charge Transfer Absorption for Narrowband Light Detection in the Near-Infrared

A.1 Device Architecture

Layer	Function	Thickness [nm]											
Glass	Substrate	10 ⁶											
Ag	Contact / mirror	100											
HATNA-F ₆	ETL / hole blocking	6											
BPhen:Cs (1:1)	ETL	25	25	25	75	75	75	125	125	125	125	150	
HATNA-F ₆	ETL / hole blocking	6											
C ₆₀	ETL	5											
C ₆₀ :D8 (5 wt% D8)	BHJ	25	50	75	25	50	75	25	50	75	100	50	
BF-DPB	HTL	12											
BF-DPB:F ₆ -TCNNQ (7 wt% F ₆ -TCNNQ)	HTL	26	26	26	76	76	76	126	126	126	126	176	
MoO ₃	Seed	3											
Au	Seed	1											
Ag	Contact / mirror	25											
Ag	Protection [†]	75											
MoO ₃	Protection	10											
Device results													
Full width at half maximum [nm]		38	44	47	42	45	50	59	40	53	58	50	
Resonance peak [nm]		605	707	810	*908	1032	*1150	1244	1370	1484	1581	*1665	

Table A.1: Device architectures for cavity-enhanced photodetectors with the donor 2,2',6,6'-tetra-(2-methylthienyl)-4,4'-bithiopyranylidene (short: D8). The devices were deposited by thermal evaporation from the bottom layer to the top, and illuminated from the bottom. The resonance wavelength was varied from 605 nm to 1665 nm by changing the thickness of the layers: BPhen:Cs (1:1), C₆₀:D8 and/or BF-DPB:F₆-TCNNQ (7 wt% F₆-TCNNQ). The materials used were silver (Ag; K. J. Lesker, UK), 2,3,8,9,14,15-hexafluoro-5,6,11,12,17,18-hexatriazaazatriphenylene (HATNA-F₆; IAPP), 4,7-diphenyl-1,10-phenanthroline (BPhen; Lumtec, Taiwan), caesium (Cs; SAES Getters, Italy), buckminsterfullerene (C₆₀; CreaPhys, Germany), N4,N4'-bis(9,9-dimethyl-9H-fluoren-2-yl)-N4,N4'-diphenylbiphenyl-4,4'-diamine (BF-DPB; Synthron), 2,2'-(perfluoronaphthalene-2,6-diylidene)dimalononitrile (F₆-TCNNQ; Novaled, Germany), gold (Au; Allgemeine Gold und Silberscheidanstalt, Germany) and molybdenum trioxide (MoO₃; Sigma-Aldrich, USA). (†) Ag layer outside the photoactive area to mechanically stabilize the thin Ag layer. (*) Photodetectors with resonances at 908 nm, 1150 nm and 1665 nm were investigated regarding their spectral linewidth and noise spectral density in Figure 5.8 and Figure 5.9 in Chapter 5.

A.2 Cyclic Voltammetry

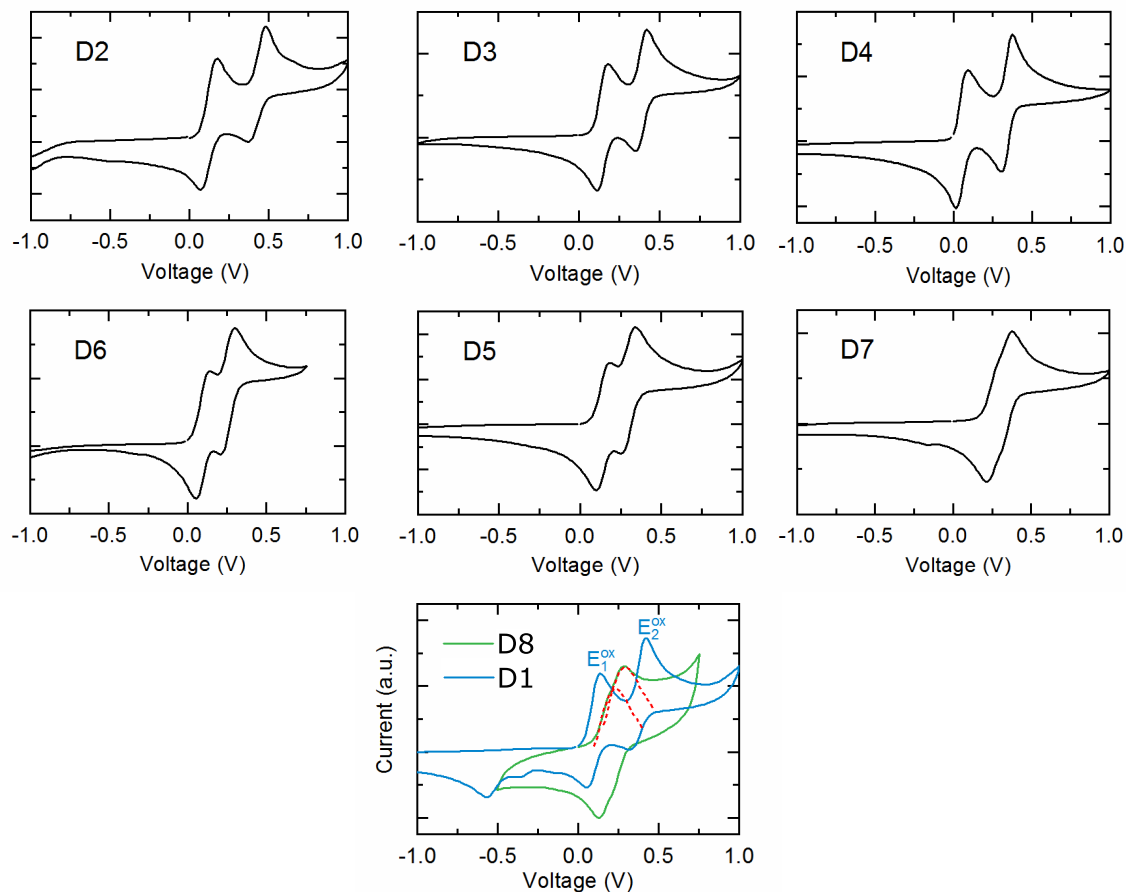


Figure A.1: Cyclic voltammograms for donor molecules D1 to D8 recorded in N,N-dimethylformamide showing a reversible two-step oxidation. Donor molecules were characterised by either a pyranilidene or a thiopyranilidene core, which governs the potential difference between the first and second oxidation potential (E_1^{ox} and E_2^{ox}) as exemplified for D1 (blue line) and D8 (green line) in the bottom figure. E_1^{ox} and E_2^{ox} are highlighted with red dashed lines for D8.

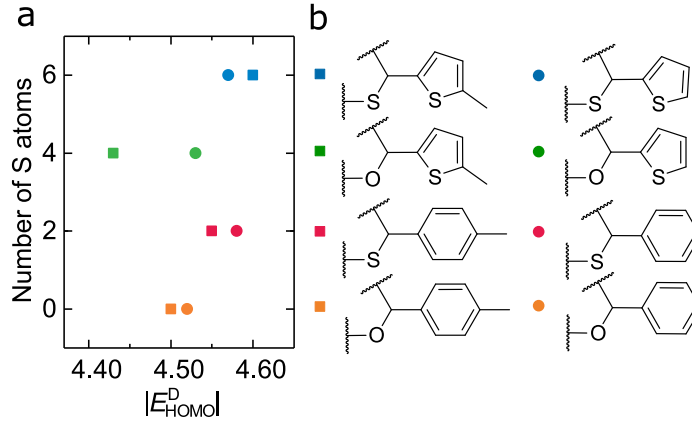


Figure A.2: **a** The absolute HOMO energy level $|E_{\text{HOMO}}^{\text{D}}|$ of the donor molecules estimated from the first oxidation potential $|E_1^{\text{ox}}|$ recorded in a cyclic voltammetry experiment (see Figure A.1). $E_{\text{HOMO}}^{\text{D}}$ in eV was obtained through internal referencing to the Fc/Fc^+ redox couple according to $E_{\text{HOMO}}^{\text{D}} = E_{\text{Fc}/\text{Fc}^+} - E_1^{\text{ox}} + 4.8$ eV. -4.8 eV is the HOMO energy level of ferrocene against vacuum. **b** Characteristic molecular features of the donor molecules, where squares represent methylated donors and circles represent nonmethylated donors.

A.3 Density Functional Theory Calculations

Gas phase values for vertical ionization potential IP_0 and electron affinity EA_0 of the neutral molecule as well as the ionization potential IP_+ of the cation are determined using

$$IP_+ = E_{++}(q_+) - E_+(q_+) \quad (\text{A.1})$$

$$IP_0 = E_+(q_0) - E_0(q_0) \quad (\text{A.2})$$

$$EA_0 = E_0(q_0) - E_-(q_0) \quad (\text{A.3})$$

where q_i and E_i are the relaxed geometry and the ground-state energy for differently charged states, respectively. Molecular relaxation is characterized by the internal reorganization energies λ_{Di} , which is obtained using the potential energy surface method.²¹ Polarization corrections can be calculated by assuming spherically shaped molecules with an ionic radius r_i of the respectively charged species extracted from DFT calculations^{160, 204, 205}

$$P_i = \frac{q^2 e^2}{8\pi\epsilon_0 r_i} \left(\frac{1}{E_{\text{rel}} - 1} \right) < 0, \quad (\text{A.4})$$

with $E_{\text{rel}} = 37.219$ for N,N-dimethylformamide and $q^2 = 1$ for all charged states. With these considerations, the cyclic voltammetry (CV) energy levels are given as

$$E_{\text{OX2}} = -IP'_+ = -(IP_+ + 3P_+ - \lambda_{D++}/2), \quad (\text{A.5})$$

$$E_{\text{HOMO}} = -IP'_0 = -(IP_0 + P_0 - \lambda_{D+}/2), \quad (\text{A.6})$$

$$E_{\text{LUMO}} = -EA'_0 = -(EA_0 - P_0 + \lambda_{D-}/2). \quad (\text{A.7})$$

APPENDIX A MANIPULATING THE CHARGE TRANSFER ABSORPTION FOR
NARROWBAND LIGHT DETECTION IN THE NEAR-INFRARED

Molecule	Gas phase energies [eV]	Reorganization energy [meV]	Polarization energy [eV]	Simulated CV energies [eV]	Experimental CV energies [eV]
D1	$IP_+ = 9.14$ $IP_0 = 5.76$ $EA_0 = 0.66$	$\lambda_{++} = 630$ $\lambda_+ = 290$ $\lambda_- = 322$	$P_+ = 1.37$ $P_0 = 1.35$ $P_0 = 1.35$	$E_{OX2} = 4.72$ $E_{HOMO} = 4.27$ $E_{LUMO} = 2.17$	$E_{OX2} = -4.80$ $E_{HOMO} = -4.52$ $E_{LUMO} = --$
D2	$IP_+ = 8.82$ $IP_0 = 5.57$ $EA_0 = 0.55$	$\lambda_{++} = 625$ $\lambda_+ = 293$ $\lambda_- = 304$	$P_+ = 1.26$ $P_0 = 1.26$ $P_0 = 1.26$	$E_{OX2} = 4.72$ $E_{HOMO} = 4.16$ $E_{LUMO} = 1.96$	$E_{OX2} = -4.79$ $E_{HOMO} = -4.50$ $E_{LUMO} = --$
D3	$IP_+ = 8.97$ $IP_0 = 5.77$ $EA_0 = 0.91$	$\lambda_{++} = 550$ $\lambda_+ = 286$ $\lambda_- = 206$	$P_+ = 1.34$ $P_0 = 1.37$ $P_0 = 1.37$	$E_{OX2} = 4.66$ $E_{HOMO} = 4.26$ $E_{LUMO} = 2.38$	$E_{OX2} = -4.77$ $E_{HOMO} = -4.53$ $E_{LUMO} = -2.58$
D4	$IP_+ = 8.57$ $IP_0 = 5.53$ $EA_0 = 0.78$	$\lambda_{++} = 532$ $\lambda_+ = 303$ $\lambda_- = 196$	$P_+ = 1.29$ $P_0 = 1.29$ $P_0 = 1.29$	$E_{OX2} = 4.44$ $E_{HOMO} = 4.09$ $E_{LUMO} = 2.16$	$E_{OX2} = -4.73$ $E_{HOMO} = -4.43$ $E_{LUMO} = -2.49$
D5	$IP_+ = 9.05$ $IP_0 = 5.84$ $EA_0 = 0.91$	$\lambda_{++} = 525$ $\lambda_+ = 286$ $\lambda_- = 462$	$P_+ = 1.33$ $P_0 = 1.30$ $P_0 = 1.30$	$E_{OX2} = 4.80$ $E_{HOMO} = 4.41$ $E_{LUMO} = 2.49$	$E_{OX2} = -4.72$ $E_{HOMO} = -4.58$ $E_{LUMO} = -2.27$
D6	$IP_+ = 8.83$ $IP_0 = 5.68$ $EA_0 = 0.80$	$\lambda_{++} = 623$ $\lambda_+ = 284$ $\lambda_- = 546$	$P_+ = 1.28$ $P_0 = 1.24$ $P_0 = 1.24$	$E_{OX2} = 4.68$ $E_{HOMO} = 4.29$ $E_{LUMO} = 2.32$	$E_{OX2} = -4.71$ $E_{HOMO} = -4.55$ $E_{LUMO} = -2.23$
D7	$IP_+ = 8.84$ $IP_0 = 5.92$ $EA_0 = 1.24$	$\lambda_{++} = 464$ $\lambda_+ = 269$ $\lambda_- = 399$	$P_+ = 1.37$ $P_0 = 1.35$ $P_0 = 1.35$	$E_{OX2} = 4.51$ $E_{HOMO} = 4.43$ $E_{LUMO} = 2.78$	$E_{OX2} = -4.66$ $E_{HOMO} = -4.57$ $E_{LUMO} = -2.50$
D8	$IP_+ = 8.54$ $IP_0 = 5.70$ $EA_0 = 1.14$	$\lambda_{++} = 462$ $\lambda_+ = 356$ $\lambda_- = 367$	$P_+ = 1.30$ $P_0 = 1.26$ $P_0 = 1.26$	$E_{OX2} = 4.43$ $E_{HOMO} = 4.26$ $E_{LUMO} = 2.59$	$E_{OX2} = -4.68$ $E_{HOMO} = -4.60$ $E_{LUMO} = -2.48$

Table A.2: Experimental and simulated CV results under consideration of relaxation and polarization effects.

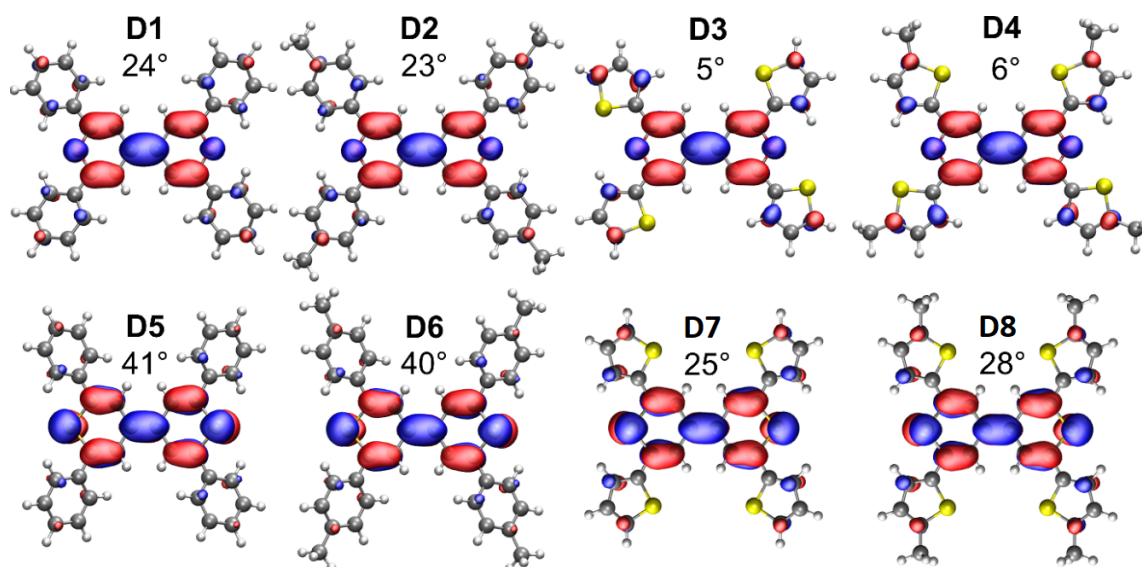


Figure A.3: HOMO distribution of the studied donor molecules and “dihedral angles” between the backbone and the side chains (D1 – D4 with oxygen in the backbone; D5 – D8 with sulfur in the backbone).



Figure A.4: HOMO orbital extension of the donor D1 (oxygen in the backbone) on the left and of the donor D5 (sulfur in the backbone) on the right. The orbital features at the sulfur atoms are more pronounced compared to oxygen atoms leading a stronger extension perpendicular to the molecular plane as well as to reduced features at the side groups.

Appendix B

Universal Urbach Rule for Organic Semiconductors

B.1 Temperature-dependent EQE

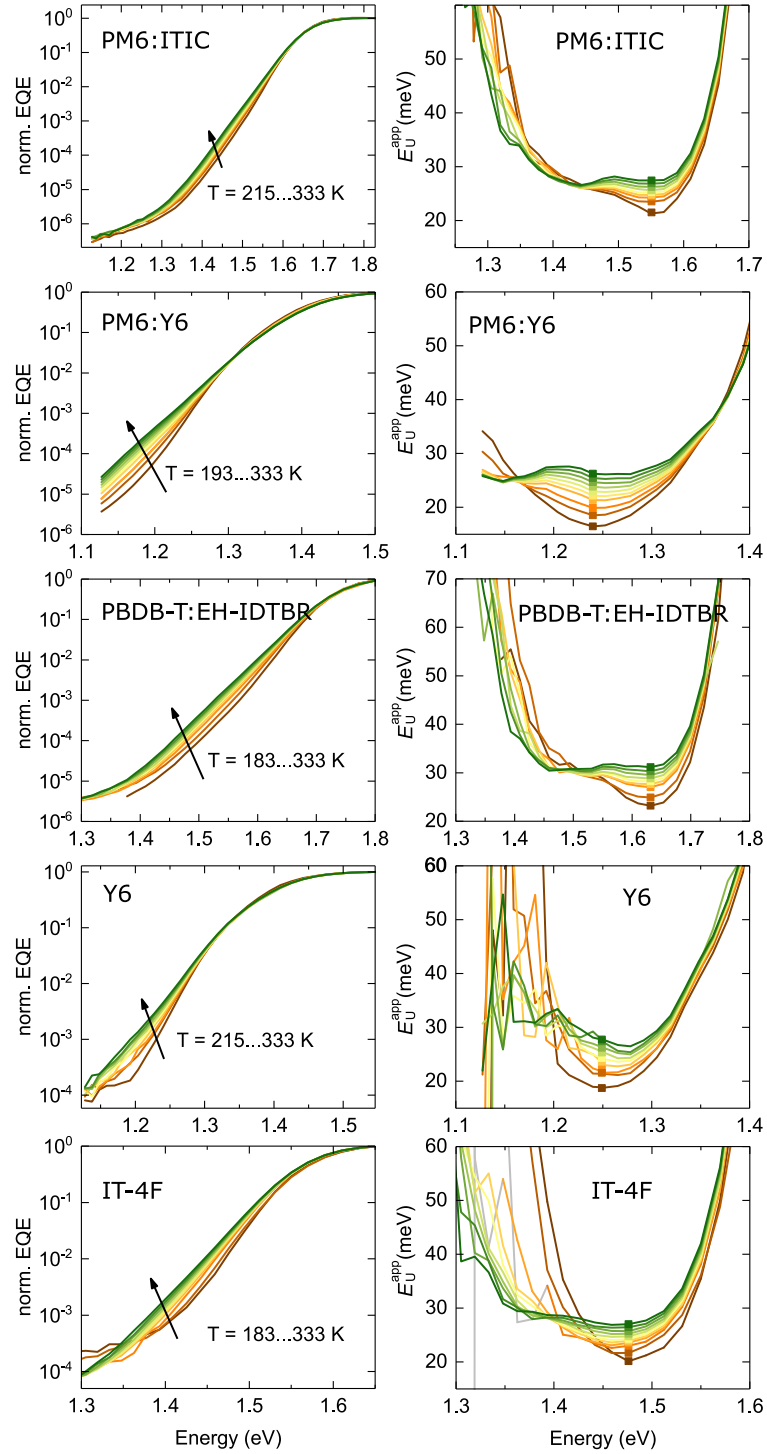


Figure B.1: Temperature-dependent, normalized external quantum efficiency (EQE) and respective apparent Urbach energy (E_U^{app}) spectra of blend (PM6:ITIC, PM6:Y6, PBDB-T:EH-IDTBR) and neat (Y6, IT-4F) material systems with device architecture ITO (100 nm)/ZnO (30 nm)/active layer/MoO₃ (8 nm)/Ag (100 nm).

B.2 Marcus Theory for Unequal Potentials

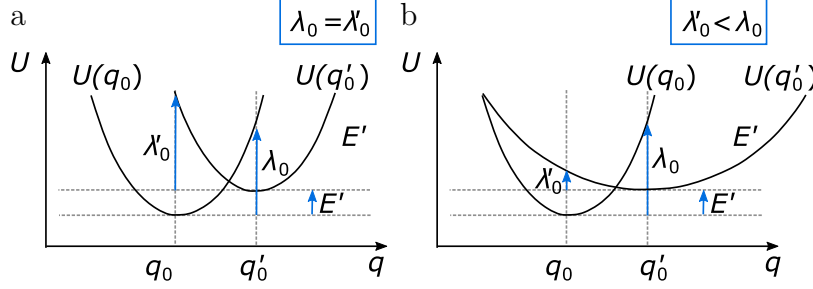


Figure B.2: Profile of the potential energy surfaces (PESs) of the ground state and the excited state, $U(q_0)$ and $U(q'_0)$, respectively. **a** Equal curvature of the PESs lead to equal reorganization energies λ_0 and λ'_0 for the ground state and the excited state, respectively. **b** Broadening of one PES with respect to the other leads to unequal reorganization energies.

In Marcus theory, the curvature of the potential energy surfaces (PES) describes the vibrational frequency of the modes and is directly related to the reorganization energy. Figure B.2 illustrates the PES as a function of the nuclear coordinate q , where $U(q_0)$ and $U(q'_0)$ denote the ground state and the excited state, respectively. Two cases can be distinguished: a) For the standard Marcus theory, the curvatures of the PESs are equal and so are the reorganization energies of the ground state λ_0 and the excited states λ'_0 . b) In the general case, the curvatures of the PESs are different resulting in different reorganization energies for the ground state and the excited state. Case b) can be viewed as an extension to the standard Marcus theory with the generalized Marcus transfer rate now reading^{181, 182}.

$$\kappa = \frac{2\pi}{\hbar} \frac{|\nu|^2 (\tilde{k}_+ + \tilde{k}_-)}{\sqrt{4 \left[\lambda'_0 + \left(1 - \frac{\lambda'_0}{\lambda_0}\right) (E' - E) \right] \pi kT}}. \quad (\text{B.1})$$

Here, E' is the energy difference between the ground state and excited state, while

$$\tilde{k}_+ = \exp \left(- \frac{\lambda_0}{kT} \left[\frac{E' - E + \lambda'_0}{\lambda'_0 + \sqrt{\lambda_0'^2 + (\lambda_0 - \lambda'_0)(E' - E + \lambda'_0)}} \right]^2 \right) \quad (\text{B.2})$$

$$\tilde{k}_- = \exp \left(- \frac{\lambda_0}{kT} \left[\frac{E' - E + \lambda'_0}{\lambda'_0 - \sqrt{\lambda_0'^2 + (\lambda_0 - \lambda'_0)(E' - E + \lambda'_0)}} \right]^2 \right) \quad (\text{B.3})$$

for $E < E' + \frac{\lambda_0 \lambda'_0}{\lambda_0 - \lambda'_0}$. Note that the rate reduces back to the standard Marcus charge-transfer rate for $\lambda'_0 \rightarrow \lambda_0$, as expected. This is demonstrated in Figure B.3, where the full expression of κ from Eq. B.1 is simulated for different ratios of λ'_0/λ_0 . Figure B.3a shows that the spectral lineshape of κ resembles a Gaussian function for λ'_0/λ_0 close to 1, while for $\lambda'_0/\lambda_0 \rightarrow 0$, it converges to an exponential function with an inverse logarithmic slope of kT . As a result, the apparent Urbach energy E_U^{app} approaches kT for $\lambda'_0/\lambda_0 \rightarrow 0$, as illustrated in Figure B.3b.

In the case of distribution for E' (e.g. Gaussian or exponential DOS), the generalized Marcus rate needs simplification since a direct integration of Eq. B.1 for a given DOS is in general analytically intractable. However, for $\lambda_0 > \lambda'_0$, the transfer rate at low photon energies, corresponding to the absorption tail, can be approximated by

$$\kappa = \frac{2\pi}{\hbar} \frac{|\nu|^2}{\sqrt{\left[\lambda'_0 + \left(1 - \frac{\lambda'_0}{\lambda_0}\right)(E' - E)\right]\pi kT}} \exp\left(-\frac{E' - E + \lambda'_0}{kT} \frac{\lambda_0}{\lambda_0 - \lambda'_0}\right) \quad (\text{B.4})$$

If $\lambda_0 \gg \lambda'_0$ (i.e. a more localized ground state and a more diffuse excited state), the dominant photon energy dependence of the absorption tail is of the form

$$\kappa \propto \exp\left(\frac{E - E'}{kT}\right) \quad (\text{B.5})$$

becoming governed by a simple Boltzmann factor. Under such conditions, the generalized Marcus rate can be approximated with a simple MA-type expression.

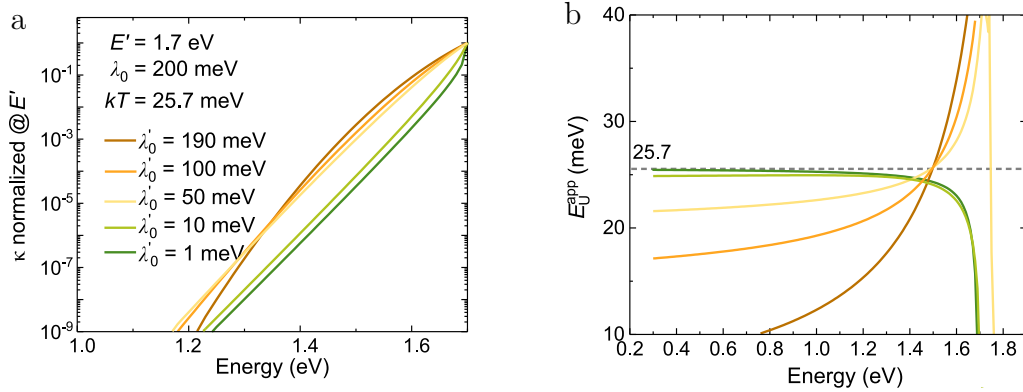


Figure B.3: **a** Generalized Marcus transfer rate simulated for different λ'_0 at room temperature assuming $\lambda_0 = 200$ meV and $E' = 1.7$ eV. κ approaching a Gaussian spectral line-shape for $\lambda'_0/\lambda_0 \rightarrow 1$ and an exponential line-shape for $\lambda'_0/\lambda_0 \rightarrow 0$. **b** Apparent Urbach energy E_U^{app} approaching kT for $\lambda'_0/\lambda_0 \rightarrow 0$.

Appendix C

Mid-gap Trap State Mediated Dark Current in Organic Photodiodes

C.1 Absorbance Spectra of Low-Gap Donor Polymers

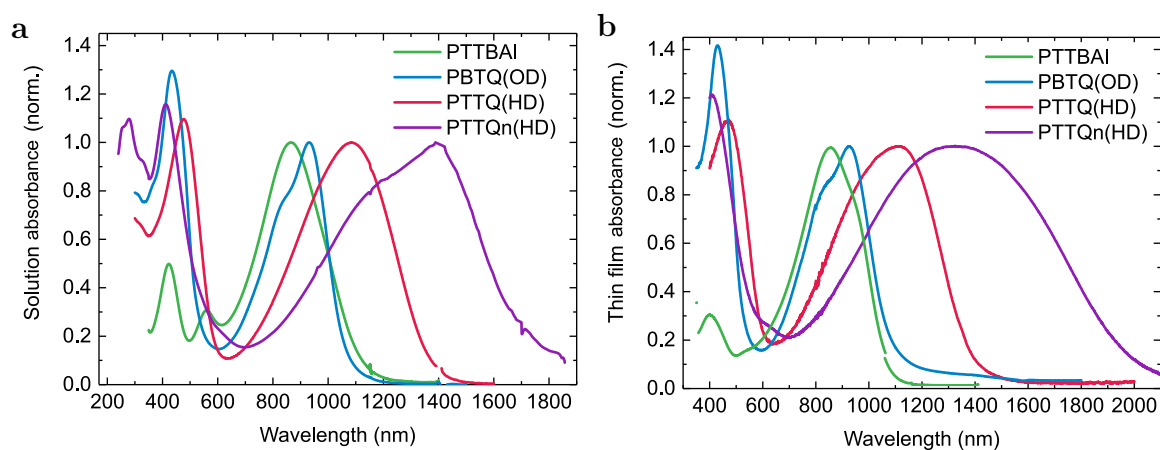


Figure C.1: Normalized absorbance of the low-gap donor polymers PTTBAI, PBTQ(OD), PTTQn(HD) and PTTQ(HD) in solution (**a**) and as a spin-coated thin-film on glass (**b**).

C.2 Current-Voltage Characteristics of Low-gap Blends

Material	I_D at -0.1 V [A]	I_{ph} at -0.1 V [A]	I_{ph}/I_D	Measured V_{OC} [V]	E_{CT} [eV]	# ref.
PTTPBAI	2.00E-6	2.00E-3	1.00E3	0.330	-	206
PTTQ(BO)	7.24E-7	2.60E-4	3.59E2	0.160	-	119
PTTQ(OD)	7.45E-8	6.07E-5	8.15E2	0.280	-	119
PBiTTQ(HD)	1.84E-7	7.30E-5	3.96E2	0.220	-	119
PBiTTQ(OD)	6.97E-8	2.07E-4	2.97E3	0.250	-	119
PTTTQ((OD)	1.38E-7	2.23E-4	1.62E3	0.260	-	119
PBTTT	1.00E-9	1.00E-2	1.00E7	0.550	1.150	119
SdiCNPBI	1.00E-5	1.00E-3	1.00E2	0.100	-	119
TPDP	1.00E-7	1.00E-3	1.00E4	0.250	-	131
m-MTDATA	3.00E-9	1.00E-3	3.33E5	0.358	0.954	131
C ₃₈ H ₃₂ S ₂ (D5)	1.90E-7	8.00E-5	4.21E2	0.307	0.856	177
TPDP	3.10E-8	1.10E-4	3.55E3	0.309	0.913	207
m-MTDATA	1.00E-9	8.70E-5	8.70E4	0.434	0.954	207
Spiro-MeO-TPD	3.90E-10	1.70E-4	4.36E5	0.531	1.369	207
ZnPc	3.10E-10	5.60E-4	1.81E6	0.583	1.132	131
ZnPc	6.70E-9	7.50E-3	1.12E6	0.553	1.180	131
TAPC	4.20E-10	1.60E-3	3.81E6	0.648	1.448	207
m-MTDATA	2.70E-7	1.27E-3	4.70E3	0.358	0.954	207
MeO-TPD	1.95E-7	3.89E-3	1.99E4	0.612	1.195	207
DMFL-NPD	2.35E-7	3.73E-3	1.59E4	0.686	1.272	207
BF-DPB	1.21E-7	4.58E-3	3.80E4	0.795	1.342	207
TCTA	1.56E-7	4.64E-3	2.98E4	0.988	1.507	207
BPAPF	2.95E-8	4.43E-3	1.50E5	0.998	1.548	207
BDA-DTP	4.01E-5	1.69E-4	4.22E0	0.034	0.730	207
BDA-DTP	7.54E-5	3.26E-4	4.33E0	0.044	0.730	207
BDA-DTP	6.52E-5	4.67E-4	7.16E0	0.106	0.751	207
BDA-BT	1.26E-7	2.30E-4	1.83E3	0.283	1.050	207

Figure C.2: Information on the materials added to Figure 7.2. Literature materials were tested in standard structure ITO/MoO₃/Donor:C₆₀/BPhen/Al devices (except for the devices from ref. ¹¹⁹ and ²⁰⁶ in which an inverted architecture glass/ITO/ZnO-PEIE/active layer/MoO₃/Ag was used), in which the active material was either a small molecule or a polymer, either solution or vacuum processed. Light current was measured under 1 sun illumination.

C.3 EQE_{EL} SPECTRA

Material	I_D at -0.1 V [A]	I_{ph} at -0.1 V [A]	I_{ph}/I_D	Measured V_{OC} [V]	E_{CT} [eV]	# ref.
BDTA-BT	1.88E-7	4.74E-4	2.52E3	0.316	1.020	207
BDTA-BT	1.77E-7	4.17E-4	2.36E3	0.364	0.999	207
P4-Ph4-DIP	1.49E-7	5.67E-3	3.81E4	1.010	1.608	207
BP-Bodipy (D8)	2.47E-7	6.93E-3	2.81E4	0.870	1.453	207
ZnPc	3.00E-7	5.39E-3	1.80E4	0.788	1.369	131
2-TNATA	2.07E-7	1.47E-3	7.08E3	0.409	1.011	207
BDTA-DTP	5.68E-5	4.61E-4	8.12E0	0.108	0.751	207
TPDP	2.08E-7	9.86E-4	4.75E3	0.256	0.913	207
C ₃₀ H ₂₄ O ₂ S ₄ (D3)	1.33E-5	9.52E-4	7.14E1	0.148	0.821	177
C ₃₀ H ₂₄ S ₆ (D2)	4.55E-6	1.44E-3	3.16E2	0.199	0.866	177
C ₃₄ H ₂₄ S ₂ (D6)	1.60E-6	1.39E-3	8.70E2	0.266	0.913	177
C ₃₈ H ₃₂ S ₂ (D5)	4.32E-6	9.05E-4	2.10E2	0.175	0.845	177
TPDP	2.07E-6	1.06E-3	5.13E2	0.251	0.902	207
C ₃₈ H ₃₂ O ₂ (D4)	7.40E-6	9.29E-4	1.26E2	0.174	0.825	177
C ₂₆ H ₁₆ S ₆ (D1)	1.47E-7	1.88E-3	1.28E4	0.309	0.959	177
C ₂₆ H ₁₆ S ₆ (D1)	8.35E-7	2.19E-3	2.62E3	0.328	0.963	177
C ₂₆ H ₁₆ S ₆ (D1)	5.04E-7	2.13E-3	4.23E3	0.387	0.975	177
C ₂₆ H ₁₆ O ₂ S ₄ (D7)	1.14E-6	1.29E-3	1.13E3	0.267	0.920	177
C ₃₀ H ₂₄ S ₆ (D2)	4.74E-6	9.76E-4	2.06E2	0.175	0.868	177
C ₃₀ H ₂₄ S ₆ (D2)	3.65E-6	1.57E-3	4.30E2	0.213	0.868	177
α -6T	1.82E-6	2.61E-3	1.43E3	0.446	1.080	207
α -6T	5.83E-7	4.03E-3	6.91E3	0.460	1.080	207
α -6T	3.77E-7	4.64E-3	1.23E4	0.982	1.550	207
α -6T	3.56E-7	6.22E-3	1.75E4	0.916	1.480	207
α -6T	4.66E-7	6.15E-3	1.32E4	0.933	1.490	207

Figure C.3: Information on the materials added to Figure 7.2. Literature materials were tested in standard structure ITO/MoO₃/Donor:C₆₀/BPhen/Al devices (except for the devices from ref.¹¹⁹ and²⁰⁶ in which an inverted architecture glass/ITO/ZnO-PEIE/active layer/MoO₃/Ag was used), in which the active material was either a small molecule or a polymer, either solution or vacuum processed. Light current was measured under 1 sun illumination..

C.3 EQE_{EL} Spectra

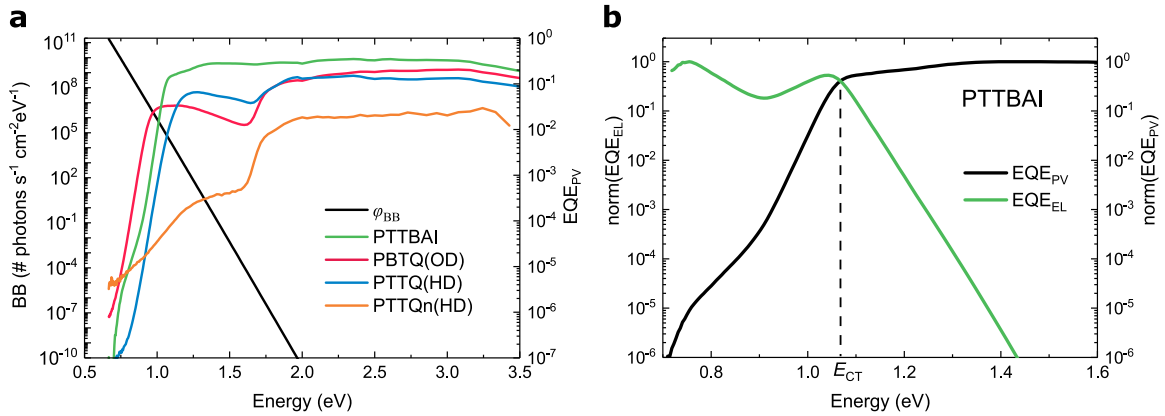


Figure C.4: **a** Plot of the EQE_{PV} spectrum and the black body radiation ϕ_{BB} in function of energy. **b** EQE_{PV} (in black) and EQE_{EL} (in red) spectra. The intercept marks E_{CT} as highlighted with a dashed vertical line.

C.4 Shockley-Read-Hall Recombination Mediated Dark Current

An organic diode device is considered that consists of contacts that are assumed to be ohmic for holes at the anode ($x = 0$) and electrons at the cathode ($x = d$), with the thickness of the active organic layer being given by d . The recombination rate between free electrons and holes, of densities n and p , inside the active layer is assumed to be dominated by trap-assisted recombination. The corresponding trap-mediated dark current density is given by

$$J = q \int_0^d U_{\text{SRH}} dx, \quad (\text{C.1})$$

where U_{SRH} is the net recombination-generation rate taking place via traps. In the Shockley-Read-Hall (SRH) formalism, U_{SRH} takes the form

$$U_{\text{SRH}} = \frac{c_n c_p N_t (np - n_i^2)}{c_n (n + n_1) + c_p (p + p_1)} \quad (\text{C.2})$$

as described in Section 2.2.3. Here, N_t is the trap density, while c_n and c_p are the capture coefficient for a free electron and hole to find an available trap site, respectively. Furthermore, $n_1 = N_C \exp\left(\frac{E_t - E_C}{kT}\right)$ and $p_1 = N_V \exp\left(\frac{E_V - E_t}{kT}\right)$, with E_C and E_V being the conduction and valence level, while E_t is the energy of the traps and kT is the thermal energy; N_C and N_V are the available density of states for free electrons and holes, respectively. Note that $n_1 p_1 = n_i^2 \equiv N_C N_V \exp\left(\frac{-E_g}{kT}\right)$, where $E_g = E_C - E_V$ is the electrical energy level gap.

In general, the carrier densities are given by $n = N_C \exp\left(\frac{E_{F_n} - E_C}{kT}\right)$ and $p = N_V \exp\left(\frac{E_V - E_{F_p}}{kT}\right)$, where E_{F_n} and E_{F_p} are the corresponding quasi-Fermi levels. For Ohmic contacts, the applied voltage may be approximated as $V = (E_{F_n} - E_{F_p})/q$, where q is the elementary charge; hence, $np = n_i^2 \exp(qV/kT)$. For not too high injection current levels, the electrical potential outside the contact regions is to a good approximation linear with x . In this case,

$$\begin{aligned} n &\approx n_{\text{cat}} \exp\left(\frac{-q[V_{\text{bi}} - V]}{kT} \left[1 - \frac{x}{d}\right]\right) \\ p &\approx p_{\text{an}} \exp\left(\frac{-q[V_{\text{bi}} - V]}{kT} \frac{x}{d}\right) \end{aligned} \quad (\text{C.3})$$

for $V \leq V_{\text{bi}}$, where n_{cat} and p_{an} are the virtual electron and hole density at the cathode and anode contact, respectively, whereas V_{bi} is an effective built-in voltage which accounts for the energy-level bending at the anode and cathode contacts: $qV_{\text{bi}} = kT \ln\left(\frac{p_{\text{an}} n_{\text{cat}}}{n_i^2}\right)$. Then, making use of $np = n_i^2 \exp(qV/kT)$, the dark current for $V < V_{\text{bi}}$ can be expressed as

$$J(V) = J_0(V) \left[\exp\left(\frac{qV}{kT}\right) - 1 \right] \quad (\text{C.4})$$

with

$$J_0(V) = qc_n c_p N_t n_i^2 \int_0^d \frac{dx}{c_n(n + n_1) + c_p(p + p_1)}. \quad (\text{C.5})$$

This integral can be approximated by making use of the following regional approximation. At the anode side, the hole density dominates in the SRH recombination rate. In this region, the contribution from electrons may be neglected. On the other hand, on the cathode side the reverse is true. In this region electrons dominate and the contribution from holes to the SRH rate is negligibly small. Hence, with

$$\begin{aligned} c_p p &\gg c_n n, x < x_{1/2} \\ c_p p &\ll c_n n, x > x_{1/2} \end{aligned} \quad (\text{C.6})$$

where $c_p p(x_{1/2}) = c_n n(x_{1/2})$ at $x = x_{1/2}$, or equivalently, $p(x_{1/2}) = \sqrt{\frac{c_n}{c_p}} n_i \exp\left(\frac{qV}{2kT}\right)$. At flat-band conditions, $V = V_{bi}$, it can be assumed that $c_p p_{an} = c_n n_{cat}$ and $p_{an} = \sqrt{\frac{c_n}{c_p}} n_i \exp\left(\frac{qV_{bi}}{2kT}\right)$. Based on the above regional approximation, Eq. C.6, the integral $J_0(V)$ may be split into two simpler integrals:

$$J_0(V) \approx qc_n c_p N_t n_i^2 \left[\int_{x_{1/2}}^d \frac{dx}{c_n n + c_n n_1 + c_p p_1} + \int_0^{x_{1/2}} \frac{dx}{c_p p + c_n n_1 + c_p p_1} \right] \quad (\text{C.7})$$

Then, after making use of Eq. C.3, Eq. C.7 can be evaluated as

$$J_0(V) = J_{0,\text{SRH}} \frac{2kT}{q[V_{bi} - V]} \times \ln \left[\frac{1 + 2B \exp\left(\frac{-qV}{2kT}\right)}{1 + 2B \exp\left(\frac{-qV_{bi}}{2kT}\right)} \right] \quad (\text{C.8})$$

allowing for the total trap-mediated current density in the dark to be obtained for $V \leq V_{bi}$ via Eq. C.4. Here, $B \equiv \frac{1}{2} \left(\sqrt{\frac{\tau_p}{\tau_n}} \frac{n_1}{n_i} + \sqrt{\frac{\tau_n}{\tau_p}} \frac{p_1}{n_i} \right)$, with $\tau_n \equiv \frac{1}{c_n N_t}$ and $\tau_p \equiv \frac{1}{c_p N_t}$ being the related lifetimes for electrons and holes, respectively, while

$$J_{0,\text{SRH}} = \frac{qn_i^2 d}{\tau_p n_1 + \tau_n p_1} \quad (\text{C.9})$$

is the actual reverse-bias dark saturation current density in the presence of trap-assisted recombination. Finally, in the case of mid-gap trap states ($n_1 \approx p_1 \approx n_i$), the associated dark current density at large forward bias (but well below V_{bi}) and at high reverse bias can be approximated by

$$J \approx J_{0,\text{SRH}} \times \begin{cases} \frac{2BkT}{q[V_{bi} - V]} \exp\left(\frac{qV}{2kT}\right), & V \gg \frac{2kT}{q} \\ \frac{V}{q[V_{bi} + |V|]}, & -V \gg \frac{2kT}{q} \end{cases} \quad (\text{C.10})$$

respectively, where $J_{0,\text{SRH}} = qn_i d / (\tau_p + \tau_n)$. On the other hand, in the limit $V \rightarrow V_{\text{bi}}$ (flat-band conditions), the dark current density (Eq. C.4 and Eq. C.8) approaches

$$J \rightarrow \frac{2BJ_{0,\text{SRH}}}{2B + \exp\left(\frac{qV_{\text{bi}}}{2kT}\right)} \left[\exp\left(\frac{qV_{\text{bi}}}{2kT}\right) - 1 \right]. \quad (\text{C.11})$$

Bibliography

- ¹ Luigi Atzori, Antonio Iera, and Giacomo Morabito. The Internet of Things: A survey. *Computer Networks*, 54(15):2787–2805, oct 2010.
- ² Philip C. Y. Chow and Takao Someya. Organic Photodetectors for Next-Generation Wearable Electronics. *Advanced Materials*, 32(15):1902045, apr 2020.
- ³ Achala Satharasinghe, Theodore Hughes-Riley, and Tilak Dias. Photodiodes embedded within electronic textiles. *Scientific Reports*, 8(1):1–13, 2018.
- ⁴ Photodiode Sensor Market Research Report by Type, by Material, by End Use, by Region-Global Forecast to 2026- Cumulative Impact of COVID-19 (accessed: August 2021), 2021.
- ⁵ S. M. Sze and Kwok K. Ng. *Physics of Semiconductor Devices*. Wiley, New York, 1981.
- ⁶ Xiaodong Liu, Yiwei Lin, Yingjie Liao, Jiazun Wu, and Yonghao Zheng. Recent advances in organic near-infrared photodiodes. *Journal of Materials Chemistry C*, 6(14):3499–3513, 2018.
- ⁷ F. Pelayo García de Arquer, Ardan Armin, Paul Meredith, and Edward H. Sargent. Erratum: Corrigendum: Solution-processed semiconductors for next-generation photodetectors. *Nature Reviews Materials*, 2(3):17012, mar 2017.
- ⁸ Alexandra F. Paterson, Saumya Singh, Kealan J. Fallon, Thomas Hodsden, Yang Han, Bob C. Schroeder, Hugo Bronstein, Martin Heeney, Iain McCulloch, and Thomas D. Anthopoulos. Recent Progress in High-Mobility Organic Transistors: A Reality Check. *Advanced Materials*, 30(36):1–33, 2018.
- ⁹ You Seung Rim, Sang-Hoon Bae, Huajun Chen, Nicholas De Marco, and Yang Yang. Recent Progress in Materials and Devices toward Printable and Flexible Sensors. *Advanced Materials*, 28(22):4415–4440, jun 2016.
- ¹⁰ Hsiang Yu Chen, Michael K.F. Lo, Guanwen Yang, Harold G. Monbouquette, and Yang Yang. Nanoparticle-assisted high photoconductive gain in composites of polymer and fullerene. *Nature Nanotechnology*, 3(9):543–547, 2008.
- ¹¹ Flexible, Printed OLED Displays 2020-2030: Forecasts, Markets, Technologies (accessed: August 2021).
- ¹² Jinfeng Han, Ji Qi, Xiuping Zheng, Yukun Wang, Liuyong Hu, Chang Guo, Yang Wang, Yuning Li, Dongge Ma, Wenqiang Qiao, and Zhi Yuan Wang. Low-bandgap donor–acceptor polymers for photodetectors with photoresponsivity from 300 nm to 1600 nm. *Journal of Materials Chemistry C*, 5(1):159–165, 2017.
- ¹³ Wenbin Wang, Fujun Zhang, Mingde Du, Lingliang Li, Miao Zhang, Kai Wang, Yongsheng Wang, Bin Hu, Ying Fang, and Jinsong Huang. Highly Narrowband Photomultiplication Type Organic Photodetectors. *Nano Letters*, 17(3):1995–2002, 2017.

BIBLIOGRAPHY

- ¹⁴ Bernhard Siegmund, Andreas Mischok, Johannes Benduhn, Olaf Zeika, Sascha Ullbrich, Frederik Nehm, Matthias Böhm, Donato Spoltore, Hartmut Fröb, Christian Körner, Karl Leo, and Koen Vandewal. Organic narrowband near-infrared photodetectors based on intermolecular charge-transfer absorption. *Nature Communications*, 8(15421):1–6, 2017.
- ¹⁵ Kwang Hyup An, Brendan O'Connor, Kevin P. Pipe, and Max Shtein. Organic photodetector with spectral response tunable across the visible spectrum by means of internal optical microcavity. *Organic Electronics: physics, materials, applications*, 10(6):1152–1157, 2009.
- ¹⁶ Andreas Mischok, Bernhard Siegmund, Dhriti Sundar Ghosh, Johannes Benduhn, Donato Spoltore, Matthias Böhm, Hartmut Fröb, Christian Körner, Karl Leo, and Koen Vandewal. Controlling Tamm Plasmons for Organic Narrowband Near-Infrared Photodetectors. *ACS Photonics*, 4(9):2228–2234, 2017.
- ¹⁷ Nicholas P. Sergeant, Afshin Hadipour, Bjoern Niesen, David Cheyns, Paul Heremans, Peter Peumans, and Barry P. Rand. Design of transparent anodes for resonant cavity enhanced light harvesting in organic solar cells. *Advanced Materials*, 24(6):728–732, 2012.
- ¹⁸ C. K. Chiang, C. R. Fincher, Y. W. Park, A. J. Heeger, H. Shirakawa, E. J. Louis, S. C. Gau, and Alan G. MacDiarmid. Electrical conductivity in doped polyacetylene. *Physical Review Letters*, 39(17):1098–1101, 1977.
- ¹⁹ Barbara H. Stuart. Organic Molecules. In *Infrared Spectroscopy: Fundamentals and Applications*, pages 71–93. jul 2005.
- ²⁰ R A Marcus. Relation between charge transfer absorption and fluorescence spectra and the inverted region. *The Journal of Physical Chemistry*, 93(8):3078–3086, apr 1989.
- ²¹ Veaceslav Coropceanu, A Demetrio, Silva Filho, Yoann Olivier, Robert Silbey, and Jean-luc Bre. Charge Transport in Organic Semiconductors. *Chem. Rev.*, 107:926–952, 2007.
- ²² Hua Geng, Yingli Niu, Qian Peng, Zhigang Shuai, Veaceslav Coropceanu, and Jean-Luc Brédas. Theoretical study of substitution effects on molecular reorganization energy in organic semiconductors. *The Journal of Chemical Physics*, 135(10):104703, sep 2011.
- ²³ Zhigang Shuai, Weitang Li, Jiajun Ren, Yuqian Jiang, and Hua Geng. Applying Marcus theory to describe the carrier transports in organic semiconductors: Limitations and beyond. *The Journal of Chemical Physics*, 153(8):080902, aug 2020.
- ²⁴ Rudolph A. Marcus. Electron transfer reactions in chemistry. Theory and experiment. *Rev. Mod. Phys.*, 65(3):599, 1993.

-
- ²⁵ Rodrigo Noriega, Jonathan Rivnay, Koen Vandewal, Felix P. V. Koch, Natalie Stingelin, Paul Smith, Michael F. Toney, and Alberto Salleo. A general relationship between disorder, aggregation and charge transport in conjugated polymers. *Nature Materials*, 12(11):1038–1044, nov 2013.
- ²⁶ Heinz Bässler and Anna Köhler. Charge Transport in Organic Semiconductors. In Robert M. Metzger, editor, *Unimolecular and Supramolecular Electronics I: Chemistry and Physics Meet at Metal-Molecule Interfaces*, pages 1–65. Springer Berlin Heidelberg, 2011.
- ²⁷ H. Bässler. Charge Transport in Disordered Organic Photoconductors a Monte Carlo Simulation Study. *Physica Status Solidi (B)*, 175(1):15–56, 1993.
- ²⁸ Franz Urbach. The long-wavelength edge of photographic sensitivity and of the electronic Absorption of Solids. *Physical Review*, 92(5):1324, 1953.
- ²⁹ J. I. Pankove. Absorption Edge of Impure Gallium Arsenide. *Physical Review*, 140(6A):A2059–A2065, dec 1965.
- ³⁰ M.A. Kastner, Tineke Thio, and Don Monroe. Thermally generated defects in liquid and glassy As₂Se₃. *Journal of Non-Crystalline Solids*, 66(1-2):309–314, 1984.
- ³¹ D. J. Dunstan. Evidence for a common origin of the Urbach tails in amorphous and crystalline semiconductors. *Journal of Physics C: Solid State Physics*, 15(13), 1982.
- ³² C. Q. Hu, F. F. Meng, M. Wen, Z. Q. Gu, J. Y. Wang, X. F. Fan, and W. T. Zheng. Relationship between dielectric coefficient and Urbach tail width of hydrogenated amorphous germanium carbon alloy films. *Applied Physics Letters*, 101(4), 2012.
- ³³ Bhavtosh Bansal, V. K. Dixit, V. Venkataraman, and H. L. Bhat. Alloying induced degradation of the absorption edge of InAs_xSb_{1-x}. *Applied Physics Letters*, 90(10):101905, mar 2007.
- ³⁴ G. D. Cody, T. Tiedje, B. Abeles, B. Brooks, and Y. Goldstein. Disorder and the optical-absorption edge of hydrogenated amorphous silicon. *Physical Review Letters*, 47(20):1480–1483, 1981.
- ³⁵ Ismardo Bonalde, Ernesto Medina, Miguel Rodríguez, S. M. Wasim, G. Marín, C. Rincón, A. Rincón, and C. Torres. Urbach tail, disorder, and localized modes in ternary semiconductors. *Physical Review B*, 69(19):195201, may 2004.
- ³⁶ Richard Corkish and Martin A. Green. Erratum: “Band edge optical absorption in intrinsic silicon: Assessment of the indirect transition and disorder models” [J. Appl. Phys. 73, 3988 (1993)]. *Journal of Applied Physics*, 74(10):6462–6462, nov 1993.
- ³⁷ John D. Dow and David Redfield. Toward a Unified Theory of Urbach’s Rule and Exponential Absorption Edges. *Physical Review B*, 5(2):594–610, 1972.

BIBLIOGRAPHY

- ³⁸ Andrej Classen, Christos L. Chochos, Larry Lüer, Vasilis G. Gregoriou, Jonas Wortmann, Andres Osvet, Karen Forberich, Iain McCulloch, Thomas Heumüller, and Christoph J. Brabec. The role of exciton lifetime for charge generation in organic solar cells at negligible energy-level offsets. *Nature Energy*, 2020.
- ³⁹ Jing Liu, Shangshang Chen, Deping Qian, Bhoj Gautam, Guofang Yang, Jingbo Zhao, Jonas Bergqvist, Fengling Zhang, Wei Ma, Harald Ade, Olle Inganäs, Kenan Gundogdu, Feng Gao, and He Yan. Fast charge separation in a non-fullerene organic solar cell with a small driving force. *Nature Energy*, 1(7):1–7, 2016.
- ⁴⁰ D. Baran, T. Kirchartz, S. Wheeler, S. Dimitrov, M. Abdelsamie, J. Gorman, R. S. Ashraf, S. Holliday, A. Wadsworth, N. Gasparini, P. Kaienburg, H. Yan, A. Amassian, C. J. Brabec, J. R. Durrant, and I. McCulloch. Reduced voltage losses yield 10% efficient fullerene free organic solar cells with >1 V open circuit voltages. *Energy Environ. Sci.*, 9(12):3783–3793, 2016.
- ⁴¹ Koen Vandewal, Kristofer Tvingstedt, Abay Gadisa, Olle Inganäs, and Jean V. Manca. Relating the open-circuit voltage to interface molecular properties of donor:acceptor bulk heterojunction solar cells. *Physical Review B*, 81(12):125204, mar 2010.
- ⁴² Kristofer Tvingstedt, Johannes Benduhn, and Koen Vandewal. Temperature dependence of the spectral line-width of charge-transfer state emission in organic solar cells; static vs. dynamic disorder. *Materials Horizons*, 7(7):1888–1900, 2020.
- ⁴³ Michel Panhans, Sebastian Hutsch, Johannes Benduhn, Vasileios C Nikolis, Tim Vangerven, Koen Vandewal, Karl Sebastian Schellhammer, and Frank Ortman. Molecular vibrations reduce the maximum achievable photovoltage in organic solar cells. *Nature Communications*, (2020):1–10, 2020.
- ⁴⁴ Clemens Göhler, Maria Saladina, Yazhong Wang, Donato Spoltore, Johannes Benduhn, Karl Leo, and Carsten Deibel. Temperature-Dependent Charge-Transfer-State Absorption and Emission Reveal the Dominant Role of Dynamic Disorder in Organic Solar Cells. *Physical Review Applied*, 15(6):064009, jun 2021.
- ⁴⁵ Andrew Skumanich and J. C. Scott. Photothermal Deflection Spectroscopy: A Sensitive Absorption Technique for Organic Thin Films. *Molecular Crystals and Liquid Crystals Incorporating Nonlinear Optics*, 183(1):365–370, 2007.
- ⁴⁶ A. C. Boccara, Warren Jackson, Nabil M. Amer, and D. Fournier. Sensitive photothermal deflection technique for measuring absorption in optically thin media: erratum. *Optics Letters*, 6(1):51, 1981.
- ⁴⁷ Stefaan De Wolf, Jakub Holovsky, Soo Jin Moon, Philipp Löper, Bjoern Niesen, Martin Ledinsky, Franz Josef Haug, Jun Ho Yum, and Christophe Ballif. Organometallic halide perovskites: Sharp optical absorption edge and its relation to photovoltaic performance. *Journal of Physical Chemistry Letters*, 5(6):1035–1039, 2014.

- ⁴⁸ Stefan Zeiske, Christina Kaiser, Paul Meredith, and Ardalan Armin. Sensitivity of Sub-Bandgap External Quantum Efficiency Measurements of Solar Cells under Electrical and Light Bias. *ACS Photonics*, 7(1):256–264, 2019.
- ⁴⁹ Ardalan Armin, Ivan Kassal, Paul E. Shaw, Mike Hambsch, Martin Stolterfoht, Dani M. Lyons, Jun Li, Zugui Shi, Paul L. Burn, and Paul Meredith. Spectral dependence of the internal quantum efficiency of organic solar cells: Effect of charge generation pathways. *Journal of the American Chemical Society*, 136(32):11465–11472, 2014.
- ⁵⁰ Koen Vandewal, Steve Albrecht, Eric T Hoke, Kenneth R Graham, Johannes Widmer, Jessica D Douglas, Marcel Schubert, William R Mateker, Jason T Bloking, George F Burkhard, Alan Sellinger, J M Frechet, Aram Amassian, Moritz K Riede, Michael D McGehee, Dieter Neher, and Alberto Salleo. Efficient charge generation by relaxed charge-transfer states at organic interfaces. *Nature Materials*, 13(1):63–68, 2014.
- ⁵¹ Jona Kurpiers, Thomas Ferron, Steffen Roland, Marius Jakoby, Tobias Thiede, Frank Jaiser, Steve Albrecht, Silvia Janietz, Brian A. Collins, Ian A. Howard, and Dieter Neher. Probing the pathways of free charge generation in organic bulk heterojunction solar cells. *Nature Communications*, 9(1):1–11, 2018.
- ⁵² Mathias List, Tanmoy Sarkar, Pavlo Perkhun, Jörg Ackermann, Chieh Luo, and Uli Würfel. Correct determination of charge transfer state energy from luminescence spectra in organic solar cells. *Nature Communications*, 9(1):1–8, 2018.
- ⁵³ Jean Luc Bredas. Mind the gap! *Materials Horizons*, 1(1):17–19, 2014.
- ⁵⁴ Zhi-An Lan, Guigang Zhang, Xiong Chen, Yongfan Zhang, Kai A. I. Zhang, and Xinchun Wang. Reducing the Exciton Binding Energy of Donor–Acceptor-Based Conjugated Polymers to Promote Charge-Induced Reactions. *Angewandte Chemie International Edition*, 58(30):10236–10240, jul 2019.
- ⁵⁵ Lingyun Zhu, Yuaping Yi, Liping Chen, and Zhigang Shua. Exciton binding energy of electronic polymers: A first principles study. *Journal of Theoretical and Computational Chemistry*, 07(04):517–530, 2008.
- ⁵⁶ S. Alvarado, P. Seidler, D. Lidzey, and D. Bradley. Direct Determination of the Exciton Binding Energy of Conjugated Polymers Using a Scanning Tunneling Microscope. *Physical Review Letters*, 81(5):1082–1085, aug 1998.
- ⁵⁷ R. W. Lof, M. A. van Veenendaal, B. Koopmans, H. T. Jonkman, and G. A. Sawatzky. Band gap, excitons, and Coulomb interaction in solid C60. *Physical Review Letters*, 68(26):3924–3927, 1992.
- ⁵⁸ M. Knupfer. Exciton binding energies in organic semiconductors. *Applied Physics A*, 77(5):623–626, oct 2003.

BIBLIOGRAPHY

- ⁵⁹ Yifan Dong, Hyojung Cha, Jiangbin Zhang, Ernest Pastor, Pabitra Shakya Tuladhar, Iain McCulloch, James R. Durrant, and Artem A. Bakulin. The binding energy and dynamics of charge-transfer states in organic photovoltaics with low driving force for charge separation. *Journal of Chemical Physics*, 150(10), 2019.
- ⁶⁰ Simon Gélinas, Olivier Paré-Labrosse, Colin Nadeau Brosseau, Sebastian Albert-Seifried, Christopher R. McNeill, Kiril R. Kirov, Ian A. Howard, Richard Leonelli, Richard H. Friend, and Carlos Silva. The binding energy of charge-transfer excitons localized at polymeric semiconductor heterojunctions. *Journal of Physical Chemistry C*, 115(14):7114–7119, 2011.
- ⁶¹ Stavros Athanasopoulos, Franz Schauer, Vojtech Nádaždy, Mareike Weiß, Frank Julian Kahle, Ullrich Scherf, Heinz Bässler, and Anna Köhler. What is the Binding Energy of a Charge Transfer State in an Organic Solar Cell? *Advanced Energy Materials*, 9(24):1–11, 2019.
- ⁶² Johannes Benduhn, Kristofer Tvingstedt, Fortunato Piersimoni, Sascha Ullbrich, Yeli Fan, Manuel Tropiano, Kathryn A. McGarry, Olaf Zeika, Moritz K. Riede, Christopher J. Douglas, Stephen Barlow, Seth R. Marder, Dieter Neher, Donato Spoltore, and Koen Vandewal. Intrinsic non-radiative voltage losses in fullerene-based organic solar cells. *Nature Energy*, 2(6):17053, jun 2017.
- ⁶³ G. Yu, J. Gao, J. C. Hummelen, F. Wudl, and A. J. Heeger. Polymer Photovoltaic Cells: Enhanced Efficiencies via a Network of Internal Donor-Acceptor Heterojunctions. *Science*, 270:1789–1791, 1995.
- ⁶⁴ Safa Shoaee, Tracey M. Clarke, Chun Huang, Stephen Barlow, Seth R. Marder, Martin Heeney, Iain McCulloch, and James R. Durrant. Acceptor energy level control of charge photogeneration in organic donor/acceptor blends. *Journal of the American Chemical Society*, 132(37):12919–12926, 2010.
- ⁶⁵ Weiwei Li, Koen H. Hendriks, Alice Furlan, Martijn M. Wienk, and René A.J. Janssen. High quantum efficiencies in polymer solar cells at energy losses below 0.6 eV. *Journal of the American Chemical Society*, 137(6):2231–2234, 2015.
- ⁶⁶ Yufei Zhong, Martina Causa', Gareth John Moore, Philipp Krauspe, Bo Xiao, Florian Günther, Jonas Kublitski, Rishi Shivhare, Johannes Benduhn, Eyal BarOr, Subhrangsu Mukherjee, Kaila M. Yallum, Julien Réhault, Stefan C.B. Mannsfeld, Dieter Neher, Lee J. Richter, Dean M. DeLongchamp, Frank Ortmann, Koen Vandewal, Erjun Zhou, and Natalie Banerji. Sub-picosecond charge-transfer at near-zero driving force in polymer:non-fullerene acceptor blends and bilayers. *Nature Communications*, 11(1):1–10, 2020.
- ⁶⁷ Elham Rezasoltani, Anne A.Y. Guilbert, Jun Yan, Xabier Rodríguez-Martínez, Mohammed Azzouzi, Flurin Eisner, Sachetan M. Tuladhar, Zeinab Hamid, Andrew Wadsworth, Iain McCulloch, Mariano Campoy-Quiles, and Jenny Nelson.

- Correlating the Phase Behavior with the Device Performance in Binary Poly-3-hexylthiophene: Nonfullerene Acceptor Blend Using Optical Probes of the Microstructure. *Chemistry of Materials*, 32(19):8294–8305, 2020.
- ⁶⁸ Yuliar Firdaus, Vincent M. Le Corre, Safakath Karuthedath, Wenlan Liu, Anastasia Markina, Wentao Huang, Shirsopratim Chattopadhyay, Masrur Morshed Nahid, Mohamad I. Nugraha, Yuanbao Lin, Akmaral Seitkhan, Aniruddha Basu, Weimin Zhang, Iain McCulloch, Harald Ade, John Labram, Frédéric Laquai, Denis Andrienko, L. Jan Anton Koster, and Thomas D. Anthopoulos. Long-range exciton diffusion in molecular non-fullerene acceptors. *Nature Communications*, 11(1), 2020.
- ⁶⁹ Hyojung Cha, George Fish, Joel Luke, Ahmad Alraddadi, Hyun Hwi Lee, Weimin Zhang, Yifan Dong, Saurav Limbu, Andrew Wadsworth, Iuliana P. Maria, Laia Francàs, Hou Lon Sou, Tian Du, Ji-Seon Kim, Martyn A. McLachlan, Iain McCulloch, and James R. Durrant. Suppression of Recombination Losses in Polymer:Nonfullerene Acceptor Organic Solar Cells due to Aggregation Dependence of Acceptor Electron Affinity. *Advanced Energy Materials*, 9(27):1901254, jul 2019.
- ⁷⁰ Safa Shoaee, Selvam Subramaniam, Hao Xin, Chaz Keiderling, Pabitra Shakya Tuladhar, Fiona Jamieson, Samson A. Jenekhe, and James R. Durrant. Charge photogeneration for a series of thiazolo-thiazole donor polymers blended with the fullerene electron acceptors PCBM and ICBA. *Advanced Functional Materials*, 23(26):3286–3298, 2013.
- ⁷¹ Artem A. Bakulin, Akshay Rao, Vlad G. Pavelyev, P. H. M. van Loosdrecht, Maxim S. Pshenichnikov, Dorota Niedzialek, Jérôme Cornil, David Beljonne, and Richard H. Friend. The Role of Driving Energy and Delocalized States for Charge Separation in Organic Semiconductors. *Science*, 335(6074):1340–1344, mar 2012.
- ⁷² Julien Gorenflot, Michael C. Heiber, Andreas Baumann, Jens Lorrmann, Matthias Gunz, Vladimir Dyakonov, and Carsten Deibel. Nongeminate recombination in neat P3HT and P3HT:PCBM blend films. *Journal of Applied Physics*, 115(14):0–9, 2014.
- ⁷³ Safa Shoaee, Ardalán Armin, Martin Stolterfoht, Seyed Mehrdad Hosseini, Jona Kurpiers, and Dieter Neher. Decoding Charge Recombination through Charge Generation in Organic Solar Cells. *Solar RRL*, 3(11):1900184, nov 2019.
- ⁷⁴ Timothy M Burke, Sean Sweetnam, Koen Vandewal, and Michael D McGehee. Beyond Langevin Recombination : How Equilibrium Between Free Carriers and Charge Transfer States Determines the Open-Circuit Voltage of Organic Solar Cells. *Advanced Energy Materials*, 1500123:1–12, 2015.
- ⁷⁵ W. Shockley and W. T. Read. Statistics of the recombinations of holes and electrons. *Physical Review*, 87(5):835–842, 1952.
- ⁷⁶ R.N. Hall. Recombination processes in semiconductors. *Proceedings of the IEE - Part B: Electronic and Communication Engineering*, 106(17S):923–931, may 1959.

BIBLIOGRAPHY

- ⁷⁷ Chih Tang Sah, Robert N. Noyce, and William Shockley. Carrier Generation and Recombination in P-N Junctions and P-N Junction Characteristics. *Proceedings of the IRE*, 45(9):1228–1243, 1957.
- ⁷⁸ Sarah R. Cowan, Natalie Banerji, Wei Lin Leong, and Alan J. Heeger. Charge formation, recombination, and sweep-out dynamics in organic solar cells. *Advanced Functional Materials*, 22(6):1116–1128, 2012.
- ⁷⁹ Steven A. Hawks, Gang Li, Yang Yang, and Robert A. Street. Band tail recombination in polymer: Fullerene organic solar cells. *Journal of Applied Physics*, 116(7), 2014.
- ⁸⁰ Paula Hartnagel and Thomas Kirchartz. Understanding the Light-Intensity Dependence of the Short-Circuit Current of Organic Solar Cells. *Advanced Theory and Simulations*, 3(10):1–11, 2020.
- ⁸¹ M. Magdalena Mandoc, Welmoed Veurman, L. Jan Anton Koster, Bert De Boer, and Paul W.M. Blom. Origin of the reduced fill factor and photocurrent in MDMO-PPV:PCNEPV all-polymer solar cells. *Advanced Functional Materials*, 17(13):2167–2173, 2007.
- ⁸² Jiangzhao Chen and Nam Gyu Park. Causes and Solutions of Recombination in Perovskite Solar Cells. *Advanced Materials*, 31(47):1–56, 2019.
- ⁸³ Phil Calado, Dan Burkitt, Jizhong Yao, Joel Troughton, Trystan M. Watson, Matt J. Carnie, Andrew M. Telford, Brian C. O’Regan, Jenny Nelson, and Piers R.F. Barnes. Identifying Dominant Recombination Mechanisms in Perovskite Solar Cells by Measuring the Transient Ideality Factor. *Physical Review Applied*, 11(4):1, 2019.
- ⁸⁴ Nasim Zarrabi, Oskar J. Sandberg, Stefan Zeiske, Wei Li, Drew B. Riley, Paul Meredith, and Ardalan Armin. Charge-generating mid-gap trap states define the thermodynamic limit of organic photovoltaic devices. *Nature Communications*, 11(1):5567, dec 2020.
- ⁸⁵ Jonas Kublitski, Andreas Hofacker, Bahman K Boroujeni, Johannes Benduhn, Vasileios C Nikolis, Christina Kaiser, Donato Spoltore, Hans Kleemann, Axel Fischer, Frank Ellinger, Koen Vandewal, and Karl Leo. Reverse dark current in organic photodetectors and the major role of traps as source of noise. *Nature Communications*, 12(1):551, dec 2021.
- ⁸⁶ Stefan Zeiske, Oskar J. Sandberg, Nasim Zarrabi, Wei Li, Paul Meredith, and Ardalan Armin. Direct observation of trap-assisted recombination in organic photovoltaic devices. *Nature Communications*, 12(1):3603, dec 2021.
- ⁸⁷ Alexander Wagenpfahl, Carsten Deibel, and Vladimir Dyakonov. Organic solar cell efficiencies under the aspect of reduced surface recombination velocities. *IEEE Journal on Selected Topics in Quantum Electronics*, 16(6):1759–1763, 2010.

-
- ⁸⁸ Oskar J. Sandberg and Ardalan Armin. On the effect of surface recombination in thin film solar cells, light emitting diodes and photodetectors. *Synthetic Metals*, 254(June):114–121, 2019.
- ⁸⁹ Jun Kai Tan, Rui Qi Png, Chao Zhao, and Peter K.H. Ho. Ohmic transition at contacts key to maximizing fill factor and performance of organic solar cells. *Nature Communications*, 9(1):1–8, 2018.
- ⁹⁰ E.A. Silinsh, G.A. Shlihta, and A.J. Jurgis. A model description of charge carrier transport phenomena in organic molecular crystals. II. Perylene. *Chemical Physics*, 155(3):389–399, sep 1991.
- ⁹¹ Jiye Lee, Koen Vandewal, Shane R. Yost, Matthias E. Bahlke, Ludwig Goris, Marc A. Baldo, Jean V. Manca, and Troy Van Voorhis. Charge transfer state versus hot exciton dissociation in polymer-fullerene blended solar cells. *Journal of the American Chemical Society*, 132(34):11878–11880, 2010.
- ⁹² Saeed-uz-zaman Khan, Giacomo Londi, Xiao Liu, Michael A Fusella, Gabriele D’Avino, Luca Muccioli, Alyssa N Brigeman, Bjoern Niesen, Terry Chien-jen Yang, Yoann Olivier, Jordan T Dull, Noel C Giebink, David Beljonne, and Barry P Rand. Multiple Charge Transfer States in Donor–Acceptor Heterojunctions with Large Frontier Orbital Energy Offsets. *Chemistry of Materials*, 31(17):6808–6817, sep 2019.
- ⁹³ Ching Hong Tan, Andrew Wadsworth, Nicola Gasparini, Scot Wheeler, Sarah Holliday, Raja S. Ashraf, Stoichko D. Dimitrov, Derya Baran, Iain McCulloch, and James R. Durrant. Excitation Wavelength-Dependent Internal Quantum Efficiencies in a P3HT/Nonfullerene Acceptor Solar Cell. *Journal of Physical Chemistry C*, 123(10):5826–5832, 2019.
- ⁹⁴ Lorena Perdigón-Toro, Huotian Zhang, Anastasia Markina, Jun Yuan, Seyed Mehrdad Hosseini, Christian M. Wolff, Guangzheng Zuo, Martin Stolterfoht, Yingping Zou, Feng Gao, Denis Andrienko, Safa Shoaee, and Dieter Neher. Barrierless Free Charge Generation in the High-Performance PM6:Y6 Bulk Heterojunction Non-Fullerene Solar Cell. *Advanced Materials*, 32(9), 2020.
- ⁹⁵ Le Quang Phuong, Seyed Mehrdad Hosseini, Oskar J. Sandberg, Yingping Zou, Han Young Woo, Dieter Neher, and Safa Shoaee. Quantifying Quasi-Fermi Level Splitting and Open-Circuit Voltage Losses in Highly Efficient Nonfullerene Organic Solar Cells. *Solar RRL*, 5(1):1–6, 2021.
- ⁹⁶ Kyra N. Schwarz, Paul B. Geraghty, Valerie D. Mitchell, Saeed Uz Zaman Khan, Oskar J. Sandberg, Nasim Zarrabi, Bryan Kudisch, Jegadesan Subbiah, Trevor A. Smith, Barry P. Rand, Ardalan Armin, Gregory D. Scholes, David J. Jones, and Kenneth P. Ghiggino. Reduced Recombination and Capacitor-like Charge Buildup in an Organic Heterojunction. *Journal of the American Chemical Society*, 142(5):2562–2571, 2020.

BIBLIOGRAPHY

- ⁹⁷ Ardalan Armin, Jegadesan Subbiah, Martin Stolterfoht, Safa Shoaee, Zeyun Xiao, Shirong Lu, David J. Jones, and Paul Meredith. Reduced Recombination in High Efficiency Molecular Nematic Liquid Crystalline: Fullerene Solar Cells. *Advanced Energy Materials*, 6(22), 2016.
- ⁹⁸ Carr Hoi Yi Ho, Sin Hang Cheung, Ho-Wa Li, Ka Lok Chiu, Yuanhang Cheng, Hang Yin, Mau Hing Chan, Franky So, Sai-Wing Tsang, and Shu Kong So. Using Ultralow Dosages of Electron Acceptor to Reveal the Early Stage Donor-Acceptor Electronic Interactions in Bulk Heterojunction Blends. *Advanced Energy Materials*, 7(12):1602360, jun 2017.
- ⁹⁹ L. Goris, K. Haenen, M. Nesládek, P. Wagner, D. Vanderzande, L. De Schepper, J. D’haen, L. Luisen, and J. V. Manca. Absorption phenomena in organic thin films for solar cell applications investigated by photothermal deflection spectroscopy. *Journal of Materials Science*, 40(6):1413–1418, 2005.
- ¹⁰⁰ Giulio Simone, Matthew J. Dyson, Christ H. L. Weijtens, Stefan C. J. Meskers, Reinder Coehoorn, René A. J. Janssen, and Gerwin H. Gelinck. On the Origin of Dark Current in Organic Photodiodes. *Advanced Optical Materials*, 8(1):1901568, jan 2020.
- ¹⁰¹ Yichu Zheng, Axel Fischer, Natalia Sergeeva, Sebastian Reineke, and Stefan C.B. Mannsfeld. Exploiting lateral current flow due to doped layers in semiconductor devices having crossbar electrodes. *Organic Electronics*, 65(July 2018):82–90, 2019.
- ¹⁰² Andrew H Steinbach, John M Martinis, and Michel H Devoret. Observation of Hot-Electron Shot Noise in a Metallic Resistor. *Physical Review Lett*, 76(20):3806–3809, 1996.
- ¹⁰³ R J Schoelkopf, P J Burke, A A Kozhevnikov, and D E Prober. Frequency Dependence of Shot Noise in a Diffusive Mesoscopic Conductor. *Physical Review Letters*, 78(17):7–10, 1997.
- ¹⁰⁴ K E Nagaev. Frequency-Dependent Shot Noise in Long Disordered Superconductor – Normal-Metal – Superconductor Contacts. *Physical Review Letters*, 86(14):4–7, 2001.
- ¹⁰⁵ Koen Vandewal. Interfacial Charge Transfer States in Condensed Phase Systems. *Annual Review of Physical Chemistry*, 67(1):113–133, 2016.
- ¹⁰⁶ Martin Stolterfoht, Bronson Philippa, Safa Shoaee, Hui Jin, Wei Jiang, Ronald D. White, Paul L. Burn, Paul Meredith, and Almantas Pivrikas. Charge Transport without Recombination in Organic Solar Cells and Photodiodes. *Journal of Physical Chemistry C*, 119(48):26866–26874, 2015.
- ¹⁰⁷ Aren Yazmaciyan, Martin Stolterfoht, Paul L. Burn, Qianqian Lin, Paul Meredith, and Ardalan Armin. Recombination Losses Above and Below the Transport Percolation Threshold in Bulk Heterojunction Organic Solar Cells. *Advanced Energy Materials*, 8(18), 2018.

-
- ¹⁰⁸ Gerasimos Konstantatos, Jason Clifford, Larissa Levina, and Edward H. Sargent. Sensitive solution-processed visible-wavelength photodetectors. *Nature Photonics*, 1(9):531–534, 2007.
- ¹⁰⁹ Fawen Guo, Bin Yang, Yongbo Yuan, Zhengguo Xiao, Qingfeng Dong, Yu Bi, and Jinsong Huang. A nanocomposite ultraviolet photodetector based on interfacial trap-controlled charge injection. *Nature Nanotechnology*, 7(12):798–802, 2012.
- ¹¹⁰ Ming Liu, Jian Wang, Zijin Zhao, Kaixuan Yang, Pablo Durand, Fabien Ceugniet, Gilles Ulrich, Lianbin Niu, Yao Ma, Nicolas Leclerc, Xiaoling Ma, Liang Shen, and Fujun Zhang. Ultra-Narrow-Band NIR Photomultiplication Organic Photodetectors Based on Charge Injection Narrowing. *Journal of Physical Chemistry Letters*, 12(11):2937–2943, 2021.
- ¹¹¹ P. Peumans, V. Bulović, and S. R. Forrest. Efficient, high-bandwidth organic multilayer photodetectors. *Applied Physics Letters*, 76(26):3855–3857, 2000.
- ¹¹² Mohammad Sedghi, Asghar Gholami, Fatemeh Jahangard, and Hosein Zabolian. Bandwidth and transient analysis of bilayer organic photodetectors. *Organic Electronics*, 49:262–268, 2017.
- ¹¹³ Dezhi Yang, Kai Xu, Xiaokang Zhou, Yanping Wang, and Dongge Ma. Comprehensive studies of response characteristics of organic photodetectors based on rubrene and C60. *Journal of Applied Physics*, 115(24), 2014.
- ¹¹⁴ Francesco Arca, Sandro F. Tedde, Maria Sramek, Julia Rauh, Paolo Lugli, and Oliver Hayden. Interface trap states in organic photodiodes. *Scientific Reports*, 3, 2013.
- ¹¹⁵ Jonas Kublitski, Axel Fischer, Shen Xing, Lukasz Baisinger, Eva Bittrich, Donato Spoltore, Johannes Benduhn, Koen Vandewal, and Karl Leo. Enhancing sub-bandgap external quantum efficiency by photomultiplication for narrowband organic near-infrared photodetectors. *Nature Communications*, 12(1):4259, dec 2021.
- ¹¹⁶ Ardalan Armin, Mike Hambsch, Il Ku Kim, Paul L. Burn, Paul Meredith, and Ebinazar B. Namdas. Thick junction broadband organic photodiodes. *Laser and Photonics Reviews*, 8(6):924–932, 2014.
- ¹¹⁷ Zhenghui Wu, Weichuan Yao, Alexander E. London, Jason D. Azoulay, and Tse Nga Ng. Elucidating the Detectivity Limits in Shortwave Infrared Organic Photodiodes. *Advanced Functional Materials*, 28(18):1–9, 2018.
- ¹¹⁸ Alexander E. London, Lifeng Huang, Benjamin A. Zhang, M. Belén Oviedo, Joshua Tropp, Weichuan Yao, Zhenghui Wu, Bryan M. Wong, Tse Nga Ng, and Jason D. Azoulay. Donor-acceptor polymers with tunable infrared photoresponse. *Polymer Chemistry*, 8(19):2922–2930, 2017.
- ¹¹⁹ Frederik Verstraeten, Sam Gielen, Pieter Verstappen, Jorne Raymakers, Huguette Penxten, Laurence Lutsen, Koen Vandewal, and Wouter Maes. Efficient

BIBLIOGRAPHY

- and readily tuneable near-infrared photodetection up to 1500 nm enabled by thiadiazoloquinoxaline-based push–pull type conjugated polymers. *Journal of Materials Chemistry C*, 8(29):10098–10103, 2020.
- ¹²⁰ Antonio Rogalski. *Infrared Detectors*. CRC Press, 2nd edition, 2010.
- ¹²¹ Chih Cheng Hsieh, Chung Yu Wu, Far Wen Jih, and Tai Ping Sun. Focal-plane-arrays and CMOS readout techniques of infrared imaging systems. *IEEE Transactions on Circuits and Systems for Video Technology*, 7(4):594–605, 1997.
- ¹²² Liang Shen, Yang Zhang, Yang Bai, Xiaopeng Zheng, Qi Wang, and Jinsong Huang. A filterless, visible-blind, narrow-band, and near-infrared photodetector with a gain. *Nanoscale*, 8(26):12990–12997, 2016.
- ¹²³ Andrea Centrone. Infrared Imaging and Spectroscopy Beyond the Diffraction Limit. *Annual Review of Analytical Chemistry*, 8(1):101–126, jul 2015.
- ¹²⁴ Jianquan Zhang, Huei Shuan Tan, Xugang Guo, Antonio Facchetti, and He Yan. Material insights and challenges for non-fullerene organic solar cells based on small molecular acceptors. *Nature Energy*, 3(9):720–731, sep 2018.
- ¹²⁵ Guichuan Zhang, Xian Kai Chen, Jingyang Xiao, Philip C.Y. Chow, Minrun Ren, Grit Kupgan, Xuechen Jiao, Christopher C.S. Chan, Xiaoyan Du, Ruoxi Xia, Ziming Chen, Jun Yuan, Yunqiang Zhang, Shoufeng Zhang, Yidan Liu, Yingping Zou, He Yan, Kam Sing Wong, Veaceslav Coropceanu, Ning Li, Christoph J. Brabec, Jean Luc Bredas, Hin Lap Yip, and Yong Cao. Delocalization of exciton and electron wavefunction in non-fullerene acceptor molecules enables efficient organic solar cells. *Nature Communications*, 11(1):1–10, 2020.
- ¹²⁶ Sylvia J. Lou, Jodi M. Szarko, Tao Xu, Luping Yu, Tobin J. Marks, and Lin X. Chen. Effects of additives on the morphology of solution phase aggregates formed by active layer components of high-efficiency organic solar cells. *Journal of the American Chemical Society*, 133(51):20661–20663, 2011.
- ¹²⁷ Nicola Gasparini, Helen Bristow, Polina Jacoutot, Alberto D. Scaccabarozzi, Maxime Babics, Maximilian Moser, Andrew Wadsworth, Thomas D. Anthopoulos, Artem Bakulin, and Iain McCulloch. Nonfullerene-based organic photodetectors for ultrahigh sensitivity visible light detection. *ACS Applied Materials and Interfaces*, 12(43):48836–48844, 2020.
- ¹²⁸ Jong Baek Park, Jong Woon Ha, Sung Cheol Yoon, Changjin Lee, In Hwan Jung, and Do Hoon Hwang. Visible-Light-Responsive High-Detectivity Organic Photodetectors with a 1 μm Thick Active Layer. *ACS Applied Materials and Interfaces*, 10(44):38294–38301, 2018.
- ¹²⁹ Ardalan Armin, Ross D. Jansen-van Vuuren, Nikos Kopidakis, Paul L. Burn, and Paul Meredith. Narrowband light detection via internal quantum efficiency manipulation of organic photodiodes. *Nature Communications*, 6:6343, 2015.

-
- ¹³⁰ Boming Xie, Ruihao Xie, Kai Zhang, Qingwu Yin, Zhicheng Hu, Gang Yu, Fei Huang, and Yong Cao. Self-filtering narrowband high performance organic photodetectors enabled by manipulating localized Frenkel exciton dissociation. *Nature Communications*, 11(1):1–9, 2020.
- ¹³¹ Zheng Tang, Zaifei Ma, Antonio Sánchez-Díaz, Sascha Ullbrich, Yuan Liu, Bernhard Siegmund, Andreas Mischok, Karl Leo, Mariano Campoy-Quiles, Weiwei Li, and Koen Vandewal. Polymer:Fullerene Bimolecular Crystals for Near-Infrared Spectroscopic Photodetectors. *Advanced Materials*, 1702184:1702184, 2017.
- ¹³² Sascha Ullbrich, Bernhard Siegmund, Andreas Mischok, Andreas Hofacker, Johannes Benduhn, Donato Spoltore, and Koen Vandewal. Fast Organic Near-Infrared Photodetectors Based on Charge-Transfer Absorption. *Journal of Physical Chemistry Letters*, 8(22):5621–5625, 2017.
- ¹³³ William T. Hammond and Jiangeng Xue. Organic heterojunction photodiodes exhibiting low voltage, imaging-speed photocurrent gain. *Applied Physics Letters*, 97(7):2–5, 2010.
- ¹³⁴ Jae Woong Lee, Do Young Kim, and Franky So. Unraveling the gain mechanism in high performance solution-processed PbS infrared PIN photodiodes. *Advanced Functional Materials*, 25(8):1233–1238, 2015.
- ¹³⁵ Hye Ryun Sim, Mingyun Kang, Seong Hoon Yu, Geon Hee Nam, Bogyu Lim, and Dae Sung Chung. Design and Synthesis of a New Non-Fullerene Acceptor for High-Performance Photomultiplication-Type Organic Photodiodes. *Advanced Optical Materials*, 9(4):1–8, 2021.
- ¹³⁶ Riming Nie, Xianyu Deng, Lei Feng, Guiguang Hu, Yangyang Wang, Gang Yu, and Jianbin Xu. Highly Sensitive and Broadband Organic Photodetectors with Fast Speed Gain and Large Linear Dynamic Range at Low Forward Bias. *Small*, 13(24):1–10, 2017.
- ¹³⁷ J. Piotrowski and W. Gawron. Ultimate performance of infrared photodetectors and figure of merit of detector material. *Infrared Physics and Technology*, 38(2):63–68, 1997.
- ¹³⁸ G. Tregnago, C. Fléchon, S. Choudhary, C. Gozálvez, A. Mateo-Alonso, and F. Cacialli. Virtually pure near-infrared electroluminescence from exciplexes at polyfluorene/hexaazatrinaphthylene interfaces. *Applied Physics Letters*, 105(14):1–5, 2014.
- ¹³⁹ Wichard J.D. Beenken, Felix Herrmann, Martin Presselt, Harald Hoppe, Sviatoslav Shokhovets, Gerhard Gobsch, and Erich Runge. Sub-bandgap absorption in organic solar cells: Experiment and theory. *Physical Chemistry Chemical Physics*, 15(39):16494–16502, 2013.

BIBLIOGRAPHY

- ¹⁴⁰ Frank Julian Kahle, Alexander Rudnick, Heinz Bässler, and Anna Köhler. How to interpret absorption and fluorescence spectra of charge transfer states in an organic solar cell. *Materials Horizons*, 5(5):837–848, 2018.
- ¹⁴¹ S. Nunomura, I. Sakata, and K. Matsubara. Impact of band tail distribution on carrier trapping in hydrogenated amorphous silicon for solar cell applications. *Journal of Non-Crystalline Solids*, 436:44–50, 2016.
- ¹⁴² M. Vanecek and A. Poruba. Fourier-transform photocurrent spectroscopy of microcrystalline silicon for solar cells. *Applied Physics Letters*, 80(5):719–721, 2002.
- ¹⁴³ J. W. Tamm, A. Jaeger, A. Bärwolff, T. Elsaesser, A. Gerhardt, and J. Donecker. Aging properties of high power laser diode arrays analyzed by Fourier-transform photocurrent measurements. *Applied Physics Letters*, 71(16):2233–2235, 1997.
- ¹⁴⁴ Nabil M. Amer. Optical Properties of Defect States in a-Si:H. In *Semiconductors and Semimetals*, chapter 3, pages 83–112. Volume 21, edition, 1984.
- ¹⁴⁵ Z. E. Smith, V. Chu, K. Shepard, S. Aljishi, D. Slobodin, J. Kolodzey, S. Wagner, and T. L. Chu. Photothermal and photoconductive determination of surface and bulk defect densities in amorphous silicon films. *Applied Physics Letters*, 50(21):1521–1523, 1987.
- ¹⁴⁶ Qianqian Lin, Ardalan Armin, Dani M. Lyons, Paul L. Burn, and Paul Meredith. Low noise, IR-blind organohalide perovskite photodiodes for visible light detection and imaging. *Advanced Materials*, 27(12):2060–2064, 2015.
- ¹⁴⁷ Xiao Liu, Kan Ding, Anurag Panda, and Stephen R. Forrest. Charge Transfer States in Dilute Donor-Acceptor Blend Organic Heterojunctions. *ACS Nano*, 10(8):7619–7626, 2016.
- ¹⁴⁸ Mohammed Azzouzi, Jun Yan, Thomas Kirchartz, Kaikai Liu, Jinliang Wang, Hongbin Wu, and Jenny Nelson. Nonradiative Energy Losses in Bulk-Heterojunction Organic Photovoltaics. *Physical Review X*, 8(3):31055, 2018.
- ¹⁴⁹ Wenchao Zhao, Deping Qian, Shaoqing Zhang, Sunsun Li, Olle Inganäs, Feng Gao, and Jianhui Hou. Fullerene-Free Polymer Solar Cells with over 11% Efficiency and Excellent Thermal Stability. *Advanced Materials*, 28(23):4734–4739, 2016.
- ¹⁵⁰ Ester Buchaca-Domingo, Koen Vandewal, Zhuping Fei, Scott E. Watkins, Fiona H. Scholes, James H. Bannock, John C. De Mello, Lee J. Richter, Dean M. DeLongchamp, Aram Amassian, Martin Heeney, Alberto Salleo, and Natalie Stingelin. Direct correlation of charge transfer absorption with molecular donor:acceptor interfacial area via photothermal deflection spectroscopy. *Journal of the American Chemical Society*, 137(16):5256–5259, 2015.
- ¹⁵¹ Yajie Jiang, Supriya Pillai, and Martin A Green. Re-evaluation of literature values of silver optical constants. *Optics Express*, 23(3):187–190, 2015.

- ¹⁵² J D'Errico. Bound constrained optimization using fminsearch. *MATLAB Central File Exchange* (retrieved January 12, 2010), 2010.
- ¹⁵³ William H. Press, Saul A. Teukolsky, William T. Vetterling, and Brian P. Flannery. Numerical Recipes in Fortran: The Art of Scientific Computing. In *Numerical Recipes in Fortran: The Art of Scientific Computing*, volume 62, pages 394–444. 2 edition, 1992.
- ¹⁵⁴ Christina Kaiser. Subgapk (source: <https://github.com/KaiserChristina/Subgapk>; date of access: 18.08.2021), 2019.
- ¹⁵⁵ Koen Vandewal, Kristofer Tvingstedt, Abay Gadisa, Olle Inganäs, and Jean V. Manca. On the origin of the open-circuit voltage of polymer–fullerene solar cells. *Nature Materials*, 8(11):904–909, 2009.
- ¹⁵⁶ Carolin M. Sutter-Fella, D. Westley Miller, Quynh P. Ngo, Ellis T. Roe, Francesca M. Toma, Ian D. Sharp, Mark C. Lonergan, and Ali Javey. Band Tailing and Deep Defect States in CH₃NH₃Pb(I_{1-x}Br_x)₃ Perovskites As Revealed by Sub-Bandgap Photocurrent. *ACS Energy Letters*, 2(3):709–715, mar 2017.
- ¹⁵⁷ Jerome H. Perlstein. „Organische Metalle” – Die intermolekulare Wanderung der Aromatizität. *Angew. Chem.*, 89(8):534–549, 1977.
- ¹⁵⁸ J. Alizon, J. Gallice, H. Robert, G. Delplanque, C. Weyl, C. Fabre, and H. Strzelecka. Nouveaux Complexes de Transfert de Charge à Partir des Dipyranylidènes. *Molecular Crystals and Liquid Crystals*, 33(1-2):91–100, 1976.
- ¹⁵⁹ H. Strzelecka, W. Schoenfelder, and J. Rivory. Electrical and Optical Properties of Conducting TCNQ salts. *Mol. Cryst. Liq. Cryst.*, 52:307–318, 1979.
- ¹⁶⁰ A. Weller. Photoinduced Electron Transfer in Solution: Exciplex and Radical Ion Pair Formation Free Enthalpies and their Solvent Dependence. *Zeitschrift für Physikalische Chemie*, 133(1):93–98, 1982.
- ¹⁶¹ Dmitri V. Konarev, Rimma N. Lyubovskaya, Natalya V. Drichko, Evgeniya I. Yudanov, Yury M. Shul'ga, Aleksey L. Litvinov, Viktor N. Semkin, and Boris P. Tarasov. Donor–acceptor complexes of fullerene C₆₀ with organic and organometallic donors. *Journal of Materials Chemistry*, 10(4):803–818, 2000.
- ¹⁶² Kenneth R. Graham, Patrick Erwin, Dennis Nordlund, Koen Vandewal, Ruipeng Li, Guy O. Ngongang Ndjawa, Eric T. Hoke, Alberto Salleo, Mark E. Thompson, Michael D. McGehee, and Aram Amassian. Re-evaluating the role of sterics and electronic coupling in determining the open-circuit voltage of organic solar cells. *Advanced Materials*, 25(42):6076–6082, 2013.
- ¹⁶³ D. V. Konarev, Et al, V N Semkin, A Graja, and R N Lyubovskaya. Steric conditions for donor-acceptor interactions in C₆₀ complexes with planar organic donors. *Journal of Molecular Structure*, 450(1-3):11–22, 1998.

BIBLIOGRAPHY

- ¹⁶⁴ M. V. Kurik. Urbach rule. *Physica Status Solidi (a)*, 8(1):9–45, nov 1971.
- ¹⁶⁵ C. H. Grein and Sajeev John. Temperature dependence of the Urbach optical absorption edge: A theory of multiple phonon absorption and emission sidebands. *Physical Review B*, 39(2):1140–1151, jan 1989.
- ¹⁶⁶ Boris I. Shklovskii and Alex L. Efros. *Electronic Properties of Doped Semiconductors*, volume 45 of *Springer Series in Solid-State Sciences*. Springer Berlin Heidelberg, Berlin, Heidelberg, 1984.
- ¹⁶⁷ Khosrow Rahimi, Ioan Botiz, John O. Agumba, Sajedeh Motamen, Natalie Stingelin, and Günter Reiter. Light absorption of poly(3-hexylthiophene) single crystals. *RSC Advances*, 4(22):11121–11123, 2014.
- ¹⁶⁸ N. Felekidis, A. Melianas, and M. Kemerink. The Role of Delocalization and Excess Energy in the Quantum Efficiency of Organic Solar Cells and the Validity of Optical Reciprocity Relations. *The journal of physical chemistry letters*, 11(9):3563–3570, 2020.
- ¹⁶⁹ Deping Qian, Zilong Zheng, Huifeng Yao, Wolfgang Tress, Thomas R. Hopper, Shula Chen, Sunsun Li, Jing Liu, Shangshang Chen, Jiangbin Zhang, Xiao Ke Liu, Bowei Gao, Liangqi Ouyang, Yingzhi Jin, Galia Pozina, Irina A. Buyanova, Weimin M. Chen, Olle Inganäs, Veaceslav Coropceanu, Jean Luc Bredas, He Yan, Jianhui Hou, Fengling Zhang, Artem A. Bakulin, and Feng Gao. Design rules for minimizing voltage losses in high-efficiency organic solar cells. *Nature Materials*, 17(8):703–709, 2018.
- ¹⁷⁰ Niva A. Ran, John A. Love, Christopher J. Takacs, Aditya Sadhanala, Justin K. Beavers, Samuel D. Collins, Ye Huang, Ming Wang, Richard H. Friend, Guillermo C. Bazan, and Thuc Quyen Nguyen. Harvesting the Full Potential of Photons with Organic Solar Cells. *Advanced Materials*, 28(7):1482–1488, 2016.
- ¹⁷¹ Sha Liu, Jun Yuan, Wanyuan Deng, Mei Luo, Yuan Xie, Quanbin Liang, Yingping Zou, Zhicai He, Hongbin Wu, and Yong Cao. High-efficiency organic solar cells with low non-radiative recombination loss and low energetic disorder. *Nature Photonics*, 14(5):300–305, 2020.
- ¹⁷² Nakul Jain, Naresh Chandrasekaran, Aditya Sadhanala, Richard H. Friend, Christopher R. McNeill, and Dinesh Kabra. Interfacial disorder in efficient polymer solar cells: The impact of donor molecular structure and solvent additives. *Journal of Materials Chemistry A*, 5(47):24749–24757, 2017.
- ¹⁷³ James C. Blakesley and Dieter Neher. Relationship between energetic disorder and open-circuit voltage in bulk heterojunction organic solar cells. *Physical Review B*, 84(7):075210, aug 2011.
- ¹⁷⁴ Ardalan Armin, Nasim Zarrabi, Oskar J. Sandberg, Christina Kaiser, Stefan Zeiske, Wei Li, and Paul Meredith. Limitations of Charge Transfer State Parameterization

- Using Photovoltaic External Quantum Efficiency. *Advanced Energy Materials*, 10(41):2001828, nov 2020.
- ¹⁷⁵ Christina Kaiser, Stefan Zeiske, Paul Meredith, and Ardan Armin. Determining Ultralow Absorption Coefficients of Organic Semiconductors from the Sub-Bandgap Photovoltaic External Quantum Efficiency. *Advanced Optical Materials*, 8(1):1901542, jan 2020.
- ¹⁷⁶ Sam Gielen, Christina Kaiser, Frederik Verstraeten, Jonas Kublitski, Johannes Benduhn, Donato Spoltore, Pieter Verstappen, Wouter Maes, Paul Meredith, Ardan Armin, and Koen Vandewal. Intrinsic Detectivity Limits of Organic Near-Infrared Photodetectors. *Advanced Materials*, 32(47):2003818, nov 2020.
- ¹⁷⁷ Christina Kaiser, Karl Sebastian Schellhammer, Johannes Benduhn, Bernhard Siegmund, Manuel Tropiano, Olaf Zeika, Frank Ortmann, Paul Meredith, Ardan Armin, and Koen Vandewal. Manipulating the Charge Transfer Absorption for Narrowband Light Detection in the Near-Infrared. *Chemistry of Materials*, 31(22):9325–9330, 2019.
- ¹⁷⁸ T. M. Searle and W. A. Jackson. Static versus electron-phonon disorder in amorphous Si: H and its alloys. *Philosophical Magazine B*, 60(2):237–255, aug 1989.
- ¹⁷⁹ G. D. Cody. Urbach edge of crystalline and amorphous silicon: a personal review. *Journal of Non-Crystalline Solids*, 141(C):3–15, 1992.
- ¹⁸⁰ François Leblanc, Yoshihito Maeda, Masahiko Ando, Masatoshi Wakagi, and Tetsuro Minemura. Accurate Determination of the Urbach Energy of a-Si:H Thin Films by Correction for the Interference Effect. *Japanese Journal of Applied Physics*, 33(Part 2, No. 12B):L1755–L1758, dec 1994.
- ¹⁸¹ Jau Tang. Electron-transfer reactions involving non-linear spin-boson interactions. *Chemical Physics*, 188(2-3):143–160, nov 1994.
- ¹⁸² Jesús Casado-Pascual, Manuel Morillo, Igor Goychuk, and Peter Hänggi. The role of different reorganization energies within the Zusman theory of electron transfer. *The Journal of Chemical Physics*, 118(1):291–303, jan 2003.
- ¹⁸³ Thomas H. Keil. Theory of the Urbach Rule. *Physical Review*, 144(2):582–587, apr 1966.
- ¹⁸⁴ Samantha N Hood, Aron Walsh, Clas Persson, Konstantina Iordanidou, Dan Huang, Mukesh Kumar, Zacharie Jehl, Maykel Courel, Johan Lauwaert, and Sanghyun Lee. Status of materials and device modelling for kesterite solar cells. *Journal of Physics: Energy*, 1(4):042004, 2019.
- ¹⁸⁵ Allen Miller and Elihu Abrahams. Impurity conduction at low concentrations. *Physical Review*, 120(3):745–755, 1960.

BIBLIOGRAPHY

- ¹⁸⁶ Yong Cui, Huifeng Yao, Jianqi Zhang, Kaihu Xian, Tao Zhang, Ling Hong, Yuming Wang, Ye Xu, Kangqiao Ma, Cunbin An, Chang He, Zhixiang Wei, Feng Gao, and Jianhui Hou. Single-Junction Organic Photovoltaic Cells with Approaching 18% Efficiency. *Advanced Materials*, 32(19):1–7, 2020.
- ¹⁸⁷ Byeongseop Song, Cedric Rolin, Jeramy D. Zimmerman, and Stephen R. Forrest. Effect of mixed layer crystallinity on the performance of mixed heterojunction organic photovoltaic cells. *Advanced Materials*, 26(18):2914–2918, 2014.
- ¹⁸⁸ Deepak Venkateshvaran, Mark Nikolka, Aditya Sadhanala, Vincent Lemaure, Mateusz Zelazny, Michal Kepa, Michael Hurhangee, Auke Jisk Kronemeijer, Vincenzo Pecunia, Iyad Nasrallah, Igor Romanov, Katharina Broch, Iain McCulloch, David Emin, Yoann Olivier, Jerome Cornil, David Beljonne, and Henning Sirringhaus. Approaching disorder-free transport in high-mobility conjugated polymers. *Nature*, 515(7527):384–388, 2014.
- ¹⁸⁹ William Shockley and Hans J. Queisser. Detailed balance limit of efficiency of p-n junction solar cells. *Journal of Applied Physics*, 32(3):510–519, 1961.
- ¹⁹⁰ Yanjun Fang, Ardalan Armin, Paul Meredith, and Jinsong Huang. Accurate characterization of next-generation thin-film photodetectors. *Nature Photonics*, 13(1):1–4, 2019.
- ¹⁹¹ Xiaowen Hu, Kai Wang, Chang Liu, Tianyu Meng, Yang Dong, Shengjian Liu, Fei Huang, Xiong Gong, and Yong Cao. High-detectivity inverted near-infrared polymer photodetectors using cross-linkable conjugated polyfluorene as an electron extraction layer. *Journal of Materials Chemistry C*, 2(45):9592–9598, 2014.
- ¹⁹² Katie D. Rosenthal, Michael P. Hughes, Benjamin R. Luginbuhl, Niva A. Ran, Akchheta Karki, Seo Jin Ko, Huawei Hu, Ming Wang, Harald Ade, and Thuc Quyen Nguyen. Quantifying and Understanding Voltage Losses Due to Nonradiative Recombination in Bulk Heterojunction Organic Solar Cells with Low Energetic Offsets. *Advanced Energy Materials*, 9(27):1–11, 2019.
- ¹⁹³ Thorlabs. Thorlabs Calibrated Photodiodes (source: https://www.thorlabs.de/newgrouppage9.cfm?objectgroup_id=2822 ; date of access: 15.08.2021).
- ¹⁹⁴ Ke Zhou, Yanfeng Liu, Awwad Alotaibi, Jian Yuan, Chuanxiu Jiang, Jingming Xin, Xinfeng Liu, Brian A. Collins, Fengling Zhang, and Wei Ma. Molecular and Energetic Order Dominate the Photocurrent Generation Process in Organic Solar Cells with Small Energetic Offsets. *ACS Energy Letters*, 5(2):589–596, 2020.
- ¹⁹⁵ Mohammed Azzouzi, Thomas Kirchartz, and Jenny Nelson. Factors Controlling Open-Circuit Voltage Losses in Organic Solar Cells. *Trends in Chemistry*, 1(1):49–62, 2019.

- ¹⁹⁶ Andrew Wadsworth, Maximilian Moser, Adam Marks, Mark S. Little, Nicola Gasparini, Christoph J. Brabec, Derya Baran, and Iain McCulloch. Critical review of the molecular design progress in non-fullerene electron acceptors towards commercially viable organic solar cells. *Chemical Society Reviews*, 48(6):1596–1625, 2019.
- ¹⁹⁷ Zhiwei Zhang, Guoqing Miao, Hang Song, Dabing Li, Hong Jiang, Zhiming Li, Yiren Chen, and Xiaojuan Sun. High in content InGaAs near-infrared detectors: growth, structural design and photovoltaic properties. *Applied Physics A*, 123(4):219, apr 2017.
- ¹⁹⁸ Kristofer Tvingstedt and Carsten Deibel. Temperature Dependence of Ideality Factors in Organic Solar Cells and the Relation to Radiative Efficiency. *Advanced Energy Materials*, 6(9):1–13, 2016.
- ¹⁹⁹ Lin Zhang, Heng Zhao, Baojun Lin, Jian Yuan, Xianbin Xu, Jingnan Wu, Ke Zhou, Xia Guo, Maojie Zhang, and Wei Ma. A blade-coated highly efficient thick active layer for non-fullerene organic solar cells. *J. Mater. Chem. A*, 7:22265–22273, 2019.
- ²⁰⁰ Adane Desta Fenta, Chun-fu Lu, Abraha Tadesse Gidey, and Chin-ti Chen. High Efficiency Organic Photovoltaics with a Thick (300 nm) Bulk Heterojunction Comprising a Ternary Composition of a PFT Polymer–PC71BM Fullerene–IT4F Nonfullerene Acceptor. *ACS Applied Energy Materials*, 4(5):5274–5285, may 2021.
- ²⁰¹ Guanghong Liu, Tengfei Li, Xiaowei Zhan, Hongbin Wu, and Yong Cao. High-Sensitivity Visible-Near Infrared Organic Photodetectors Based on Non-Fullerene Acceptors. *ACS Applied Materials and Interfaces*, 12(15):17769–17775, 2020.
- ²⁰² Tianyi Zhang, Maximilian Moser, Alberto D Scaccabarozzi, Helen Bristow, Polina Jacoutot, Andrew Wadsworth, Thomas D Anthopoulos, Iain McCulloch, and Nicola Gasparini. Ternary organic photodetectors based on pseudo-binaries nonfullerene-based acceptors. *Journal of Physics: Materials*, 4(4):045001, oct 2021.
- ²⁰³ Woongsik Jang, Shafket Rasool, Byung Gi Kim, Jehan Kim, Jinhwan Yoon, Sergei Manzhos, Hang Ken Lee, Il Jeon, and Dong Hwan Wang. Superior Noise Suppression, Response Time, and Device Stability of Non-Fullerene System over Fullerene Counterpart in Organic Photodiode. *Adv. Funct. Mater.*, 30(2001402):1–12, 2020.
- ²⁰⁴ Reinhard Scholz, Regina Luschtinetz, Gotthard Seifert, Till Jägeler-Hoheisel, Christian Körner, Karl Leo, and Mathias Rapacioli. Quantifying charge transfer energies at donor–acceptor interfaces in small-molecule solar cells with constrained DFTB and spectroscopic methods. *Journal of Physics: Condensed Matter*, 25(47):473201, 2013.
- ²⁰⁵ Xinyang Wang, Fan Zhang, Karl Sebastian Schellhammer, Peter Machata, Frank Ortmann, Gianaurelio Cuniberti, Yubin Fu, Jens Hunger, Ruizhi Tang, Alexey A. Popov, Reinhard Berger, Klaus Müllen, and Xinliang Feng. Synthesis of NBN-Type

BIBLIOGRAPHY

- Zigzag-Edged Polycyclic Aromatic Hydrocarbons: 1,9-Diaza-9a-boraphenylene as a Structural Motif. *Journal of the American Chemical Society*, 138(36):11606–11615, 2016.
- ²⁰⁶ Frederik Verstraeten, Sam Gielen, Pieter Verstappen, Jurgen Kesters, Epimitheas Georgitzikis, Jorne Raymakers, David Cheyns, Pawel Malinowski, Michaël Daenen, Laurence Lutsen, Koen Vandewal, and Wouter Maes. Near-infrared organic photodetectors based on bay-annulated indigo showing broadband absorption and high detectivities up to 1.1 μm . *Journal of Materials Chemistry C*, 6(43):11645–11650, 2018.
- ²⁰⁷ Koen Vandewal, Johannes Benduhn, Karl Sebastian Schellhammer, Tim Vangerven, Janna E. Rückert, Fortunato Piersimoni, Reinhard Scholz, Olaf Zeika, Yeli Fan, Stephen Barlow, Dieter Neher, Seth R. Marder, Jean Manca, Donato Spoltore, Gianaurelio Cuniberti, and Frank Ortmann. Absorption tails of donor:C60 blends provide insight into thermally activated charge-transfer processes and polaron relaxation. *Journal of the American Chemical Society*, 139(4):1699–1704, 2017.